Thermal and Magnetic Studies of Spin Ice Compounds

Jonathan Arthur Bloxsom

UCL

PhD

I, Jonathan Arthur Bloxsom confirm that the work presented in this thesis is my own. Where information has been derived from other sources, I confirm that this has been indicated in the thesis.

Dysprosium titanate and holmium titanate crystals were provided by D. Prabhakaran of the University of Oxford. Cadmium erbium selenite powder was provided by J. Lago of the University del Pas Vasco. Praseodymium zirconate crystal was provided by K. Matsuhira of the Kyushu Institute of Technology.

Experiments were performed by L. Bovo of the London Centre for Nanotechnology, University College London. Magnetic relaxation data for dysprosium titanate was provided by C. Paulsen of the Université Joseph Fourier. Specific heat data for praseodymium zirconate was digitised from publication by K. Kimura *et al.*.

Abstract

In recent years a great deal of interest has been attracted by the materials called 'spin ices', and the monopole-like quasiparticle excitations inside them. Spin ices are frustrated Ising ferromagnets with a high level of frustration arising from a spin configuration akin to the proton configuration of water ice. Excitations of the ground state configurations can produce local arrangements of spins which behave similarly to magnetic monopoles, including carrying an effective magnetic charge and experiencing Coulomb interactions with one another. By taking these 'monopoles' as the units of analysis, theories of charged particle interaction can be applied to magnetic spin ice crystals.

This thesis will examine the applicability of a number of theories based on this model to experimental data of the real properties of spin ice, along with a novel experimental method, and in turn report on what the results suggest about the physical nature of the spin ices in question. The main materials studied are dysprosium titanate ($Dy_2Ti_2O_7$) and holmium titanate ($Ho_2Ti_2O_7$), and additional investigations are performed on cadmium erbium selenide ($CdEr_2Se_4$) and praseodymium zirconate ($Pr_2Zr_2O_7$).

First, a new derivation of the Debye-Hückel theory of electrolytes adapted for spin ice is presented, incorporating a microscopically correct partition function and the effects of higher-energy excitations, called 'double monopoles'. The theory is compared to specific heat experimental and simulation data for $Ho_2Ti_2O_7$ and $Dy_2Ti_2O_7$ and experimental data for $CdEr_2Se_4$. It is found that Debye-Hückel theory is an effective analytic theory of spin ice magnetic heat capacity even into high temperatures of 6 K or more, in contrast to earlier work which held that such temperatures are out of the effective region of the spin ice model. Extensions of the theory to account for lattice geometry, Bjerrum pairing and 'entropic charge' are considered.

Second, several theories for describing the magnetic relaxation of spin ice are compared to experimental data from $Dy_2Ti_2O_7$ at 0.4 to 0.6 K. The theories encompass the Wien effect seen in electrolytes, surface effects and the failure of the samples to equilibrate on experimental timescales. The results are inconclusive and suggest that multiple effects must be considered to form a complete theory of

spin ice relaxation at low temperatures.

Third, an absolute measurement of the entropy of the quantum spin ice $Pr_2Zr_2O_7$ using a recently introduced method is reported and compared to previous work on the material, along with a prediction of its specific heat using Debye-Hückel theory. The results demonstrate that the method is effective at low temperatures and suggest that the low-temperature entropy of $Pr_2Zr_2O_7$ is less than that of classical spin ices, and that its monopole dynamics are significantly different.

Acknowledgements

I would like to thank my principal supervisor Steven Bramwell for his support and patience over the course of this PhD. Whenever I went to him with a problem I would leave feeling I had not just understanding of the problem, but new insight.

I would like to thank Laura Bovo, for her tireless assistance in the laboratory. I would like to thank Des McMorrow, Simon Banks, Michael Faulkner, Marion Brooks-Bartlett and all the members of the Spin Ice Group for support and discussions. I would like to thank all the LCN staff for their assistance whenever I required it. I would like to thank the family and friends who supported me over the last few years.

Lastly, I would like to thank UCL and the EPSRC for funding this research.

Contents

List of Figures

List of Tables

Chapter 1

Introduction

A critical difference between electricity and magnetism in traditional theory is the nonexistence of true magnetic charges. Despite the predictions of many unification theories and extensive searches, fundamental magnetic charges, or monopoles, have not been observed [1]. Nevertheless the notion of the magnetic monopole has recently found use in describing the behaviour of certain frustrated magnets. Members of the 'spin ice' class of magnetically frustrated crystals [2] emulate the electric structure of water ice magnetically, and this extends to replicating electric charge defects in water with effective magnetic charge defects in crystals [3]. This surprising result gives rise to a symmetry between electrical and magnetic behaviour that extends to the remarkable possibility of modelling spin ice not as a crystal containing magnetic dipoles, but as a Coulomb gas of magnetic monopoles.

Based on this interpretation, the Debye-Hückel theory of electrolytes has been adapted and applied to the 'magnetolyte' of spin ice [4]. This unusual marriage has been successful in modelling spin ice behaviour, but also revealed a number of problems that impede the creation of a complete theory. In chapter 3 of this thesis the theory and its implementation is explored, the problems are highlighted, and the current progress on solving the problems and expanding the theory is outlined.

Beyond Debye-Hückel theory, which considers the system in zero field, the magnetic relaxation behaviour of spin ices is distinctive and worthy of study, due to the way magnetic charges are generated, destroyed and move inside the system. Chapter 4 of this thesis will consider recent studies of low-temperature relaxation

[5, 6, 7] and compare several distinct models against relaxation data.

In chapter 5, a recently devised method for determining the magnetic entropy of materials will be tested on a candidate quantum spin ice [8], to both investigate its physical properties and relation to the classical spin ices and the strengths and limitations of the method.

It is hoped that exploration of emergent monopoles will reveal new physics and possibilities in condensed matter, aid in the understanding of water ice, and perhaps better equip us to tackle fundamental monopoles if and when they are discovered.

1.1 Electricity and Magnetism

Of the four traditional physical interactions, the one that dominates scales from the atomic to the terrestrial is electromagnetism. As the name suggests this is the union of the electrical and magnetic interactions known to premodern science, as described by the macroscopic Maxwell equations [9]:

$$\nabla \cdot \mathbf{E} = \frac{\rho_e}{\epsilon_0} \tag{1.1}$$

$$\nabla \cdot \mathbf{B} = 0 \tag{1.2}$$

$$-\nabla \times \mathbf{E} = \frac{\partial \mathbf{B}}{\partial t} \tag{1.3}$$

$$\nabla \times \mathbf{B} = \mu_0 \left(\mathbf{J} + \epsilon_0 \frac{\partial \mathbf{E}}{\partial t} \right) \tag{1.4}$$

where $\mathbf{E}$ is the electrical field, $\mathbf{B}$ is the magnetic field, ρ_e is electrical charge density, $\mathbf{J}$ is the current density, ϵ_0 is the electric permittivity of free space, and μ_0 is the magnetic permeability of free space.

There is a limited but incomplete symmetry between these equations. The missing element is 'magnetic charge', defined by divergence in $\mathbf{B}$ ($\nabla \cdot \mathbf{B} \neq 0$). Electrical fields can have net divergence in a given volume, represented by ρ_e in equation 1.1. This divergence is associated with fundamental particles carrying electric charge. If an equivalent magnetic charge existed, it could be added to the equations to obtain the following symmetric Maxwell equations:

$$\nabla \cdot \mathbf{E} = \frac{\rho}{\epsilon_0} \tag{1.5}$$

$$\nabla \cdot \mathbf{B} = \mu_0 q \tag{1.6}$$

$$-\nabla \times \mathbf{E} = \mathbf{J}_m + \frac{\partial \mathbf{B}}{\partial t} \tag{1.7}$$

$$\nabla \times \mathbf{B} = \mu_0 \left(\mathbf{J} + \epsilon_0 \frac{\partial \mathbf{E}}{\partial t} \right) \tag{1.8}$$

where q is the magnetic charge density and $\mathbf{J}_m$ is the magnetic current density.

In 1931 Paul Dirac [10] theoretically defined the necessary characteristics of this magnetic charge despite its never having being observed experimentally. He found that the existence of a magnetic monopole imposes a quantisation condition on the electron:

$$\frac{eg}{4\pi\hbar} = \frac{n}{2} \tag{1.9}$$

where e is the electronic charge, g is the magnetic charge, and n is some integer. Thus the existence of true magnetic charge would underpin the discrete nature of electric charge. A reversed argument shows that electric charge guarantees that magnetic charge is quantised. However, this theoretical desirability, reflected in more modern fundamental physical theories, has not given way to empirical discovery, despite one tantalising but unreplicated signature in a 1982 superconducting loop experiment [11].

It is worth noting at this point that the existence or nonexistence of true magnetic charge is not objective and fundamental, but is partly an artefact of conventions. Jackson 1998 [12] notes that the quantities can be transformed as follows:

$$\mathbf{E} = \mathbf{E}'\cos\,\xi + \mathbf{B}'\sin\,\xi \tag{1.10}$$

$$\mathbf{B} = -\mathbf{E}'\sin\,\xi + \mathbf{B}'\cos\,\xi \tag{1.11}$$

and the sources similarly:

$$\rho = \rho'\cos\,\xi + q'\sin\,\xi \tag{1.12}$$

$$q = \rho' \sin \xi + q' \cos \xi \tag{1.13}$$

with equivalent transformations for $\mathbf{J}$ and $\mathbf{J}_m$. If one envisions electromagnetic charge as defined by points in a two-dimensional plane with the x axis representing electric charge and the y axis magnetic, this transformation represents a rotation of the coordinate axes by an angle ξ.

Under these transformations the Maxwell relations still apply. When $\xi = 0$ there is no change in values, and $q = 0$ implies $q' = 0$. However, if we choose $\xi \neq 0$, $q = 0$ applied to equation 1.13 directly yields $\rho'/q' = -\cos \xi / \sin \xi$. The new electric and magnetic charge are connected by a constant ratio, which applies to all charged particles. If $q \neq 0$ however, this relation does not hold. As such we can see that the most fundamental question is not whether magnetic charge exists, which is a matter of convention, but whether the interaction of a particle with the electromagnetic force is specified by one number, or two.

The concept of magnetic charge used in condensed matter physics, and of magnetic monopoles used in this work, does not require violation of the traditional Maxwell equations or the introduction of a second electromagnetic variable in fundamental physics [3]. Nevertheless it stands as an example of how condensed matter systems can produce counterintuitive results that emulate unusual physical properties.

1.1.1 Magnetism in Materials

Electromagnetism is the interaction that holds atoms and atomic structures together. The complex electric microstructure of materials can give rise to equally complex magnetic structure. The treatment here is primarily derived from Blundell 2001 [13].

As can be seen from the Maxwell equations, magnetic fields can be generated by loops of current. Consider a current I around the circumference of an area dS, defined by a vector $d\mathbf{S}$ of length equal to the area and perpendicular to its plane. This defines a magnetic moment $d\mu = I d\mathbf{S}$.

These loops can be created not just macroscopically but also on the scale of individual atoms. An electron bound to a nucleus possesses an angular momentum composed of its inherent spin and its orbital angular momentum, and this angular

momentum of a charge defines a current around the nucleus, which generates a magnetic field. This field takes the form of a dipole and so atoms whose orbital electrons have net angular momentum can be considered in classical analogy as bar magnets. Macroscopic solid magnets are composed of large numbers of similarly-aligned magnetic atoms, often referred to as 'spins'.

The orbital and intrinsic (or 'spin') angular momentum of electrons in atoms are governed by quantum mechanics. The magnitude of the orbital angular momentum is given by $L = \sqrt{l(l+1)}\hbar$ and its component along a particular fixed axis (typically the z-axis) by $m_l\hbar$, with l and m_l quantum numbers and l some integer. The equivalent quantities for intrinsic spin are defined similarly using S, s and m_s, with $s = 1/2$ for electrons. The magnitude of the components of angular momentum can only take the values defined by $m_l = l, l-1, ... -l$, and similarly for m_s. Due to the uncertainty principle, it is not possible to know more than one component of the spin simultaneously, but it is possible to know one component and the total magnitude of the spin simultaneously.

The magnetic moment created by an atom is proportional to its total angular momentum $\mathbf{J} = \mathbf{L} + \mathbf{S}$, where $\mathbf{L}$ and $\mathbf{S}$ are the total orbital and spin angular momenta respectively of all the electrons in the atom. The magnetic moment is given by $\mu = \gamma\mathbf{J}$, where γ is called the 'gyromagnetic ratio'. The gyromagnetic ratio is $\gamma = -g_J\mu_B$, where μ_B is the Bohr magneton, the ground state magnetic moment of a hydrogen atom, and g_J is called the Landè g-factor.

The possible values of the orbital and intrinsic angular momenta define the occupiable states of the system. Electrons are fermions, a class of particle with half-integer spin, which are constrained by the Pauli exclusion principle, which holds that only one fermion can occupy a given quantum state at a given time [13]. As electrons are fermions, they cannot share quantum states, and the addition of electrons to the system will fill up available states. If all the electrons in an atom of a given m_l and m_s value can be paired with another with the opposite m_l and m_s values, then the atom can have $\mathbf{J} = \mathbf{L} = \mathbf{S} = 0$ and no magnetic moment unless one is created by external fields. If it has unpaired electrons however, it has an inherent magnetic moment even in the absence of a field.

The combination of angular momentum quantum numbers that minimises the energy is estimated by three principles called Hund's rules. The rules are ordered

in descending order of typical energy level and so importance for electron ordering [13].

Hund's first rule is to maximise **S**, by aligning all electron spins in one direction. Pauli exclusion means that electrons cannot share states, so electrons with identical spin states cannot occupy the same spaces. Separating them this way reduces their Coulomb repulsion energy.

The second rule is to maximise **L**. In classical analogy, electrons orbiting in the same direction will meet less often, again reducing their Coulomb repulsion.

The third rule states that the value of **J** is given by $|J| = |L - S|$ if the outermost shell is half or less full, and $|J| = |L + S|$ otherwise. This effect arises from the spin-orbit coupling, whereby the magnetic field created at the electron site by the nucleus orbiting in its frame of reference splits the levels of the electron spin. This effect couples the orbital and spin angular momenta of the electron. It is sufficently small that it is often overriden by additional factors such as the crystal field (see section 1.1.4), but is effective for rare earth ions such as Dy^{3+} and Ho^{3+}.

Atomic states are written in the form ${}^{X}Y_{Z}$, where $X = 2S + 1$, Y is a letter code representing L as defined in table 1.1, and $Z = J$.

Table 1.1: Atom L Values

L	0	1	2	3	4	5	6
	S	P	D	F	G	H	I

In this notation, the ground state of free Ho^{3+} ions is ${}^{5}I_{8}$, and the ground state of free Dy^{3+} ions is ${}^{6}H_{15/2}$. Hund's third rule applies additively in each case.

1.1.2 Magnetisation and Susceptibility

The magnetic moment per unit volume of a material is the magnetisation **M**. This is distinct from the magnetic field generated by those moments and other sources such as externally applied fields. This field is denoted by **H**. At any point in space the magnetic field **B** is defined as

$$\mathbf{B} = \mu_0(\mathbf{H} + \mathbf{M}). \tag{1.14}$$

In free space with no magnetic moments, this resolves to $\mathbf{B} = \mu_0\mathbf{H}$ and the one vector field is simply a scaled version of the other. Inside a magnetic material where $\mathbf{M} \neq 0$, the magnetisation must be considered. The two vector fields $\mathbf{M}$ and $\mathbf{H}$ affect one another, as magnetic moments will be aligned by the field and will in turn generate a field of their own. In a material where there is a linear relationship, called a linear material, they have the relation $\mathbf{M} = \chi\mathbf{H}$, with χ being the dimensionless 'magnetic susceptibility' of the material. For this case, equation 1.14 becomes:

$$\mathbf{B} = \mu_0(1 + \chi)\mathbf{H} = \mu_0\mu_r\mathbf{H}, \tag{1.15}$$

defining $\mu_r = 1 + \chi$ as the 'relative permeability' [13].

The above susceptibility is the 'volume susceptibility' for the magnetic moment by volume. The molar susceptibility χ_m and the mass susceptibility χ_g can also be defined, in relation to the magnetic moment per mole or mass.

Magnetic response is not instantaneous, as will be explored in chapter 4 of this thesis. When the applied field oscillates with frequency ω, this is called an a.c. ('alternating current') field after the electric equivalent of an oscillating voltage producing an 'alternating' rather than 'direct' current. In such conditions the susceptibility becomes the complex a.c. susceptibility $\chi(\omega)$ where $\chi(0)$ is equal to the normal (d.c., 'direct current') susceptibility. The a.c. susceptibility consists of a magnitude (here $|\chi|$) and a phase shift ϕ by which the oscillation of the magnetisation lags the oscillation of the driving field. The a.c. susceptibility is often treated as having two parts, the real part χ' and the imaginary part χ'':

$$\chi = |\chi|e^{i\phi} = |\chi|(\cos\phi + i\sin\phi) \tag{1.16}$$

$$\chi' = |\chi|\cos\phi \tag{1.17}$$

$$\chi'' = |\chi|\sin\phi \tag{1.18}$$

When the field does not oscillate but is constant, the magnetisation is called

the d.c. magnetisation.

The reciprocal effect of $\mathbf{M}$ on $\mathbf{H}$ must also be considered. Consider a field $\mathbf{H}_a$ applied to a magnetic material. The material contains magnetic moments aligned in some fashion to create magnetisation field $\mathbf{M}$ throughout the sample. These magnetic moments will create a magnetic field that adds to the applied magnetic field $\mathbf{H}_a$ to create the internal magnetic field $\mathbf{H}_i$. So at some point $\mathbf{r}$ in the material:

$$\mathbf{H}_i = \mathbf{H}_a + \mathbf{F}(\mathbf{r}), \tag{1.19}$$

where $\mathbf{F}$ is the field created by all moments in the sample at that point in the sample. This depends not just on the magnetic physics of the material but also on its shape, and in general can be complex to work out. It is most easily defined for the special case of an ellipsoidal sample with field applied along a principal axis. For such samples, $\mathbf{F} = -N\mathbf{M}$, with N being a constant for that ellipsoid called the 'demagnetising factor'. This yields

$$\mathbf{H}_i = \mathbf{H}_a - N\mathbf{M}, \tag{1.20}$$

and if we define an applied $\mathbf{B}_a$ and an internal $\mathbf{B}_i$ similarly to $\mathbf{H}$, we obtain:

$$\mathbf{B_i} = \mu_0(\mathbf{H}_i + \mathbf{M}) = \mu_0(\mathbf{H}_a + (1 - N)\mathbf{M}). \tag{1.21}$$

Since the applied field has no magnetisation component, $\mathbf{B}_a = \mu_0\mathbf{H}_a$, so

$$\mathbf{B_i} = \mathbf{B}_a + \mu_0(1 - N)\mathbf{M}. \tag{1.22}$$

This definition of $\mathbf{B}$ in terms of two fields $\mathbf{M}$ and $\mathbf{H}$ allows us to see how objects akin to magnetic monopoles can exist without violating the Maxwell equations. Note in equation 1.2 that only $\mathbf{B}$ is required to have a divergence of 0 at all points. As $\mathbf{B}$ is defined in equation 1.14 as the linear sum of two other quantities, divergence in these quantities can exist so long as divergence in one is exactly cancelled by divergence in the other at all points:

$$\nabla \cdot \mathbf{M} = -\nabla \cdot \mathbf{H}. \tag{1.23}$$

This allows the definition of an effective magnetic charge density $\rho_H = \nabla \cdot \mathbf{H}$, which has applications in the practical study of magnets [3]. However, this quantity is not discrete on all scales. It necessarily cannot be defined on scales smaller than the magnetic moments that constitute the material in question, and does not typically resolve into discrete objects like the true charges of electrostatics.

1.1.3 Paramagnetism

If χ is positive, the system is called paramagnetic, and if negative it is diamagnetic. Paramagnetism will arise in a system with magnetic atoms (atoms with unpaired electrons) and weak interactions between the magnetic moments. Diamagnetism will arise in systems with paired electrons. All systems exhibit a degree of diamagnetism as all systems contain paired electrons, but the effect is weak and easily dominated by other interactions if present [13].

In the limit of low field, the susceptibility of paramagnets is described by the Curie law [13]:

$$\chi = \frac{n\mu_0\mu_{\text{eff}}^2}{3k_BT}, \tag{1.24}$$

where μ_{eff} is an effective moment given by $\mu_{\text{eff}} = g_J\mu_B\sqrt{J(J+1)}$. The existence of a $1/T$ proportionality in χ is an experimental signature of paramagnetism. It can be written as

$$\chi = \frac{C}{T} \tag{1.25}$$

where C is the Curie constant.

1.1.4 The Crystal Field

In an ideal Curie-law paramagnet spins have no interaction with their neighbouring spins or the crystal environment, but this is not always a reasonable approximation. Often spins are strongly constrained by these factors. All atoms in solids are affected by their electronic environment, as it is electrostatic interactions that bind solids together. But besides fixing the physical location of a given atom, the surrounding crystal environment also interacts with the electronic orbitals and so alters the magnetic properties of the atom.

Different L and m_L values generate different spatial distributions of the orbiting electron around the nucleus. As electrons have electrostatic charge they exist in energy potentials relative to one another, and so differing spatial distributions of an orbiting electron will have differing energy levels depending on how they are arranged relative to the orbiting electrons of the surrounding atoms, which are subject to the same effect from their surrounding atoms. This effect lifts the degeneracy of the orbitals and favours states that distribute the electrons away from contact with their neighbours. The field generated by surrounding environment is called the 'crystal electric field' or 'crystal field' [13].

As atomic magnetic properties are dominated by electron angular momenta, this favouring of particular orbital states also favours particular magnetic states. An example key to spin ice is the Ising spin, in which the ground state of the outer electron orbitals has the maximum angular momentum parallel or antiparallel to the z-axis, producing a powerful magnetic dipole moment oriented likewise. So long as it remains in the ground state, the atom can flip between these orientations without passing through any intervening states.

In holmium titanate, the crystal field of the oxide ions surrounding the Ho^{3+} splits the ${}^5I_8$ free ion state. The ground state is an almost pure $J = 8$, $m_J = \pm 8$ doublet, where the angular momentum is constrained to point parallel or antiparallel to the z-axis [14]. Dysprosium ions are similarly constrained in dysprosium titanate [15]. This type of two-state single-axis spin state distribution is called an Ising spin. Directional dependence of this sort is known as 'anisotropy', and Ising spins are a form of 'easy-axis anisotropy'.

1.1.5 Dipole Interaction

Besides the electrostatic interaction with nearby atoms, atoms can also interact magnetically.

The most obvious magnetic interaction mechanism is the dipole interaction. This is the familiar attraction and repulsion of magnets realised on the microscopic scale. The dipolar Hamiltonian for two magnetic moments μ_1 and μ_2 at a distance r is given by [13]:

$$\hat{H} = \frac{\mu_0}{4\pi r^3}\left[\mu_1 \cdot \mu_2 - \frac{3}{r^2}(\mu_1 \cdot \mathbf{r})(\mu_2 \cdot \mathbf{r})\right]. \tag{1.26}$$

For two dipoles of magnitude $\mu = \mu_B$ separated by $r = 1$ Å, the energy is of order 10^{-23}J, approximately equivalent to 1 K. However many magnetic systems can maintain order at much higher temperatures than 1 K, so more ordering principles must be at work in these materials [13].

1.1.6 Exchange Interaction

The dominant interaction governing magnetic ordering in materials is the exchange interaction [13]. Exchange is an electrostatic interaction arising from the constraints placed on the electron wavefunctions by the Pauli principle. This principle requires that a wavefunction of two fermions, such as electrons, must be antisymmetric under exchange of the particles. The wavefunction of two elections is the product of a spatial function and a spin function and so for the product to be antisymmetric one of these functions must be symmetric and the other antisymmetric.

As the electrons have electric charge, a change in their spatial distribution produces a change in their energy. As spatial and spin functions are connected via the Pauli principle, this coupling between charge spatial distributions produces an effective coupling between their spins, and so their magnetic moments.

So the exchange Hamiltonian of a two-electron system can be given by

$$\hat{H}_{\text{exchange}} = -2J_{1,2}\mathbf{S}_1 \cdot \mathbf{S}_2. \tag{1.27}$$

where J is the exchange coupling constant. If J is negative the exchange interaction is antiferromagnetic (favours opposite spin directions). If it is positive the exchange interaction is ferromagnetic (favours similar spin directions).

There are several classes of exchange interaction. 'Direct exchange' is the simplest and refers to interactions between electrons on neighbouring atoms. If neighbouring orbitals overlap their electrons can become correlated, forming a bonding (spatially symmetric) or more rarely antibonding (spatially antisymmetric) orbital. These lower energy by expanding the volume over which the electrons are distributed to the orbitals of both atoms, akin to increasing the size of a

particle-in-a-box model. This phenomenon is the 'covalent bond' that underlies many molecular structures. However, its significance for magnetic structure is limited. It is often the case that magnetic orbitals of neighbouring atoms do not significantly overlap. 'Indirect exchange' is an exchange interaction that operates via some mediator that connects the magnetic orbitals.

Superexchange is exchange mediated by a third nonmagnetic atom with which the two magnetic orbitals overlap. In figure 1.1 an example is shown for two transition metal atoms with single electrons in their outer shell. The three atoms have bonds over which their electrons can delocalise. If the two electrons on the magnetic atoms have opposite spin alignment, they can be separated between the atoms, or both occupy either single magnetic atom. This expands their occupation volume and reduces the energy of the electrons as described above. If they have a parallel alignment, however, they are forbidden from occupying the same atom orbital by Pauli exclusion, and do not benefit from the expanded occupation volume and lowered energy. Superexchange is usually antiferromagnetic, but ferromagnetic superexchange can occur [13].

The RKKY (Ruderman, Kittel, Kasuya and Yoshida) interaction, also called 'itinerant exchange', is a form of exchange found in metals [13]. It is mediated by conduction electrons which are polarised by one magnetic moment and then, thus polarised, couple to a different magnetic moment. For large r, the coupling constant takes the form

$$J_{\mathrm{RKKY}} \propto \frac{\cos(2k_F r)}{r^3} \tag{1.28}$$

where k_F is the radius of the Fermi surface. The oscillatory dependence on separation introduced by the cosine term leads to an interaction that is ferromagnetic or antiferromagnetic dependent on distance.

Double exchange arises in systems containing magnetic ions which can exist in multiple oxidation states (differing oxidation states are differing numbers of electrons associated with the nucleus). This flexibility of oxidation state may allow electrons on the outermost shells to hop to the outermost shells of neighbouring ions. Hopping being possible allows a saving of kinetic energy, as it expands the spatial range of the hopping electrons.

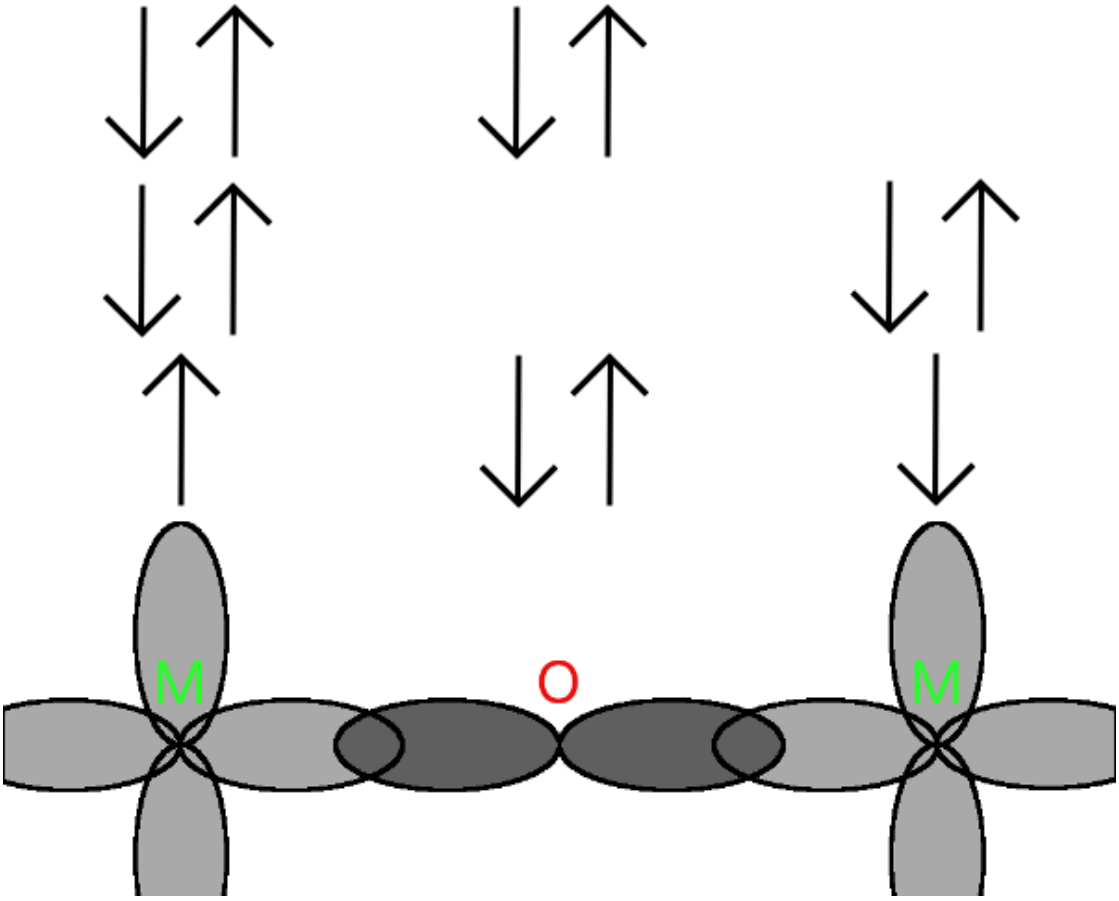

Figure 1.1: Antiferromagnetic superexchange interaction between single outer shell electrons in two transition metal atoms (M) mediated by oxygen (O). The overlapping orbitals are shown at the base of the diagram. The antiferromagnetic ground state configuration of electron spins is shown above that, then two excited states. By mixing with the excited states, the electrons can delocalise over the three atoms and reduce their kinetic energy.

If the electrons in the outermost shells have an exchange interaction with electrons in an inner shell, then they will be constrained to a particular relative orientation. Hopping does not change the spin orientation of the electron. Therefore, to minimise the energy of the hopping electron, the exchange-linked inner shells must be ordered ferromagnetically between ions. This ordering allows the electron to hop through the crystal, rendering it metallic [13].

1.1.7 Magnetic Order

The effect of these inter-spin interactions is to produce order in the spin system.

In ferromagnetic materials, inter-spin interactions (typically ferromagnetic exchange interactions) favour neighbouring spins aligned in the same direction. A simple Hamiltonian for such a system in a magnetic field B is [13]

$$\hat{H} = -\Sigma_{i,j} J_{i,j} \mathbf{S}_i \cdot \mathbf{S}_j + g\mu_B \Sigma_j \mathbf{S}_j \cdot \mathbf{B} \tag{1.29}$$

where J is the exchange coupling constant (see equation 1.27) and is positive, $\mathbf{B}$ is the applied field, and the sum runs over all spins i and j. The interaction between spins can be represented by an effective 'molecular field' $\mathbf{B}_{\mathrm{mf}}$, using the following expression for the molecular field for the ith spin:

$$\mathbf{B}_{\mathrm{mf}} = -\frac{2}{g\mu_B} \Sigma_j J_{i,j} \mathbf{S}_j, \tag{1.30}$$

and then

$$-2\mathbf{S}_i \cdot \Sigma_j J_{i,j} \mathbf{S}_j = \mu_B \Sigma_i \mathbf{S}_j \cdot \mathbf{B}_{\mathrm{mf}} \tag{1.31}$$

where the left hand side is the conventional exchange interaction and the right hand side is the expression in terms of molecular field. Then, making the assumption for simplicity that the molecular field is the same for all spins, the Hamiltonian can be written

$$\hat{H} = g\mu_B \Sigma_i \mathbf{S}_i \cdot (\mathbf{B} + \mathbf{B}_{\mathrm{mf}}) \,. \tag{1.32}$$

The consequence of the $\mathbf{B} + \mathbf{B}_{\mathrm{mf}}$ term is that spins can experience an effective field even in the absence of an applied field. The molecular field is related to the magnetisation by $\mathbf{B}_{\mathrm{mf}} = \lambda \mathbf{M}$ where λ is a constant scaling factor. This model of ferromagnetism is called the 'Weiss model' [13].

As the effect of the field is to align the spins and so magnetise the material, and the magnetisation of the material strengthens the field in turn, magnetisation in the sample is self-sustaining at low temperatures. Entire ferromagnetic samples do not necessarily have a macroscopic net magnetisation in zero field as they may be separated internally into 'domains' of spins parallel to one another but with different orientations to those in other domains, but these domains can be aligned by applying a magnetic field and will then retain the magnetisation when the field is removed. At higher temperatures, thermal fluctuations begin to disrupt the

magnetisation until spontaneous magnetic order cannot be preserved. The critical temperature at which magnetic order vanishes in zero field is the ferromagnetic transition (Curie) temperature T_C [13].

In antiferromagnets, inter-spin interactions favour neighbouring spins aligned in opposite directions. For such materials, J in equation 1.29 is negative for neighbouring spins. Such systems can often be considered as two interpenetrating 'sublattices' defined as occupying alternating points on the total lattice. In the Weiss model, each sublattice will have a molecular field:

$$\mathbf{B}_+ = -|\lambda|\mathbf{M}_- \tag{1.33}$$

$$\mathbf{B}_- = -|\lambda|\mathbf{M}_+ \tag{1.34}$$

where the sublattices are labelled + and −. The low-temperature ordered state of such a system is for one lattice to point all in one direction and the other lattice to point all in the opposite direction, akin to two ferromagnets, satisfying the condition of opposite directions between any pair of neighbouring spins.

If the spins in each sublattice have the same magnetic moment, this configuration yields a total magnetic moment of 0. This order will, like that of a ferromagnet, be destroyed by thermal fluctuations as temperature increases, until it is destroyed at the Néel temperature T_N [13].

Ferrimagnetism is a variety of antiferromagnetism in which the sublattices do not have the same moment per spin. As such the total system will have a net magnetisation even when both sublattices are perfectly anti-aligned, and the two lattices can have differing temperature dependencies. This produces a complex temperature dependence for the total magnetisation. It may even change sign if the sublattice with largest magnetisation changes from one to the other at some temperature (called the 'compensation temperature') [13].

Helical ordering is a form of order where spins laid in layers shift direction by some angle θ each layer. It is found in some rare earth metals with magnetic interactions mediated by the RKKY interaction [13].

In spin glasses, a lack of order in the spin sites or the interaction strengths and orientations between them leads to a lack of order in the magnetic moments. They do not exhibit long-range structure but instead randomly mixed interactions.

Below a freezing temperature T_{f}, spin glasses freeze into one of many metastable disordered ground states with slow relaxation behaviour. Spin glasses are treated in greater detail in section 1.3.

1.1.8 Curie-Weiss Law

The magnetic susceptibility of ferromagnets in the paramagnetic state above the Curie temperature T_C is predicted by the Weiss model to be a function of $T - T_C$:

$$\chi \propto \frac{1}{T - T_C}. \tag{1.35}$$

The same model predicts for antiferromagnets for $T > T_N$:

$$\chi \propto \frac{1}{T + T_N}. \tag{1.36}$$

These two expressions have a very similar form. The more general version is the 'Curie-Weiss law' [13]:

$$\chi = \frac{C}{T - \theta}. \tag{1.37}$$

where C is the Curie constant for the material and θ is called the Weiss temperature. For $\theta > 0$, the material is a ferromagnet with $T_C = \theta$. For $\theta < 0$, the material is an antiferromagnet with $T_N = -\theta$ (under ideal conditions for the Weiss model, in real antiferromagnets $-\theta/T_N$ can be greater than 5 [13]). If $\theta = 0$ the material is paramagnetic and the equation is simply the Curie law described in section 1.1.3. This expression can be used to interpret data on magnetic materials in the paramagnetic state. It can determine if they are ferromagnets or antiferromagnets and estimate their critical transition temperature.

1.1.9 Nuclear Magnetism

Besides electrons, atomic nuclei are also charged and can carry angular momentum, and so can have a magnetic moment. This moment is very small compared to the electronic moment with typical values on the order of 10^{-3} to 10^{-4} μ_{B}. There is also no spatial extension of the nucleus outside the centre of the atom, so the

coupling of nuclei to one another is extremely weak, so systems do not exhibit nuclear magnetic ordering at typically achievable laboratory temperatures [13]. In copper, the antiferromagnetic Néel temperature is 58 nK, and in silver it is 560 pK [13]. These extremely low temperatures can only be achieved by adiabatic demagnetisation (a technique in which the sample is magnetised while connected to a low-temperature heat bath, then allowed to demagnetise while isolated), exploiting the fact that the nuclei can have a different temperature to the atomic lattice due to weak coupling between nuclear and electronic spins [13].

Nuclear spin is governed by the quantum number I which can take an integer or half-integer value. Its component in the z-direction is m_I, which can take a value between $-I$ and I in integer steps, similarly to electronic orbital and spin momentum.

Nuclear spin is coupled to electronic spin. While there is no powerful exchange interaction, the magnetic field created by the orbital electrons associated with a nucleus will split the nuclear magnetic energy levels. These are typically smaller than the electronic energy level structure, even the fine structure, and are termed 'hyperfine structure'. While usually negligible, this structure can become thermodynamically significant at low temperatures as will be seen in section 3.2.2.

1.2 Thermodynamics

The study of thermodynamics concerns itself with bulk properties of physical systems that have a temperature. It is a theory of remarkable power and universality, that obtains general results that apply across systems with enormous microscopic variety. The summary in this section is based on Finn 1993 [16] and Mandl 1988 [17].

Macroscopically, temperature (T) is the potential that determines heat flow. If two systems with different temperatures are brought into thermal contact, heat (energy) will flow from the one with higher temperature to the one with lower temperature, and this heat flow will bring the temperatures toward one another until their temperatures are equal. If their temperatures are equal they are in thermal equilibrium and there is no heat flow, and if two systems both have equal temperature to a third system, they have equal temperature to one another. Sys-

tems in equilibrium do not change with time. Equilibrium in general is a state of the system that does not change with time. If a system is put out of equilibrium it will begin to move through the space of possible states according to its particular physical properties, until it reaches an equilibrium state [16]. A system returning to equilibrium from a perturbation is called 'relaxation' and is characterised by a 'relaxation time' τ.

Microscopically, the temperature of a system defines the probability that its components will occupy a particular state. The probability of an object being in a certain state i is given by the Boltzmann expression [17]:

$$P = \frac{g_i e^{-\epsilon_i/k_B T}}{Z}, \tag{1.38}$$

where g_i is the number of macroscopically indistinguishable states associated with the state i, called its statistical weight or degeneracy (this concept is discussed in more detail in section 1.2.2), ϵ_i is its energy, and Z is the 'partition function'. The partition function is a summation and weighting of all the possible states of the object. It is given by:

$$Z = \Sigma_i g_i e^{-\epsilon_i/k_B T}, \tag{1.39}$$

summing over all possible states i.

Reciprocally, the temperature of a system in equilibrium is determined by its physical state. Temperature is one of a set of 'state variables'. In a given system, if all but one of the state variables are known, the remaining variable is also determined. In gases with a fixed amount of substance, the additional variables are pressure (P) and volume (V). In magnetic solids with a fixed amount of substance, they are field (H) and total magnetic moment ($I = MV$). So one can write [16]:

$$T = T(P, V), \tag{1.40}$$

$$T = T(H, I). \tag{1.41}$$

The latter can be easily seen by recalling $I = MV$, then considering the cases in magnetism where $\chi = \chi(T)$, so $M = \chi(T)H$, so any two of T, M and H specify

the third. Systems where both magnetic and mechanical physics are significant have all five state variables with any four independent, yielding:

$$T = T(P, V, H, I) \tag{1.42}$$

The internal energy U of a system is the total kinetic and potential energy of its components. It can change both by heat flow and by doing work on the system. Heat is nonmechanical exchange of energy due to temperature difference, while work is other forms of energetic interaction such as equalising a pressure difference by moving a piston. Generally the change in internal energy is of more interest than attempting to measure the energy itself. The general equation for change in internal energy is $dU = dW + dQ$, where dQ is heat flow and dW is work done, which for a magnetic system is given by [16]

$$dU = HdI + dQ, \tag{1.43}$$

and for a gaseous system

$$dU = dQ - PdV, \tag{1.44}$$

provided the process is 'reversible'. A reversible process is one which can be reversed and bring not just the system but its surroundings back to their initial state. Such processes are 'quasistatic' in that they move the system through a sequence of equilibrium states, and involve no action by dissipative forces such as friction, that impose costs on moving the system through states. Very often a reversible process is an idealisation, but they can be used to obtain results for processes in general. For a system exhibiting both types of physics the composite equation for dU is:

$$dU = HdI - PdV + dQ. \tag{1.45}$$

1.2.1 Heat Capacity

Assuming no other factors, positive heat flow into a system raises its temperature. The amount of heat required to raise the temperature by a certain amount is the heat capacity. More precisely, heat capacity C is the amount of heat reversibly added to the system divided by the temperature rise, in the limit of small quantity

of heat and small rise [16]:

$$C = \frac{dQ}{dT}, \tag{1.46}$$

and specific heat c is the heat capacity per unit mass.

There are however multiple reversible paths on the state diagram between the two ends of ΔT, and they may have differing dQ and so heat capacities. Two elementary examples for a gaseous system are the heat capacity at constant volume C_V and the heat capacity at constant pressure C_P. For the first, if V is constant, $dV = 0$, so

$$C_V = \frac{dQ_V}{dT} = \frac{dU}{dT}. \tag{1.47}$$

i.e. the heat input is identical to the increase in internal energy, because no work is done.

For C_P, we can obtain a similar result by first defining a new quantity the 'enthalpy' H_E (to disinguish from magnetic field H)

$$H_E = U + PV, \tag{1.48}$$

$$dH_E = dU + PdV + VdP = dQ + VdP, \tag{1.49}$$

from equation 1.44. If $dP = 0$, this resolves simply to $dH_E = dQ_P$.

Therefore

$$C_P = \frac{dQ_P}{dT} = \frac{dH}{dT}. \tag{1.50}$$

1.2.2 Entropy

In 1855 Clausius showed [16] that for a system in contact with thermal reservoirs at temperature T and undergoing a process with identical initial and final states,

$$\oint \frac{dQ}{T} \leq 0. \tag{1.51}$$

That is, such a process can only occur if net heat transfer is out of the system into the reservoirs, or zero. If there is net heat transfer out then there must be commensurate work done on the system, because $dU = dW + dQ = 0$. If the cycle

is reversible, then:

$$\oint_R \frac{dQ}{T} = -\oint_R \frac{dQ}{T} = 0. \tag{1.52}$$

So a cyclic process can dissipate work into heat, but not vice versa.

If a system is taken along a reversible path from an initial state i to a final state f, then back along a different reversible path from f to i, then the total path is a reversible cycle and so:

$$\int_i^f \frac{dQ}{T} + \int_f^i \frac{dQ}{T} = 0, \tag{1.53}$$

$$\int_i^f \frac{dQ}{T} = -\int_f^i \frac{dQ}{T}. \tag{1.54}$$

This holds independently of the particular paths chosen so long as the path is reversible. This allows the definition of a state variable S, called 'entropy', with the difference in entropy between two states defined as:

$$\Delta S = S_f - S_i = \int_i^f \frac{dQ}{T}, \tag{1.55}$$

which can be noted to be the integral with respect to T of C/T. This is the macroscopic definition of entropy, which defines entropy changes only. Significantly, over any process, the entropy of the universe (the entropy of the system plus the entropy of its surroundings) cannot decrease [16].

From equations 1.55 and 1.44, a new statement of the internal energy can be written:

$$dU = TdS - PdV. \tag{1.56}$$

Entropy also has a microscopic definition, which bridges macroscopic and microscopic physics. Any given state defined by the thermodynamic state variables will have a number of possible microscopic states which, while microscopically distinct, produce the same aggregate state variables. An illustrative example is provided by Mandl 1988 [17]. Consider a paramagnet in an applied magnetic field $\mathbf{B}$. Each of the N spins in the paramagnet has spin 1/2 and the only states it can occupy in the field are to to be parallel or antiparallel to it. The energy E of the

system is given by

$$E = (N - 2n)\mu B \tag{1.57}$$

where n is the number of spins aligned parallel to the field, μ is the magnetic moment of the spins and B the magnitude of the field. The (magnetic) energy and magnetisation of a given state is determined solely by n. However, a given n can correspond to a large number of spin configurations, given by the number of ways n parallel spins can be chosen out of N spins total:

$$\Omega = \frac{N!}{n!(N-n)!} \tag{1.58}$$

where Ω is called the 'statistical weight' of the state determined by E, M and B. This macroscopic state is called the macrostate and each possible spin configuration is called a microstate, and Ω for a macrostate is equal to the number of microstates that correspond to that macrostate. This applies for all thermodynamic systems, be they orientations of spins in a paramagnet or positions of particles in an ideal gas.

Ω defines the entropy of the macrostate, but not in a linear relation. Entropy is an 'extensive quantity', so the total entropy of two independent bodies B_1 and B_2 with entropies S_1 and S_2 is $S = S_1 + S_2$. However, the statistical weight of the total macrostate of the two bodies is $\Omega = \Omega_1\Omega_2$, as the bodies are independent and the choice of microstate in one does not constrain the choice of microstate in the other. Therefore, the statistical weight is linked to the absolute value of the entropy by [17]:

$$S = k_B \ln\Omega. \tag{1.59}$$

The absolute value of entropy is related to the third law of thermodynamics. The third law states that systems in equilibrium at absolute zero have an entropy of zero. At absolute zero, all systems will be in their ground state, and if unique, this state will have a statistical weight of 1 and an entropy of 0.

Systems with a degenerate ground state may appear to violate this principle. As will be discussed in more detail in section 1.3, spin ice can be considered to have a degenerate ground state and so a ground state entropy. Such systems, however, will not actually violate the third law if their apparent positive entropy

ground state is merely a collection of states barely above a true ground state, from which the equilibration toward the ground state is extremely slow. Such a system is not in equilibrium, even though reaching equilibrium may be so slow that the system is effectively in a positive entropy ground state for experimental purposes. Whether the system can be treated in this way despite the technical violation of the equilibrium conditions for thermodynamics is an empirical matter [16].

1.2.3 Free Energies

With the entropy, two more thermodynamic state functions can be defined: the Helmholtz (F) and Gibbs (G) free energies. Both help define the amount of useful energy in the system in the light of the limitations placed by increasing entropy.

Changes in the Helmholtz free energy $F = U - TS$ are related to the maximum work theoretically extractable from a system with no change in temperature between the endpoints of the process. If a system is held at constant volume (or equivalent for non-gaseous systems) and in thermal contact with a reservoir, its equilibrium condition is for F to be minimised. The Helmholtz function also provides a point of connection between macroscopic and microscopic physics. For systems of N objects that are distinguishable from one another and weakly interacting, the Helmholtz free energy can be defined in the 'thermodynamic bridge equation' [16]:

$$F = -Nk_BT\ln Z. \tag{1.60}$$

The Gibbs free energy $G = H_E - TS$ is to enthalpy as the Helmholtz free energy is to internal energy. It has a similar relation to work, but in this case G defines the amount of 'useful work' that can be extracted from the system. The Gibbs free energy also defines an equilibrium condition: for a system in thermal and mechanical (or equivalent) contact with a heat and pressure reservoir, G must be minimised for the system to be in equilibrium.

Recalling that universal entropy cannot decrease, and noting that energy is conserved, we see that universal free energy must over time decrease. This leads to the cosmological concept of the 'heat death of the universe', a theoretical future state where free energy is zero and no useful work can be performed by any process.

From U, H_E, F and G four important relations can be derived. From a defini-

tion of U [16]:

$$dU = TdS - PdV, \tag{1.61}$$

$$dU = \left(\frac{\partial U}{\partial S}\right)_V dS + \left(\frac{\partial U}{\partial V}\right)_S dV, \tag{1.62}$$

$$T = \left(\frac{\partial U}{\partial S}\right)_V \text{ and } \mathrm{P} = -\left(\frac{\partial \mathrm{U}}{\partial \mathrm{V}}\right)_{\mathrm{S}}. \tag{1.63}$$

As the value of U is determined entirely by the state variables, integrations of dU are path-independent, and $dU = TdS - PdV$ is an exact differential. Therefore:

$$\left(\frac{\partial T}{\partial V}\right)_S = -\left(\frac{\partial P}{\partial S}\right)_V. \tag{1.64}$$

This is the first Maxwell relation. The remaining, from H_E, F and G respectively are [16]

$$\left(\frac{\partial T}{\partial P}\right)_S = \left(\frac{\partial V}{\partial S}\right)_P, \tag{1.65}$$

$$\left(\frac{\partial P}{\partial T}\right)_V = \left(\frac{\partial S}{\partial V}\right)_T, \tag{1.66}$$

$$\left(\frac{\partial V}{\partial T}\right)_P = -\left(\frac{\partial S}{\partial P}\right)_T, \tag{1.67}$$

Magnetic equivalents can be defined easily by substituting $P \to -H$ and $V \to I$. These should not be confused with the 'Maxwell equations' governing electromagnetism, discussed in section 1.1.

1.2.4 Chemical Potential

Thermodynamic theory can be extended to include changes in the quantity of matter, not just of energy [16]. This extends the thermodynamic equation once more:

$$dU = TdS - PdV + \Sigma_i \mu_i dN_i, \tag{1.68}$$

where N_i is the number of particles of type i in the system and μ_i is the respective 'chemical potential', which is, for this gaseous system, the increase in energy per

particle added under constant S, V and $N_{j\neq i}$:

$$\left(\frac{\partial U}{\partial N}\right)_{V,S,N_{j\neq i}} = \mu_i. \tag{1.69}$$

This can also be defined in terms of the free energies. For the Helmholtz free energy:

$$F = U - TS, \tag{1.70}$$

$$dF = dU - TdS - SdT, \tag{1.71}$$

$$dF = \Sigma_i \mu_i dN_i - PdV - SdT, \tag{1.72}$$

$$\left(\frac{\partial F}{\partial N}\right)_{V,T,N_{j\neq i}} = \mu_i, \tag{1.73}$$

which depends on T rather than S being constant, and for the Gibbs free energy:

$$G = U + PV - TS, \tag{1.74}$$

$$dF = dU - TdS - SdT, \tag{1.75}$$

$$dF = VdP + \Sigma_i \mu_i dN_i - SdT, \tag{1.76}$$

$$\left(\frac{\partial G}{\partial N}\right)_{P,T,N_{j\neq i}} = \mu_i, \tag{1.77}$$

which depends on T and P being constant.

1.3 Frustration

Frustration as a physical term refers to a property of certain systems in which it is impossible to minimise the energy of every interaction simultaneously [18]. The canonical example is a triangular array of three antiferromagnetically coupled Ising spins (see section 1.1.4) with Ising axis perpendicular to the lattice (shown in figure 1.2), where two will minimise energy by adopting opposite orientations but the third cannot orient opposite to both its neighbours simultaneously. In this system the ground state is degenerate, with six possibilities corresponding to the six possible arrangements of two spins in one direction and the third in the other.

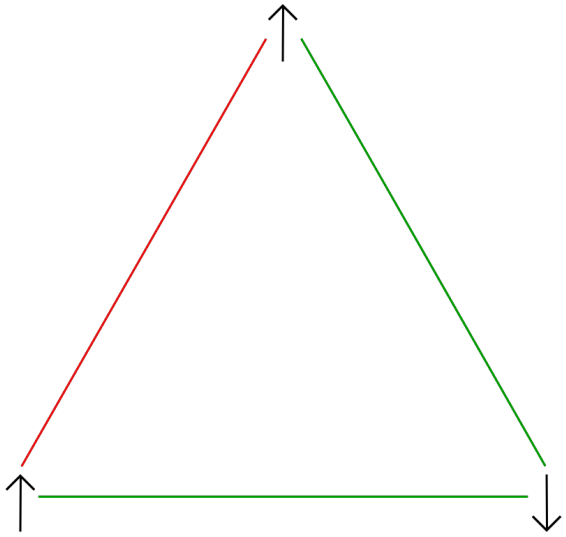

Figure 1.2: Frustrated antiferromagnetic triangle. Spins are antiferromagnetically coupled along the lines, and constrained to point up or down. The spins along the base have a minimised interaction, but only one has a minimised interaction with the remaining spin. Neither orientation of the top spin can minimise interactions with both base spins simultaneously.

The first frustrated system to be identified was water ice [19], which later became the model for spin ice [14]. Water ice crystals in the I_h form (the usual form found in nature on Earth, henceforth just called 'ice') have a tetrahedral structure, with each oxygen atom having four equidistant oxygen neighbours [20]. Each oxygen-oxygen hydrogen bond contains a proton (hydrogen ion) which may be situated closer to one oxygen or the other, as shown in figure 1.3. Bernal and Fowler [19] proposed the rule that each oxygen should have two protons close to it and two far. These 'ice rules' were proven by Pauling [21] to produce ground state degeneracy in the crystal that diverges exponentially with the number of water molecules. His estimate predicted a very large zero point entropy of $R\ \ln(3/2)$ per mole H_2O that is consistent with earlier experiments by Giaque *et al.* [22].

An ice crystal containing N oxygen atoms, each with four O-O bonds each shared with another oxygen atom has 2^{2N} possible configurations of the hydrogen ions. Of these configurations, 6 of the 16 possible for any given ion are in the ground state. So Pauling found:

$$\Omega = 2^{2N}\left(\frac{6}{16}\right)^N = \left(\frac{3}{2}\right)^N \tag{1.78}$$

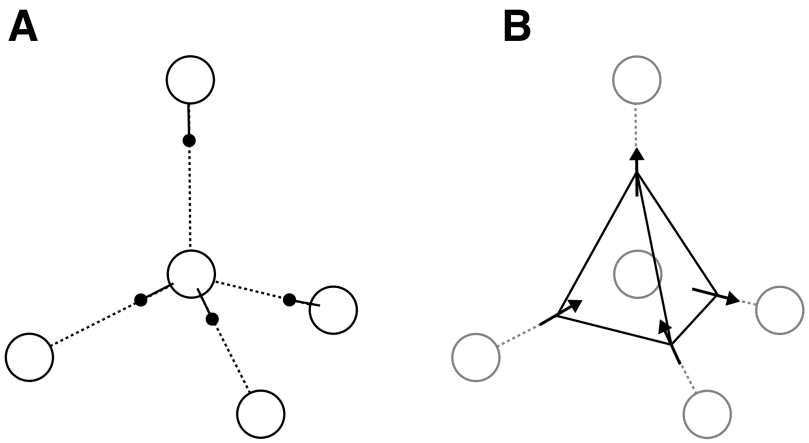

Figure 1.3: A: Proton structure of water ice. Hydrogen ions (black spheres) are positioned along bonds between oxygen ions (white spheres) in a 2-near 2-far arrangement. B: Magnetic structure of spin ice. Magnetic moments (arrows) are positioned between titanium atoms (white spheres) in 2-in 2-out arrangement. From 'Spin Ice State in Frustrated Magnetic Pyrochlore Materials' by S.T. Bramwell and M.J.P. Gingras, Science 2001 [2]. Reprinted with permission from AAAS.

$$S = k_{\mathrm{B}} \ln \Omega = k_{\mathrm{B}} \ln (3/2)^N = k_{\mathrm{B}} N \ln (3/2), \tag{1.79}$$

which yields $R \ln(3/2)$ for $N = N_A$, Avogadro's number. The exact entropy is higher by the order of approximately 1% [23], but this minor discrepancy is not important for this investigation.

A further consequence of this structure is that it allows the creation of ionic defects. Defects are imperfections in otherwise regular structures, such as absence of an atom from a typically occupied crystal lattice site, or in this case a violation of the typical ordering rule of protons in ice. If a proton tunnels from one end of a hydrogen bond to the other, then a system that otherwise obeys the ice rules will now have one negatively-charged oxygen site and one positively-charged oxygen site [24]. This proton mobility contributes to the electrical conductivity of ice [24].

Since the discovery of water ice's properties extensive work has been done on characterising frustration in magnetic, rather than electric systems [25, 26]. The enormous variety of possible magnetic materials with different combinations of geometric structure and spin interactions, and of experimental techniques for probing them, makes magnetic systems an excellent laboratory for examining frustrated

behaviour.

Frustrated magnetic systems can achieve long-range ordered ground states, but often with low critical temperatures such that $|\theta|/T_c > 10$ [25], where θ is the Weiss temperature and T_c the critical temperature for transition into the ground state. However, not all frustrated systems can achieve long-range order even at low temperatures. Among those those that do not, many are found on the kagome and pyrochlore lattices.

If the frustrated antiferromagnetic triangle described above is extended into a corner-sharing triangular lattice, this creates a frustrated 'kagome lattice', shown in figure 1.4. If kagome lattices are stacked vertically with an offset and interstitial triangular planes, this creates the 'pyrochlore lattice' of corner-sharing tetrahedra, shown in figure 1.5. This lattice takes its name from the class of cubic pyrochlore oxides ($A_2B_2O_7$) that realise it in nature and provide many examples of frustrated magnetic systems [26].

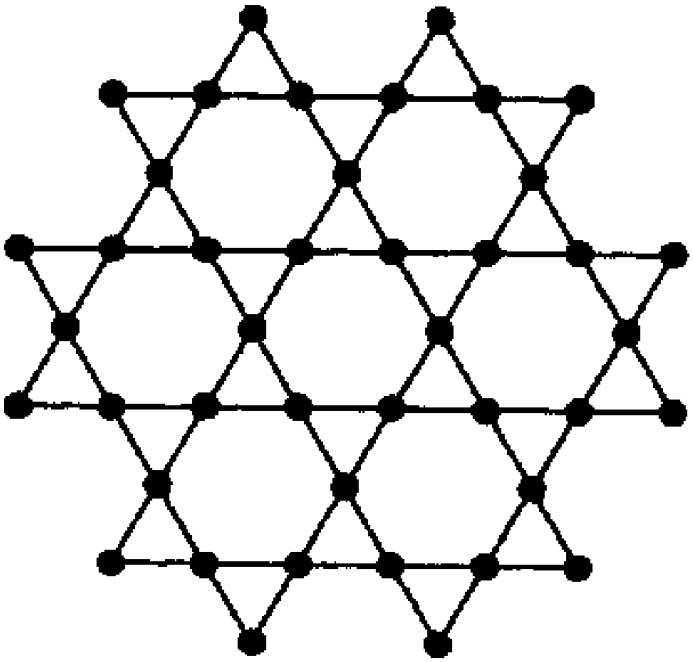

Figure 1.4: Kagome lattice of corner-sharing triangles. Reproduced from Greedan *et al.* [25] with permission of the Royal Society of Chemistry.

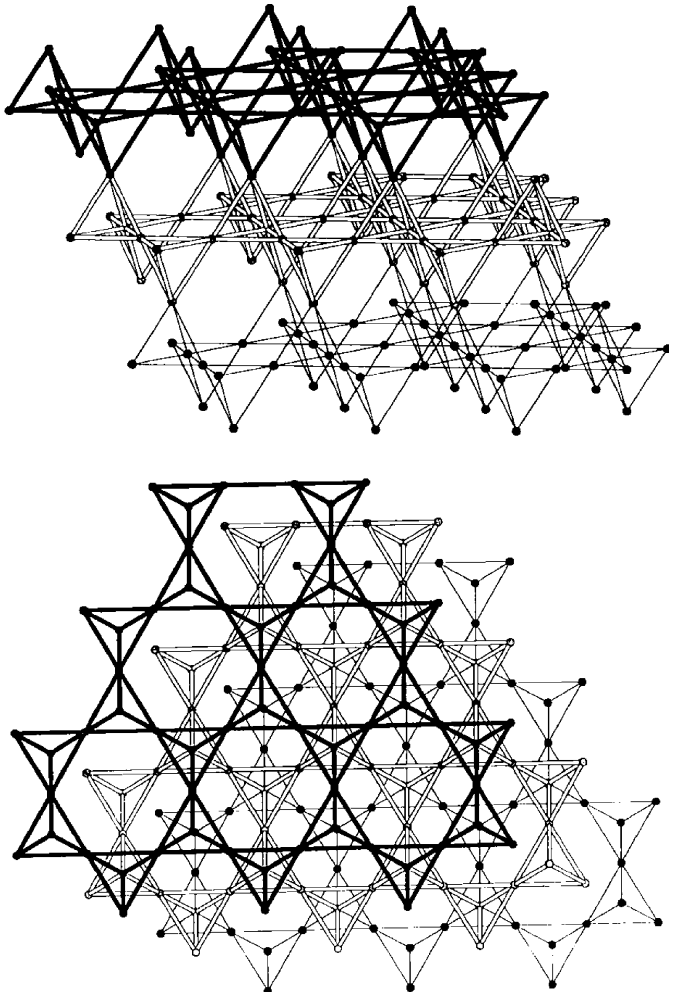

Figure 1.5: Construction of a corner-sharing tetrahedral lattice from multiple kagome layers. Reproduced from Greedan *et al.* [25] with permission of the Royal Society of Chemistry.

Spin glasses, mentioned in section 1.1.7, do freeze but do not exhibit long-range order. Instead, the interactions are randomly mixed due to lack of regular structure in the positions or interactions of the spins [13]. They are found among the pyrochlores in the forms of $Y_2Mo_2O_7$ and $Tb_2Mo_2O_7$ [26], among other possibilities, but better understood are spin glasses formed by alloys or diluted magnetic crystals.

Positional disorder or 'site-randomness' arises from the magnetic spins being in variable locations relative to one another [13]. Spin glasses of this sort can be achieved in alloys such as $Au_{1-x}Fex$ [26] (for x 0.05) or $Cu_{1-x}Mn_x$ [13] (for

$x \ll 1$). As the spins in these metals interact via the RKKY interaction (see section 1.1.7) which varies between ferro- and antiferromagnetic coupling with distance, the variation in distance means the interaction of each spin with its neighbours is random and frustrated by competing interactions.

Another possibility is 'bond-randomness', in which the locations of the spins are regular but their interactions are randomly varied [13]. This can be achieved in crystals such as $Rb_2Cu_{1-x}Co_xF_4$, where both Cu and Co are effective spin-1/2 Ising spins, but the sign and magnitude of the superexchange between spins depends on which elements are involved and how their orbitals are occupied [13].

Spin glasses freeze into one of many metastable ground states as the system temperature goes below a freezing temperature T_f. As they approach T_f from above, the spins form into locally correlated clusters, connected to one another by spins not in clusters. Fluctuations inside the clusters slow down and the interactions between spins become longer-range, until the system as a whole freezes into a state with no long-range order. Near the transition at T_f, there is a peak in the real part of the a.c. susceptibility $\chi(\omega)$, which is a signature of spin glass behaviour [13].

'Cooperative paramagnetism', first identified by Villain in 1979 [27], is a frustrated state in which only local correlations between spins exist and there is no long-range order, but the spins do not freeze and remain dynamic down to low temperatures [25]. It can be realised theoretically by extending the frustrated antiferromagnetic triangle to kagome and pyrochlore lattices as described above [13]. Cooperative paramagnetic spins on the antiferromagnetic pyrochlore lattice order under the constraint $\Sigma_i S_i = 0$ for each tetrahedron, where i runs over all spins on the tetrahedron. $Tb_2Ti_2O_7$ has been proposed as a physical realisation of this state, and remains unfrozen down to 0.07 K [28], but work since has complicated this characterisation and suggested it has some spin-ice like properties and may even be a form of quantum spin ice [26, 29].

Other pyrochlores such as $Er_2Sn_2O_7$ and $Er_2Ti_2O_7$ realise the 'XY antiferromagnet', a sort of inverse of the Ising spin in which the spins can rotate freely in the plane perpendicular to the [111] axis: an easy-plane anisotropy. These enter ordered ground states at 0.1 K and 1.2 K respectively [26], the latter by an 'order by disorder' transition in which a ground state is stabilised from a degenerate

manifold by quantum fluctuations [30].

As is evident pyrochlores manifest a wide variety of magnetic behaviour. However one class replicates the physics of the original water ice frustrated system much more closely, and so has been termed 'spin ice'.

1.4 Spin Ice

In 1997 Harris *et al.* [14] discovered a magnetic equivalent to the proton degeneracy of water ice in the ferromagnetic pyrochlore $Ho_2Ti_2O_7$ (HTO).

In HTO, Ho^{3+} ions are arranged in a tetrahedral lattice as shown in figure 1.6. The crystal field experienced by the holmium ions creates a ground state doublet dominated by the $m_J = |8\rangle$ states of the ${}^5I_8$ free ion state, with the resultant easy-axis anisotropy producing effective Ising spins constrained to point along the $\langle 111 \rangle$ direction that connects the centre of each pyrochlore tetrahedron with its neighbours. This structure could also be considered a diamond lattice with the Ho^{3+} ions situated on the bonds between lattice sites, and from that perspective forms a clear analogy with the proton bond structure of water ice, as shown in figure 1.3.

This structure was discerned using elastic neutron scattering, a technique in which the nuclear and magnetic structure of the sample is used to scatter incident neutrons, which have an inherent magnetic moment [13]. In 2001 Bramwell *et al.* [32] presented diffuse neutron scattering results that demonstrated conclusively that holmium titanate has a spin ice structure. These results are displayed in figure 1.7. This paper also settled a dispute regarding the nature of HTO which will be summarised in section 3.2.

A theoretical precursor to this spin ice structure had been outlined by Anderson in 1956 [34]. It consisted of antiferromagnetic Ising moments on the same pyrochlore lattice, with Ising axis parallel to a global z-direction. However, this global z-preference violates the cubic symmetry of the pyrochlore lattice, and the spin system remained a theoretical curiosity with no real material counterparts [32]. The innovation of Harris *et al.* was to realise that ferromagnetic Ising spins parallel to the local axis have the same relations to their neighbours as antiferromagnetic spins with a global parallelism. This local parallelism also preserves the

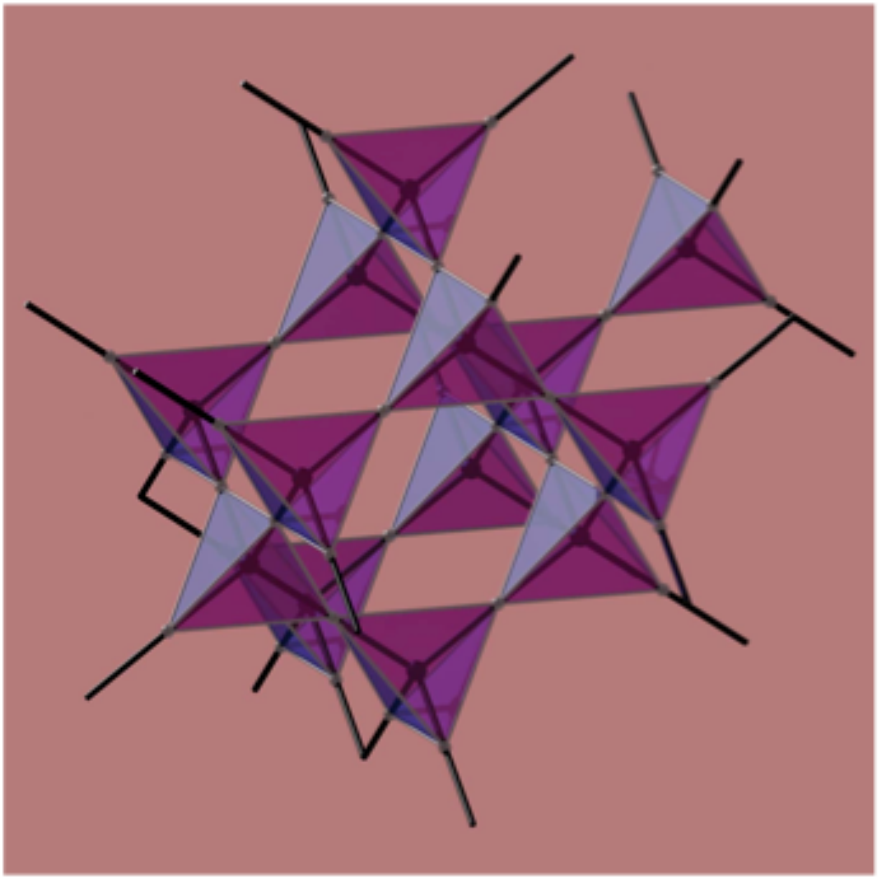

Figure 1.6: Pyrochlore crystal unit cell. Magnetic rare earth ions are situated on the tetrahedral vertices, nonmagnetic ions at tetrahedon centres. Oxygen structure is not shown. Spins exist on the tetrahedral lattice, while emergent monopoles exist on the diamond lattice. Reprinted by permission from Macmillan Publishers Ltd: Nature (Castelnovo *et al.* 2008 [31]), copyright 2008

cubic symmetry of the pyrochlore crystal.

It is surprising that a ferromagnet, which prefers all magnetic moments to point in the same direction, should exhibit frustration, macroscopic degeneracy and no long range order. It is variable direction of the Ising axes that allows this: it impossible for a tetrahedral cell to simultaneously align four Ising spins at its vertices with axes passing through the centre of the cell. Consider the case shown in figure 1.9, where the top spin has been oriented upward and then the bottom three spins oriented to be as closely aligned with the top spin as permitted by the lattice geometry. The interaction energy of the top spin with each of three base spins has been minimised. However, if the perspective of one of the three

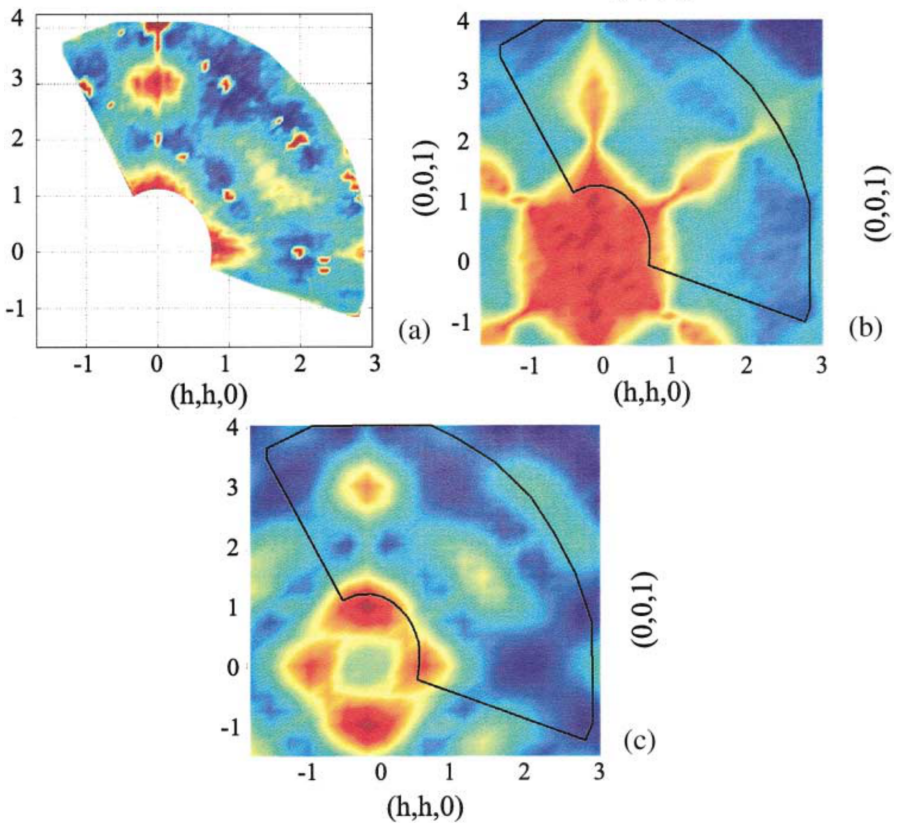

Figure 1.7: Image (a) is the experimental neutron scattering pattern of HTO at $T = 50$ mK. Intensity increases from dark blue to dark red. Images (b) and (c) are the predictions of the nearest neighbour and dipolar spin ice models at 0.15 K and 0.6 K respectively, with the region investigated in image (a) marked. Reprinted figure with permission from [S. T. Bramwell *et al.*, Physical Review Letters 87, 047205 2001 [32]. Copyright 2001 by the American Physical Society.

base spins is considered, while its interaction energy with the top spin has been minimised, its interaction energy with the other two base spins is maximised, as they are pointing relatively toward one another.

The minimum total energy is obtained by having two spins point in and two out on each tetrahedron. There are six degenerate configurations satisfying this condition, which are shown in figure 1.10. For each configuration, each spin on a tetrahedron is parallel to two of the other spins and antiparallel to the third.

The ground state of holmium titanate is this 2-in 2-out formation on each individual tetrahedron. This is an exact map to the 2-close 2-distant ice rules for proton ordering. Hence, holmium titanate was identified as the first 'spin

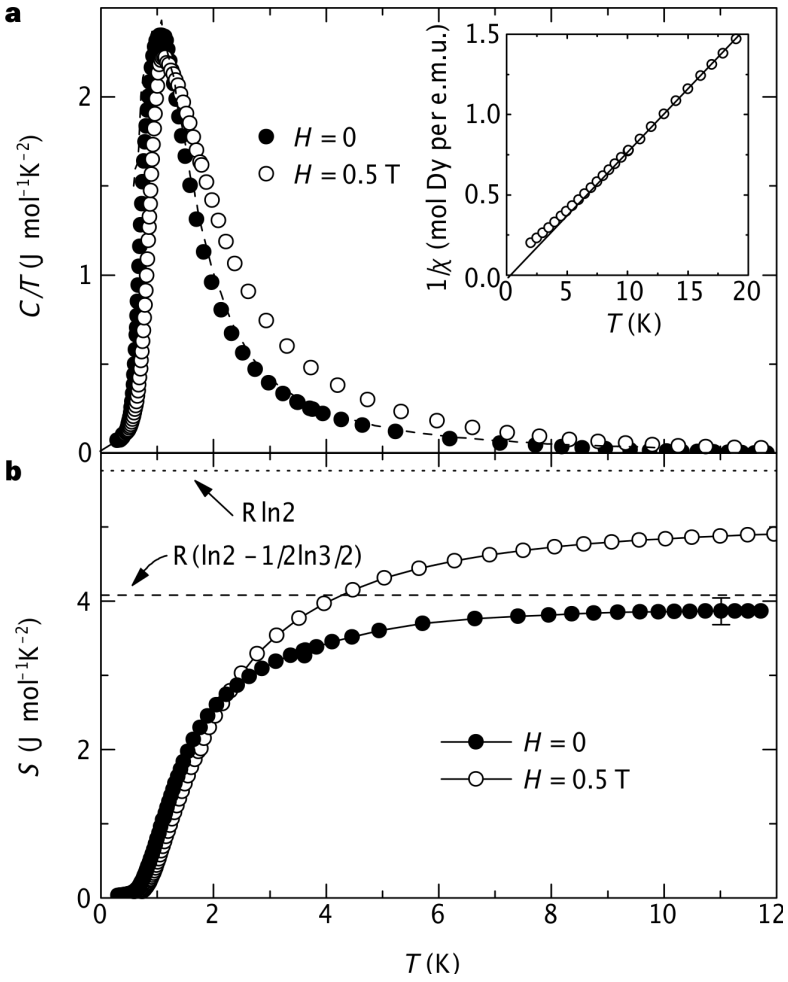

Figure 1.8: Specific heat (a) and entropy (b) of DTO in zero and 0.5 T field. In inset, the inverse magnetic susceptibility of DTO. Reprinted by permission from Macmillan Publishers Ltd: Nature (Ramirez *et al.* 1999 [33]), copyright 1999.

ice'. The closely related compound dysprosium titanate ($Dy_2Ti_2O_7$, DTO) was found to also exhibit spin ice behaviour and a 1999 thermal study by Ramirez *et al.* [33] confirmed the entropy change between zero and high temperature to correspond to the ground and maximum ice entropies predicted by Pauling, as well as producing the first example of the characteristic Schottky anomaly specific heat form. A Schottky anomaly [13] is a broad peak caused by elements of the system transitioning between a ground and an excited state, in this case ice rule and non-ice-rule spin configurations on tetrahedra. These results can be seen in figure 1.8 reproduced from their paper.

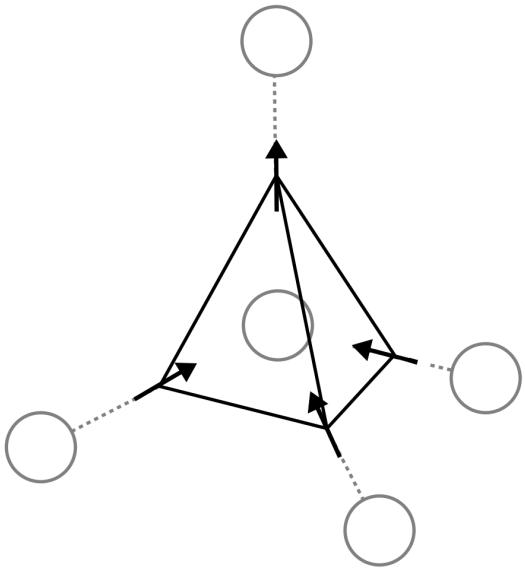

Figure 1.9: Ice-rule violating tetrahedron with all spins aligned with top spin. Modified from 'Spin Ice State in Frustrated Magnetic Pyrochlore Materials' by S.T. Bramwell and M.J.P. Gingras, Science 2001 [2]. Reprinted with permission from AAAS.

In later work, spin ice behaviour has been observed in $Ho_2Sn_2O_7$ [35] (HSO), $Ho_2Ge_2O_7$ [36] (HGO), $Dy_2Sn_2O_7$ [37] (DSO), $Dy_2Ge_2O_7$ [36] (DGO), outlining a broad range of dysprosium and holmium spin ices.

There has also been work [38] investigating a potential class of spin ices in which quantum fluctuations of the ice rules manifold create new types of excitation. These 'quantum spin ices' will be introduced in more detail in chapter 5, in which a suggested [8] quantum spin ice praseodymium zirconate ($Pz_2Zr_2O_7$, PZO) will be examined.

Beyond the pyrochlores, the spinel crystal $CdEr_2Se_4$ [39] (CES) has also been identified as a spin ice. DTO, HTO, PZO and CES will all be examined in this thesis.

Beyond the natural ices, recent years have seen the creation of 'artificial spin ices' from larger-scale magnets which display a range of similar and related behaviours [40, 41].

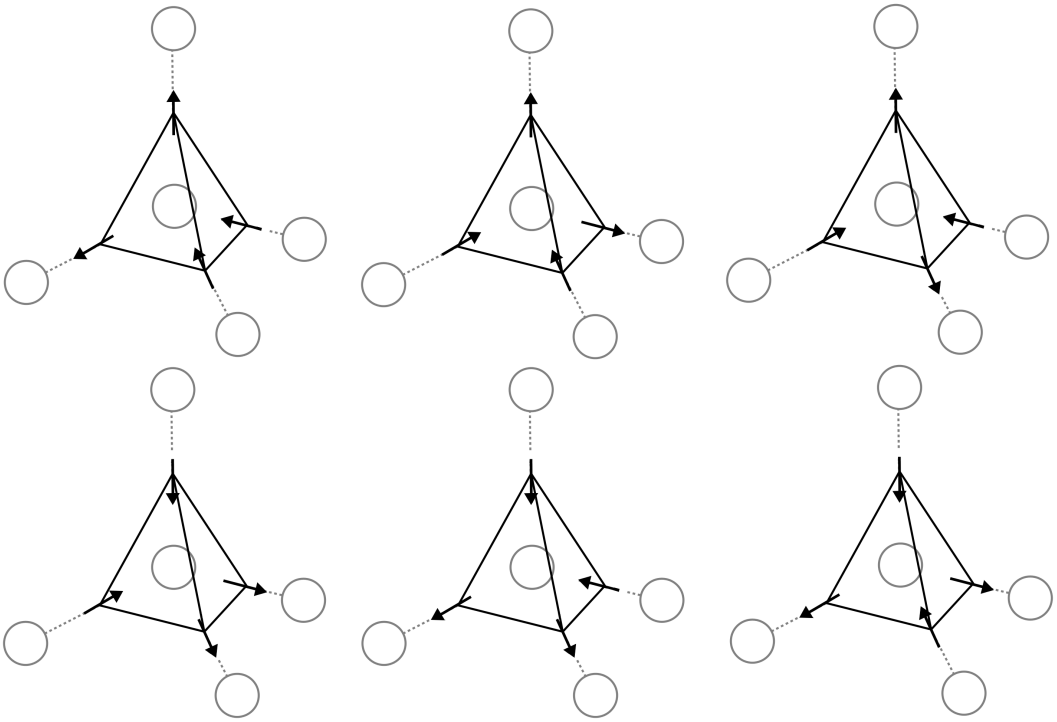

Figure 1.10: The six degenerate ice-rule following spin configurations of a tetrahedral lattice site in spin ice. Modified from 'Spin Ice State in Frustrated Magnetic Pyrochlore Materials' by S.T. Bramwell and M.J.P. Gingras, Science 2001 [2]. Reprinted with permission from AAAS.

1.4.1 Dipolar Spin Ice

An unusual property of holmium and dysprosium spin ices is the relative strength of their exchange and dipole interactions. In most materials where they coexist, the exchange interaction is the dominant effect [13], however in spin ice the two are of similar strength due to a strong magnetic moment and weak exchange coupling, and so the dipole interaction cannot be discounted [42]. The dipolar spin ice Hamiltonian was written down by den Hertog *et al.* in 1999 as [43]

$$\hat{H} = -J \sum_{<i,j>} \mathbf{S}_i \cdot \mathbf{S}_j + D r_{nn}^3 \sum_{i>j} \left[\frac{\mathbf{S}_i \cdot \mathbf{S}_j}{|\mathbf{r}_{ij}|^3} - \frac{3(\mathbf{S}_i \cdot \mathbf{r}_{ij})(\mathbf{S}_i \cdot \mathbf{r}_{ij})}{|\mathbf{r}_{ij}|^5} \right] \tag{1.80}$$

where J is the exchange coupling, D the dipole-dipole coupling and r_{nn} the distance between nearest neighbour rare earth ions. $\mathbf{r}_{ij}$ acts as a unit of measurement.

The first term represents the exchange interaction and the second the dipolar interaction, which decays as $|\mathbf{r}_{ij}|^{-3}$ and so is long range. This long-range interaction presents a problem for the macroscopic degeneracy of spin ice, as it could render the energy of a given tetrahedron dependent on the configuration of neighbouring or more distant tetrahedra and so split the degeneracy of the ground state.

Monte Carlo simulations [44] by B. C. den Hertog and M. J. P. Gingras in 2000 [43] suggested that the dipole interactions were on the contrary responsible for the spin ice behaviour, and were capable of overriding antiferromagnetic exchange interactions at nearest-neighbour distances. In 2004 Isakov *et al.* [45] found analytically that the dipole interaction is almost perfectly self-screening when projected over long distances and reduces to a near-neighbour effect. This 'projective equivalence' means the effective interaction of the spins is entirely nearest-neighbour. Further neutron scattering work by Fennell et al. [46] made a detailed experimental test of this in 2009. The combined role of the exchange and dipole interactions in nearest-neighbour interactions can be expressed with an effective exchange constant

$$J_{\text{eff}} = J_{\text{nn}} + D_{\text{nn}} \tag{1.81}$$

where J_{nn} is the nearest neighbour exchange energy and D_{nn} the nearest neighbour dipolar energy [32]. A consequence is that so long as $J_{\text{eff}} > 0$, the material may be ferromagnetic and exhibit spin ice properties, even if J_{nn} is antiferromagnetic, as is in fact the case in holmium titanate [32] and dysprosium titanate [43].

1.5 Electrolytes

An electrolyte is a solution of charged ions. It consists of solvent molecules, in which are mixed compound, undissociated and dissociated ions. Electrolytes are considered 'weak' or 'strong' depending on whether the degree of molecular dissociation is small or large respectively. This is not to be confused with the dilution of the electrolyte.

1.5.1 Debye-Hückel Theory

Debye-Hückel theory was created in 1923 [47] by P. Debye and E. Hückel. It is a theory of the free energy arising from electrostatic interactions between ions in solution. A change in free energy will have consequences for other thermodynamic quantities such as the specific heat and the entropy, and so modelling it is of theoretical interest. The theory presented here is taken from the presentation in Moore [48].

As charges in a gas are subject to the Coulomb interaction, their distribution will not be random. Charges will attract charges of the opposite sign and so the charge atmosphere around each ion in equilibrium will have charge opposite to that of the ion itself. In the extreme situation of dominating electrostatic interaction the ions would achieve an order akin to that of an ionic crystal, but the thermal energy of the solution represented by kinetic collisions prevents such an ideal ordering. Nevertheless the atmosphere will have a net electrostatic energy.

First, the potential Φ experienced by a representative ion due to the other ions muse be determined. This potential derives from the ionic atmosphere, which is considered to be symmetric, and is related to the charge density by the Poisson equation:

$$\frac{1}{r^2}\frac{d}{dr}\left(r^2\frac{d\Phi(r)}{dr}\right) = \frac{-\rho}{\epsilon_0\epsilon} \tag{1.82}$$

with $\Phi(r)$ the potential, ρ the charge density of the atmosphere, ϵ_0 the permittivity of free space and ϵ the permittivity of the electrolyte. To obtain a solution, ρ must be formulated as $\rho(\Phi)$ and substituted into equation 1.82. The charge density ρ is defined by the distribution of charges, and the number of charges of type i in unit volume that have energy E_i above the average E_0 is given by

$$N_i' = N_i e^{-E_i/kT} \tag{1.83}$$

where N_i is the total number of charges of type i in unit volume. To bring a charge Q_i into a region of potential Φ requires work $Q_i\Phi$, and the energy of all charges can be defined this way. The average of this work across the whole solution of positive and negative charges will be zero, so all $E_0 = 0$. Therefore state:

$$N_i' = N_i e^{-Q_i\Phi/k_BT} \tag{1.84}$$

Charge density ρ in a unit volume is the sum of the charge per unit volume of each type of charge.

$$\rho = \sum (Q_i N_i') = \sum \left(Q_i N_i e^{-Q_i\Phi/k_BT}\right) \tag{1.85}$$

To simplify this one can make an important approximation. If the charges are sufficiently sparse or the temperature sufficiently high relative to their interaction energy, we can take $-Q_i\Phi/k_BT \ll 1$. The start of the expansion of the exponential $e^{-Q_i\Phi/k_BT}$ is:

$$e^{-Q_i\Phi/kT} = 1 - \frac{Q_i\Phi}{k_BT} + \frac{1}{2!}\left(\frac{Q_i\Phi}{k_BT}\right)^2 \tag{1.86}$$

which if terms in $Q_i\Phi/k_BT$ to the second power or higher are negligible, gives:

$$\rho = \sum (Q_i N_i) - \sum \left(Q_i N_i \frac{Q_i\Phi}{k_BT}\right) = \sum (Q_i N_i) - \frac{\Phi}{k_BT}\sum \left(Q_i^2 N_i\right) \tag{1.87}$$

That this linearisation of the exponential only holds for low concentrations or high temperatures represents a problem for Debye-Hückel theory, as one may often want to investigate the properties of an electrolyte that is not highly dilute.

The electrolyte is assumed to be overall charge-neutral, so the first term vanishes:

$$\rho = -\frac{\Phi}{k_BT}\sum Q_i^2 N_i. \tag{1.88}$$

With this equation $\rho(\Phi)$ has been obtained, so can be substituted into equation 1.82:

$$\frac{1}{r^2}\frac{d}{dr}\left(r^2\frac{d\Phi(r)}{dr}\right) = \frac{\Phi\sum Q_i^2 N_i}{k_BT\epsilon_0\epsilon} \tag{1.89}$$

$$\frac{d}{dr}\left(r^2\frac{d\Phi(r)}{dr}\right) = \Phi r^2\kappa^2 \tag{1.90}$$

where

$$\kappa^2 = \frac{\sum Q_i^2 N_i}{k_BT\epsilon_0\epsilon} \tag{1.91}$$

κ^{-1} is called the Debye length l_D.

To solve equation 1.90, substitute $u = r\Phi$:

$$\frac{d}{dr}\left(r^2 \frac{d\frac{u}{r}}{dr}\right) = \kappa^2 r u \tag{1.92}$$

simplifying by the chain rule to obtain:

$$\frac{d^2u}{dr^2} = \kappa^2 u \tag{1.93}$$

allowing a standard exponential solution:

$$u = Ae^{-\kappa r} + Be^{\kappa r}, \tag{1.94}$$

$$\Phi = \frac{A}{r}e^{-\kappa r} + \frac{B}{r}e^{\kappa r}. \tag{1.95}$$

Examining the boundary conditions, the Coulomb field of the central charge must vanish as as r approaches infinity, and so must the net field of the perturbation it creates in the charged atmosphere, as that is itself caused by the central charge field. So the total potential Φ of these fields must also vanish. e^{-r}/r converges to zero in the limit of infinite r, however e^{r}/r does not, so $B = 0$, leaving:

$$\Phi = \frac{A}{r}e^{-\kappa r} \tag{1.96}$$

which is the screened Coulomb potential. To find the value of A, substitute back into equation 1.82:

$$\frac{1}{r^2}\frac{d}{dr}\left(r^2 \frac{d\frac{A}{r}e^{-\kappa r}}{dr}\right) = \frac{-\rho}{\epsilon_0 \epsilon} \tag{1.97}$$

$$\rho = \frac{-A\kappa^2 \epsilon_0 \epsilon}{r}e^{-\kappa r} \tag{1.98}$$

This is the charge density of the monopole cloud around a single charge. But the total net charge of the cloud must be equal to the charge of the central charge, as the Coulomb gas is overall neutral. Therefore, integrating charged shells from the lattice distance a out to infinity,

$$\int_a^\infty 4\pi r^2 \rho(r) dr = -Q_i \tag{1.99}$$

$$\frac{A\kappa^2\epsilon_0\epsilon}{\int}_a^\infty 4\pi r e^{-\kappa r} dr = Q_i \tag{1.100}$$

$$\frac{A\kappa^2\epsilon_0\epsilon}{Q_i} = \frac{\kappa^2 e^{\kappa a}}{4\pi(1+a\kappa)} \tag{1.101}$$

$$A = \frac{Q_i}{4\pi\epsilon_0\epsilon}\frac{e^{\kappa a}}{1+\kappa a} \tag{1.102}$$

The final result for Φ is:

$$\Phi_i = \frac{Q_i}{4\pi\epsilon_0\epsilon}\frac{e^{\kappa a}}{1+\kappa a}\frac{e^{-\kappa r}}{r} \tag{1.103}$$

This is the potential around a charge in a free Coulomb gas sufficiently dilute that $Q\Phi \ll kT$. This potential is formed from the Coulomb potential of the charge plus the potential contributed by the ionic atmosphere. This form is that of a screened Coulomb potential, with the electrostatic force exerted by the central charge screened by its tendency to surround itself with opposite-sign charges. The effect of this screening is encapsulated in the Debye length $\kappa^{-1} = l_D$, which is the approximate distance over which the influence of one charge extends before it is screened out by the electrostatic fields of other charges. This quantity is also called the 'thickness of the ionic atmosphere' [48].

Now Debye-Hückel theory can be used to estimate the additional Coulomb energy obtained by introducing an ion to the Coulomb gas. First split the potential into its atmospheric and central components:

$$\Phi_i = \frac{Q_i}{4\pi\epsilon_0\epsilon r} + \frac{Q_i}{4\pi\epsilon_0\epsilon r}\left(\frac{e^{\kappa a}}{1+\kappa a}e^{-\kappa r} - 1\right) = \Phi_{ic} + \Phi_{ia} \tag{1.104}$$

No atmospheric ions can approach closer than a, so the potential due to the atmosphere at the central site will be equal to the atmospheric potential at $r = a$.

$$\Phi_{ia,r=a} = \frac{Q_i}{4\pi\epsilon_0\epsilon a}\left(\frac{e^{\kappa a}}{1+\kappa a}e^{-\kappa a} - 1\right) = -\frac{Q_i}{4\pi\epsilon_0\epsilon}\left(\frac{\kappa}{1+\kappa a}\right) \tag{1.105}$$

From this the energy required to introduce an ion of charge Q_i into the ionic atmosphere can be determined. Integrate the potential from 0 to Q_i:

$$\Delta E_i = \int_0^{Q_i} \Phi dQ_i' = -\int_0^{Q_i} \frac{Q_i'}{4\pi\epsilon_0\epsilon}\left(\frac{\kappa}{1+\kappa a}\right) dQ_i' = -\frac{Q_i^2}{8\pi\epsilon_0\epsilon}\frac{\kappa}{1+\kappa a} \tag{1.106}$$

This energy will feature prominently later as the Coulomb correction to the chemical potential, ν_{iC}:

$$\nu_{iC} = -\frac{Q_i^2}{8\pi\epsilon_0\epsilon}\frac{\kappa}{1+\kappa a} = -k_B T\frac{l_{Ti}}{a}\frac{\kappa a}{1+\kappa a} = -k_B T\frac{l_T}{l_D + a} \tag{1.107}$$

where l_{Ti} is the Bjerrum length associated with the ion type:

$$l_{Ti} = \frac{Q_i^2}{8\pi\epsilon_0\epsilon k_B T}. \tag{1.108}$$

The Bjerrum length is the distance at which the Coulomb interaction between two charges matches the thermal energy scale $k_B T$.

1.5.2 Conductivity

Electrolytes can conduct electrical charge due to the mobility of the dissolved ions. At the most basic level, the presence of an electric field will exert force on ions in the electrolyte:

$$\mathbf{F} = q\mathbf{E}. \tag{1.109}$$

However, the ions do not exist in a vacuum where they can move freely without competing interactions, but in a solvent medium. There are three effects that retard ion motion in electrolytes.

The ion is physically obstructed by the other atoms in the solvent (more precisely, by mutual electron repulsion if it moves too close). This obligates it to move not in a straight line but in a biased Brownian path as it finds gaps in the liquid solvent, causing acceleration to be frequently halted. This is the 'viscous effect'.

The viscous effect impedes all movement through a viscous medium. However there are two other effects particular to ions. First, we have seen above in the

treatment of Debye-Hückel theory that ions attract an oppositely-charged ionic atmosphere. When an ion moves, this atmosphere will not move with it immediately, but will take time to reform around the ion, and will be persistently chasing it if the ion movement is fast enough. This means there will be an oppositely-charged region of the electrolyte centred on the place the ion just left, which will attract it back to its original location. This creates a drag on ion movement called the 'asymmetry effect'.

Secondly, the ionic atmosphere will itself move under the electric field, in the opposite direction to the central ion. These moving ions will in turn move solvent molecules along with them, producing a current in the solvent medium against the central ion motion. This is called the 'electrophoretic effect'.

1.5.3 Wien Effect

Conductivity is typically described by Ohm's law [9]:

$$\mathbf{i} = \kappa \mathbf{E} \tag{1.110}$$

where $\mathbf{i}$ is the current density (Am^{-2}), $\mathbf{E}$ is electric field, and κ is the conductivity, a constant independent of the magnitude of $\mathbf{E}$. However, experiments demonstrated that the conductivity of electrolytes deviates from Ohm's law above low values of $\mathbf{E}$. This phenomenon is explained by the first and second Wien effects [48].

The first Wien effect is connected to the ionic atmosphere. As the applied field increases, the drift velocity increases, and will eventually overwhelm the random Brownian motion, creating a permanent movement in the field induced direction and preventing the formation of an ionic atmosphere. This eliminates the electrophoretic effect that retards ion conduction.

The second Wien effect is called the 'field dissociation effect'. A weak electrolyte has a certain 'degree of dissociation' α which describes the number of ions that exist as free ions relative to the number that remain in bound or closely associated pairs. A dissociatable compound of positive (P) and negative (N) ions can undergo the following reversible reaction:

$$\mathrm{PN} = \mathrm{P}^{+}\mathrm{N}^{-} = \mathrm{P}^{+} + \mathrm{N}^{-} \tag{1.111}$$

An applied field will act on the second step. It applies a force in opposite directions on the positive and negative ions, which will tend to separate them. Onsager [49] found in 1934 that for a strong field acting on a weak electrolyte, the ratio of dissociation constant in field to zero field was given by

$$\frac{K(\mathbf{E})}{K(0)} = \frac{J_1\left(4\sqrt{-b/2}\right)}{2\sqrt{-b/2}} \tag{1.112}$$

where $J_1(X)$ is the first order Bessel function, and

$$b = \frac{e^3|\mathbf{E}|}{8\pi\epsilon_0\epsilon k^2 T^2}. \tag{1.113}$$

For $b < 3$ this can be approximated by the power series

$$\frac{K(\mathbf{E})}{K(0)} = 1 + b + \frac{b^2}{3} + \frac{b^3}{18} + \frac{b^4}{180}\frac{b^5}{2700} + ..., \tag{1.114}$$

while for $b > 3$ this can be approximated by

$$\frac{K(\mathbf{E})}{K(0)} = \left(\frac{2}{\pi}\right)^{1/2} (8b)^{-3/4} e^{(8b)^{1/2}}. \tag{1.115}$$

1.6 Experimental Techniques

1.6.1 Magnetisation

The heat capacity measurements presented in this thesis were primarily taken using the magnetometry probe of a Quantum Design Physical Property Measurement System (PPMS).

Magnetisation can be measured in 'd.c.' or 'a.c.' form. To measure d.c. magnetisation, the sample is held in a nonmagnetic sample mount and exposed to the appropriate magnetic field. Then, the sample is passed through a set of conducting coils. The movement of a magnetised sample though the coil induces a voltage in accordance with equation 1.3. This current can be used to derive a value for the field generated by the magnetic moments inside the sample, and so

a value for the net magnetisation.

To measure a.c. magnetisation, the sample is positioned inside one of two detection coils, and then a driving field is applied by a drive coil. The field is allowed to cycle repeatedly and the measurements are averaged over the cycles to eliminate noise. The measurement is then repeated on a counter-wound coil, and this result again averaged.

The instruments themselves introduce error into the measurement due to time lag in the coil and electronics, which introduces a phase shift. This time lag may vary with the experimental parameters such as temperature, field and frequency. Eliminating this error source requires calibrating for the phase shift during each measurement.

1.6.2 Heat Capacity

Thermodynamics defines many quantities of theoretical interest, but not all of them are amenable to direct measurement. One easily accessible quantity is heat capacity, which gives access to the entropy and other quantities. This quantity is the focus of the investigation of Debye-Hückel theory in this thesis.

The heat capacity measurements presented in this thesis are primarily taken using the calorimetry probe of a Quantum Design PPMS. In this method the sample is mounted on a platform using thermal grease to ensure good thermal and mechanical coupling. The platform in turn is suspended in vacuum by wires, which form a weaker thermal link to the rest of the apparatus, which functions as a heat bath.

To take a measurement, the platform and the surroundings are stabilised at a test temperature. Then power is applied to a heater in the sample platform for a determined length of time, raising its temperature and that of the sample. The power is terminated, and the sample platform is allowed to relax to match the surroundings. The platform temperature is monitored throughout this process, and together with the heater power data provides the raw experimental data.

The heat capacity of the sample can be extracted by fitting the relaxation profile to a theoretical model. The PPMS instrument uses two models, one that assumes perfect thermal contact between the sample and the platform, another

that introduces separate sample-platform and platform-surroundings relaxation times.

The simple model is based on the equation:

$$P = (C_a + C_x)\frac{dT_p}{dt} + K_1(T_p - T_0) \tag{1.116}$$

where P is the heater power, C_a and C_x are the heat capacities of the sample and the addendum (the remainder of the complex added to the platform, *e.g.* thermal grease), T_p and T_0 are the sample and bath temperatures respectively, K_1 is the thermal conductance between sample and bath and t is time. The equation can be integrated and fitted to empirical T_p vs. t data to yield the unknown C_x.

The more complex model is based on the simultaneous differential equations:

$$P = C_a\frac{dT_p}{dt} + K_2(T_p - T_x) + K_1(T_p - T_0) \tag{1.117}$$

$$0 = C_x\frac{dT_x}{dt} + K_2(T_x - T_p) \tag{1.118}$$

where K_2 is the thermal conductance between sample and platform and T_x is the sample temperature. For $K_2 \ll K_1$, $T_p = T_x$ is a good approximation and equations 1.117 and 1.118 simplify to equation 1.116.

In 2014 Bovo *et al.* [50] investigated the accuracy of these methods by examining the performance of the PPMS specific heat measurements on bulk and thin film spin ice, whose small heat capacity makes accuracy essential. They highlighted two potential sources of error: K_2/K_1 not being large enough, requiring the decision by the system to use the full thermal equations, and a strongly temperature-dependent C_x.

If K_2/K_1 is not large, the relaxation has two time constants τ_1 and τ_2, for the coupling of the platform to the bath and the sample to the platform respectively. In the event that τ_2 is small, the least squares fitting procedure is unreliable, so the system adopts the simplified model of equation 1.116. Bovo *et al.* [50] however found that the error introduced by the simplified model was negligible. If C_x is strongly temperature-dependent, the investigation found that the fitting procedure introduced significant errors, but only for heating pulse times significantly longer than those used in specific heat experiments.

The PPMS system automatically selects the relaxation model that is most appropriate for a particular measurement and sample. As the usage of the PPMS in the current work is an entirely conventional specific heat measurement of bulk spin ice samples, like those tested by Bovo *et al.* [50], no significant systematic error is expected. Single standard deviation random errors are introduced by the instrument.

Chapter 2

Magnetic Monopoles in Spin Ice

Just as the ground state of water ice is equivalent the ground state of spin ice, there exists an analogy between a form of thermal defect in 1_h water ice and a form of thermal defect in spin ice. A violation of the ice rule for a given oxygen atom in water produces an electrically charged 'ionic defect' with either three (H_3O^+) or one (OH^-) protons near to it [24]. Likewise a given tetrahedron obeying the ice rule may be transformed into a 3-in-1-out (3-1) or 1-in-3-out (1-3) defect by flipping one of its four spins [3]. Such defects are created in pairs, as a proton or spin in an ice connects two sites, and moving the proton or flipping the spin in an otherwise ice-rule configuration creates a defect on both. At higher energy cost, 4-0 (H_4O^{2+}) and 0-4 (O^{2-}) 'double defects' carrying twice the charge can be created, and these are essential to the physics of spin ice in the high-temperature regime.

In 2005 Ryzhkin [3] demonstrated that such magnetic defects carry effective positive and negative magnetic charges. This result was independently obtained and reinforced in 2008 by Castelnovo, Moessner and Sondhi (CMS) who explicitly identified such charges as 'magnetic monopoles' [31]. Figures 2.1 and 2.2 from their paper demonstrate the phenomenon visually. The quasiparticles are not monopoles in the fundamental sense of divergences in the magnetic field **B**. However if examined above the atomic scale they constitute opposite divergences in the fields **H** and **M** [3, 31] which sum to prevent a violation of the Maxwell equations, and exhibit many properties appropriate to independent and disconnected north and

south poles. So magnetic charge density can be defined:

$$q = -\nabla \cdot \mathbf{M} \tag{2.1}$$

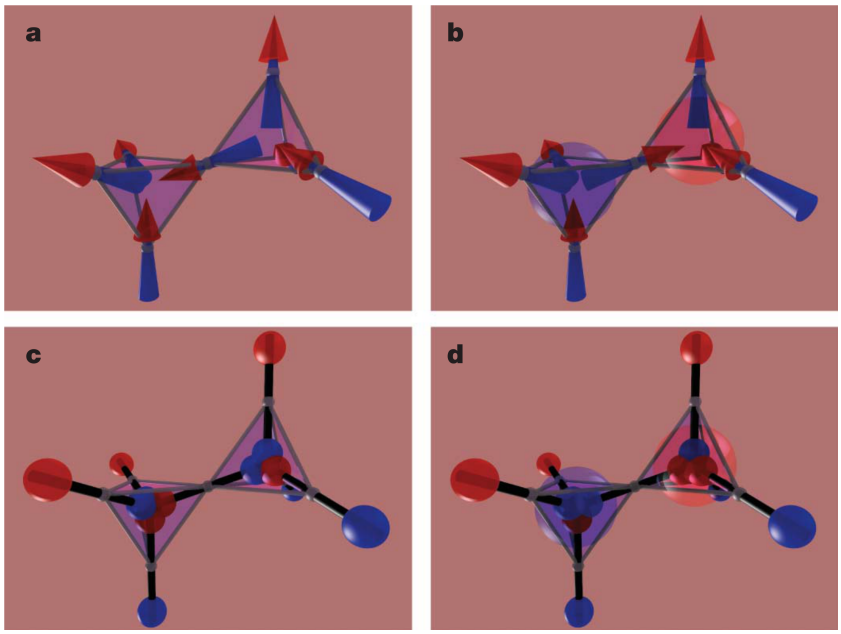

Figure 2.1: a) A pair of dipolar model ice sites in the ground state. b) The same pair with the connecting spin flipped, producing two monopoles. c) A pair of dumbbell model ice sites in the ground state. d) The same pair with the connecting dipole flipped. Reprinted by permission from Macmillan Publishers Ltd: Nature (Castelnovo *et al.* 2008 [31]), copyright 2008.

A chain of identical dipoles generates an H field equivalent to that of two magnetic charges, each placed at one end of the chain[12]. Once a defect pair has been created in spin ice, it can be extended by further spin flips or proton movements (see Figure 2e). If a 3-1 or 1-3 defect exists on a site adjacent to a 2-2 site and is connected to that site by one of the three majority spins, flipping that spin will return the defect site to a 2-2 configuration but alter the 2-2 site to an equivalent defect configuration. In effect, insofar as we consider the defect a quasiparticle in its own right, it has moved from the initial site to the second. Such an operation makes no net change to the nearest-neighbour dipole configuration and so costs no energy in itself [31]. This is in contrast to a similar operation of extending a dipole flip chain in, for example, a conventional ferromagnet. The energy cost that does exist is entailed by the violation of the ice rules and is

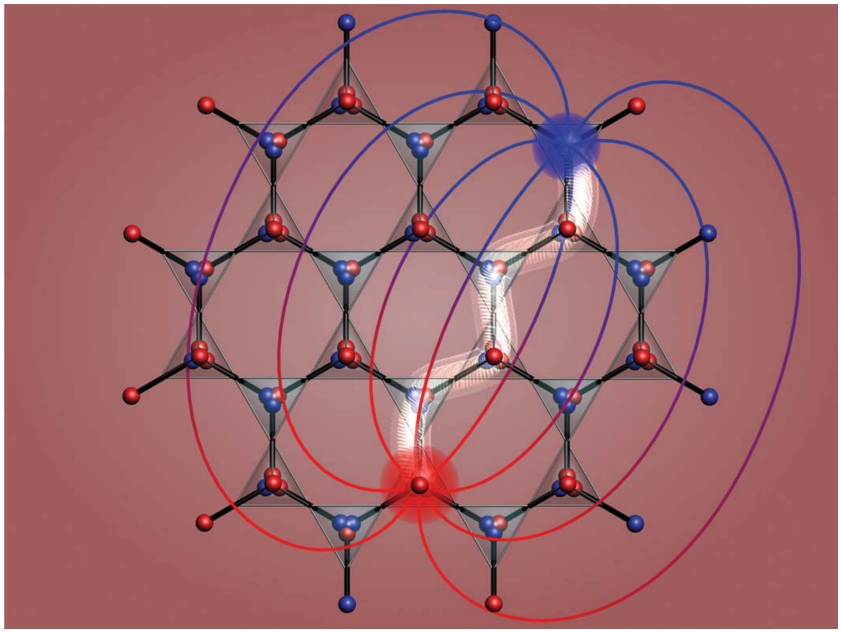

Figure 2.2: A network of dumbbell sites with a monopole pair separated by a spin chain. Reprinted by permission from Macmillan Publishers Ltd: Nature (Castelnovo *et al.* 2008 [31]), copyright 2008.

determined by the distance between the two defects, and is a Coulomb interaction [31]:

$$E = \frac{-\mu_0 q_m^2}{4\pi r} \tag{2.2}$$

where μ_0 is the permeability of free space, q_m is the monopole charge, and r is their separation. Compare the electrostatic Coulomb interaction between charges of like magnitude [9]:

$$E = \frac{-q_e^2}{4\pi\epsilon_0 r} \tag{2.3}$$

where μ_0 substitutes for its electric equivalent $1/\epsilon_0$.

This energy is bounded as the dipoles are separated to infinity and so the defects are not only mobile but are deconfined, and not restricted to remain near one another except by the physical limits of the crystal [31].

Furthermore, the defects once created cannot in general be uniquely identified with a partner by a single or even small number of dipole chains. In spin ice one can draw arbitrary chains by entering each tetrahedron on an in-spin and leaving on

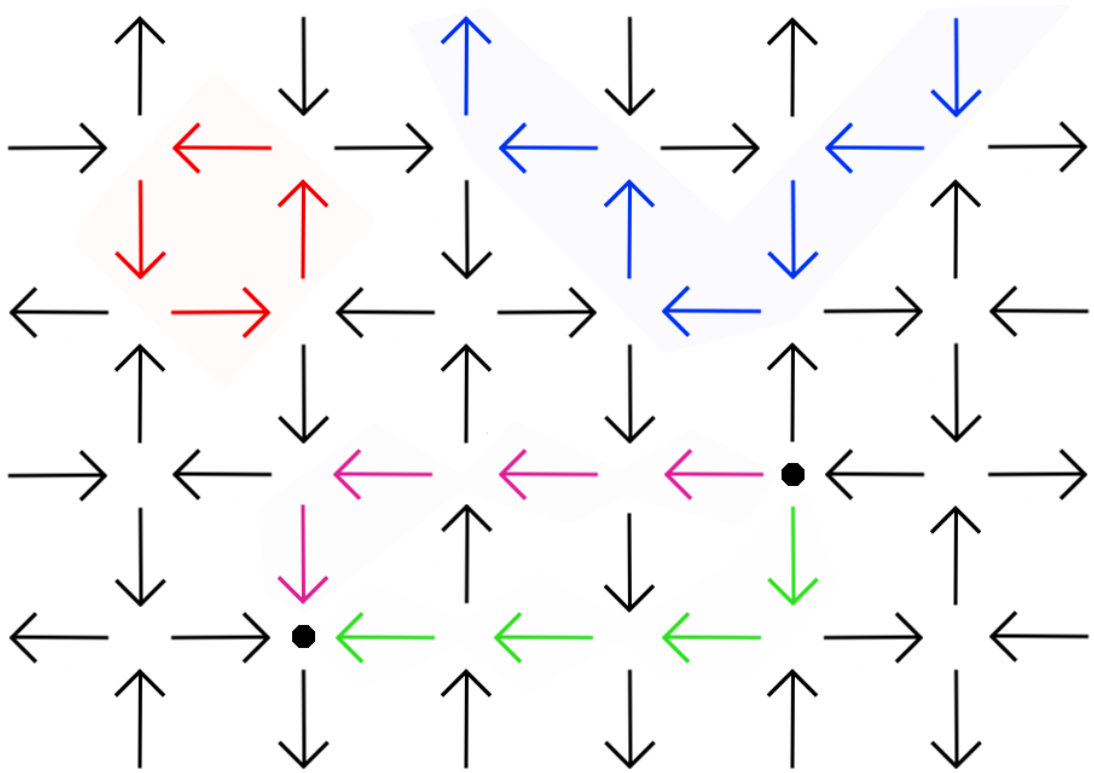

Figure 2.3: Representation of a 2D square spin lattice. The red arrows describe a closed loop. The blue arrows describe a spin chain terminating on the surface. The green and purple arrows present two alternative spin chains connecting the monopoles, represented by black circles. Similar topological features are present in a 3D diamond spin lattice.

one of the out-spins. In the ground state configuration, if every dipole is traversed only once, all chains chosen may only terminate on the crystal surface or close upon themselves and form a loop. However in a configuration with defects, such a chain may terminate on a defect. In such a circumstance a summation of all chains in one chosen configuration will reveal net charge at each defect site, but there are a very large number of possible chain networks that could be drawn, each valid and revealing the same result. The historical dipole chain the defect traversed is irrelevant to the physics of the system except in extreme ordering cases. Figure 2.3 shows a sample spin configuration in a two-dimensional spin ice network that illustrates these features.

This picture of unconstrained monopoles in an open sea is not perfect. The charges are defined by and so constrained by the vector geometry of the spin lattice.

A defect of a given polarity can move from one site to another by flipping a spin from one particular orientation to the opposite orientation. Movement of charges in one direction and their opposed charges in the opposite direction will polarise the spin network. This introduces a fundamental geometric constraint on monopole motion, in that the same spin cannot be traversed by the same charge of monopole in the same direction consecutively, but even at low monopole concentrations the polarisation reduces the entropy of the network. This is analogous to the theory of electrical relaxation in ice via proton movement derived by Jaccard in 1964 [51].

In zero field this constraint is not critical, but if the crystal is exposed to a magnetic field then all defects of one type will move with the field, and their opposites will move against it. This movement will rapidly polarise the network and produce a counteracting force that halts the magnetic current. Due to this constraint, it is impossible to sustain DC magnetic currents even in an infinite spin ice crystal [42]. When the crystal is polarised in this way, the Dirac strings become observable by diffuse neutron scattering as reported by Morris *et al.* in 2009 [52].

A 2011 theoretical result by Ryzhkin [53] shows that the DC current inhibition also hampers the ability of such crystals to screen external magnetic fields. Even in zero field it has been proposed that this constraint affects monopole dynamics by realising an 'entropic charge'. The work on this possibility will be discussed in section 3.1.4.

2.1 Dumbbell Model

An approximation of the dipolar model (see section 1.4.1) to a dumbbell model is used by Castelnovo *et al.* in their 2008 paper. [31]. In this model each magnetic dipole is transformed into a 'dumbbell' with a positive magnetic charge at one end and a negative charge at the other. Each charge is situated at the centre of one of the tetrahedra.

Given N dumbbells, corresponding to dipoles, each with a magnetic charge q or $-q$ at either end, we have $2N$ charges labelled q_i where $i = 1, 2, ..., 2N$. Now if we define that identically located charges have a same-site-interaction energy factor ν_S, and otherwise a Coulomb interaction, we obtain:

$$V_{ij} = \begin{cases} \frac{\mu_0 q_i q_j}{4\pi r_{ij}}, & r_{ij} \neq 0 \\ \nu_S q_i q_j, & r_{ij} = 0 \end{cases}, \tag{2.4}$$

where V_{ij} is the interaction energy between charges i and j and r_{ij} their separation, and other symbols have their usual meaning.

Each diamond lattice site is the meeting point of four dumbbells, so contains four charges. Summing the charges at each site a obtains $Q_a = q_{a1} + q_{a2} + q_{a3} + q_{a4}$, and then for sites $a, b, ...$:

$$V_{ab} = \begin{cases} \frac{\mu_0 Q_a Q_b}{4\pi r_{ab}}, & a \neq b \\ \frac{1}{2}\nu_S Q_a^2, & a = b \end{cases}. \tag{2.5}$$

The quantity $\frac{1}{2}\nu_S Q^2$ is equal to the ν_0 defined in section 3.1.2.

In their paper [31] Castelnovo *et al.* derive a value for ν_S:

$$\nu_S = \left(\frac{a}{\mu}\right)^2 \left(\frac{J}{3} + \frac{4}{3}\left[1 + \sqrt{\frac{2}{3}}\right] D\right) \tag{2.6}$$

where a is the diamond lattice constant, μ the magnetic moment of the spins, and J and D the exchange and dipolar coupling constants respectively [2]. However in the work presented in this report the monopole energy is occasionally allowed to float as a fitting variable.

This approximation automatically gives 'projective equivalence' (discussed in section 1.4.1), as each 2-in 2-out tetrahedron will have a net charge of zero at all points, and so no net influence on the rest of the dumbbells. Only when the spin ice state contains defects will local charge exist, as in such cases there will be three charges of one sign and one of the opposite at the defect site, resulting in a net charge of magnitude $2q$. In the most extreme case, four charges of one sign may occupy a single lattice site to produce a charge of magnitude $4q$. These net charges will mean the other charges in the dumbbell network experience a net magnetostatic force from the defect site.

2.2 Magnetolyte Model

The final abstraction of spin ice physics is to consider it as a system of monopoles in the grand canonical ensemble. At this point we have abstracted quite far from the magnetic-pyrochlore basis, but the model is nevertheless remarkably effective at describing the physics of spin ice above the ground state.

In this model the material is understood as a vacuum from which magnetically charged quasiparticles emerge. The particles move diffusively between sites on a diamond lattice and interact via the Coulomb interaction, forming a Coulomb gas [42]. This picture of a Coulomb gas of particles corresponds closely to a classical electrolyte, a surprising result given the very different physical realities underlying the two.

However, the correspondence is not perfect. Magnetic charge quasiparticles exist on a lattice rather than in free space, which constrains their motion. Furthermore, even if one defines an electrolyte on a lattice, the spin ice magnetolyte is constrained by the configurations of the underlying spin network. Importantly, sustained DC currents are impossible in a magnetolyte due to polarisation of the network by the monopole movement [42], as discussed at the start of this chapter.

Of the effects on conduction in electrolytes described in section 1.5.2, not all are applicable to magnetolytes. The viscous and electrophoretic effects are dependent on the particular microscopic physics of electrolytes, and will not apply to the magnetolytes, which have no solvent medium. However spin ice defects do not gain momentum and must search for permissible spin-flip routes to move through the diamond lattice, which is an effect similar to the viscous effect.

2.3 Debye-Hückel Theory for Magnetic Monopoles

If spin ice is modelled as a gas of magnetic charges, it can be treated with the same techniques, despite its radically different microscopic nature. The possibility of this unlikely union was first demonstrated by Castelnovo, Moessner and Sondhi [4] in 2011. Their derivation of Debye-Hückel theory, presented below, produced the theoretical specific heat seen in figure 2.4 reproduced from their paper, compared against experimental data. The theory has some success at low temperatures but

less as temperature increases. Also shown in figure 2.4 is their interpretation of the effective limits of Debye-Hückel theory, which halts at 2 K, beyond which they contend, in line with typical interpretations of Debye-Hückel theory, that high monopole density causes the theory to break down. However, even for $T < 2$ K their theory diverges significantly from the experimental data.

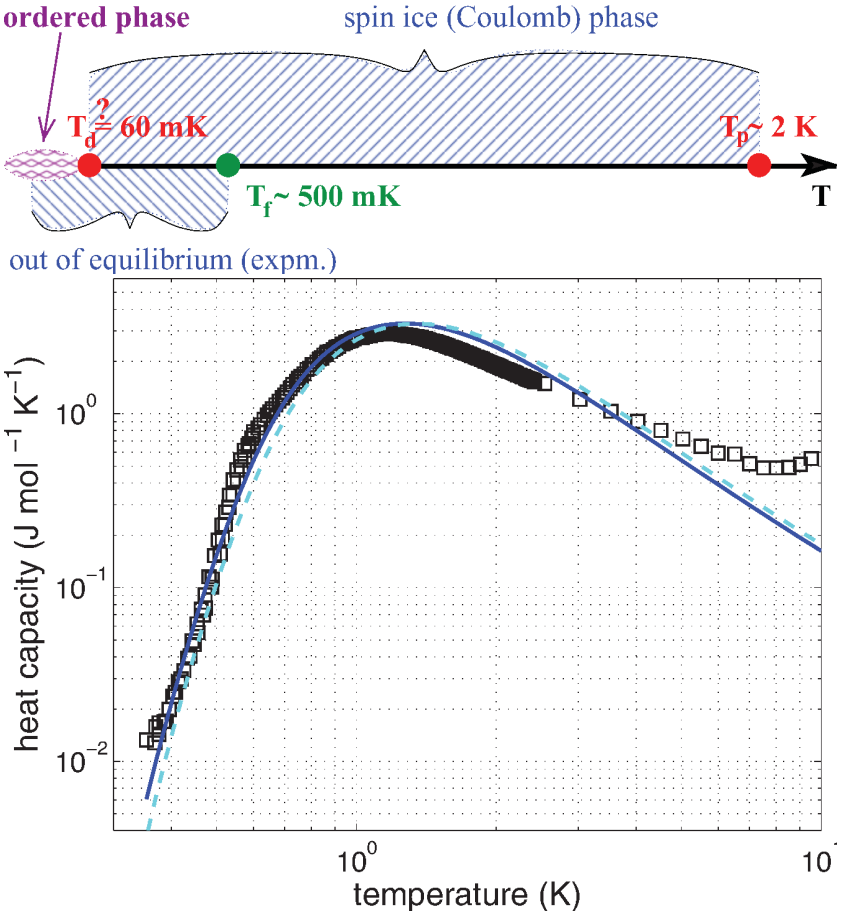

Figure 2.4: Upper figure: Regions of DTO physics according to Castelnovo *et al.*. Note proposed end of Coulomb phase at 2 K. Lower figure: heat capacity of DTO. Black squares are experimental results, solid blue line is CMS Debye-Hückel theory with $\nu_0 = 4.37$ K, dashed cyan line is CMS Debye-Hückel theory with $\nu_0 = 4.57$ K. Reprinted figures with permission from C. Castenovo *et al.*, Physical Review B, 84, 144435, 2011 [4]. Copyright 2011 by the American Physical Society.

The CMS derivation takes a different approach to the derivation of a Debye-Hückel theory to the derivation given in section 1.5.1. To begin their derivation they describe a system of non-interacting monopoles. They write internal energy

U as:

$$U = N\Delta = N_t x \Delta, \tag{2.7}$$

where N is the monopole count, Δ is the energy cost of an isolated monopole (measured here in Kelvin), N_t is the pyrochlore lattice site count, and x is the dimensionless monopole density N/N_t. N monopoles will consist of $N/2$ positive and $N/2$ negative monopoles, which can be organised among N_t lattice sites in W ways:

$$W = \frac{N_t!}{(N/2)!^2(N_t - N)!}. \tag{2.8}$$

N_t and N are assumed large, so using Stirling's approximation and equation 1.59:

$$S = -k_B N_t[2(x/2)\ln(x/2) + (1-x)\ln(1-x)]. \tag{2.9}$$

This allows the definition of the free energy per spin:

$$\frac{F_{nn}}{N_s} = \frac{Uk_B - TS}{N_s} \tag{2.10}$$

where $N_s = 2N_t$ is the spin count. The k_B attached to U converts the units of Δ to Joules.

Minimising this, they obtain an expression for monopole density:

$$x_n n = \frac{2e^{-\Delta/T}}{1 + 2e^{-\Delta/T}}. \tag{2.11}$$

This is a Boltzmann distribution over the partition function for a system of two types of monopole and one type of ground state site.

This result is only for non-interacting monopoles. To account for the Coulomb interaction between monopoles they deploy the following approximation used by Debye and Hückel in 1923:

$$\frac{F_{el}}{N_s K_B} = -\frac{NT}{4N_s \pi x_V a_d^3}\left[\frac{(a_d\kappa)^2}{2} - (a_d\kappa) + \ln(1 + a_d\kappa)\right], \tag{2.12}$$

where κ is the Debye length seen in equation 1.91. x_v is the volume density of

monopoles, N/V. This simplifies to

$$\frac{F_{el}}{N_s K_B} = -\frac{T}{3\sqrt{3}\pi}\left[\frac{(a_d\kappa)^2}{2} - (a_d\kappa) + \ln(1+a_d\kappa)\right]. \tag{2.13}$$

This expression allows the definition of a mean-field free energy per spin, measured in Kelvin:

$$\frac{F}{N_s k_B} = \frac{x}{2}\Delta + \frac{Tx}{2}\ln\left(\frac{x/2}{1-x}\right) + \frac{T}{2}\ln(1-x) - \frac{T}{3\sqrt{3}\pi}\left(\frac{\alpha^2 x}{2} - \alpha\sqrt{x} + \ln(1+\alpha\sqrt{x})\right), \tag{2.14}$$

where

$$\alpha(T) = \sqrt{\frac{3\sqrt{3}\pi E_{nn}}{2T}} \tag{2.15}$$

and $E_{nn} = (\mu_0 Q^2)/(4\pi a_d k_B)$ is the Coulomb energy between a pair of neighbouring monopoles.

Searching as before for a minimisation of free energy, they find:

$$\frac{d(F/N_s k_B)}{dx} = \Delta + T\ln\left(\frac{x/2}{1-x}\right) - \frac{E_{nn}}{2}\frac{\alpha\sqrt{x}}{1+\alpha\sqrt{x}} = 0 \tag{2.16}$$

$$x = \frac{2e^{-\left(\frac{\Delta}{T} - \frac{E_{nn}}{2T}\frac{\alpha\sqrt{x}}{1+\alpha\sqrt{x}}\right)}}{1+2e^{-\left(\frac{\Delta}{T} - \frac{E_{nn}}{2T}\frac{\alpha\sqrt{x}}{1+\alpha\sqrt{x}}\right)}}. \tag{2.17}$$

This pair of equations cannot be solved analytically, but CMS solve it numerically with a recursive approach. However, as discussed later these expressions are theoretically inaccurate in some respects, and a main result of this thesis is an improvement of the Debye-Hückel theory of spin ice.

2.4 Monopole Dynamics

The description of the magnetic structure of spin ice in terms of monopoles also proved a valuable perspective for investigating the magnetic behaviour of spin ice. If spin ice magnetic defects act as monopoles macroscopically they will be mobile under field and their flow will partially if not wholly constitute the magnetic response of the system. The initial theoretical work was done by Ryzhkin in his

original 2005 paper [3] (after the example of Jaccard 1964 [51]) in which he defined the 'configuration vector' $\mathbf{\Omega}$ as follows:

$$\mathbf{\Omega}(\mathbf{r}) = \frac{a}{2}\Sigma_{i\alpha}\sigma_{i\alpha}\frac{\hat{e}_{i\alpha}}{V} \tag{2.18}$$

summing over all spins in a macroscopically small volume V around r. $\sigma_{i\alpha}$ defines the direction of the Ising spin and $\hat{e}$ the unit vector along which it points. a is the diamond lattice constant. Thus, $\mathbf{\Omega}$ is a quantity measuring the local 'directionality' of the spins, with an additional $a/2$ factor.

Multiplying $\mathbf{\Omega}$ by the magnetic moment μ of the spins and dividing by $a/2$ yields the total local magnetic moment $\mathbf{M}$:

$$\mathbf{M}(\mathbf{r}) = \frac{2\mu}{a}\mathbf{\Omega}(\mathbf{r}) \tag{2.19}$$

So recalling $Q = 2\mu/a$:

$$\mathbf{\Omega} = \mathbf{M}/Q \tag{2.20}$$

The change in configuration vector also defines the defect flux. A spin flip will either move a defect or create a defect pair, which is magnetically equivalent to moving a defect away from a site on which it was stacked with an opposite defect. As such a spin flip from $\mathbf{e}$ to $-\mathbf{e}$ is equivalent to the displacement of a positive defect by $a\mathbf{e}$ or a negative defect by $-a\mathbf{e}$.

$$d\mathbf{\Omega} = d\mathbf{r}_+ N_+ - d\mathbf{r}_- N_- \tag{2.21}$$

where N_+ is the number of positive defects moved by $d\mathbf{r}_+$ and N_- the number of negative defects moved by $d\mathbf{r}_-$. In time-dependent form this becomes

$$\frac{\partial \mathbf{\Omega}}{\partial t} = \mathbf{j}_+ - \mathbf{j}_- \tag{2.22}$$

And in integral form:

$$\mathbf{\Omega}(t) - \mathbf{\Omega}(0) = \int_0^t (\mathbf{j}_+ - \mathbf{j}_-)dt' \tag{2.23}$$

where $\mathbf{j}_{(+,-)}$ is the positive or negative defect flux $d\mathbf{r}_{(+,-)}/dt \times N_{(+,-)}V$.

He relates the defect flux to applied field and configuration vector as:

$$\mathbf{j_i} = u_i n_i \mu_0 (Q_i \mathbf{H} - \eta_i \Phi \mathbf{\Omega}) \tag{2.24}$$

where $n_{1,2}$ is the defect concentration $x_i N$ (N the number of tetrahedra, x_i the proportion occupied by defects of type i), $u_{1,2}$ is the mobility, $\eta_{1,2} = \pm 1$ and $\Phi = (8/\sqrt{3})akT$. The permeability of free space μ_0 is added to the expression in his paper [3] due to a difference in units.

Equations 2.23 and 2.24 can be solved for $\mathbf{\Omega}$ and $\mathbf{j_i}$ given $\mathbf{H}(t)$. Using this and applying an oscillating field that varies as $H \propto e^{-i\omega t}$, Fourier transformations lead to

$$\mathbf{M}_\omega = \chi_T(\omega)\mathbf{H}_\omega, \tag{2.25}$$

$$\chi_T(\omega) = \frac{Q^2}{\Phi[1 - i\omega\tau]}, \tag{2.26}$$

a theoretical prediction for the frequency dependent magnetic susceptibility. For a constant field frequency ω is zero so this becomes:

$$\chi_T = Q^2/\Phi. \tag{2.27}$$

2.4.1 Brownian and Other Monopole Motion

In 2013 Bovo *et al.* [54] presented a study of the mechanisms of monopole diffusion and high-frequency AC response and made an explicit test of Ryzhkin's dynamical theory. Monopoles follow diffusive dynamics because they are massless quasiparticles that 'move' via random spin flips rather than massive particles with substantial momentum, but the more precise nature of these dynamics was not previously known. Bovo *et al.* [54] found from relaxation time measurements that the mobility below 10 K is proportional to $1/T$ as seen in figure 2.5 from their paper. This is consistent with the Nernst-Einstein equation describing Brownian motion [54]:

$$u = \frac{DQ}{k_B T} \tag{2.28}$$

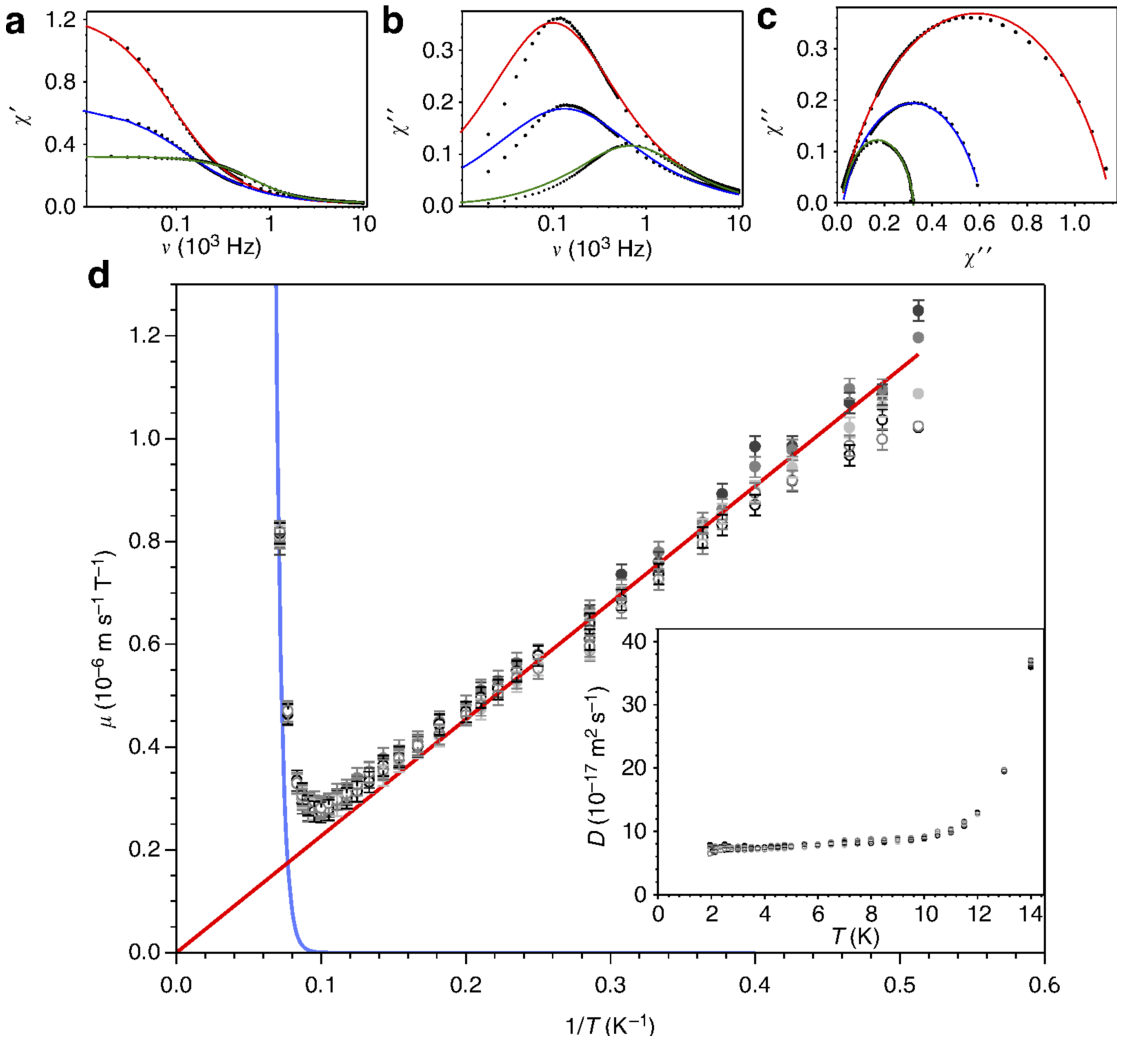

Figure 2.5: a: Real DTO susceptibility versus frequency. b: Imaginary DTO susceptibility versus frequency. c: Cole-Cole plot (argand diagram) for DTO. Coloured lines are fits to χ_T, χ_S, α and τ from equation 2.29 at temperatures $T = 4.5$ K (red), $T = 8$ K (blue) and $T = 14$ K (green). d: Monopole mobility measured at applied fields $\mu_0|H| = 0$ (fullblack), 3 (fulldarkgrey), 10 (fulllightgrey), 18.5 (openblack), 38.5 (opengrey) mT. Bars represent standard deviation. Red line is $u = A/T$, a Brownian diffusion characteristic. Blue line is $u = Be^{-C/T}$ with $B = 39(1)$ ms^{-1}T^{-1} and $C = 250(1)$ K, an Orbach-like process appearing at high temperature. Reprinted by permission from Macmillan Publishers Ltd: Nature Communications (Bovo *et al.* 2013 [54]), copyright 2013.

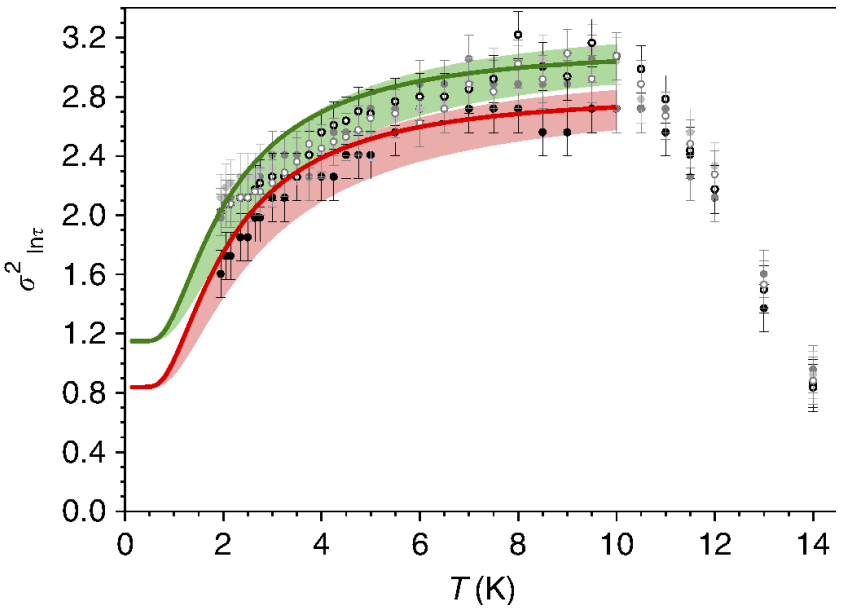

Figure 2.6: Variance in logarithmic relaxation time $\sigma^2_{ln\tau}$ (circles, bars represent standard deviation) in zero field or the set of applied fields mentioned in fig 2.5. Lines represent fitted function $\sigma_1^2 + x\sigma_2^2$ where $x(T)$ is the monopole density, fitted over the zero field data (red) or finite field data (green). Shaded areas the maximum systematic error in the monopole density. Reprinted by permission from Macmillan Publishers Ltd: Nature Communications (Bovo *et al.* 2013 [54]), copyright 2013.

where u is the monopole mobility, Q the monopole charge, T the temperature and D the diffusion constant. D here is temperature independent, and if related to the monopole hop rate ν_0 as $D = \nu_0 a^2/6$ finds a temperature independent hop rate. This temperature independence of the hop rate (also noted by Jaubert and Holdsworth [42] regarding the temperature-invariant τ_0 in the Arrhenius equation, discussed below) is evidence that spin flips in spin ice are a quantum mechanical tunnelling process.

The Coulomb correlations between monopoles are potentially destructive to the Brownian nature of their diffusion. However this effect can be suppressed in practice so long as the Debye screening length is small, in which case there will be no long-range correlations and the Nernst-Einstein equation will hold [54]. The existence of Brownian diffusion under this condition is another point of correspondence between spin ice systems and electrolytes.

The relaxation results focused on the relationship between the isothermal susceptibility χ_T, the susceptibility in the limit of low frequency (i.e. d.c. field) where

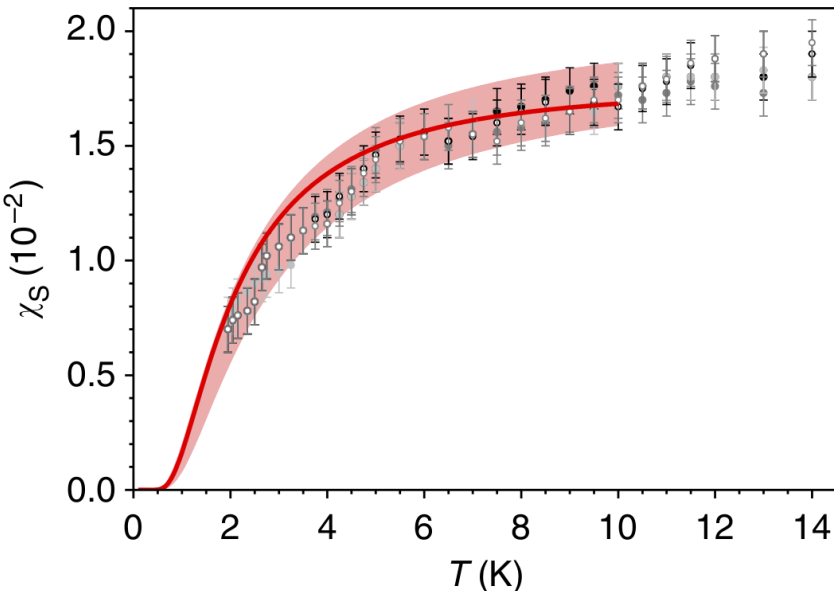

Figure 2.7: Adiabatic susceptibility χ_S against temperature. Circles are measured susceptibility at the same fields as in fig. 2.5, with bars representing standard deviation. The red line is the monopole density fitted to $\chi_S(0)$ by a scale factor, with the shaded area representing the maximum systematic uncertainty. Reprinted by permission from Macmillan Publishers Ltd: Nature Communications (Bovo *et al.* 2013 [54]), copyright 2013.

the sample can always thermally equilibrate with the environment, and the adiabatic susceptibility χ_S, which is the susceptibility in the limit of high frequency where heat transfer to the environment is zero. By modifying the theory of Ryzhkin from his original monopole paper [3], Bovo *et al.* [54] obtain the relation:

$$\frac{\chi(\omega) - \chi_S}{\chi_T - \chi_S} = \frac{1}{1 + (i\omega\tau)^{1-\alpha}} \tag{2.29}$$

where τ is a relaxation time expressible by $\tau^{-1} = \mu_0 u Q x / V_0 \chi_T$ and α is a parameter determining the width of the relaxation time distribution. This expression is based on the Cole-Cole magnetic relaxation model [55] and incorporates said distribution of relaxation times after a singular time was found to be unable to fit the data, going beyond the approximations made by Jaubert and Holdsworth [42] and Ryzhkin [3].

They theorise that the dispersion of rates is due to magnetic fields from the monopole gas affecting the flipping rates of spins, and find from this an expression

relating α to the monopole population x, allowing a direct test of the theory. In figure 2.6 reproduced from their paper, the y-axis quantity $\sigma^2_{\ln\tau}$ is the variance in logarithmic relaxation time, derived from α. It can be seen to be closely correlated with the theoretical expression $\sigma_1^2 + x\sigma_2^2$, where $\sigma_{1,2}$ are fitted parameters representing the effect of the mean square static field and mean square monopole field respectively.

By fitting equation 2.29 to the data Bovo *et al.* [54] obtain isothermal susceptibility χ_T values consistent with the previous work of Jaubert *et al.* [56] predicting a change in the relation of the susceptibility to the Curie constant with temperature. Jaubert *et al.* find the magnetic behaviour of HTO to cross over between a high temperature ($T > 100$ K) paramagnetic regime where $\chi_T = C/T$ and a low temperature ($T < 1$ K) spin-liquid regime where $\chi_T = 2C/T$. Bovo *et al.* find $\chi_T(2\text{ K}) = 1.8\text{C/T}$ and $\chi_T(10\text{ K}) = 1.2\text{C/T}$ for DTO, consistent with Jaubert *et al.*'s results. They note that this Curie behaviour of χ_T is characteristic of a spin system and reveals no direct monopole signature, and suggest that the entropic restrictions on DC monopole currents suppress the influence of monopoles at low frequencies.

At high frequencies, Bovo *et al.* [54] find an almost linear relationship between the adiabatic susceptibility $\chi_S(T)$ and the monopole density $x(T)$, visible in figure 2.7. Their theory is that this is due to a plasma-like monopole oscillation, consisting of a frictionless reversible displacement of magnetic monopoles in the applied field. This suggests plasma physics as another field of notably non-crystalline theory with potential to be profitably mined to describe spin ice, and presents ultra-high frequency a.c. susceptibility measurements as a direct probe of the monopole concentration in spin ice. It is also notable as a definitely monopolar theory, in contrast to the spin theory of χ_T, though it should be noted that the monopole model is defined in terms of the spin model and the two never conflict, even if one or the other is more useful in a certain context.

These results, however, are in the $T > 2$ K region. The fits performed by Bovo *et al.* [54] using the expression in equation 2.29 do not describe the low-frequency, low-temperature behaviour of spin ice, as shown in figure 2.5b from their paper. As noted by Jaubert and Holdsworth [42] after Snyder *et al.* [57], the low-temperature region operates under a different relaxation regime to the plateau

region where the experimental results of Bovo *et al.* are concentrated. Despite the Curie behaviour of the isothermal susceptibility χ_T even at these temperatures, the magnetic relaxation behaviour may contain subtleties on which the monopole model may shed light.

2.4.2 Numerical Study of Monopole Dynamics

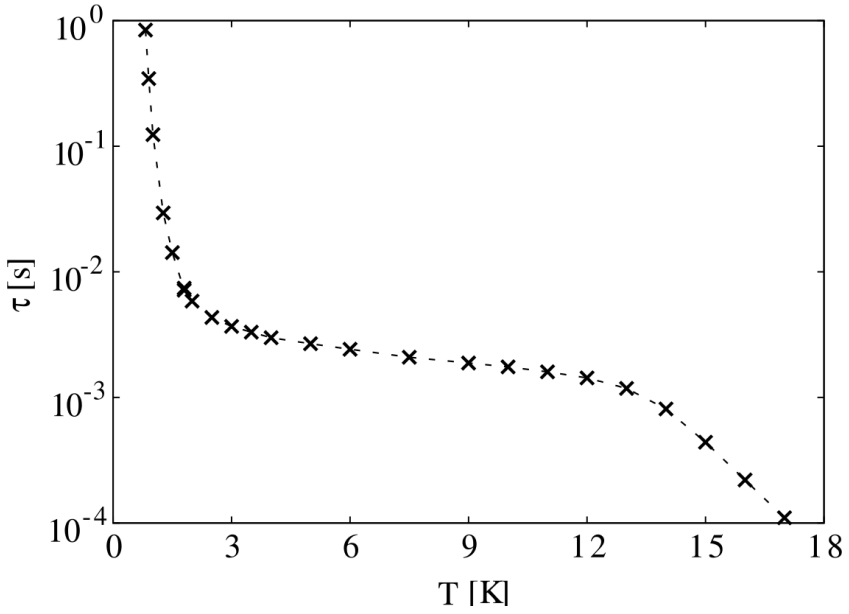

Figure 2.8: Experimental spin relaxation time τ of DTO at various temperatures. Three regions are clearly visible. Figure from [42] using data from [57].

As mentioned above, in 2011 L. D. C. Jaubert and P. C. W. Holdsworth published a detailed numerical study [42] of monopole dynamics.They drew on the 2004 work of Snyder *et al.* [57], which identified three general regimes of magnetic relaxation shown in figure 2.8: a high-temperature regime where the Ising behaviour of the spins breaks down and the spin ice model becomes inapplicable, a plateau of relaxation time τ between 3 and 12 K where the monopole population is saturated, and a low-temperature spin freezing regime where τ increases rapidly.

They found that the plateau region was successfully fitted by an Arrhenius law with an energy scale equal to the cost of creating a single monopole absent Coulombic effects, later slightly improved by a modification of this energy to allow

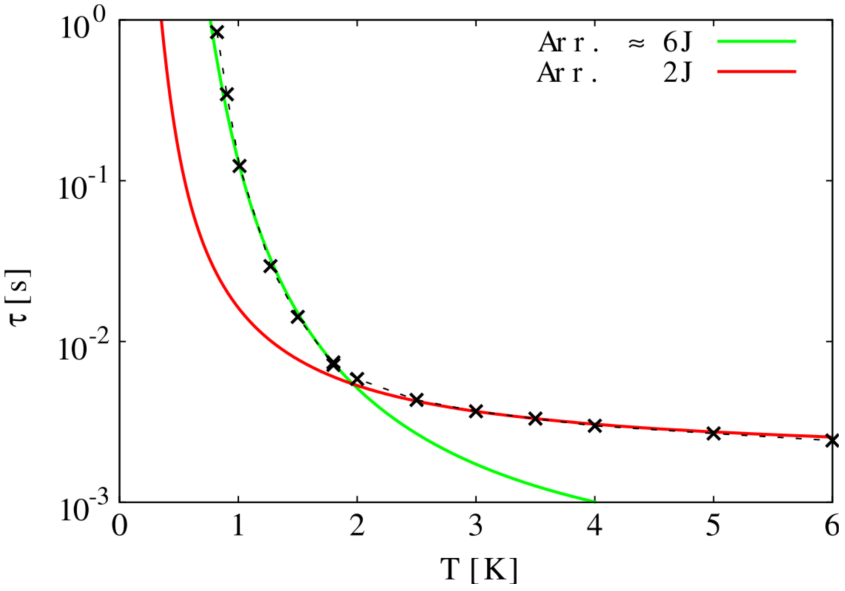

Figure 2.9: Characteristic spin relaxation time of DTO at various temperatures, experimental data from [57] and theoretical predictions of Arrhenius models. Black crosses are experimental data, with dotted guideline. Solid lines are Arrhenius predictions. Note different regions of success for different Arrhenius energies. Figure from [42].

for double defect creation. That the cost of a single monopole rather than of a pair of monopoles defines the Arrhenius energy demonstrates that the monopole pairs have fractionalised into individual poles. However, as can be seen in figures 2.9 and 2.10, this law fails to predict the relaxation timescale in the low temperature region. Previous work by Matsuhira *et al.* [58] had fitted an Arrhenius law of a higher energy scale to the magnetic relaxation of HTO and HSO in the low-temperature region with a higher characteristic energy. An approximate DTO equivalent of this is shown by the green line in figure 2.9 and it is clear that this fails to predict the relaxation timescale in the plateau region.

Simulations by Jaubert and Holdsworth [42] found that a pure nearest-neighbour spin ice (NNSI) with no dipolar effects generated similar relaxation results to the Arrhenius law, but a full dipolar spin ice model produced accurate results through both freezing and plateau regions. This indicates that the spin freezing is due to long-range dipolar interactions, the most important of which is Coulombic interactions between defects.

Further simulations examined the exact effect of the Coulomb interactions.

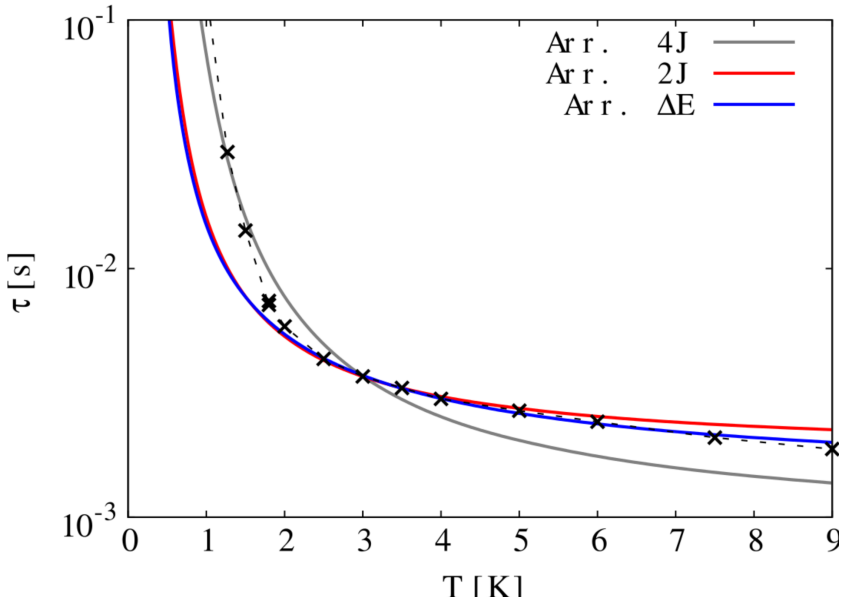

Figure 2.10: Characteristic spin relaxation time of DTO at various temperatures, experimental data from [57] and theoretical predictions of Arrhenius models. Black crosses are experimental data, with dotted guideline. Solid lines are Arrhenius predictions. Note different regions of success for different Arrhenius energies. Figure from [42].

Figure 2.11 (reproduced from their paper) shows the value of the energy cost to create a defect pair from the ground state manifold as yielded by Monte Carlo simulations of a DSI model without double charges. The energy cost increases at low temperatures, leading to a reduction in monopole population, which in turn reduces the magnetic relaxation rate (as can be seen by comparing with figures 2.9 and 2.10) as it is creation or movement of monopoles that changes the system magnetisation. The reduction of the energy cost with increasing temperature is due to Debye screening, but while this anticipates the work presented here by measuring the screening effect, it is incomplete as double charges were excluded from the calculations.

This screened monopole model of the relaxation is not contradictory to the work done on the Arrhenius law. The Arrhenius equation used is of the form:

$$\tau = \tau_0 e^{\beta \Delta E} \tag{2.30}$$

where ΔE is some characteristic energy barrier and τ_0 is typically understood as

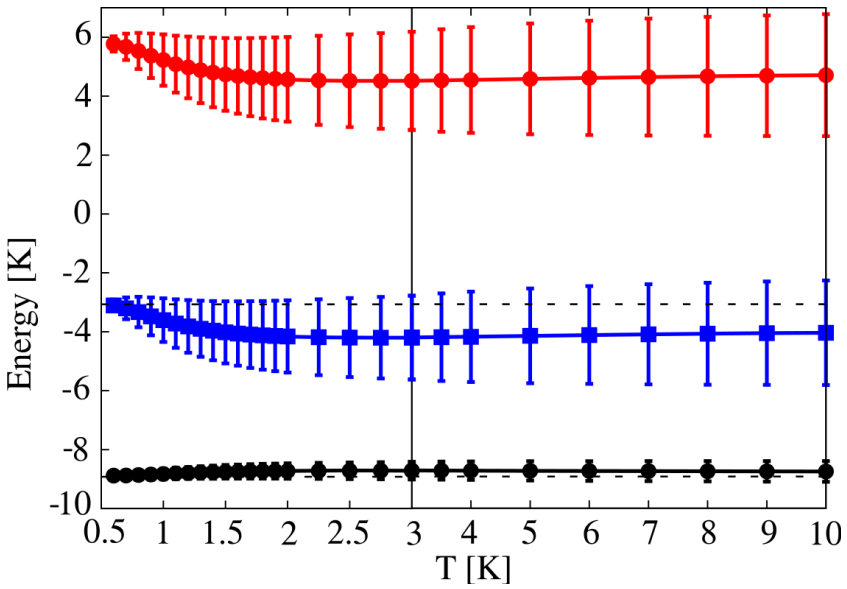

Figure 2.11: Energy required to create a pair of magnetic monopoles in Monte Carlo simulations of a dipolar spin ice model (red), or energy gained from creation of a monopole pair in simulations of a Coulomb gas (blue). Black line is the difference between them, twice the negative monopole chemical potential (-2ν). Bars are standard deviations, not errors. Upper dashed line is an analytical prediction of energy gain of creating a monopole pair in a vacuum. Lower dashed line is low-temperature limit of 2ν. Figure from [42].

the timescale for an attempt rate at that process. In the case of spin ice the process is the formation of monopoles from the ice-rules vacuum, and the Boltzmann factor $e^{\beta\Delta E}$ accounts for two thermally-governed factors: the population of monopoles which can magnetise or demagnetise the sample by moving, and the possibility of creating new monopole-antimonopole pairs by flipping spins on neutral sites. As the bulk magnetisation of the system is determined by the configuration of the spin or Dirac string network, both processes control the magnetisation.

2.4.3 Wien Effect in Spin Ice

In 2009 Bramwell *et al.* [59] presented muon spin rotation (μSR) results claiming to have established the presence of discrete magnetic Coulomb charges and measurable associated currents, along with the existence of non-Ohmic conductivity in DTO. Their method was based on demonstrating a proportionality between

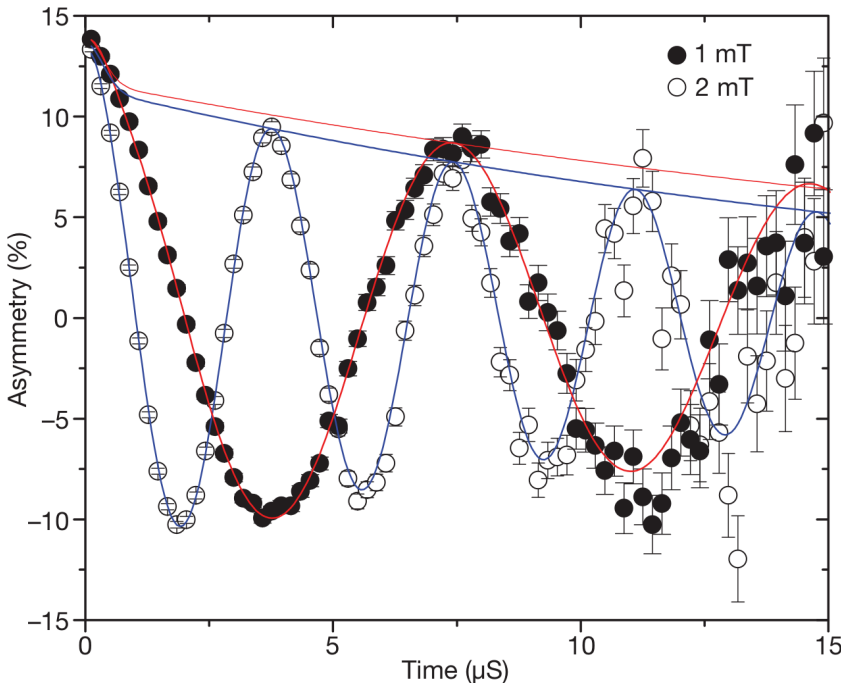

Figure 2.12: Asymmetry profile of muon decay over time in DTO sample. Reprinted by permission from Macmillan Publishers Ltd: Nature (Bramwell *et al.* 2009 [59]), copyright 2009.

magnetic moment fluctuation rate and magnetic conductivity under field.

$$\frac{\nu_\mu(B)}{\nu_\mu(0)} = \frac{\kappa(B)}{\kappa(0)} = 1 + \frac{b}{2}, \tag{2.31}$$

where ν_μ is the magnetic moment fluctuation rate, κ is the magnetic conductivity and b the Onsager factor:

$$b = \frac{Q^3|H|}{8\pi\mu_0 k_B^2 T^2}$$

for the low field limit. This is consistent with the concept that magnetic charge motion is the mechanism of magnetisation change in spin ice.

In a transverse field μSR experiment [59], spin-polarised muons are implanted into the sample and their decay (half life $\tau = 2.2$ μs) into positrons observed by opposed positron detectors. As muons are electrically charged they they precess around the local magnetic field and this precession can be measured by opposing positron detectors measuring the distribution of the direction of emitted positrons over time. A 1mT applied transverse field over the sample predicts an oscillatory

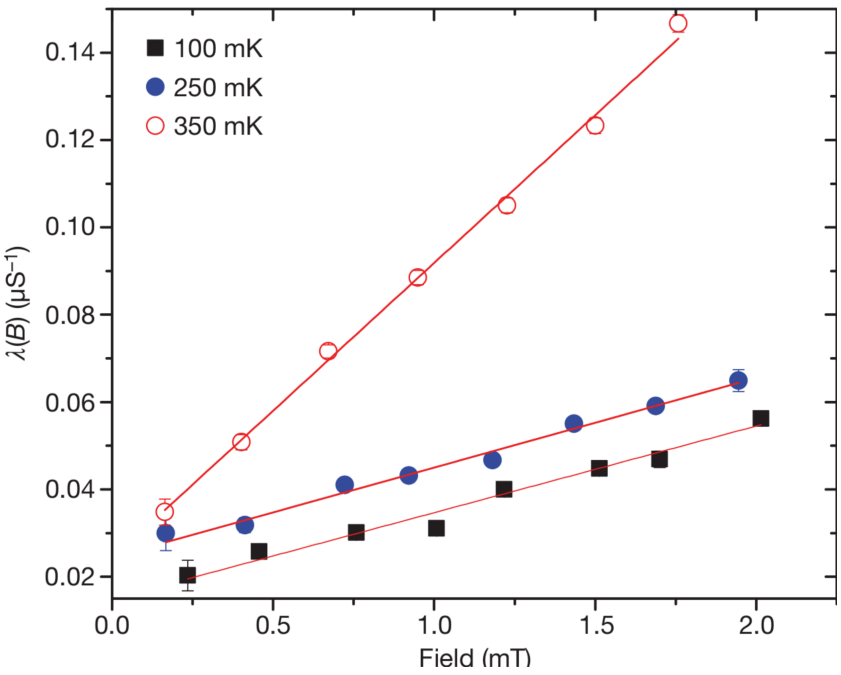

Figure 2.13: Muon relaxation rate $\lambda(B)$, proportional to magnetic charge conductivity, against field. Reprinted by permission from Macmillan Publishers Ltd: Nature (Bramwell *et al.* 2009 [59]), copyright 2009.

form for the spin precession as the muons 'orbit' the field direction. Deviations from the muon relaxation function predicted by the applied field provide evidence of the local field. In figure 2.12 reproduced from their paper, one can see both the oscillatory form and the effects of fluctuations in the local field. which manifest as the exponential shrinking and breakdown of the envelope. The exponential decay of the display envelope is governed by the muon relaxation rate λ, which at low temperatures is proportional to the magnetic moment fluctuation rate ν_μ.

In figure 2.13, relaxation rate λ is shown to increase with field, indicating a non-Ohmic increase in magnetic conductivity in line with Onsager's theory. In figure 2.14, magnetic charge Q derived from this theory is plotted against inverse temperature. Notably, the result obtained for the charge is close to the theoretical prediction yielded by the dumbbell model for DTO. For $1/T < 3$ K^{-1} the derived charge begins to anomalously increase, a phenomenon later explained by Bramwell *et al.* [60] by reference to experimental error from muons implanting outside of the sample.

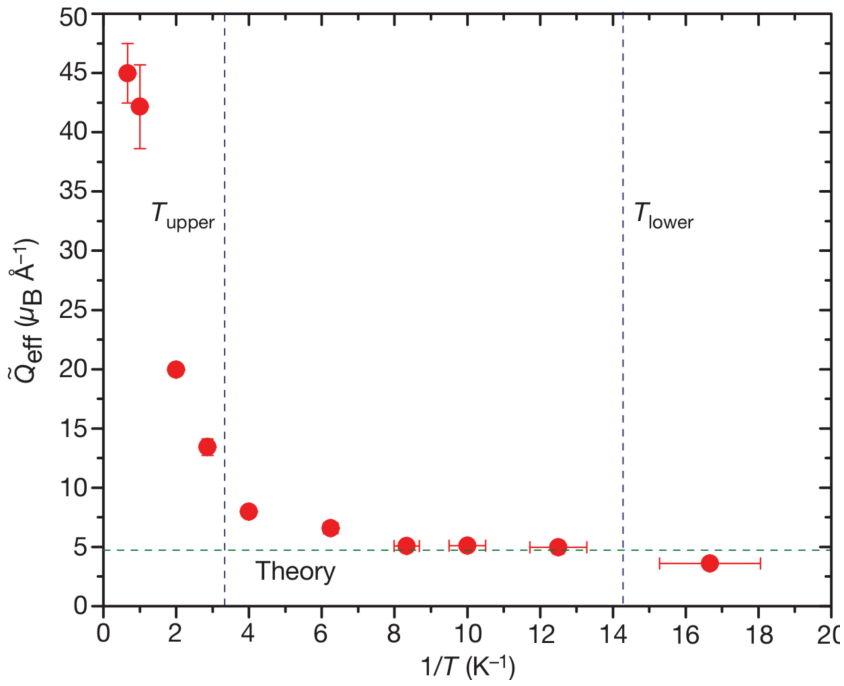

Figure 2.14: Estimated monopole charge against inverse temperature. Reprinted by permission from Macmillan Publishers Ltd: Nature (Bramwell *et al.* 2009 [59]), copyright 2009.

These results were challenged by Dunsiger *et al.* [62]. Firstly, they used Monte Carlo simulations of a microscopic model of DTO to estimate the internal field at likely muon implantation locations, and found that fields of several hundred mT were probable. Fields this large will rapidly damp the polarisation function to zero, overwhelming the effect of the 1 mT applied field. Secondly, they performed μSR measurements in a 2 mT applied field both with and without a DTO sample, and obtained similar results for the asymmetry distribution over time. Their interpretation of this was that the muon signature detected instead derived from muons landing elsewhere in the instrument than in the sample itself. Thirdly, they took μSR measurements in zero applied field and reported an unexpectedly rapid spin relaxation rate at $T < 5$ K, faster than predicted by monopolar theory.

Bramwell *et al.* have defended their result [60]. To the first point they held that their analysis was of a minority component of the muons at sites with internal fields smaller than the applied field, rather than muons in the typical sites with rapid damping. To the second point they held that below 0.4 T the effect of extra-sample muons does not dominate and that correcting for their presence eliminates

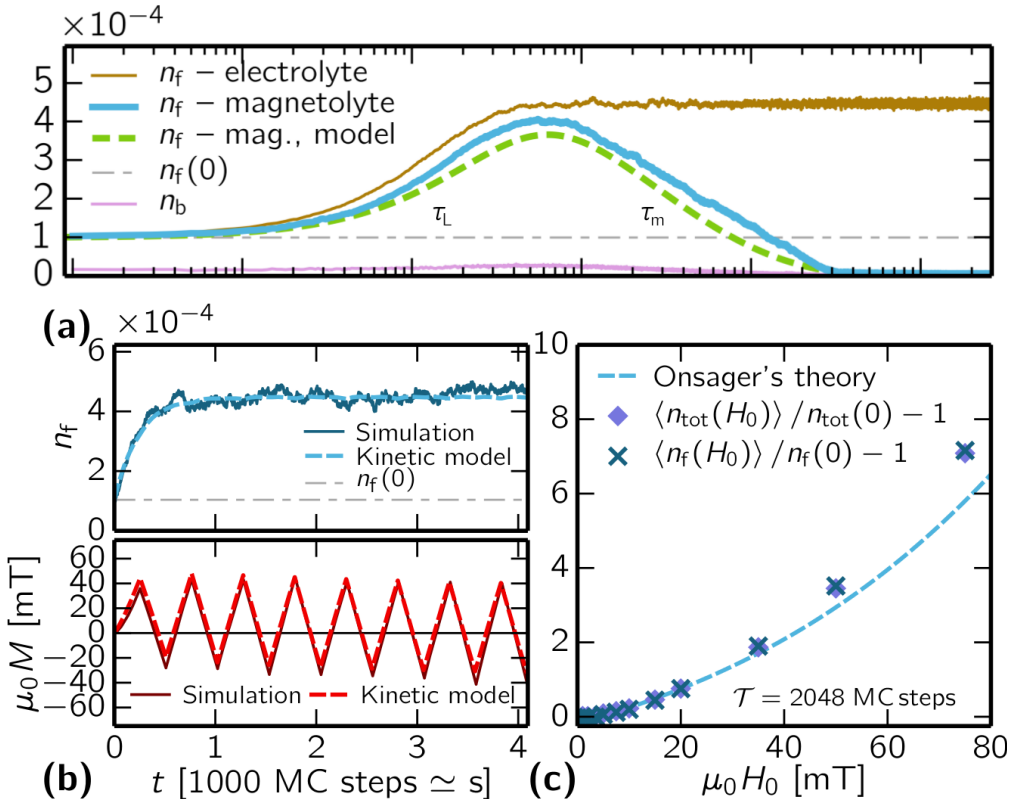

Figure 2.15: Upper figure: charge density n versus log time under field quench in simulation and according to magnetolyte model. In electrolyte, density increase is permanent, in manetolytes, transient. Figure (a): Square wave driving field stabilises increased charge density n. Figure (b): Leads to oscillating magnetisation. Figure (c): Average density increase against amplitude of applied field, and against Onsager's model. Reprinted figures with permission from V. Kaiser *et al.*, Physical Review Letters, 115, 037201, 2015 [61]. Copyright 2015 by the American Physical Society.

the anomalous rise in Q at $T > 0.3$ T seen in figure 2.12 from their original paper [59]. Repeating their experiment with non-spin ice samples or with the DTO sample blocked by a silver plate eliminated the Wien effect. Finally, they held that Dunsiger *et al.*'s experimental procedure was prone to systematic error and did not attempt to replicate their own result, which was replicated in HTO by a separately working group in 2011 [63]. The controversy has not been decisively resolved at the time of publication.

In 2014 Kaiser, Bramwell *et al.* performed Monte Carlo simulations on a periodic-boundary dumbbell model of DTO [61]. They found first of all that a

field directly applied to a magnetolyte causes a transient increase in the monopole density, consisting of an initial increase caused by the Wien effect followed by a decrease as the monopole currents caused by the field magnetise the system. They further found that using an alternating magnetic field can stabilise the density increase against this collapse. These results are summarised in Figure 2.15 reproduced from their paper, which also demonstrates the close correspondence between the magnetolyte results and similar results for a simulated weak electrolyte. Further evidence for the Wien effect will be considered in chapter 4 of this thesis.

2.4.4 Low-Temperature Dynamics and Extrinsic Defects

In 2012, work by Revell *et al.* [5] highlighted the potential importance of deviations from ideality in spin ice. They performed DC and AC magnetic relaxation measurements on DTO at temperatures from 0.475 K to 1.1 K and found that the decay of the magnetisation is not effectively described by simple monopole models. With assistance from Monte Carlo simulations they proposed that the decay was described by a stretched exponential, and affected by surface effects, a temperature-dependent attempt rate proportional to monopole density, and crystal defects that produce a long-time tail in the relaxation.

Their proposed defect type was the 'spin stuffing defect'. This type of defect replaces nonmagnetic titanium ions in DTO with magnetic dysprosium ions as shown in figure 2.16 from their paper. This changes the energy levels of local spin configurations such that monopoles have lower energy when near to the stuffed spin and monopole creation near the spin has a lower energy cost. This type of defect had previously been investigated in spin ice at occupation levels of 10% or more [64][65], but Revell *et al.* [5] found in simulations that it could have a significant effect even at less than 1% stuffing.

Their result of an attempt rate proportional to monopole density was not supported by Bovo *et al.* in the 2013 paper discussed above [54], but as the Bovo *et al.* experiments were performed at much higher temperatures, it is possible this is because the monopole population was near saturation and so not strongly dependent on temperature.

A closer examination of the Revell *et al.* [5] stretched exponential expression

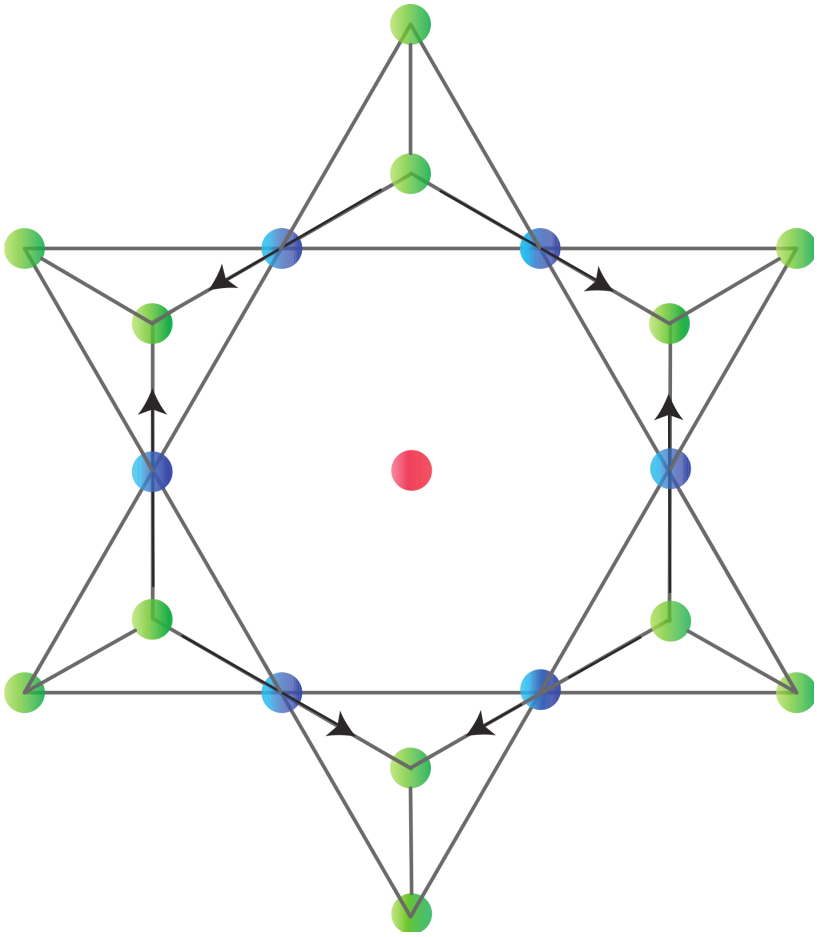

Figure 2.16: Position of an additional 'stuffed' dysprosium ion occupying a titanium site (red circle). Blue circles are the nearest-neighbour dysprosium spins with Ising axes labelled. Green circles are remaining dysprosium ions on adjacent tetrahedra. Reprinted by permission from Macmillan Publishers Ltd: Nature Physics (Revell *et al.* 2013 [5]), copyright 2013.

and its relation to other expressions and new data will be undertaken in chapter 4. However, the question of defects was taken up in recent work by Sala *et al.* [6], which empirically establishes the presence of oxygen-vacancy defects which have a similar effect.

Sala *et al.* created defect-free DTO crystals by annealing conventionally grown crystals in oxygen. Annealing is a process wherein the sample is heated sufficiently that atoms can move within the sample. By doing so within an oxygen atmosphere, oxygen atoms can diffuse into vacancies within the crystal, reducing or eliminating defects due to oxygen absences. The effect of the annealing was confirmed by them

for the closely related crystal $Y_2Ti_2O_7$ (YTO) by diffuse neutron scattering which revealed that the conventionally grown crystals had a similar diffuse scattering pattern to oxygen-depleted crystals, but the annealed crystals were missing features found in both. They also present neutron scattering plots of conventionally grown DTO to demonstrate that they show the same features as defective YTO, but the features are not very clearly visible. These results can be seen in figure 2.17 from their paper [6]. However, that a change has occurred after annealing the as-grown DTO crystals in oxygen is demonstrated by the magnetisation results.

The as-grown and annealed crystals were examined with d.c. and a.c magnetisation measurements as shown in figures 2.18 and 2.19 from their paper [6]. The d.c. measurements suggest that the as-grown crystals have reduced magnetic susceptibility, implying that present oxygen vacancies reduce the magnetic moment of associated Dy^{3+} ions.

In the AC measurements, a long-time tail seen in Revell *et al.*'s work [5] (see figure 2.19) and reproduced in the defective crystals of Sala *et al.* [6] is eliminated in the annealed crystals. This suggests first that the ascription of the long-time tail to the presence of defects is accurate, and second that the defects responsible are oxygen vacancies that can be mostly eliminated through treatment of the crystal, rather than stuffed dysprosium spins as Revell *et al.* hypothesised.

Sala *et al.* [6] go on to present a model for the structure of the oxygen defects based on CEF calculations. As shown in figure 2.20 from their paper, the oxygen vacancy creates a tetrahedron with four XY-type spins (see section 1.3) rather than Ising spins. Monopoles cannot exist, or even be defined, on this site, and it is surrounded by four tetrahedra with 3 Ising spins and one XY spin each, to which the ice rules do not apply. If one calculates by counting surface spins the entire five-site cluster will have a net magnetic charge that can be incremented or decremented by monopole movements in or out, but the interior of the cluster does not have monopoles defined in the same way as the crystal bulk due to a lack of normal spin ice tetrahedra. Sala *et al.* [6] calculate that a monopole moving to a defect cluster can reduce energy by quantities comparable to the monopole chemical potential, implying a strong pinning effect [6].

Returning to the low-temperature regime, the finding of Snyder *et al.* [57] that magnetic relaxation timescales dramatically extend at low temperatures is

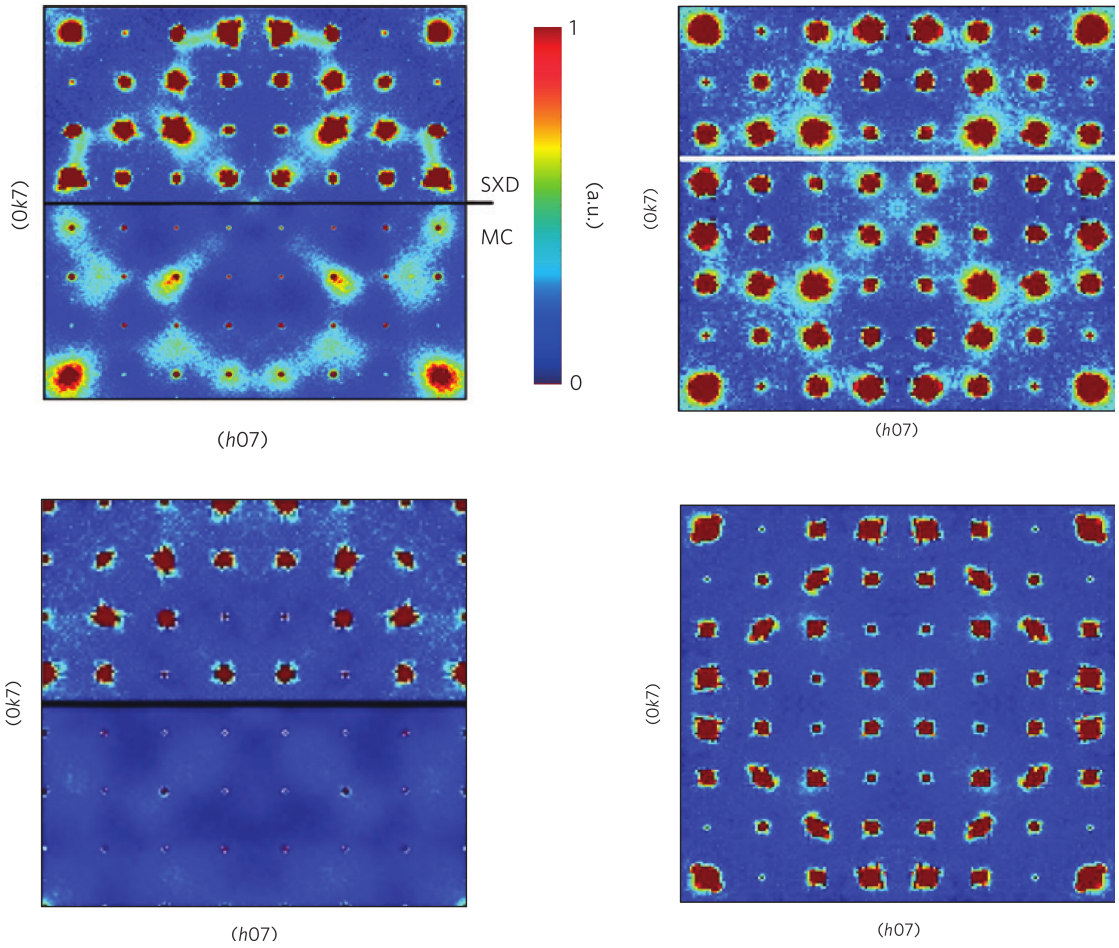

Figure 2.17: Upper left figure is diffuse neutron scattering from oxygen-deficient ($Y_2Ti_2O_{6.79}$) YTO in (hk7) plane, both experimental (upper) and in Monte Carlo simulation (lower). Pale blue cross and ring represent effects of oxygen deficiency. Upper right figure is similar experimental plot for oxygen-grown YTO, with features present, and lower right figure is for oxygen-annealed YTO, with features absent. Lower left figure is similar plot for oxygen-grown DTO, with features faintly present. Reprinted by permission from Macmillan Publishers Ltd: Nature Materials (Sala *et al.* 2014 [6]), copyright 2014.

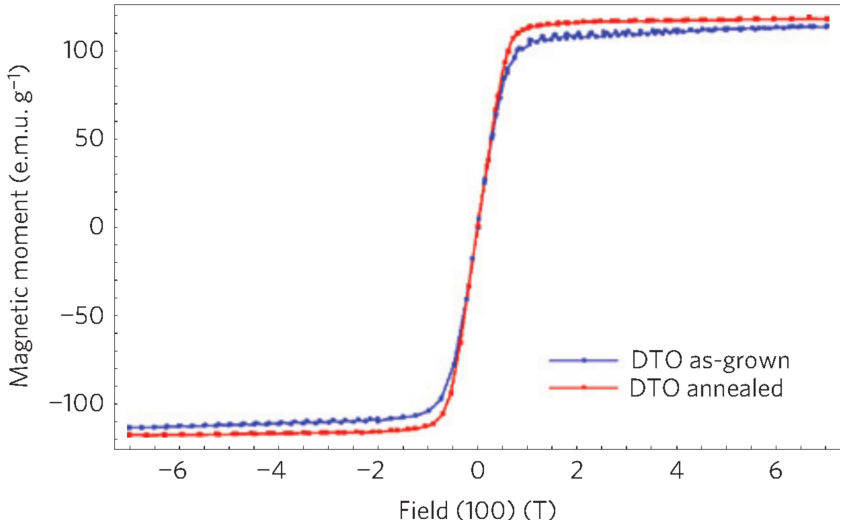

Figure 2.18: d.c. magnetisation versus applied field in [100] direction at $T = 2$ K for normal and annealed DTO crystals. Reprinted by permission from Macmillan Publishers Ltd: Nature Materials (Sala *et al.* 2014 [6]), copyright 2014.

mirrored by work from Pomaranski *et al.* in 2013 [66]. By taking extremely long-term measurements of the heat flow into and out of a DTO crystal inside a magnetically shielded dilution fridge, the authors obtain a specific heat at low temperatures larger than typically reported. When converted to entropy as shown in figure 2.21 from their paper, this yields a ground state entropy lower than the Pauling ice entropy.

This result demonstrates (as previously shown with numerical and analytic work by Melko, den Hertog and Gingras [68, 69]) that the 2004 analytic result of Isakov *et al.* [45] showing that the long-range dipolar interactions sum to leave only near-neighbour effects is only an approximation, and a sub-Pauling ground state for spin ice does exist, no matter how finely distinguished. However, as it only appears at long time scales it is insulated from the general Pauling state by some factor such as a large energy barriers or long search times. As such, in this work the ice rules state will typically be treated as the true ground state of spin ice and the Pauling entropy as the ground state entropy, as lower energy states that are only accessible on extremely long timescales are not relevant to the physics of spin ice on the shorter timescales this work deals with.

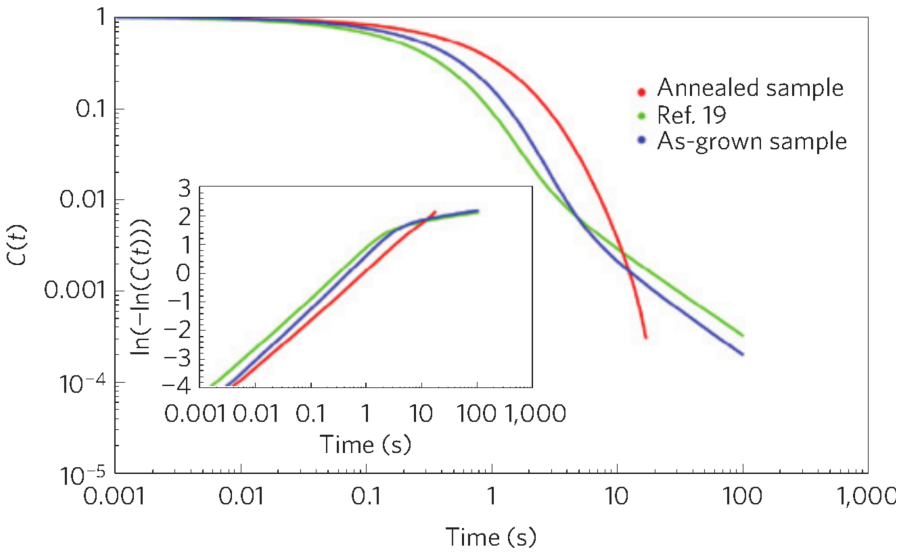

Figure 2.19: Dynamic correlation function $C(t) = \langle M(0)M(t)\rangle$ derived from a.c. susceptibility measurements. Green line is from Revell *et al.* [5]. Figure reprinted by permission from Macmillan Publishers Ltd: Nature Materials (Sala *et al.* 2014 [6]), copyright 2014.

2.5 Specific Heat Measurements of Spin Ice

There has been a substantial supply of specific heat measurements of spin ice compounds. In 1968 Blöte [70] took measurements of DTO below 2 K that suggested a large zero-point entropy. In 1999, Ramirez *et al.* [33] took measurements over a larger interval and established from the entropy that DTO was one of the recently discovered spin ices, as seen in figure 3. However, their focus was on the entropy differential quantity c/T, rather than the heat capacity c itself. At high temperatures c/T is strongly reduced by the T factor, but the phonon contribution to specific heat only becomes important above approximately 6 K. As such, it was not of great importance to their investigation, and they did not deal with it in an explicit manner. As the spin ice Debye-Hückel theory outlined below (see section 3.1) includes higher-energy excitations in the form of double charges, and its performance at high temperatures will be examined in light of this, it will be necessary to carefully consider the specific heat at temperatures on the order of 10 K and so the phonon contribution to that heat.

An attempt to deal with the phonon heat of dysprosium titanate was made in 2003 by Hiroi *et al.* [71]. They used a Debye T^3 model fitted to the experimental

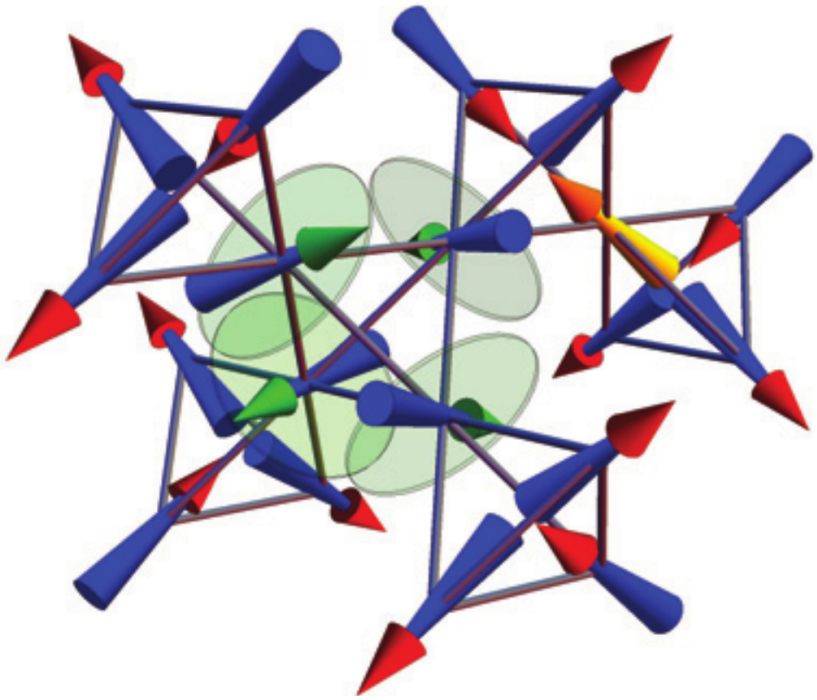

Figure 2.20: Visual depiction of oxygen defect effect on spin ice system. Note normal site manifesting monopole on far right, adjacent to sites with green XY-spins free to rotate on discs, created by central oxygen defect. Reprinted by permission from Macmillan Publishers Ltd: Nature Materials (Sala *et al.* 2014 [6]), copyright 2014.

specific heat to estimate the phonon contribution. A similar method was used in 2011 by Klemke [67], with similar results. Hiroi *et al.*'s findings are examined in detail in section 3.2.2.

Debye-Hückel theory was first explicitly compared to measured specific heat of DTO by Morris *et al.* in 2009 [52], but without an explicit presentation of their theory. The same data was compared to a completely presented theory by Castelnovo *et al.* in 2011 [4], which has been discussed above in section 2.3.

HTO has also been treated repeatedly. It was first identified as a spin ice in 1997 [14]. However on the strength of specific heat measurements, Siddharthan *et al.* [72] argued in 1999 that HTO was not a spin ice. HTO has a large low-temperature specific heat peak, larger than is predicted by nearest neighbour spin ice theory. Siddharthan *et al.* held that below 0.6 K the spins thermally decouple from the lattice and freeze into a glassy phase, and that the peak is explained by long-range dipolar and antiferromagnetic superexchange that prevent the forma-

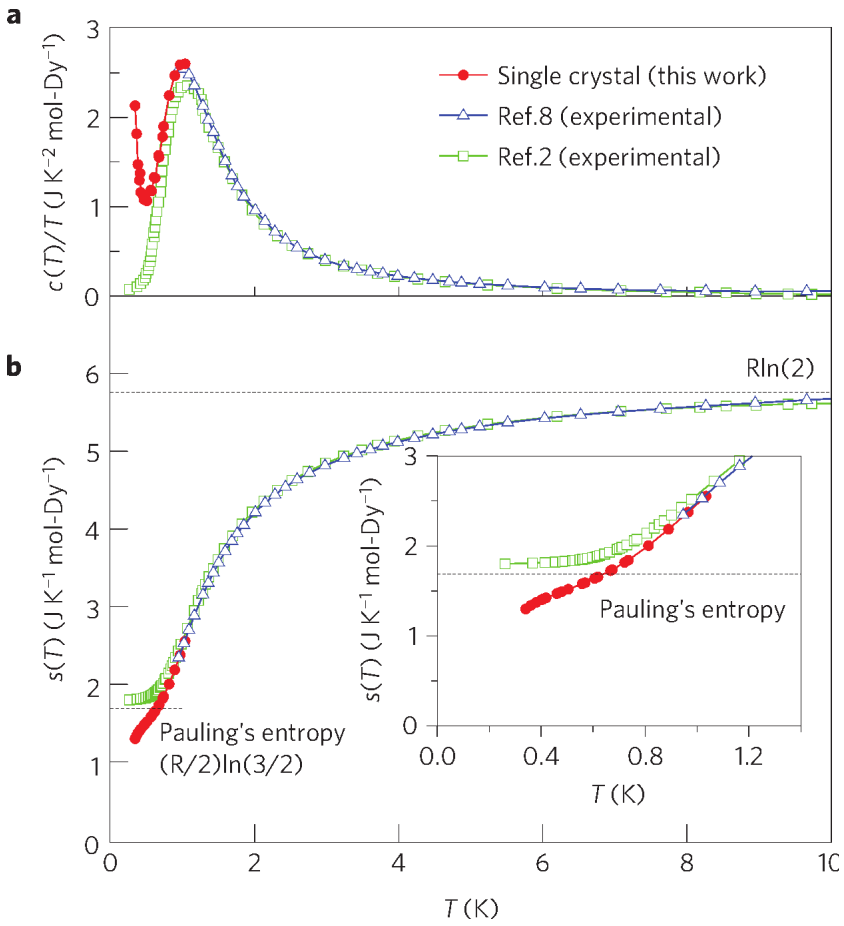

Figure 2.21: Specific heat over temperature measurements ($c(T)/T$) and derived entropy ($s(t)$ of single-crystal DTO. Red points are long relaxation time measurements by Pomaranski *et al.*. Blue and green are short relaxation time measurements from earlier work. Reprinted by permission from Macmillan Publishers Ltd: Nature Physics (Pomaranski *et al.* 2013 [66]), copyright 2013. References 2 and 8 in figure refer to [33] and [67] respectively in this work.

tion of the spin ice state. They presented simulated data to this end predicting a large peak at approximately 0.7 K, but available experimental data began at higher temperatures than the proposed peak location, and agreed poorly with the simulation. In 2001 an improved model was presented [73], but the problems were not eliminated as seen in figure 2.22. The thermal decoupling was explained by the existence of an ordered true ground state and multiple partially-ordered metastable states separated from it by infinite energy barriers. This phenomenon would lead to the spin network becoming trapped in a local minimum and unable to reach a state commensurate with the temperature of the other elements of the

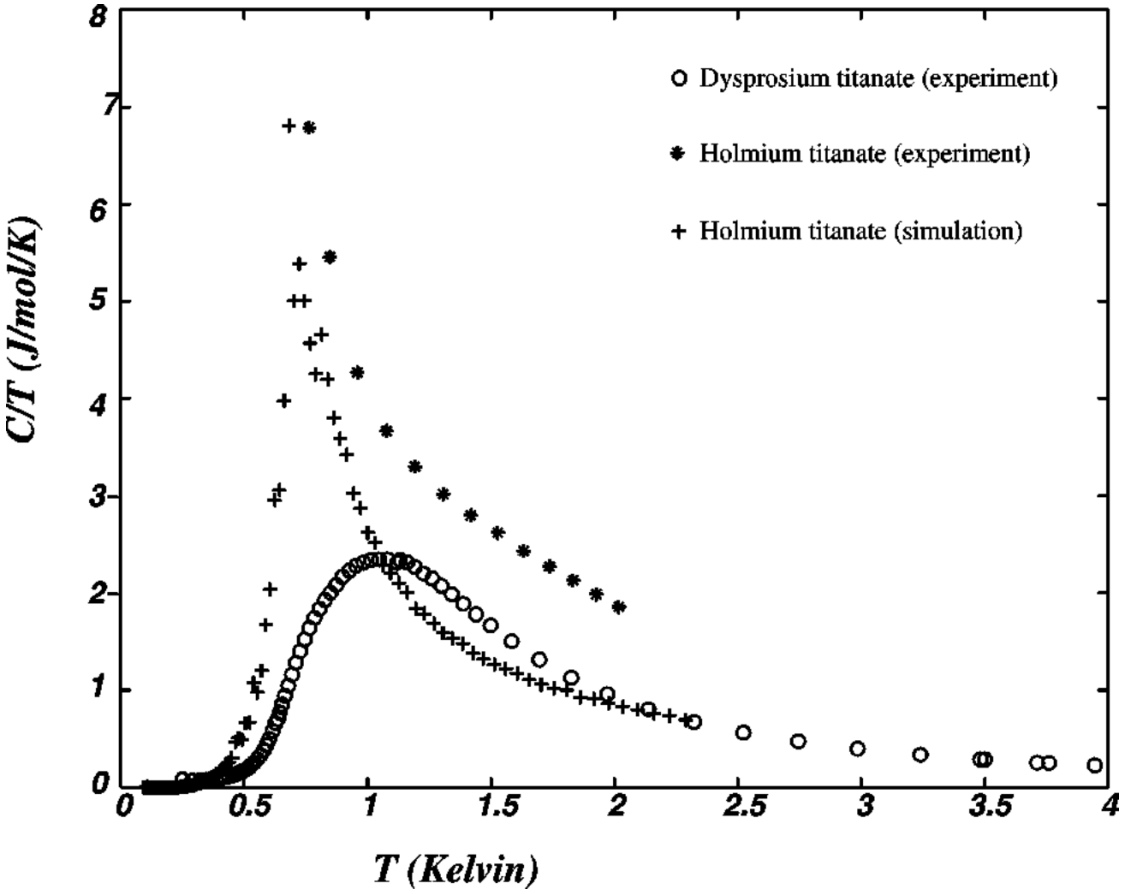

Figure 2.22: Experimental and simulated specific heat of HTO and DTO. Reprinted figure with permission from R. Siddharthan *et al.*, Physical Review B, 63, 184412, 2001 [73]. Copyright 2001 by the American Physical Society. HTO simulation data derived from the model outlined in that paper.

system, hence thermal decoupling.

Bramwell *et al.* later that year [32] explained the apparent non-spin ice behaviour of the low-temperature specific heat by referring to the 1968 measurements of Blöte *et al.* [70], which found similar behaviour at low temperature in Ho_2GaSbO_7. This behaviour was explained by introducing a Schottky anomaly of eight Holmium nuclear energy levels spaced at 0.3 K. This hyperfine correction when applied to the HTO data removes the high early peak, and the need to explain it by as shown in figure 2.23. The judgement that HTO is a spin ice material was strongly buttressed by results in the same paper that demonstrated accordance of the experimental results of HTO neutron scattering with the pre-

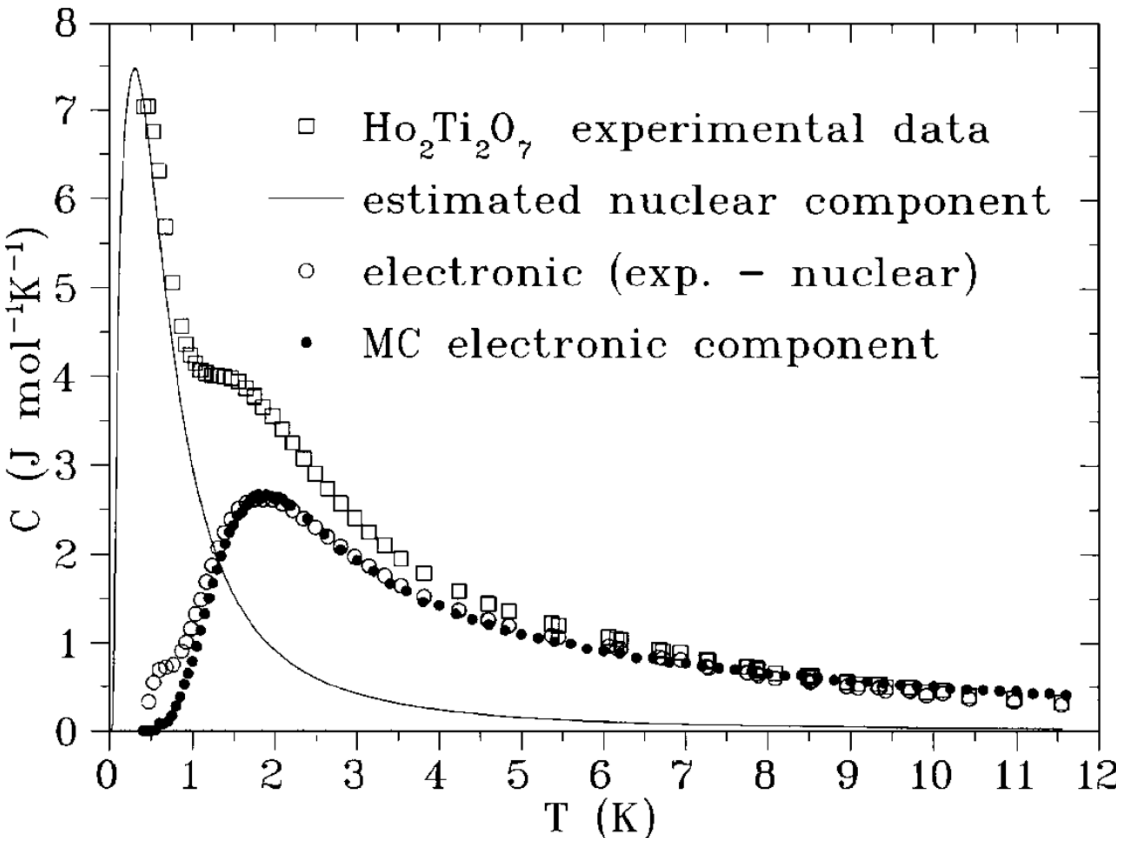

Figure 2.23: Specific heat of HTO. Empty squares are total specific heat of HTO, less lattice contribution. Line indicates theoretical nuclear contribution. Empty circles are remaining experimental specific heat after nuclear subtraction, with error around 0.7 K. Filled circles are dipolar spin ice simulation results. Reprinted figure with permission from S. T. Bramwell *et al.*, Physical Review Letters 87, 047205, 2001 [32]. Copyright 2001 by the American Physical Society.

dictions of a dipolar spin ice model using experimentally predicted spin coupling parameters. These results are shown in figure 1.7 also reproduced from Bramwell *et al.*'s paper [32].

In 2006 Lau *et al.* [64] performed a more comprehensive study that used lutetium titanate as a nonmagnetic proxy to estimate the phonon contribution. This method is investigated below in section 3.2.2. Regardless of its efficacy, their objective was to study the effects of spin doping on HTO, and no Debye-Hückel investigation has been performed on the material. Despite this its high monopole chemical potential among the spin ices make it an ideal Debye-Hückel test material if one cleans the specific heat of the obscuring nuclear and lattice contributions,

as will be demonstrated below.

2.6 Aims of This Work

The following work has two primary divisions and one additional. In the first, a new derivation of Debye-Hückel theory that extends over double charges will be presented, and some possible extensions to account for neutral dipole pairs, entropic effects on monopole configuration, and the significance of the lattice geometry will be outlined. Then, the theoretical predictions of the theory and its variations will be compared to measurements and later simulations of the specific heat of dysprosium titanate and holmium titanate, and the implications of these results for the strengths and weaknesses of Debye-Hückel theory both for spin ice and more generally will be examined. Additionally, the investigation will suggest a revision to previous results of the magnetic specific heat of dysprosium titanate in the 10 K region. Finally, the model will be applied to to specific heat measurements of the proposed non-pyrochlore spin ice cadmium erbium selenide [39]. As a spinel rather than a pyrochlore, it has a different crystal structure with lower CEF energies for its magnetic spins, allowing a test of Debye-Hückel theory's efficacy in a different crystal family.

In the second, three competing theoretical models for the magnetic relaxation of spin ice at temperatures of 0.6 K and below will be compared. Ryzhkin's original model [3] and extended models from S. T. Bramwell [74] and Revell. et al. [5] are compared in detail to relaxation data graciously provided by Paulsen et al. [7] and the implications of their strengths and deficiencies for the significance of various theories about the microscopic processes of spin ice relaxation are teased out.

In a final section a method for absolute magnetic entropy measurements recently proposed and implemented by L. Bovo [75] is applied to praseodymium zirconate and compared to previous measurements [8]. Praseodymium zirconate is of interest as it is a quantum spin ice [38], a class of spin ice distinguished by zero-temperature quantum dynamics and superposition of ice rule states. This application sheds light on the relation of praseodymium zirconate to spin ice and the utility and limitations of the method.

Chapter 3

Debye-Hückel Theory

As described in section 2.3, a derivation of Debye-Hückel theory for spin ice was presented by CMS in 2011 [4]. However, while this treatment demonstrated the basic applicability of Debye-Hückel theory, it was incomplete in some respects and inaccurate in others. Particularly, it does not account for double charges, and it is not obvious how their theory could be extended to do so. Here an alternate model derived from the different method of section 1.5.1 will be presented, which directly includes double charges, as well as an improved treatment of the partition function. The prospects for including more detailed entropic effects, bound monopole pairs, and reformulations of the theory to account for lattice geometry will also be examined.

This will enable a thorough survey of the strengths and weaknesses of Debye-Hückel theory as a description of spin ice, by comparison with experimental and simulation data for DTO and HTO and experimental data for CES. In particular, it is shown that accurate correction for the lattice specific heat is necessary in order to compare theory with experiment. A key result is that in contradiction to the previous belief expressed in figure 2.4 from [4], Debye-Hückel theory and implicitly the monopole model are effective descriptions at temperatures much higher than 2 K.

3.1 The Theory for Spin Ice

3.1.1 Monopole Population

In the theory of section 1.5.1, charge (monopole) concentration enters as a parameter in equation 1.83. In spin ice, monopoles can be constantly created and destroyed by spin flips, and the equilibrium population will be determined by the free energy associated with doing so. As such the monopole population is an endogenously determined quantity.

Define the dimensionless monopole density (the proportion of sites occupied by single defects) as

$$x = \frac{N_d}{N} \tag{3.1}$$

where N is the total number of diamond lattice sites and $N_d = N_+ + N_-$ is the total number of defects of either type. Similarly define the double defect density y:

$$y = \frac{N_{dd}}{N} \tag{3.2}$$

The ratio of defects to sites is the probability that any given site is occupied, so statistical mechanics yields the expressions, after equation 1.38:

$$x = \frac{g_1 e^{\frac{-\nu}{k_B T}}}{g_0 + g_1 e^{\frac{-\nu}{k_B T}} + g_2 e^{\frac{-\nu_2}{k_B T}}} \tag{3.3}$$

$$y = \frac{g_2 e^{\frac{-\nu_2}{k_B T}}}{g_0 + g_1 e^{\frac{-\nu}{k_B T}} + g_2 e^{\frac{-\nu_2}{k_B T}}} \tag{3.4}$$

where ν and ν_2 are the energy of a defect and double defect respectively and g_0, g_1 and g_2 the statistical weights of the ground, defect and double defect states respectively. This can be made equivalent to the expression of CMS in 2011 [4] (equation 2.11) by setting $g_0 = 1$, $g_1 = 2$ and $g_2 = 0$:

$$x = \frac{2e^{\frac{-\nu}{k_B T}}}{1 + 2e^{\frac{-\nu}{k_B T}}} \tag{3.5}$$

In this the ground state and positive and negative poles are all accounted as individual states with equal weight. However, in my view this approach is erroneous as 'monopole defect' and 'ground state' are not singular states of defects in themselves but labels for bundles of states of the spins in the tetrahedron in question. Instead the theory should follow Ryzhkin in his original 2005 paper [3] and proceed by counting states, but including the double charge states which were excluded in that paper and in the later Castelnovo *et al.* paper [4]. There are four spins, each with one of two possible orientations, for 16 total possible configurations (see figure 1.10). Of these six correspond to an ice-rules state, four correspond to each polarity of single charge, and one corresponds to each polarity of double charge. As such:

$$g_0 = 6$$

$$g_1 = 8$$

$$g_2 = 2$$

$$x = \frac{8e^{\frac{-\nu}{k_B T}}}{6 + 8e^{\frac{-\nu}{k_B T}} + 2e^{\frac{-\nu_2}{k_B T}}} = \frac{e^{\frac{-\nu}{k_B T}}}{\frac{3}{4} + e^{\frac{-\nu}{k_B T}} + \frac{1}{4}e^{\frac{-\nu_2}{k_B T}}} \tag{3.6}$$

$$y = \frac{2e^{\frac{-\nu_2}{k_B T}}}{6 + 8e^{\frac{-\nu}{k_B T}} + 2e^{\frac{-\nu_2}{k_B T}}} = \frac{\frac{1}{4}e^{\frac{-\nu_2}{k_B T}}}{\frac{3}{4} + e^{\frac{-\nu}{k_B T}} + \frac{1}{4}e^{\frac{-\nu_2}{k_B T}}} \tag{3.7}$$

If ν is known, this yields the dimensionless concentration of each type of monopole. Without double defects, this agrees with Ryzhkin's 2005 result [3].

3.1.2 The Chemical Potential

The chemical potential ν_0 of a monopole is defined as minus half the energy cost of creating and dissociating a monopole pair. To account for the additional energy associated with Coulomb interactions, an effective chemical potential ν can be defined:

$$\nu_i = \nu_{i0} - \nu_{iC} \tag{3.8}$$

where $-\nu_{iC}$ is the energy deriving from Coulomb correlations within the magnetolyte. The subscript i denotes single or double defects.

The microscopic physical meaning of ν_{i0} is the energy ϵ_i required to alter the spin configuration of a single lattice site to create a defect of type i, plus the energy required to separate this monopole to infinity from the opposite charges created adjacent to it.

$$\nu_{i0} = \epsilon_i + \frac{\mu_0 Q_i^2}{8\pi a} \tag{3.9}$$

The chemical potential ν_{i0} is determined by the microscopic crystal structure and magnetic properties of the spin ice compound. It is the single free parameter of complete spin ice Debye-Hückel theory, and cannot be directly measured in a real substance. However, it can be specified in a simulation and methods of estimating it in physical systems provide reference values used in our experimental investigation.

The Coulombic correction ν_{iC} can be estimated using Debye-Hückel theory as described in section 1.5.1. To convert the electrostatic Debye-Hückel theory to magnetic, substitute $\epsilon_0\epsilon \to 1/\mu_0$, $N_1 \to x/V_d$ and $N_2 \to y/V_d$, where V_d is the volume of one defect. This yields from equation 1.107:

$$\nu_{iC} = -k_B T \frac{l_T}{l_D + a} \tag{3.10}$$

where l_{Ti} is the Bjerrum length for the defect type and l_D is the Debye length:

$$l_{Ti} = \frac{Q_i^2}{8\pi\epsilon_0\epsilon k_B T} \tag{3.11}$$

$$l_D = \sqrt{\frac{k_B T V_d}{\mu_0 Q^2 (x + 4y)}} = \kappa^{-1}. \tag{3.12}$$

This definition of ν_C in terms of l_D and l_D in terms of x leads to circularity, as x is determined by ν_C. This circularity can be resolved by iteration to self-consistency. 10 iterations make the error negligible. In the present work x is iterated 20 times.

3.1.3 Double Charge Ratio

The theory above treats the concentrations of single and double poles seperately, as independent species, but it is useful to note that they are not independent quantities, but are determined by the same thermodynamics. As such the two can be collapsed into a single expression.

The chemical potential of a double defect is four times that of a single defect. Consider equation 3.9 again:

$$\nu_{i0} = \frac{\epsilon_i}{2} + \frac{\mu_0 Q_i^2}{8\pi a}.$$

The second term is the energy required to unbind the two defects, and scales trivially to produce a fourfold energy if the charge Q is doubled. The first term depends on ϵ_i, the energy required to create the two defects from the ground state. The internal structure of a spin ice lattice site is such that it has four Ising spins on its vertices and six interactions between these spins, corresponding to the edges of the tetrahedron.

The ferromagnetic coupling of the spins favours spins that point in the same direction absolutely, but in the language used to describe spin configurations of lattice sites they favour oppositely-oriented neighbours, as 'in' spins will face other 'in' spins in any given tetrahedron.

Define the internal energy of a lattice site [4]:

$$E = J\Sigma_{j,k,j\neq k} S_j S_k, \tag{3.13}$$

where J is the coupling constant of the spins, including any merely proportional factors. In the ground state of two spins in and two out, there will be four favoured interactions and two disfavoured interactions, so $E_0 = 2J - 4J = -2J$, where E is the total energy of the spin interactions in the lattice site. As this is the ground state and the zero charge state one can take this as the zero of energy for the thermodynamics of the system, so $\epsilon_0 = 0$ where $\epsilon = E + 2J$ is the renormalised energy. In the first excited state (single defect) there will be three favoured interactions and three disfavoured interactions, so $E_1 = 0$ and $\epsilon_1 = 2J$. In the second excited state (double defect) there will be six disfavoured interactions, so $E_2 = 6J$ and

$\epsilon_2 = 8J$. So $\epsilon_2/\epsilon_1 = 4$. This gives the desired:

$$\nu_2 = 4\nu_1 \tag{3.14}$$

The Coulomb correction ν_{iC} for a double monopole is also multiplied by factor 4. In equation 3.10 it is proportional to the Bjerrum length (equation 3.11), which is proportional to Q_i^2. It is important to note that while the expression for ν_{iC} also contains l_D (equation 3.12), l_D is a function of Q, not Q_i, and is a property of the magnetolyte invariant between consideration of single and double monopoles, unlike the i-indexed l_{Ti}. As such it does not alter the Q_i^2 scaling of ν_{iC}.

Therefore, the energy per site of a system of single and double monopoles is:

$$u = (\nu_0 - \nu_C)x + 4(\nu_0 - \nu_C)y = (\nu_0 - \nu_C)(x + 4y) \tag{3.15}$$

$$u = (\nu_0 - \nu_C)x\left(1 + 4\frac{y}{x}\right) \tag{3.16}$$

and from equations 3.5 and 3.7:

$$\frac{y}{x} = \frac{g_2 e^{\frac{-\nu_2}{k_B T}}}{g_1 e^{\frac{-\nu}{k_B T}}} \tag{3.17}$$

There are 8 spin configurations that create single charges, and 2 that produce double charges, so take $g_2/g_1 = 8/2 = 1/4$ and obtain:

$$\frac{y}{x} = \frac{e^{\frac{-\nu_2}{k_B T}}}{4e^{\frac{-\nu}{k_B T}}} \tag{3.18}$$

$$\frac{y}{x} = \frac{e^{\frac{-4(\nu_0 - \nu_C)}{k_B T}}}{4e^{\frac{-(\nu_0 - \nu_C)}{k_B T}}} \tag{3.19}$$

$$\frac{y}{x} = \frac{1}{4}e^{\frac{-3(\nu_0 - \nu_C)}{k_B T}} \tag{3.20}$$

So substituting into equation 3.16, obtain the internal energy per site:

$$u = (\nu_0 - \nu_C)x\left(1 + e^{\frac{-3(\nu_0 - \nu_C)}{k_B T}}\right) \tag{3.21}$$

And for l_D from equation 3.12:

$$l_D = \sqrt{\frac{k_B T V_d}{\mu_0 Q^2 [x + 4y]}} = \kappa^{-1} \tag{3.22}$$

$$l_D = \sqrt{\frac{k_B T V_d}{\mu_0 Q^2 x \left(1 + e^{\frac{-3(\nu_0 - \nu_C)}{k_B T}}\right)}} = \kappa^{-1} \tag{3.23}$$

This creates another self-consistency problem, as l_D and ν_C are defined in terms of one another with no easy analytic solution. This can be solved by iterating to self-consistency in the same manner as the original problem of ν_C and x.

3.1.4 Entropic Charge

The spin lattice does not just constrain the positions of poles to lattice sites, but also affects their possible motion and configurations. Likewise, any given monopole configuration places constraints on the possible configuration of spins. Movement of poles can only be accomplished by spin flips and any pole must be connected by at least one properly aligned spin chain to another, or to a system boundary.

CMS's 2011 paper [4] determined the entropic free energy contribution of the spin configuration and analogised it to a Coulomb interaction via an 'entropic charge'. This charge can be incorporated into Debye-Hückel theory.

The concept of entropic charge is not intuitively obvious, but it can be interpreted physically as follows: if two opposite charges are separated, there must be, in the absence of other charges and in periodic boundaries, at least one spin chain connecting them. The spin network has a net polarisation pointing from one spin to the other. The further apart the charges are the more the network configurations are constrained by this requirement. This constraint on the network lowers its configurational entropy and so increases the free energy of a given charge configuration as mediated by a factor T in the definition of Helmholtz free energy $F = U - TS$. There are however problems with this picture, which will become apparent later.

Their own application of the theory did not reveal a significant result, but spin ice Debye-Hückel theory has been developed from their 2011 model, so this is not

necessarily conclusive. V. Kaiser later formulated a similar implementation [76], which is used here.

Two entropic charges have the free potential energy:

$$U_{ent}(r) = -\frac{\eta q^2}{4\pi r} \tag{3.24}$$

This can be combined to produce a Poisson-Boltzmann equation:

$$\Delta\Phi(r) = -\frac{x(\mu_0 Q^2 + \eta q^2)}{k_B T V_D}\Phi(r) \tag{3.25}$$

where q the 'entropic charge' is set to 1 and

$$\eta = \frac{8ak_BT}{\sqrt{3}} \tag{3.26}$$

yielding:

$$l_D = \sqrt{\frac{k_B T V_D}{x(\mu_0 Q^2 + \eta q^2)}} \tag{3.27}$$

$$l_T = \frac{\mu_0 Q^2 + \eta q^2}{8\pi k_B T} \tag{3.28}$$

The x in these expressions can be modified with the same factor as in equation 3.16 to incorporate double charges. The quantity η previously appeared (labelled Φ) in a 1997 paper by Ryzhkin and Whitworth [77]. There it relates the configurational entropy of water ice to the configuration vector Ω. The configuration vector in water is a description of the flux of ions and defects, but in his 2005 paper [3] Ryzhkin related the configuration vector to the spin configuration and magnetisation of spin ice, as treated in more detail in section 2.4:

$$\Omega(r) = \frac{a}{2}\Sigma_{i\alpha} S_{i\alpha}\frac{e_{1\alpha}}{V} \tag{3.29}$$

$$M = Q\Omega \tag{3.30}$$

The sum in eqn. 3.29 runs over all spins i in each tetrahedron α in a macroscopically small volume V around point r. $e_{i\alpha}$ is the unit vector for each spin.

In 2013 Ryzhkin, Ryzhkin and Bramwell [78] used the relation

$$S = -\frac{1}{2}\eta\Omega^2 \tag{3.31}$$

from 14 to obtain an entropic free energy:

$$W_{ent} = \frac{4k_BTa\Omega^2}{\sqrt{3}} \tag{3.32}$$

However, they note that while this can be transformed into an entropic charge, to do so is not necessarily meaningful. This returns to the physical characterisation of entropic charge given above. In that scenario, a single pair of monopoles is created and separated in an ice-rules crystal. However in real spin ice these monopoles will exist in a system with many other monopoles. From equations 3.30 and 3.32, it can be seen that the free energy is minimised by minimising magnetisation, but a separation of two monopoles in a populated system may increase or decrease the magnetisation and hence the entropic free energy of the system.

The configuration vector being a more complete description does not demonstrate that entropic charge is not a practically useful concept. However, there is reason to suspect that it is not. If the magnetic charge of the defects in a spin ice system were nullified, under the logic of entropic charge one would expect that Coulombic behaviour would remain arising from the pure organisation of the spin network. This scenario is inaccessible to physical experiment but not to simulation. Such simulations have been performed [76] and 'nonmagnetic spin ice', rather than demonstrating a residual Coulombic interaction, instead behaves as if defects have no charge of any kind.

On the strength of this failure of entropic charge to appear when isolated, it is justifiable to conclude that it is eliminated by the complexity of practical spin ice systems. Nevertheless the theory will be examined in comparison with experimental data below.

3.1.5 Bjerrum Pairing

Debye-Hückel theory is a theory of fully dissociated charges, but this is not a complete description of Coulomb gases or of spin ice. Bjerrum [79] noted that in dilute ion solutions, closely bound pairs of ions may form a distinct species to dissociated ions.

Consider the case of charges on adjacent sites, so with separation a. If the pairs are a well-defined species separate to dissociated ions, they will have their own chemical potential and concentration. For this model:

$$\nu_B = 2\nu_0 - 2k_BT\frac{l_T}{a} \tag{3.33}$$

from combining eqns. 3.9 and 1.108, i.e. the chemical potential of a pair of monopoles that is not separated, so have k_BTl_T/a as the limiting value of their Coulomb energy as they come together. They will have a population factor [74]

$$x_B = \frac{e^{\frac{\nu_B}{k_BT}}}{1 + e^{\frac{\nu_B}{k_BT}}} \tag{3.34}$$

with no modification due to the charged atmosphere, as they are adjacent to one another. However, this naïve expression conceals a problem, as Bjerrum pairs are not truly heterogenous from normal monopoles and so their statistical weight, here taken as 1, does not have an obvious definition. This will present problems later.

Leaving aside this problem, a modification of the standard Debye-Hückel terms is also required. As Bjerrum pairing accounts for near-neighbour pairs, the minimum approach distance in Debye-Hückel theory changes from a to $2a$. Hence, the ν_C term becomes

$$\nu_C = -k_BT\frac{l_T}{l_D + 2a} \tag{3.35}$$

The Bjerrum pairs do not in theory affect ν_C beyond this, being closely associated and magnetically neutral in total.

As stated, this is under the assumption that Bjerrum pairs are a well-defined species independent of the free monopoles. At low concentrations and so low temperatures the free monopoles will typically be distant from one another and so

from bound pairs, and the two species can be treated separately in a principled fashion as described above. However as the temperature rises and the system saturates this distinction between Bjerrum pairs and free monopoles becomes less clear and the theory less applicable. We will see the consequences of this below.

Besides Bjerrum pairing, even higher-level structures may become apparent. Zhou *et al.*[36] predict that creating or discovering spin ices of progressively lower chemical potentials will reveal new correlation forms such as clusters or liquids or, in the limit of small chemical potential, a completely full lattice of alternating positive and negative charges. This extreme case is the theoretical outcome of $\nu_c > -\nu$, making double poles energetically favourable compared to the ground state.

3.1.6 Lattice Debye-Hückel Theory

The theory so far has been formulated for a continuum assumption, but this is obviously not the case in the real system. Monopoles in spin ice do not move freely but only exist in the tetrahedral sites defined by the rare earth ion spin lattice. This potentially leads to changes in the behaviour of monopoles in the system, and if the Debye length falls below the lattice spacing we might expect them to have a significant effect.

A lattice solution of Debye-Hückel theory was presented by Kobelev, Kolomeisky and Fisher in 2002 [80].

$$\nu_C = k_B T \frac{C_3 a^3}{12 V_d T^*} \left[P(1) - P\left(\frac{6}{(a/l_D)^2 + 6} \right) \right] \tag{3.36}$$

where k_B and T have their usual meanings, a is the lattice constant and V_d the volume of one defect. P, C and T^* are more complex. Reduced temperature T^* is given by

$$T^* = \frac{k_B T a 4\pi}{\mu_0 Q^2} \tag{3.37}$$

where symbols have their usual meaning. C_3 is a factor determined by the dimensionality of the system

$$C_3 = \frac{2\pi^{\frac{3}{2}}}{\Gamma(3/2)} \tag{3.38}$$

and P is the integrated lattice Green's function

$$P(\zeta) = \int_k \frac{1}{1 - \zeta J(\mathbf{k})} \tag{3.39}$$

where

$$J(\mathbf{k}) = \frac{1}{c_0} \sum_{nn} e^{i\mathbf{k}\cdot\mathbf{a}} \tag{3.40}$$

where c_0 is the number of near-neighbours and $\mathbf{a}$ is a near-neighbour vector.

For the pyrochlore system, this is

$$J(\mathbf{k}) = \frac{1}{4} \frac{e^{2i(k_x+k_y+k_z)} + e^{2ik_x} + e^{2ik_y} e^{2ik_z}}{e^{i(k_x+k_y+k_z)}} \tag{3.41}$$

The integral P has no known analytic solution, so in the model it is solved numerically.

Unfortunately, Kobelev *et al.* [80] note that their solution is only valid for the set of Bravais lattices, which does not include the diamond lattice on which spin ice monopoles are defined. This theoretical objection suggests a reason why the model may fail, but it falls to experimental investigation to determine whether it will do so in practice.

3.2 Debye-Hückel Theory and Experiment

The theory above can be used to obtain predictions for the monopolar heat capacity of spin ices. Microscopically, this would be the specific heat contribution of the Ising states of the magnetic moments. The specific heat is directly accessible to experiment, so a test of the theory is in principle straightforward.

In view of the developments outlined in section 2.5, with varied approaches being taken to the question of phonon removal and the relative importance of this to study of Debye-Hückel theory in the high temperature regime, this group decided to obtain new data for holmium and dysprosium titanate for comparison,

to ensure control over all aspects of the data processing.

We took specific heat measurements of HTO, DTO and also CES. The data so obtained is compared to the theoretical predictions of Debye-Hückel theory in detail in this section.

3.2.1 Experimental Methods

The crystals were prepared by D. Prabhakaran using the method outlined in his 2011 paper [81]. Single crystals of DTO and HTO were grown in an oxygen flow in an optical floating-zone furnace, and their purity and alignment tested with X-ray diffraction. The DTO crystal has a pale yellow colour, and the HTO orange.

The specific heat measurements were taken using the calorimetry probe of a Quantum Design PPMS, as described in section 1.6.2. The measurements were performed by L. Bovo, with the author observing for the DTO measurement. Both crystals were measured in cooling from 300 K to 0.4 K. At low temperatures, due to high specific heat but slow dynamics the equilibration time for HTO become excessively long and the measurement unreliable and as such, the data is only considered reliable down to 0.8 Kelvin. Addendum measurements were taken separately to remove the contribution of the thermal grease.

L. Bovo additionally performed specific heat measurements on the spinel cadmium erbium selenite using a powder supplied by J. Lago. Similarly to the pyrochlores, it was measured in cooling from 300 K to 0.45 K. As powder samples can have reduced internal thermal conductivity between the grains, the powder was pressed into a thin pellet of the same size as the puck platform.

3.2.2 Removal of Non-Monopolar Factors

The measurement of specific heat determines the total heat capacity of the crystal. However, our theory is only a theory of the energy stored in the Coulomb gas of monopoles. All spin ices have an additional contribution from lattice phonons and holmium titanate has an additional complication in the form of a large nuclear hyperfine contribution [32]. At temperatures higher than the main focus of our study here, higher crystal field levels may also become important.

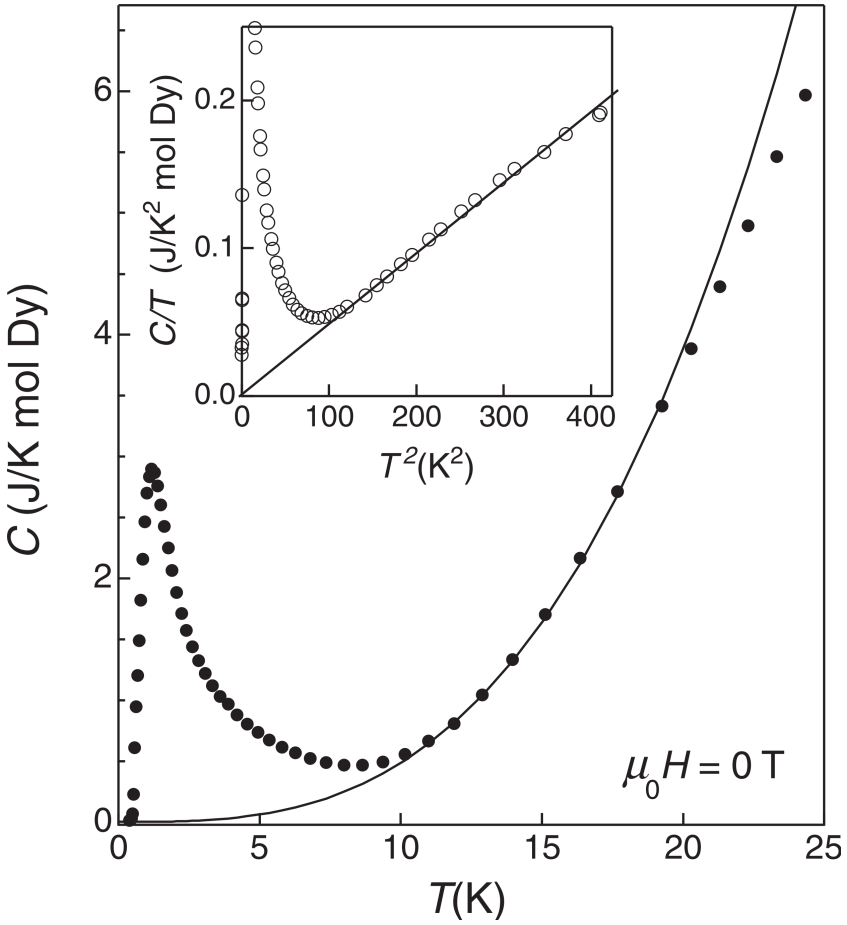

Figure 3.1: Specific heat of DTO with proposed lattice contribution $C = \alpha T^3$ with $\alpha = 4.85 \times 10^{-4}\text{JK}^{-4}\text{mol}^{-1}$. Reproduced with permission from Hiroi *et al.*, Journal of the Physical Society of Japan, 72:411418, 2003 [71].

The hyperfine contribution for HTO is the contribution of the nuclear spin of the holmium ions. Blöte [70] found that this was well-represented by a Schottky anomaly for eight energy levels spaced equidistantly at 0.3 K.

$$U = \frac{\Sigma_i \nu_i e^{\nu_i \beta}}{\Sigma_i e^{\nu_i \beta}} \tag{3.42}$$

where $\nu_i = 0.3i$ for $i =$ integers $0 \rightarrow 7$. This can be differentiated straightforwardly to yield a specific heat contribution.

Determining the contribution of the lattice is more difficult. When studying low temperatures or the quantity c/T, it can be assumed without great distortion

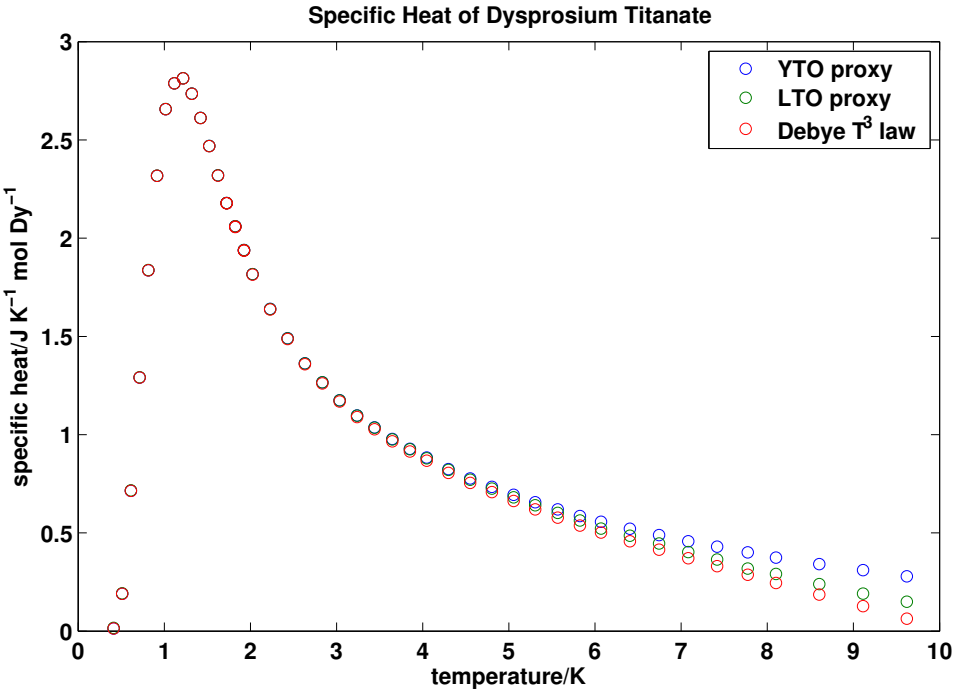

Figure 3.2: Measured specific heat of DTO under three lattice heat removal systems. Blue circles use a YTO proxy T-scaled to match high temperature specific heat of DTO. Green circles use an LTO proxy T-scaled to be tangent to the raw DTO curve. Red circles use a T^3 specific heat law after [71] and [67]

that the magnetic specific heat becomes negligible at relatively high temperatures like 10 K. This assumption is bolstered by the conventional (but as shown below, incorrect) assumption that Debye-Hückel theory is inapplicable at these high temperatures. It receives further support from the work of Hiroi *et al.* [71] who, applying a Debye T^3 model for the specific heat, found a value of 353 K for the Debye temperature of DTO, provided the magnetic heat capacity goes to zero at 12 K. Their result is shown in figure 3.1. However, there is reason to believe this conclusion is false.

Prior to examination of the evidence, it would be surprising if the monopolar contribution became negligible at 12 K. The predicted value, using the methods described in section 3.2.3 below, of the chemical potential of a single monopole in DTO is 4.35 K and of a double monopole is four times this (see section 3.1.3). Even if Debye-Hückel theory were unable to describe their behaviour, it would not

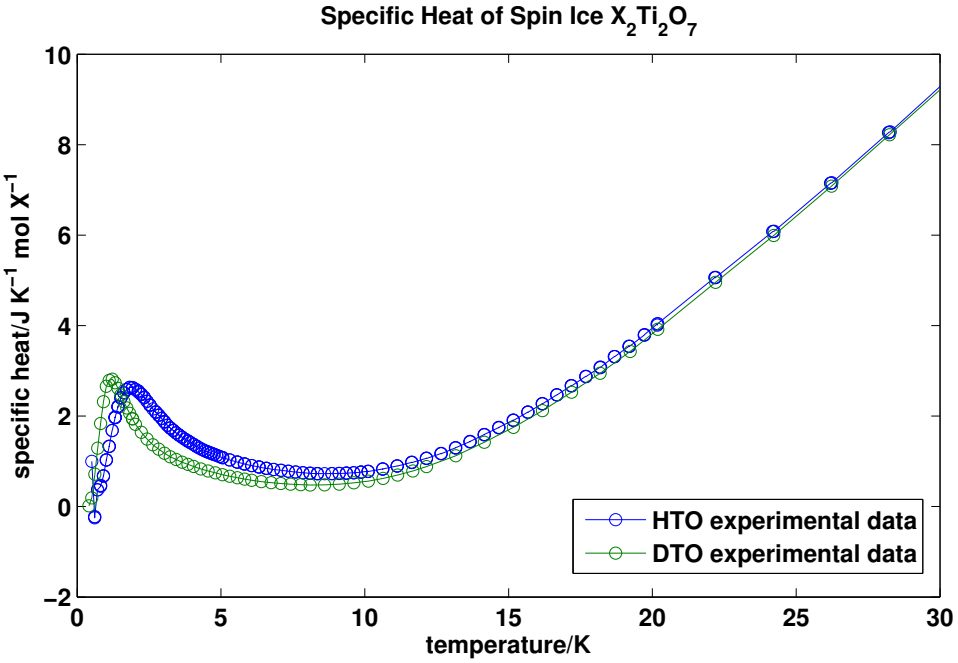

Figure 3.3: Specific heats of holmium and dysprosium titanates, including both magnetic and phonon contributions (this work). Lines are guides for the eye.

be the expected result if a magnetic system with a characteristic energy scale of this size became a negligible contribution to the thermodynamics of the system at such a comparatively low temperature. In Figure 3.2 it can be seen how the application of the Debye model of Hiroi *et al.* [71] causes the heat capacity to collapse by 10 K.

Furthermore, a direct comparison of dysprosium and holmium titanate heat capacity gives evidence of a long monopolar tail. The two rare earths have similar masses and ionic radii (see table 3.1) so we would expect their phonon heat capacities to be similar. This is borne out by a comparison of the specific heat data in figure 3.3. As such, at the point where the monopolar contribution runs out, their heat capacities should converge, excepting the contribution of the crystal field which is negligible at low temperatures. After their respective Schottky peaks the difference between the two compounds diminishes continuously but is still clear at 10 K and remains up to 25 K. As small differences in the non-monopolar heat capacity of the two pyrochlores do exist, this is not a wholly reliable method, but does suggest residual monopolar heat capacity to at least 10 K.

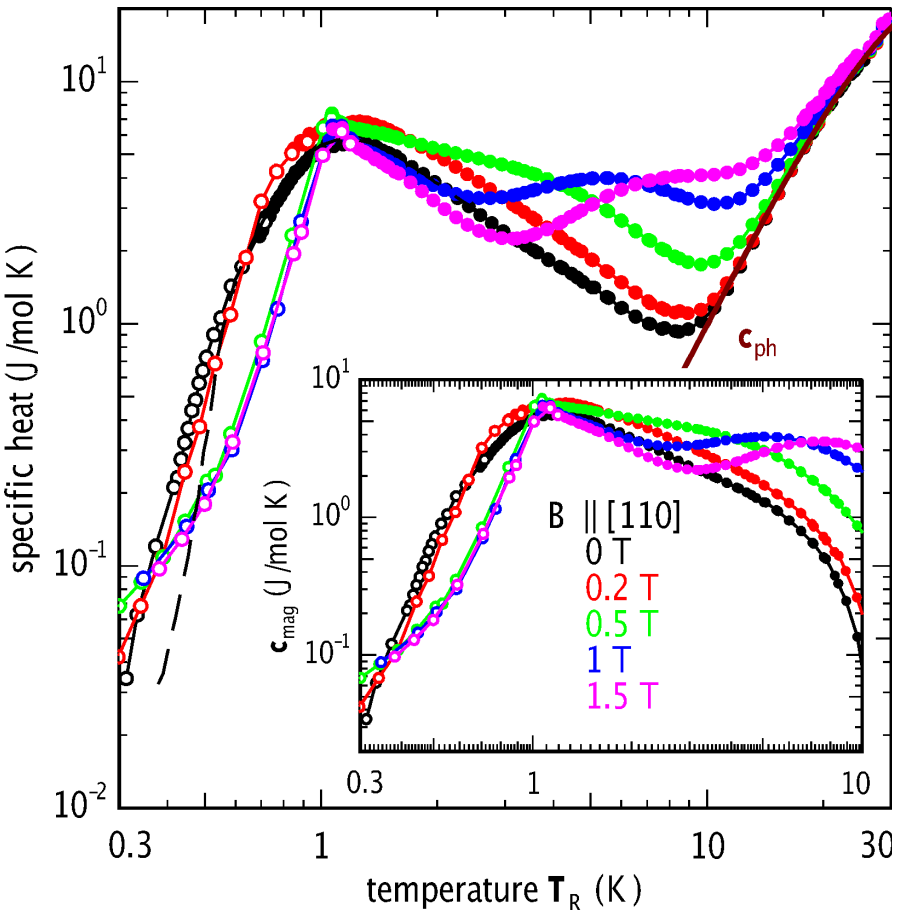

Figure 3.4: Main figure: total specific heat of DTO determined by calorimetry (full circles) or thermodynamic field theory (open circles) at various fields. Brown line denotes phonon specific heat according to T^3 law. Inset figure shows magnetic specific heat prediction on that basis. Dashed line is data from [52]. Note units of specific heat refer to moles of DTO, not Dy, so values are double figures from this work. Reproduced with permission from [67] (Klemke 2011).

The method used by Hiroi *et al.* was to fit a T^3 Curie law specific heat to DTO specific heat data. As noted above a similar methodology was used by Klemke in 2011 [67]. The Hiroi *et al.* figure is reproduced in figure 3.1 (right hand figure) and Klemke's results in figure 3.4. It can be seen that both successfully fit the experimental results between 10 K and 20 K with this approach. However while the conclusion is a reasonable one to draw from the given result in isolation it is not a completely safe one. It depends on a fitted variable and fundamentally on the assumption that the low-temperature lattice heat of DTO has a T^3 form, and does not precisely match the nonrandom shape of the specific heat curve. In view

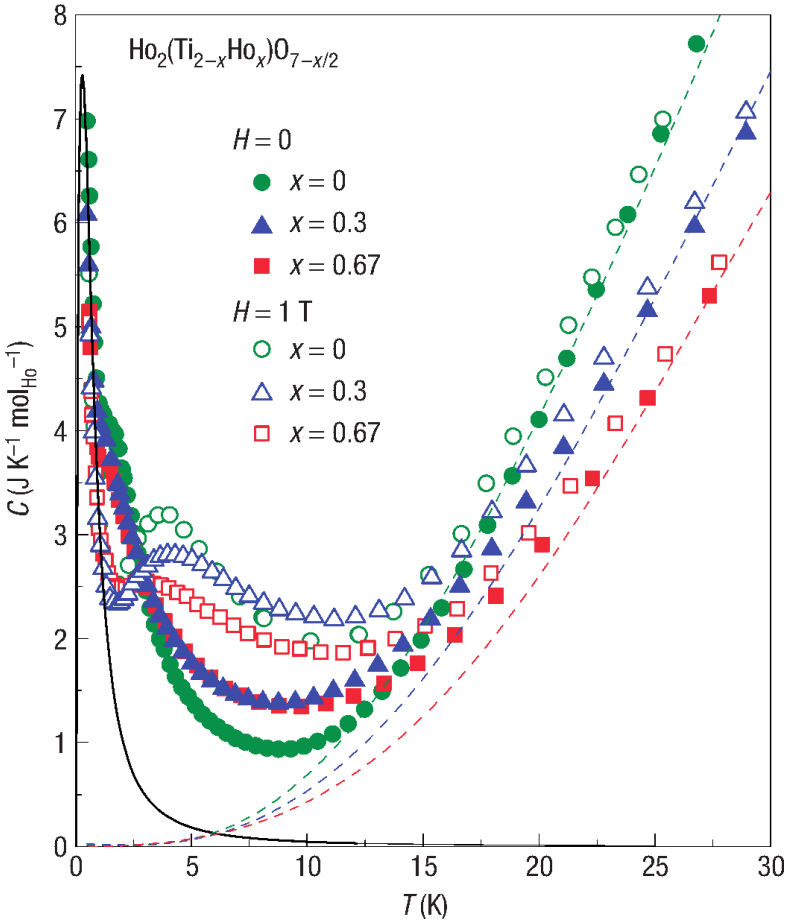

Figure 3.5: Total specific heat of $Ho_2(Ti_{2-x}Ho_x)O_{7-x/2}$ versus temperature at 0 and 1 T. Green filled circles are HTO in zero field, the quantity studied in this section. Dashed lines represent lattice contribution, solid black line the nuclear contribution. Reprinted by permission from Macmillan Publishers Ltd: Nature Physics (Lau *et al.* 2006 [64]), copyright 2006.

of these doubts and the theoretical expectation of a significant high-T monopolar heat, it was felt justified to attempt a different approach.

Our group attempted four methods: yttrium and lutetium titanate proxies, direct magnetic quenching, and magnetisation quenching.

The proxy method takes a crystal without significant magnetic behaviour and measures its specific heat on the assumption that its non-magnetic physics are relatable to those of the spin ices. Lau *et al.* [64] used this approach in 2006 for HTO. They took a polynominal fit to $Lu_2Ti_2O_7$ (lutetium titanate, LTO) specific heat data, scaled it to match HTO data and found a non-negligible magnetic

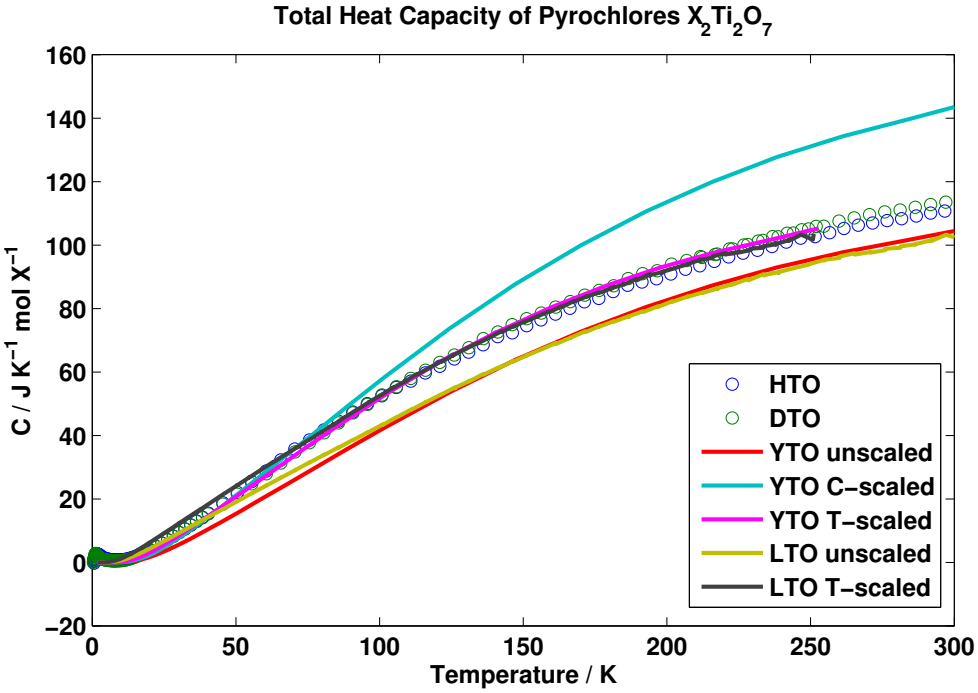

Figure 3.6: Specific heats of HTO, DTO, LTO and YTO per mole of X in $X_2Ti_2O_7$. Teal line is YTO with a C-scaling of $\times 1.37$. Purple line is YTO with a T-scaling of $\times 0.83$. Black line is LTO with a T-scaling of $\times 0.83$. Lines are abstracted from points and do not represent continuity of measurement.

specific heat at 10 K remained shown in figure 3.5.

In the investigation here both an LTO and a $Y_2Ti_2O_7$ (yttrium titanate, YTO) proxy is also tested. Both yttrium and lutetium are transition metals closely chemically related to the rare earths but without relevant magnetic behaviour. Table 3.1 summarises their relevant physical properties [82, 83].

Table 3.1: Properties of Rare Earths and Oxides

Rare Earth	R^{3+} Ionic Radius/Å	Mass/amu	Molecular Mass/amu
dysprosium	1.03	162.5	532.6
holmium	1.02	164.9	537.4
yttrium	1.015	88.9	387.6
lutetium	0.97	175	557.6

It is not immediately obvious which is preferable, as the yttrium pyrochlore

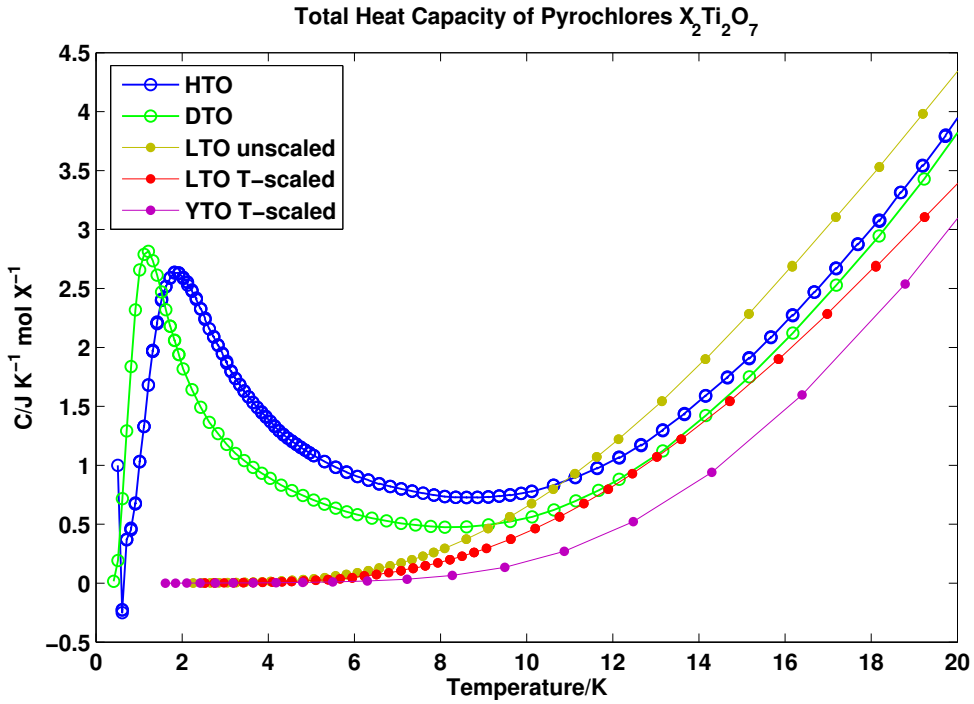

Figure 3.7: Specific heats of HTO, DTO, LTO and YTO per mole of X in $X_2Ti_2O_7$. Red points are LTO with a temperature scaling of $\times 1.12$, purple points are YTO with a temperature scaling of $\times 0.83$. All lines are guides for the eye.

has a smaller molar mass, but has an ionic radius very close to that of the rare earths. In our investigation we used both. Yttrium titanate data was taken from Johnson *et al.* [84], while the lutetium titanate heat capacity was measured by L. Bovo from 300 K to 2 K using a Quantum Design PPMS.

Figures 3.6 and 3.7 present comparisons of the spin ice heat capacities, the proxy heat capacities, and the results of scaling possibilities. It is clear that neither candidate is an ideal proxy in its raw form as YTO is predictably deficient due to its lower mass, while LTO is deficient at high temperatures but overshoots in the low-temperature region of interest, and so cannot represent a mere component of the heat capacity. These problems can be addressed by scaling the data to estimate the equivalent heat capacity for the spin ices. As the two spin ices are chemically very similar, they are assumed to have the same low-temperature specific heat.

An obvious scaling to perform on YTO is a scaling of the heat capacity (rather than temperature) in line with the molar mass difference between it and the spin

ices. However we see in figure 3.6 (upper) that this does not reproduce the shape of the spin ice curve, so if scaling is possible it must be along the lines of some other variable. The Debye theory of specific heat [85] provides justification for scaling by temperature.

Phonons are the quantisation of lattice vibrations and as such can only exist at certain energy levels. The phonon energy of a substance is equal to the energy of an occupied vibration mode multiplied by the probability of that mode being occupied, integrated over the density of available modes. This energy can be transformed into a heat capacity by differentiating with respect to temperature as usual. However, determining the density of modes in three dimensions for a real material is a difficult, so approximations are desirable if possible.

In the high-temperature classical limit, Einstein's approximation that each of the $3N$ modes of a crystal of N atoms contributes k_BT to the energy is accurate. At lower temperatures the only excited modes will be the low-frequency 'acoustic' modes, which have a density of states given by the analytically tractable

$$g(\omega) = \frac{V\omega^2}{2\pi^2}\left(\frac{1}{v_L} + \frac{2}{v_T}\right) \tag{3.43}$$

where v_L and v_T are the longitudinal and transverse sound velocities respectively.

Debye's approximation to low-temperature heat capacity assumes this relation obtains up to a limiting frequency ω_D, which is the frequency such that the total number of modes is $3N$. Above this frequency there are assumed to be no modes. Debye obtains the form:

$$C = \frac{12Nk_B\pi^4}{5}\left(\frac{T}{\Theta_D}\right)^3 \tag{3.44}$$

where $\Theta_D = \hbar\omega_D/k_B$ contains all of the information about the solid and operates as a scaling to the temperature factor. Any two curves differentiated by Θ_D values can be collapsed onto one another by scaling the temperature by the factor Θ_{D1}/Θ_{D2}.

Even though the Debye approximation itself is questionable, it does indicate the theoretical justifiability of a T scaling for the specific heat. As such in figure 3.6 (upper) a temperature scaling of $0.83 \times T$ is shown, but while this matches the DTO data well over the range 50 K $<$ T $<$ 250 K, it is less effective below

50 K, which is the region of interest, as can be seen in figure 3.7 (lower). A large deficiency is present in this region and while we expect a gap from the absence of monopolar contribution to the YTO heat capacity, the size and persistence of the deficiency rule out this as a complete explanation, since the monopolar contribution should decay with increasing temperature. For LTO, the problem is opposite, as it overestimates the heat capacity at low temperatures in its naked form and does so more severely when scaled to match the high-temperature data. An opposite course is suggested by the obvious fact that the phonon contribution to specific heat cannot exceed the total specific heat: a $1.12 \times T$ scaling in the opposite direction such that the LTO specific heat is tangent to the DTO specific heat at approximately 13 K, as seen in figure 3.7. Doing this suggests an approximate upper bound to the phonon contribution, and a negligible magnetic contribution at 13 K.

It should be noted at this point that we have seen the T scaling does not work at low temperatures even for the two nonmagnetic pyrochlores YTO and LTO, which have specific heats similar at high temperatures but different at low temperatures, so the proxy method remains an imperfect means of determining the lattice contribution to the specific heat.

A possible explanation for the discrepancies in this region is differences in the crystal field energy levels. The energies of the first excited crystal field states in DTO and HTO are on the order of 300 and 200 K respectively [2]. The specific heat contribution from these excited levels peaks in the region 80 to 120 K.

While there is no clearly accurate result from either proxy they still have use at lower temperatures before the phonon contribution becomes overwhelming. By taking the YTO value as a lower bound and the LTO value as an upper bound for this contribution, they can be used to suggest a plausible range of values for the monopolar specific heat. We see in figure 3.2 that the difference only becomes significant above 7 K, but in figure 3.11 that double charges and their high-temperature contribution to the specific heat are already important at 4 K.

Ajudicating between the two is aided by reference to simulations. V. Kaiser has performed simulations of dipolar spin ice models of DTO and HTO [86]. In figures 3.8 and 3.9 the simulated data is compared to the data using the LTO and YTO specific heat proxies. For both spin ices, the simulated values are close to the

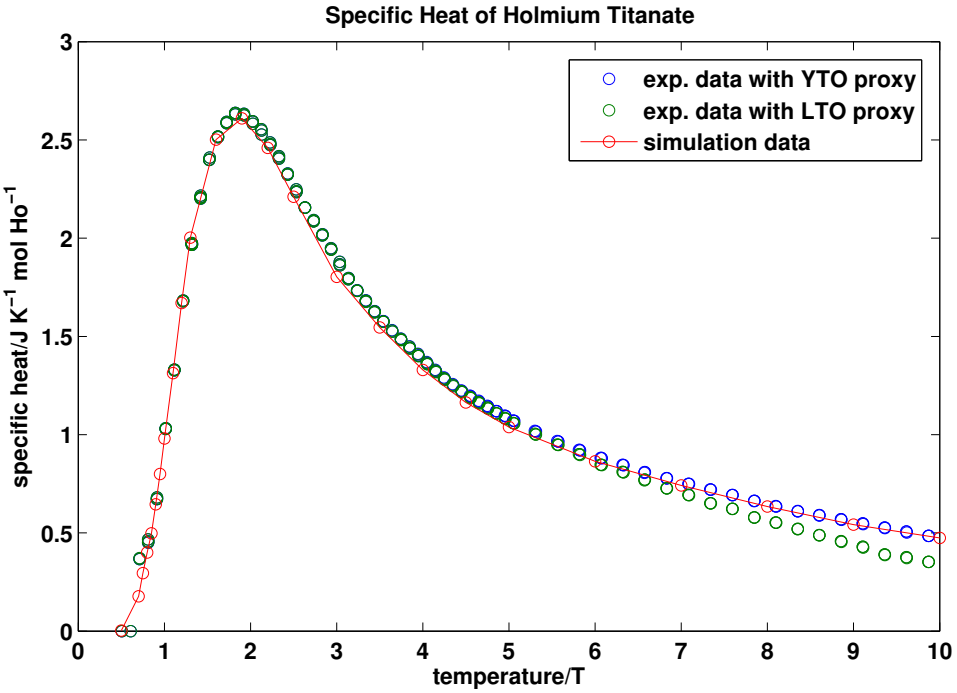

Figure 3.8: Dipolar spin ice simulation by V. Kaiser [86] (red line) vs. experimental data for HTO using YTO and LTO proxies. The red line is a guide for the eye.

YTO proxy values, indicating that unless the dipolar model breaks down by 10 K there must be a substantial residual monopolar specific heat at this temperature, and that YTO is a good proxy for DTO and HTO spin ices. However, this thesis will include the LTO proxy in figures in view of the possibility of a breakdown of the dipolar model.

Despite its utility the limitations of the proxy method are clear. Two potentially more accurate alternatives were tried, both of which attempt to measure the sample directly.

The magnetic quenching method applies a strong magnetic field to fully magnetically order the spin ice system and eliminate magnetic contributions. Then, assuming no major magnetostriction effects, the specific heat of the sample can be measured and the difference between this measurement and a zero field measurement is the contribution of the quenched behaviour to the specific heat. However, magnetic fields of at least 14 T were found to be required to fully quench the material, and these exerted sufficient mechanical force on the PPMS thermal mea-

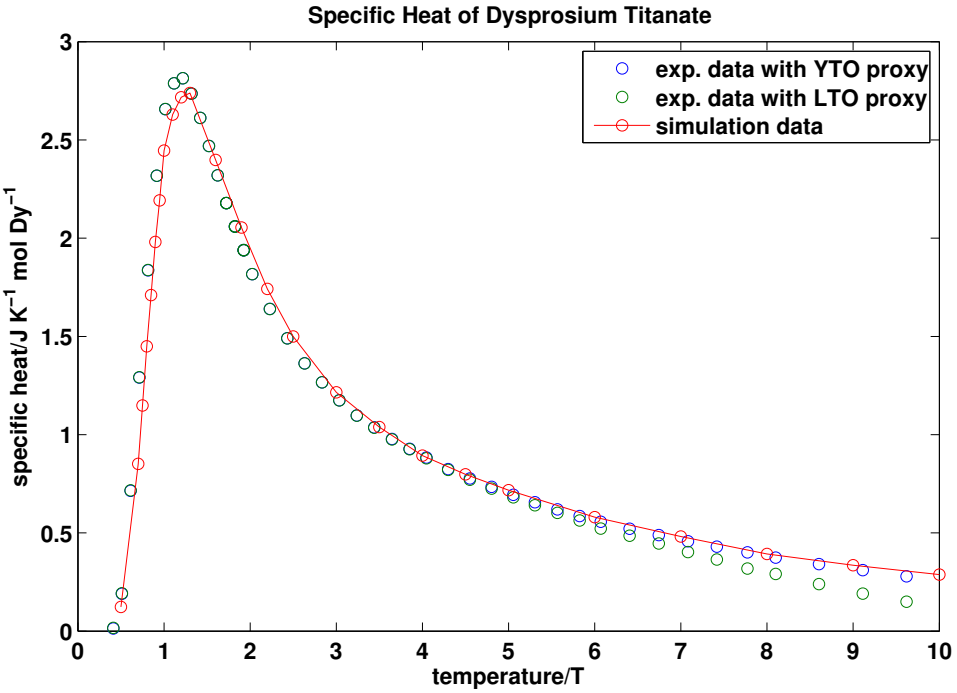

Figure 3.9: Dipolar spin ice simulation by V. Kaiser [86] (red line) vs. experimental data for DTO using YTO and LTO proxies. The red line is a guide for the eye.

surement puck to damage it and prevent measurement. The method could still be used with a more robust instrument and is the most direct way to determine the lattice contribution, but was not practical with current equipment.

An alternative method avoids using fragile specific heat pucks. L. Bovo [75] developed a method based on magnetisation, described in more detail in section 5.3. From the thermodynamics of spin ice she obtains:

$$\left(\frac{\partial I}{\partial T}\right)_{H_i} = \frac{1}{\mu_0}\left(\frac{\partial S}{\partial H_i}\right)_T \tag{3.45}$$

where I is the magnetic moment. From there integration yields:

$$\mu_0 \int_0^{H_i} \left(\frac{\partial I(T,H_i)}{\partial T}\right)_{H_i} dH_i = S(T,H_{int}) - S(T,0) \tag{3.46}$$

This enables the magnetic entropy change between two applied fields to be determined by integrating the rate of change of magnetisation with temperature as a

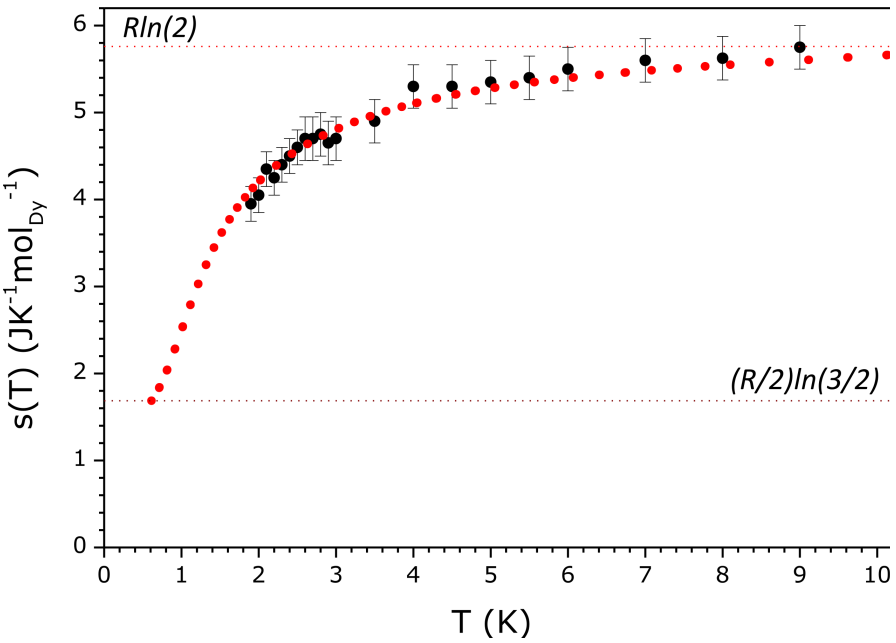

Figure 3.10: Entropy vs. temperature for DTO. Red dots are estimated by calorimetry, black dots by magnetometry as described in [75] and this work. Figure from [42]. © IOP Publishing. Reproduced with permission. All rights reserved.

function of applied field. The magnetic specific heat can then be derived using the following relation:

$$T\frac{\partial S}{\partial T} = c \tag{3.47}$$

with c the magnetic heat capacity in zero field.

However, this method is limited. The numerous numerical transformations that must be performed on the data compound experimental uncertainties to produce large error bars on yielded entropy values, as seen in figure 3.10 reproduced from [75]. As the region in question has high T, the variations in $T\partial S/\partial T$ will be so large as to completely obscure the real value of c without a large number of points measured with extreme care.

In chapter 5 of this work this method is applied to praseodymium zirconate, a candidate spin ice, and proves unable to provide good data at higher temperatures.

3.2.3 Values of the Chemical Potential

When comparing a theory to evidence it is preferable to establish as much as possible prior to the comparison, rather than defining parts post-hoc to fit experiment. What is brought to the theory beforehand is itself the result of the interpretation of other evidence in the light of theories, but if these prior results are well established they can reasonably be trusted and if not the success or failure of the new test will serve to reinforce or cast doubt on both theories together.

The theory outlined above has three parameters that vary between different spin-ice materials: the diamond lattice spacing a, the monopole charge Q, and the monopole chemical potential ν_0. The first can be determined by scattering experiments using well-established condensed matter theory [85], the second from measurements of the rare-earth ion magnetic moment and the definition $Q = 2\mu/a_d$. The third is a quantity that only has meaning in the context of monopolar spin ice theory, discussed above. It can however be compared to, and defined with the use of, similar 'third parameters' in previous spin ice theories.

As discussed in section 2.1, in 2008 CMS [31] formulated a 'dumbbell model' for spin ice, which yields the following expression for the magnetic energy of spin ice:

$$V_{ab} = \begin{cases} \frac{\mu_0 Q_a Q_b}{4\pi r_{ab}}, & a \neq b \\ \frac{1}{2}\nu_S Q_a^2, & a = b \end{cases} \tag{3.48}$$

where a and b range over all sites. The upper expression accounts for the interactions among the components of the monopole gas. The second is the 'monopole self-energy', which is the chemical potential, *i.e.* the energy associated purely with the existence of the monopole in itself. In their paper CMS find a value for ν_S:

$$\nu_S = \left(\frac{a}{\mu}\right)^2 \left(\frac{J}{3} + \frac{4}{3}\left[1 + \sqrt{\frac{2}{3}}\right] D\right) \tag{3.49}$$

where a is the diamond lattice constant, μ the magnetic moment of the spins, and J and D the exchange and dipolar coupling constants respectively. J and D are defined by den Hertog and Gingras in their 1999 paper [43] as components of the dipolar spin ice Hamiltonian (see equation 1.80). D is defined as $\mu_0\mu^2/8\pi a_p^3$ where

a_p is the pyrochlore lattice constant $= \sqrt{3/2}a$. J is determined experimentally by fitting Monte Carlo simulations to specific heat data.

In comparison to Debye-Hückel theory's trio of variables a, Q and ν_0, dipolar spin ice theory has a, μ and J, in each case with the first two externally experimentally determinable and the last a variable of the theory. However, the two theories are not equal in status. DSI theory is a fully microscopic model of spin ice. Its monopolar equivalent is the dumbbell model outlined by Castelnovo *et al.* [31]. Debye-Hückel theory by contrast is an abstraction of the dumbbell model and should be expected to be less precise. As such the use of ν_0 values determined by J values generated by fitting the DSI model is preferable to fitting ν_0 directly and this is the direction taken in the first part of the empirical investigation below. Using this approach yields ν_0 values 4.35 K for DTO and 5.7 K for HTO.

The issue is further complicated by improving measurements of the other parameters compared to those used in previous work. The Castelnovo *et al.* paper [31] that introduces the monopole model reports that for DTO, $a = 4.3356$ Å and $\mu = 10\mu_B$, while other reported values for a including the source [81] of the DTO used in this work are closer to 4.3786 Å [81, 87, 88], and μ has been measured more accurately since at $9.87\mu_B$ [89]. Due to the interdependent nature of the three values, it is inconsistent to update these values but leave J the same, however updating J would require implementing a new dipolar model simulation which would be impractical with the resources available.

As such in a second part of the empirical investigation ν_0 has been allowed to vary freely.

3.2.4 Specific Heat Theory

Making use of the data, however treated, requires a theory of the specific heat yielded by Debye-Hückel theory.

The definition of heat capacity at constant volume is:

$$c_\nu = \frac{\partial U}{\partial T} \tag{3.50}$$

Obtaining this requires an expression for the internal energy $U(T, N)$. Note

that as Debye-Hückel theory returns a value of N for a given T and set constant parameters (see sections 3.1.1 and 3.1.2), $N = N(T)$ and $T = T(N)$. As such U becomes a single variable function that can be written $U(T)$ or $U(N)$ and there is no need to use partial derivatives of N or T in the thermodynamics.

It is tempting to use the following logic: The energy per charge is the effective chemical potential $\nu = \nu_0 - \nu_c$ as in equation 3.8. As such

$$U = x\nu \tag{3.51}$$

$$\frac{dU}{dT} = \frac{dx\nu}{dT} \tag{3.52}$$

with appropriate modifications for double charges. However, this is deceptive. Properly, the total energy is obtained by integrating over the addition of the total number of charges:

$$U(N) = \int_0^N \nu(N) dN \tag{3.53}$$

Now consider:

$$\nu = \frac{dU}{dN}$$

$$c = \frac{dU}{dT}$$

$$c = \frac{dU}{dN}\frac{dN}{dT}, \tag{3.54}$$

so from equation 3.53:

$$c = \nu(N)\frac{dN}{dT}, \tag{3.55}$$

the correct equation to use.

3.2.5 Holmium Titanate

In figure 3.11 the forms of Debye-Hückel theory outlined above are compared to the experimental data for holmium titanate, using a monopole chemical potential of 5.7 K and no fitted parameters. It can immediately be seen that the data has the approximate form of a Schottky anomaly born of the two excited states that the system populates over this temperature range.

Take the Debye-Hückel theory with double charges but without entropic, lattice or Bjerrum modifications as the baseline. In the pre-peak region the theoretical projection of heat capacity increases rapidly in line with the experimental data. There is an anomalous point at 0.7 K, but this is believed to be due to the difficulties in measuring the very large hyperfine specific heat as discussed above in section 3.2.1. Past the peak, there is a long decline in which which the theory is in good agreement with the data until it becomes ambiguous at $T > 7$ K. In this region the single-charge theory drops off dramatically even in the 4 to 6 K region where the lattice heat is not yet important, demonstrating the importance of double charges even before the high-temperature tail. A partial exception arises at high temperatures ($T > 9$K) where, for the LTO lattice subtraction only, the single-charge theory is closer to the data. This difference is highlighted in figure 3.12, which compares the single- and double-charge theories directly.

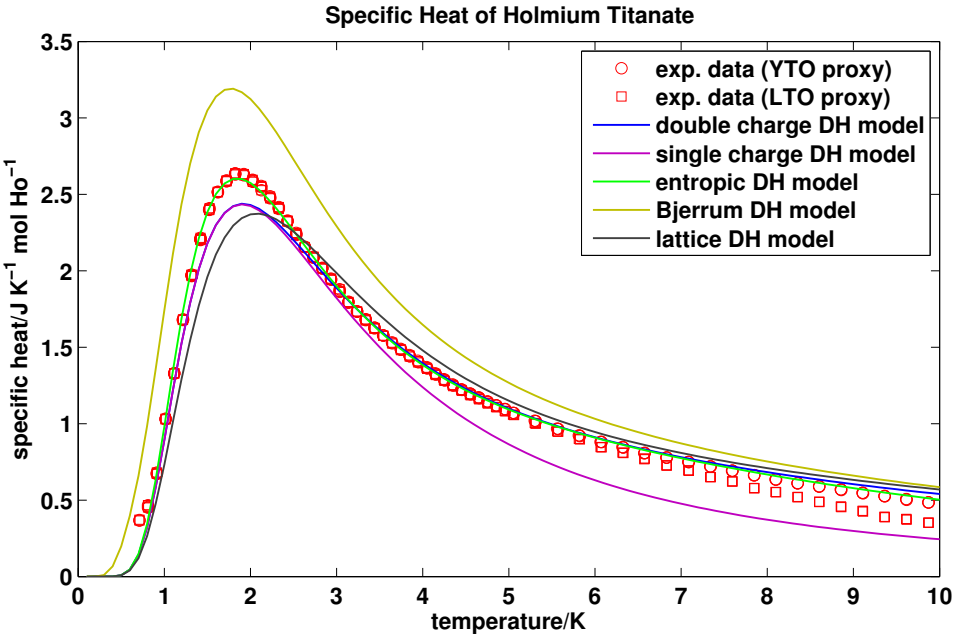

Figure 3.11: Holmium titanate experimental data and theory. The red symbols denote the two phonon heat proxies. The solid lines denote a range of Debye-Hückel theories. Blue is a continuum theory with double charges, of which the others are variants. Purple omits double charges, green includes entropic charge terms, black is calculated for a lattice and yellow includes Bjerrum pairing. There are no fitted parameters.

At the peak itself there is a significant gap between the theoretical prediction

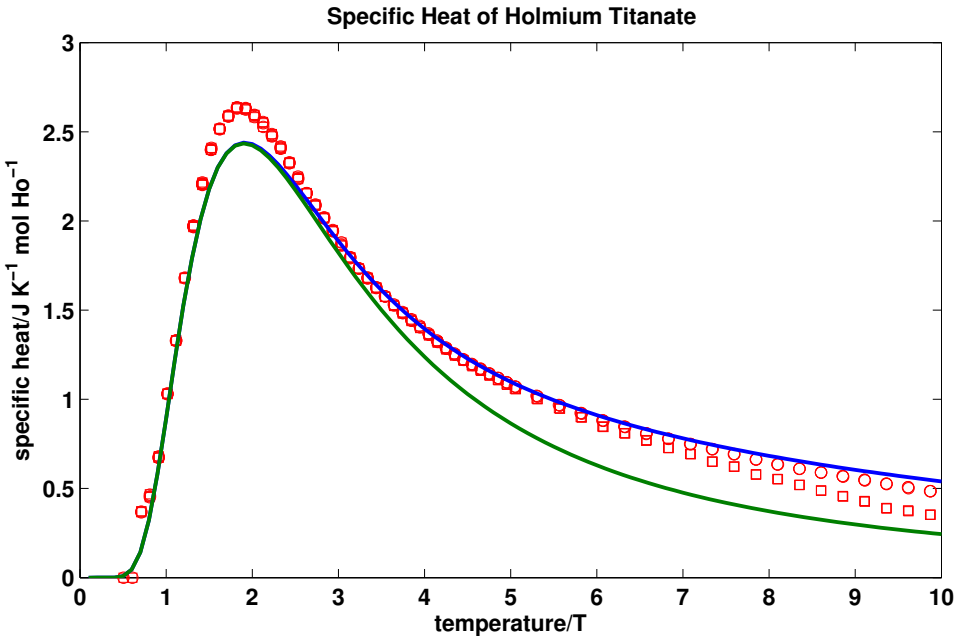

Figure 3.12: Holmium titanate experimental data and theory. The red symbols denote the two phonon heat proxies. The solid lines denote continuum Debye-Hückel theory with (blue) and without (green) double charges. There are no fitted parameters.

and the experimental result for heat capacity. This is due to the limitations of Debye-Hückel theory, which considers a gas of only independent charges. In real electrolytes and magnetolytes charges will form Bjerrum pairs and higher correlations as explored by Zhou *et al.* [36]. The implications of this failure for Debye-Hückel theory in spin ice as a whole are discussed below.

The results of adding a term for Bjerrum pairs as outlined in section 3.1.5 are shown by the teal line. It is immediately apparent that the attempt fails, and overestimates the specific heat in all regions. This failure highlights the problem of a lack of a principled distinction between the Bjerrum pairs and free charges in a dense charge gas, which means that linearly adding two separate models cannot describe the system accurately. This contrasts with the double charge correction which introduces an accounting for a wholly distinct species. This problem is fundamental as will ne demonstrated below.

The outcome of including entropic charge is very promising. The theoretical specific heat is reduced at high temperature but raised around the peak region.

The closeness of the correspondence for HTO is remarkable, with no deviations of significant size from the experimental data in reliable regions, and it is very tempting to take this as proof of the viability of the entropic charge model for high-ν spin ices, but the theoretical arguments against the concept ([78] and see section 3.1.4) remain valid and it would be premature to declare it valid on the basis of one set of data for one compound. The shift introduced by entropic charge, of an increase at the peak in exchange for a decrease at high temperatures, is the same as that to be expected from a complete Bjerrum theory, and the possibility of a misleading coincidence should not be discounted on the strength of one good fit.

Finally, the lattice theory does not deviate from the basic theory in a major way, but does demonstrate a rightward shift and depression of the peak height that worsens the accuracy of the fit. This suggests that, like the entropic charge theory is suspected to be, the accuracy of the basic theory is partially illusory, but due to the theoretical difficulties noted above this is only a tentative conclusion that awaits a lattice theory known to be valid for diamond lattices.

3.2.6 Dysprosium Titanate

In figures 3.13 and 3.14 the theory is compared to experimental data for DTO. The experimental data has the same general form as for HTO, but the Schottky peak is higher and occurs at a lower temperature.

The theoretical predictions use a chemical potential of 4.35 K and, as for HTO, no fitted parameters. The distribution of results is likewise similar but, in general, less successful. The failure of the baseline double-charge theory to reach the peak is more pronounced and accompanied by a similar failure on the upward slope of the peak, and counterbalanced by a general overestimation of the specific heat along the downward slope.

Among the variant theories the distribution of results is again similar. The Bjerrum theory fails, the single-charge theory is inferior except at higher temperatures, and the lattice theory is shifted right and down from the continuum theory, becoming less accurate. The extremely good result of the entropic charge theory for HTO is not replicated but does improve on the baseline fit, demonstrating that

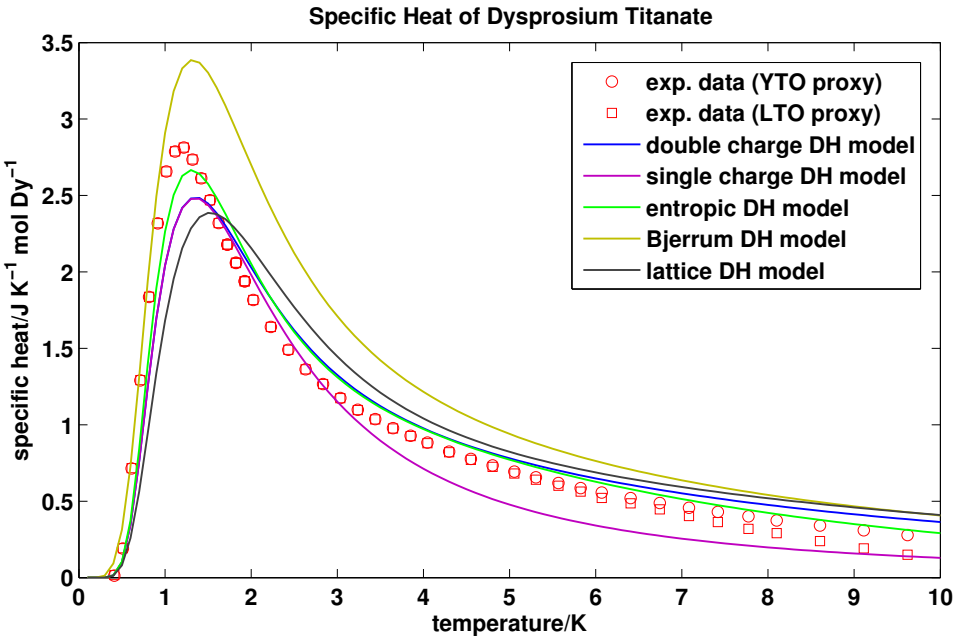

Figure 3.13: Dysprosium titanate experimental data and theory. The red symbols denote the two phonon heat proxies. The solid lines denote a range of Debye-Hückel theories. Blue is a continuum theory with double charges, of which the others are variants. Purple omits double charges, green includes entropic charge terms, black is calculated for a lattice and yellow includes Bjerrum pairing. There are no fitted parameters.

it is insufficient as a complete spin ice theory even if one were to accept it in the face of theoretical objections.

3.2.7 Discussion

Debye-Hückel theory has been tested here against two spin ices. For holmium titanate it has met with qualified success, but for dysprosium titanate its performance is noticeably worse. The largest problem is an inability to reach the peak without the use of theoretically questionable entropic charge, and the most direct method of tackling this is a failure.

The peak difficulties might be expected to arise from the formulation of the theory itself. Debye-Hückel theory relies on a linear approximation of the exponential $e^{-Q_i\Phi/kT}$, valid in the case that $Q_i\Phi \ll kT$ (see equation 1.87), i.e. that the ratio of the typical magnetostatic energy to the typical thermal energy is small. This can

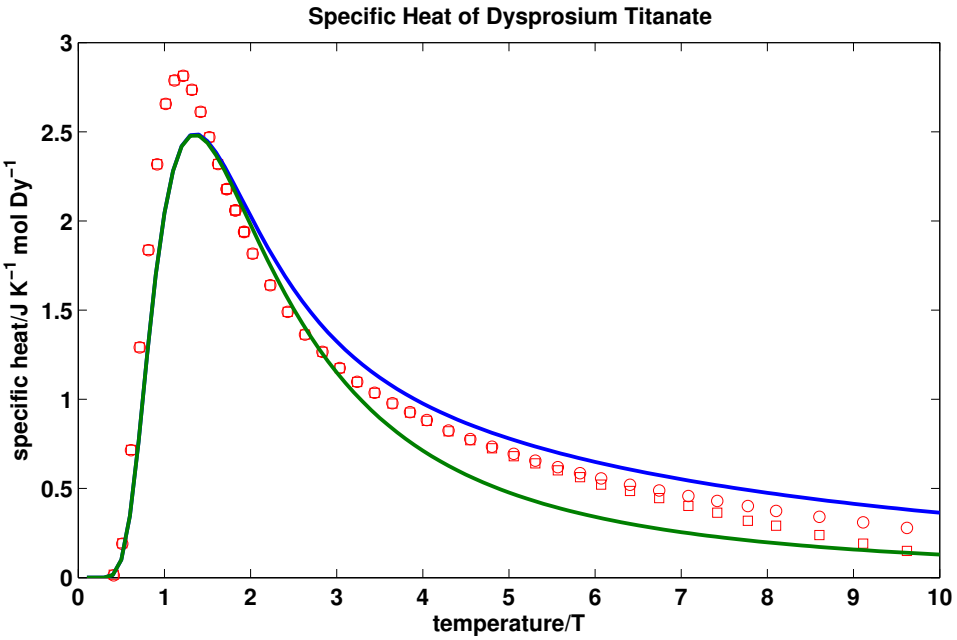

Figure 3.14: Dysprosium titanate experimental data and theory. The red symbols denote the two phonon heat proxies. The solid lines denote continuum Debye-Hückel theory with (blue) and without (green) double charges. There are no fitted parameters.

be satisfied by a low $Q\Phi$, which will be the case if there is a low concentration of charges, or by a large k_BT. By calculating the average separation distance based on the monopole concentration, and applying to the expression for Φ in equation 1.103, the value of the ratio can be estimated at each given temperature.

In figure 3.15 we see the variation of $Q\Phi/k_BT$ with temperature for single poles in dysprosium titanate, and it is clear that the quantity is at its highest in the vicinity of 1 K where the theory performs poorly. The quantity is smaller, and the theory more successful, both before and after this region. However, the decline with increasing temperature is quite slow, and there is a secondary peak at approximately 2.5 K, indicating that the effect is not necessarily very strong. Nevertheless this result and the relative success of the theory at higher temperatures give theoretical and empirical backing to the prospect of high-concentration Debye-Hückel theory, in solutions where the temperature is high enough to overcome the large $Q_i\Phi$ term.

Qualitatively, as mentioned above, this can be considered to be a consequence

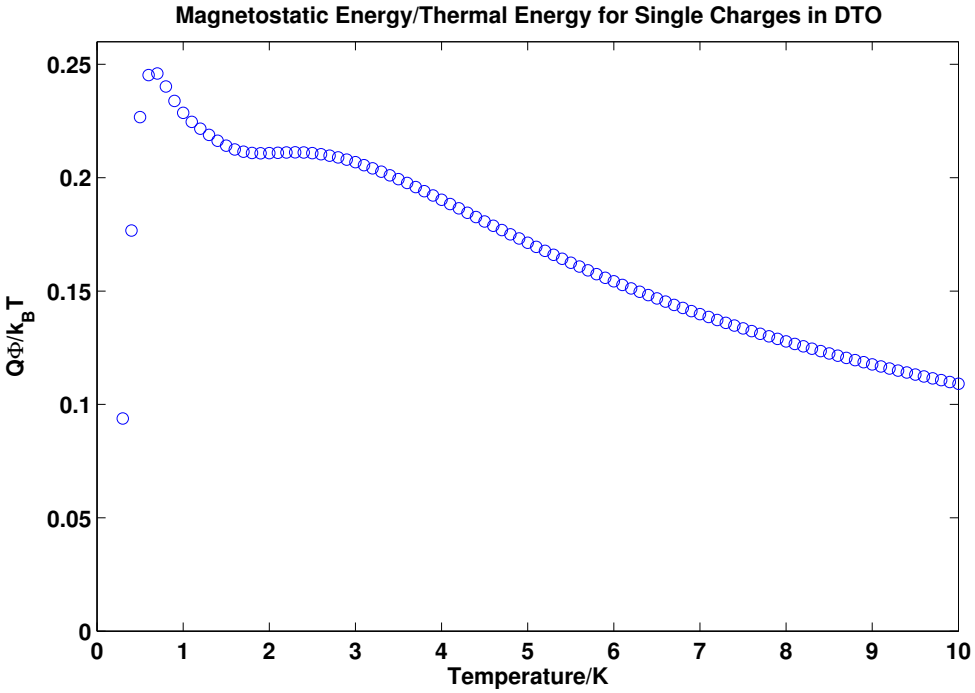

Figure 3.15: $Q\Phi/k_BT$ (the ratio of the typical magnetostatic energy to the typical thermal energy) plotted against temperature for single charges in DTO. Debye-Hückel theory relies on a linear approximation to that is in theory only applicable when $Q\Phi/k_BT \ll 1$.

of Debye-Hückel theory only considering independent charges. More closely correlated states such as Bjerrum pairs or many-ion systems are not modelled. At low populations, this is not a problem as the charges are so sparse that few complex systems will form, and at high temperatures the system will be sufficiently energetic to 'melt' any such structures. In either case the theory of independent charges will still function. DTO, with its lower chemical potential than HTO, will have a higher population of monopoles at any given temperature and so pose more problems for the Debye-Hückel approximation, hence the inferior performance of the model. The issue of charge correlations in magnetolytes as chemical potential decreases is developed more thoroughly by Zhou *et al.* in [36].

The straightforward correction is to add a term for Bjerrum pairs, but this approach failed in both test ices. It can be described as doing so due to 'double counting' of states and the lack of a distinct pair in a dense system, but the problem is fundamental in magnetolytes in a mathematically clear way.

The internal energy of the system is governed by the Boltzmann distributions which determine the population of each state:

$$x = \frac{g_i e^{\frac{-\nu_i}{k_B T}}}{g_0 + g_1 e^{\frac{-\nu}{k_B T}} + g_2 e^{\frac{-\nu_2}{k_B T}}} \tag{3.56}$$

Assuming the change in value of ν_i from screening, entropic or other considerations is finite, as T approaches zero all non-ground state terms approach zero population and the ground state approaches a population of 1. As T approaches infinity the population of each state approaches that determined by its degeneracy g in proportion with the others. This mirrors the entropy of the system. Assuming no accessible 'true ground state' below the ice rules state, at $T = 0$ K it has the Pauling entropy of an ice grid that obeys the ice rules and at infinite T it has the entropy of a system where all possible spin configurations are equally occupiable. Because it is constrained by the Boltzmann distribution the entropy increase, and hence the specific heat, predicted by Debye-Hückel theory over the course of a temperature rise from 0 to infinity must necessarily equal the difference between the Pauling and saturation entropies.

Given this, a bare addition to the specific heat such as the naïve Bjerrum theory described in the theoretical section will always cause a net overshoot, as it produces an entropy strictly larger than that produced by the bare Debye-Hückel theory which is already constrained to produce the correct total entropy regardless of its accuracy at any one specific temperature. The increase in the specific heat in the peak region must be 'paid for' by a reduction in other regions, and so a Bjerrum theory for spin ice cannot stand independently of the rest of the Debye-Hückel theory. It must either operate entirely within the same boltzmann distributions as the independent charges or produce a negative 'Bjerrum contribution' at high temperatures.

This aligns with the observed deficiencies of Debye-Hückel theory in the more trying case of DTO, where it failed to meet the peak but overshot at high temperatures. This balancing means the overall area under the c/T curve, and so the entropy, remains constant and sheds light on the way the experimental and theoretical curves change shape between HTO and DTO. As the chemical potential lowers the system populates at lower temperatures, and offsets this with a reduced

rate of population increase at higher temperatures, thus producing a lower, earlier peak.

3.2.8 Comparison with Previous Formulation of Debye-Hückel Theory

In figure 3.16 the theory developed above is compared for DTO against the results of the theory of CMS [4] described in section 2.3, digitised from figure 2.4.

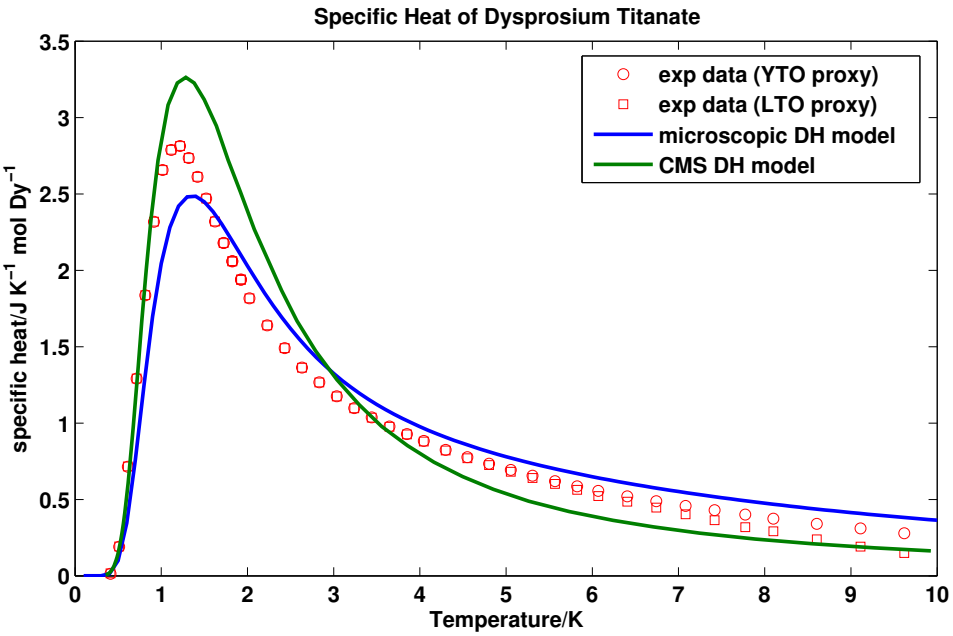

Figure 3.16: Experimental data for specific heat of DTO (red symbols) compared to Debye-Hückel theory with double charges and microscopic degeneracy for $\nu_0 = 4.35$ (blue line) and the Debye-Hückel theory of CMS for $\nu_0 = 4.37$ (red line) [4].

Before the peak, the CMS theory matches the data more closely than the new theory. As it passes the peak, it develops a severe overshoot in its estimation of the specific heat, then loses this as the temperature increases, crossing the experimental value at approximately 3 K and finishing below the YTO-proxied value, though not the LTO-proxied value.

This differences can be understood in terms of the two differences of the models. The difference in the statistical weight of the ground state changes the low-

temperature specific heat, while at high temperatures and hence energies the exclusion of double charges becomes . The performance of the model at high temperatures is similar to that of the single-charge theory in figure 3.13.

The overall comparison is not as clear-cut as might be expected given the closer match of the new theory to the fundamentals of the system. However, two further points should be registered in favour of the new theory. First, above 2 K it has a similar derivative to the experimental data using the YTO proxy favoured by simulations, yielding a similar shaped curve with a small vertical offset. The CMS theory does spend time closer to the data in the 3 K to 4 K region, but this is in the course of a collapse down to a low value that necessarily requires the curve to cross the data at some point. This is to be expected in light of the nature of the two differences, one of which increases the specific heat at low temperatures, and the other of which decreases it at high temperatures. Second, the deficiencies in the new model are easily understood in terms of known phenomena not treated by the theory, that being the failure to account for paired and other correlated monopole states, which increase the specific heat in the vicinity of the peak and, by entropic accounting, decrease it elsewhere.

It is notable that the closer match of the CMS theory to the data in the pre-peak region is similar to the performance of the Bjerrum pair theory in figure 3.13. In both cases the insufficiency of the basic theory to account for paired monopole states is addressed by a factor that increases the excited state population in the low-temperature region: for the Bjerrum theory, an explicit addition of monopole pair states that later becomes unphysical, and for the CMS theory, an overweighting of the statistical weight of the monopole state relative to the ground state.

3.2.9 Fitted Values of Specific Heat and Effective Chemical Potential

As noted in section 3.2.3, there is some uncertainty regarding the values of the microscopic parameters of DTO. The above discussion uses the values from [31]. Here, we use a lattice constant $a = 4.3786$ Å [81], and a Dy^{3+} magnetic moment of $9.87\mu_B$ for DTO [89], and allow the chemical potential ν_0 for DTO and HTO to

Table 3.2: Fitted Spin Ice Chemical Potentials

Temperature	proxy	low fit	full range	high fit
HTO	YTO	5.4453	5.5156	5.5625
HTO	LTO	5.4453	5.4922	5.3516
DTO	YTO	3.9688	3.9922	3.9219
DTO	LTO	3.9453	3.9688	3.7344

vary freely to obtain a best fit.

The data was fitted for both titanate spin ices using an unweighted least squares fitting procedure. In such a procedure a specific heat curve is generated according to Debye-Hückel theory for a given ν_0, then the sum of the squares of the differences between the theoretical values and the experimental values at each point is calculated. The value of ν_0 which gives the smallest sum is the returned estimate. The fit was run over three temperature ranges, the region before the peak ($T = 1.2$ K for DTO, $T = 1.9$ K for HTO), the full range from 0 K $< T <$ 10 K, and for 4 K $< T <$ 10 K for the YTO and LTO proxy specific heat estimates. In figures 3.17 and 3.18 we see the results for HTO and DTO respectively. The fitted ν_0 values are listed in table 3.2.

The HTO values typically vary by less than 10% from the 5.7 K established value. The DTO values vary more strongly, by more than 10% from the 4.35 K. The fits for DTO are notably superior to those using the literature parameter values. The theoretical peak has moved closer to the experimental peak, and the post-peak region is significantly improved, with little distinction between theory and experiment until $T = 5$ K, where the exact value of the magnetic heat capacity becomes uncertain.

However, this does not establish that the DTO chemical potential value predicted by the literature is incorrect. The use of a fitting procedure can create a false accuracy, which is why non-fitted curves were presented first in this investigation. Referring to table 3.2 and recalling the literature ν values of 5.7 K for HTO and 4.35 K for DTO, we see that the fitted values are always lower. This is explained by reference to the lack of accounting for Bjerrum pairs noted in the above section. Bjerrum pairs, by remaining bound and so having lower Coulomb

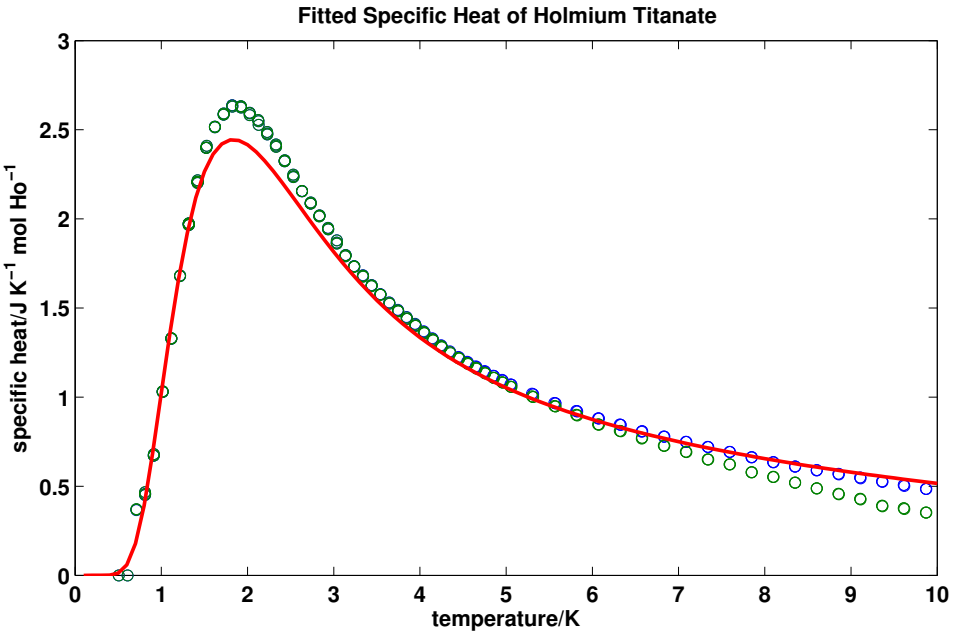

Figure 3.17: Magnetic specific heat of HTO compared to results of fitted Debye-Hückel theory. The blue symbols use a scaled YTO proxy for the phonon heat, the green symbols a scaled LTO proxy. The red line is a fit to the YTO data, with $\nu_0 = 5.52$ K for HTO and 3.99 K for DTO.

energy, allow lattice sites to become excited at lower energies than needed to create unbound free monopoles. The form of Debye-Hückel theory described above is unable to properly account for this, but it can crudely approximate it by lowering the chemical potential, which has the same theoretical effect of lowering the lattice site excitation energy and the same practical effect of increasing the height of the peak as sites are filled earlier, but decreasing the high-temperature heat capacity as the system runs out of excited states to occupy on its way to maximum entropy. As such the fitted chemical potential values are not true chemical potentials but slightly modified 'effective chemical potentials' which partially account for the presence of Bjerrum pairs and other monopole complexes.

This accounting is however only partial. The fitted curves in figures 3.17 and 3.18 are still subject to the same problems as faced by the theoretically predicted curves in figures 3.11 and 3.13. Figure 3.19 shows the results of fitting the curve to the most extreme part of the DTO data, the LTO proxied specific heat for $T > 4$ K. This result is notably worse than the earlier fits and the non-fitted

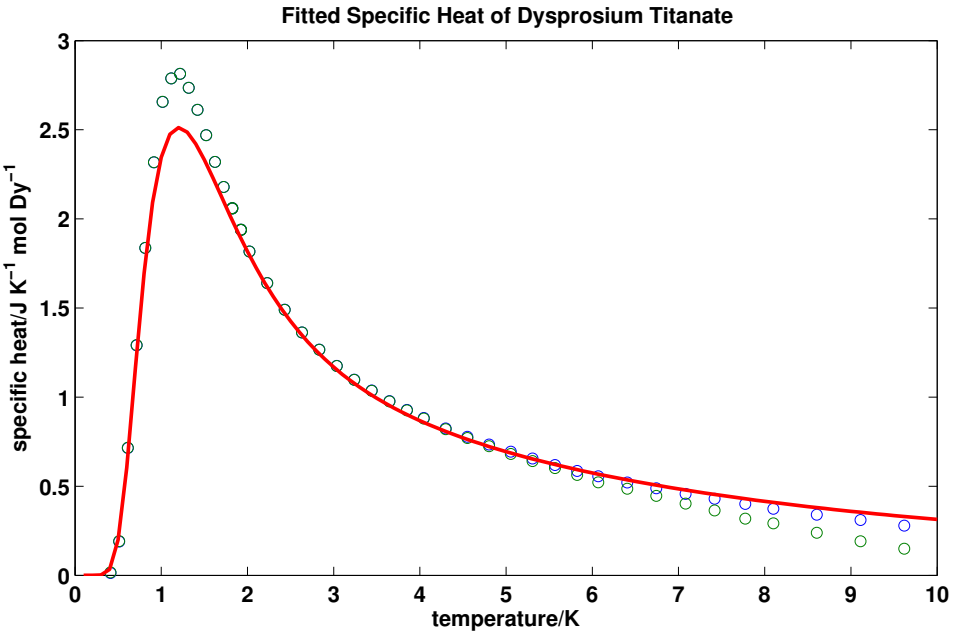

Figure 3.18: Magnetic specific heat of DTO compared to results of fitted Debye-Hückel theory. The blue symbols use a scaled YTO proxy for the phonon heat, the green symbols a scaled LTO proxy. The red lines is a fit to the YTO data, with $\nu_0 = 5.52$ K for HTO and 3.99 K for DTO.

curves, as it fails to match the shape of the curve in its fitted region, and while it raises the peak height, it also moves it to a lower temperature, resulting in a poor fit in all regions. This demonstrates that even with an effective chemical potential lowered to allow low-energy monopole formation, Debye-Hückel theory cannot account for bound monopole pairs. It also demonstrates that the theory cannot achieve low values of magnetic heat capacity at high temperatures without losing its ability to model lower temperatures, underlining the incompatibility of Debye-Hückel theory at high temperatures with some previous estimates of the phonon specific heat.

3.2.10 Comparison with Simulations

The simulations of V. Kaiser [86] were previously used to shed light on the contribution of the lattice to the heat capacity of spin ice. Here they are compared directly with the predictions of Debye-Hückel theory. Comparison with simulations offers different benefits to comparison with experiment. In a simulation the

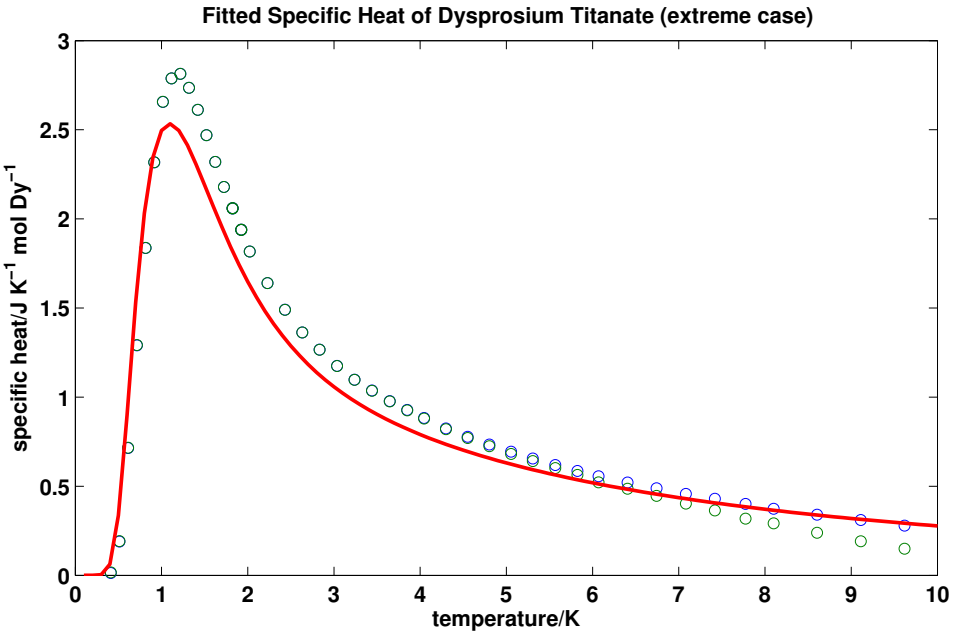

Figure 3.19: Magnetic specific heat of DTO compared to results of fitted Debye-Hückel theory. Blue symbols use a scaled YTO proxy for the phonon heat, green symbols a scaled LTO proxy. The red line is a fit to the LTO data for $T > 4$ K, with $\nu_0 = 3.73$ K.

theoretical model and its parameters can be specified exactly. While one cannot be certain that the model so specified is actually realised in the physical world (though this can itself be supported by experiment), the accordance of an analytic theory with the model it is intended to describe can be tested.

In figures 3.20 and 3.21 simulated data with and without double charges is compared against the similar Debye-Hückel theories. The simulations used values of $\nu = 4.35$ K for DTO and $\nu = 5.7$ K and for HTO, and identical parameters were used for the Debye-Hückel calculations. The double charge case is similarly successful as with the experimental data, with a peak deficiency complemented by an excess in the high-temperature tail. Notable however is that the single charge case is also effective (and flawed) in the same way. A simulation of a dipolar model with double defects excluded is described successfully by the Debye-Hückel model, demonstrating it is robust not just across varying parameter values but varying fundamental physics as well.

Also notable in the results is that the divergence of the analytic Debye-Hückel

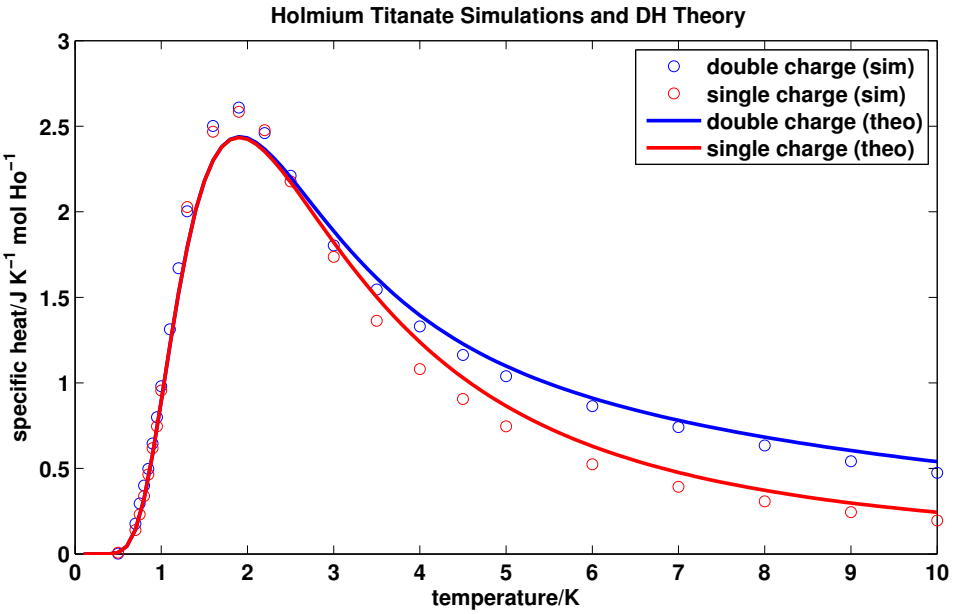

Figure 3.20: Dipolar spin ice simulations (circles) and Debye-Hückel theory (lines) for HTO. The blue includes double charges while the red excludes them.

prediction from the simulated prediction at high temperatures is very similar for both single and double charges, in each material. This indicates that the inclusion of the double-charge correction in Debye-Hückel theory captures very closely the actual effect of double charges on the high-temperature specific heat. The three-way agreement of experiment, analytic theory and simulation, especially for HTO, strongly suggests that double monopoles are an important element of the thermal physics of spin ice near saturation, and cannot be safely discounted.

3.2.11 Cadmium Erbium selenide

The discussion so far has focused on pyrochlores, but the theory is not specific to any crystal structure so long as spin ice behaviour itself exists, that is, ferromagnetically coupled Ising spins are arranged along the bonds of a diamond lattice.

The spinels (AR_2X_4) are another cubic crystal structure. The series $CdLn_2X_4$ (where Ln is a lanthanide and $X = Se, S$) has been found to be a rich source of magnetic frustration in which the lanthanide ions form a frustrated sublattice

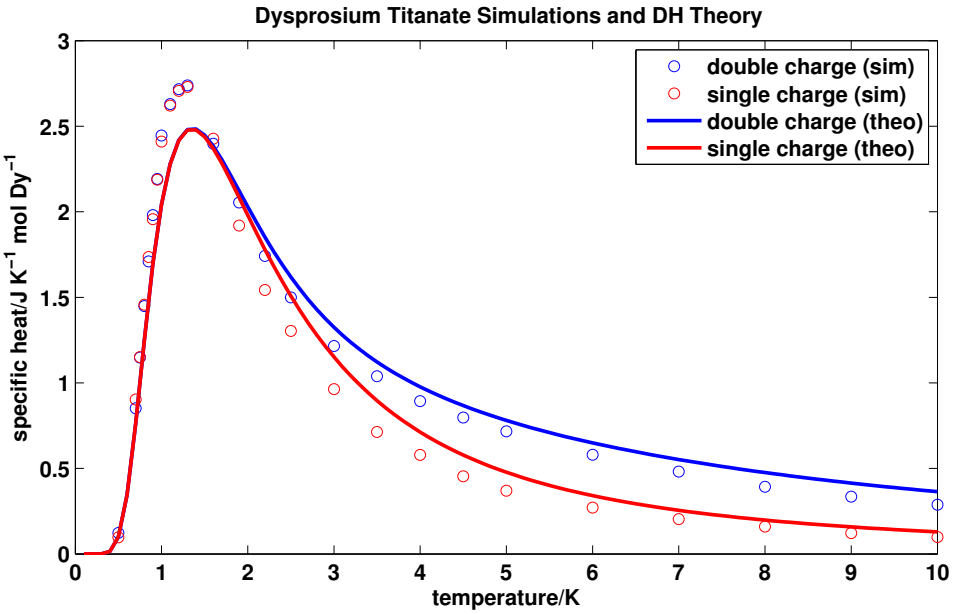

Figure 3.21: Dipolar spin ice simulations (circles) and Debye-Hückel theory (lines) for DTO. The blue includes double charges while the red excludes them.

[90]. In 2010, Lago *et al.* [39] presented evidence that the spinel cadmium erbium selenide ($CdEr_2Se_4$, CES) realises a spin ice lattice with its Er^{3+} ions. This presents a useful test case for Debye-Hückel theory, to see if it can generalise to a different crystal structure that is nevertheless similar in the ways the theory claims are important.

As with the pyrochlores it is necessary to remove the non-monopolar contributions to the specific heat. Lago *et al.* [39] identified two major contributions: the phonon contribution, as in the pyrochlores, and also the first excited state of the crystal electric field. They used fits for the energy of the first excited CEF level and the Debye temperature of a T^3 Debye phonon model, obtaining 46.96 K and 167.84 K respectively. Their findings are displayed in figure 3.22.

As with the DTO results of Hiroi *et al.* discussed in section 3.2.2, the specific heat reaches zero at 10 K in their fit, but this can similarly be called into question in light of the theoretical expectation of a non-negligible monopolar contribution at high temperatures. Slightly different parameters for the CEF excited level and the Debye temperature can obtain a magnetic specific heat persistent even to 10 K. In figure 3.23 a variation with values of 170.84 K and 48.96 K respectively is similarly

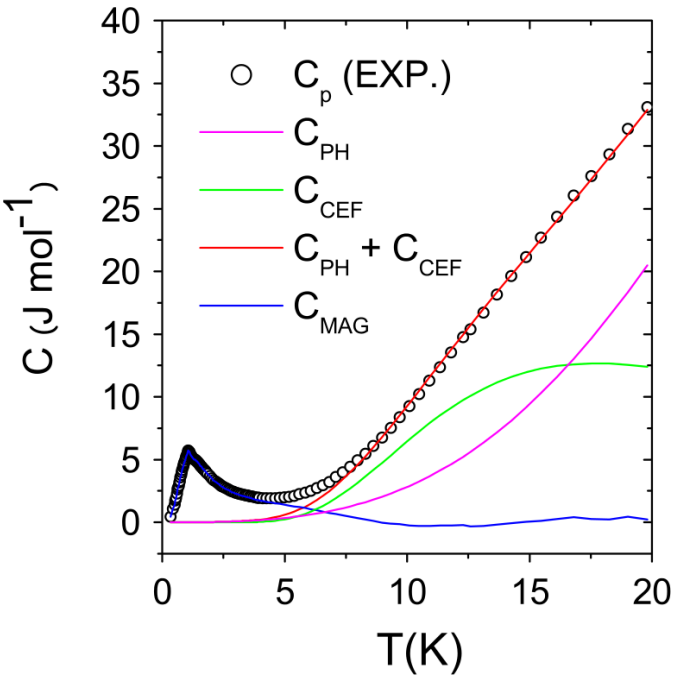

Figure 3.22: The heat capacity of $CdEr_2Se_4$ (black circles) split into its theoretical phonon (purple), crystal field (green), total non-magnetic (red) and implicit magnetic (blue) components. Reprinted figure with permission from J. Lago *et al.*, Physical Review Letters, 104, 247203, 2010. [39] Copyright 2010 by the American Physical Society.

successful in describing the specific heat for $T > 10$ K, but has significantly different results for the specific heat at 10 K in comparison to Debye-Hückel theory, as shown in figure 3.24, plotted using a chemical potential of 3.52 K derived using equation 3.49 from the J value (-0.15 K) and D value (0.97 K) provided in the Lago *et al.* paper [39].

Neither fit in figure 3.24 is wholly satisfactory. While the CES data clearly has the same Schottky peak form seen in the canonical HTO and DTO spin ices, the Debye-Hückel theory for CES does not match or exceed the experimental data in the post-peak region as it does for those compounds, despite the low ν_0 value derived from the J value. A broad secondary peak is visible which collapses down to match the theory (for the new parameters) or to zero (for the Lago *et al.* [39] parameters) at 10 K. In figure 3.25 the Debye-Hückel prediction is added to the CEF and phonon contributions and compared to the raw experimental value up to 20 K.

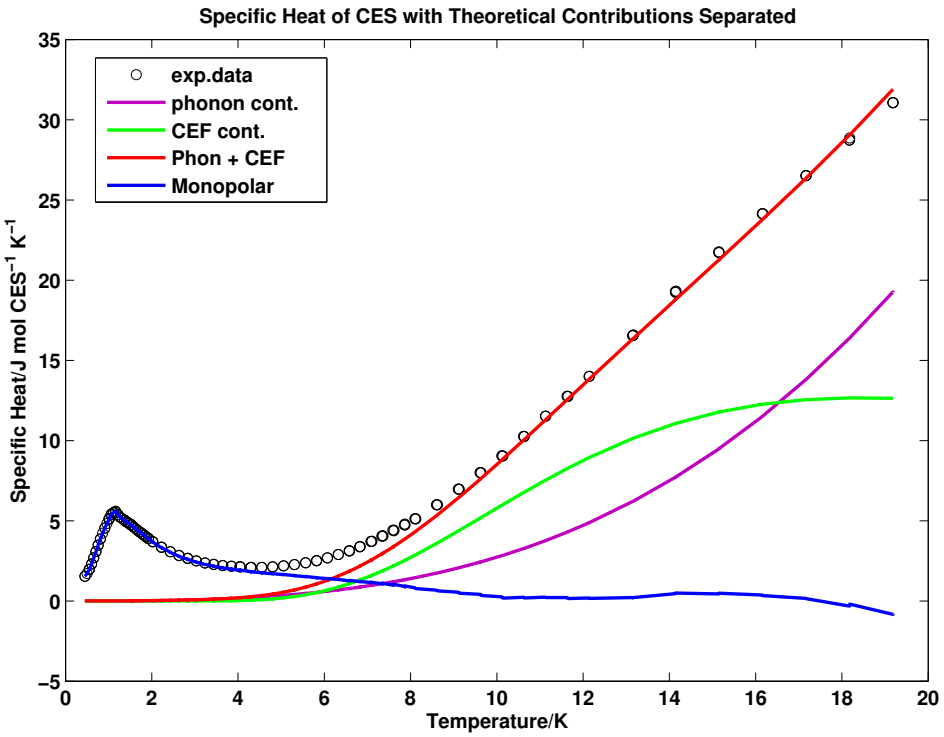

Figure 3.23: The heat capacity of $CdEr_2Se_4$ (black circles) split into its theoretical phonon (purple), crystal field (green), total non-magnetic (red) and implicit magnetic (blue) components.

Figures 3.22 and 3.23 suggests an explanation for the anomalous behaviour. The CEF curves in both begin significantly rising past 5 K and are at almost half of their maximum value at 10 K. This suggests a significant occupation of excited crystal field states at low temperatures. As the ideal spin ice state depends on the spins being bound absolutely parallel to the tetrahedral axes, such an occupation could significantly disrupt the spin ice physics, potentially producing both the broad peak and a collapse in magnetic heat capacity in line with Lago *et al.*'s fitted parameter values. However, if the broad peak is due to some additional nonmagnetic factor and the true monopolar heat capacity is obtained by subtracting it, then there is scope for the fit to be similar to those of the canonical ices within the bounds of the uncertainty of the high temperature specific heat. Careful measurements and separations of the sources of the heat capacity of CES will be required to resolve these issues.

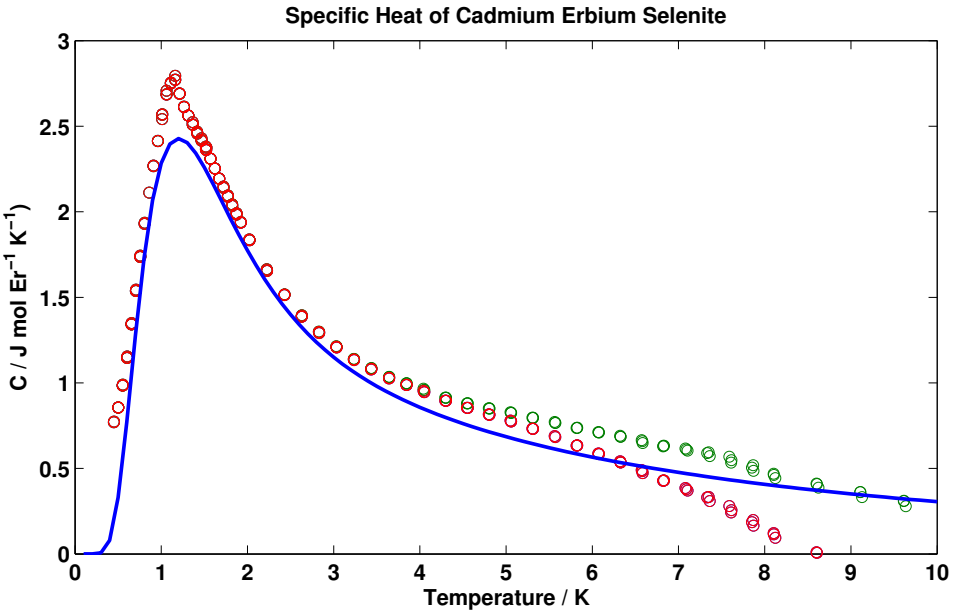

Figure 3.24: Cadmium erbium selenide experimental data and theory. The red circles represent the previous CES heat capacity work of Lago *et al.*[39]. The green circles are the divergent result obtained by slightly modifying their fitted values. The blue line is the prediction of double-charge continuum Debye-Hückel theory for this data

Despite these difficulties CES is similar in behaviour to the spin ices and Debye-Hückel theory has a degree of success in capturing its magnetic specific heat in the low-temperature region, demonstrating its applicability across variable crystal structures.

3.3 Summary

The above analysis has shown that heat capacity predictions from Debye-Hückel theory agree with experimental data for three spin ice materials of differing energy levels and crystal structures, despite the radical difference between the electrolytes the theory was originally conceived to describe and the frustrated magnetic crystals it is applied to here. The theory is theoretically improved from the version presented by Castelnovo *et al.* in 2010 [4], as it contains a microscopically correct form of the partition function and incorporates the effect of double charges. These improvements allow the theory to describe the heat capacity even

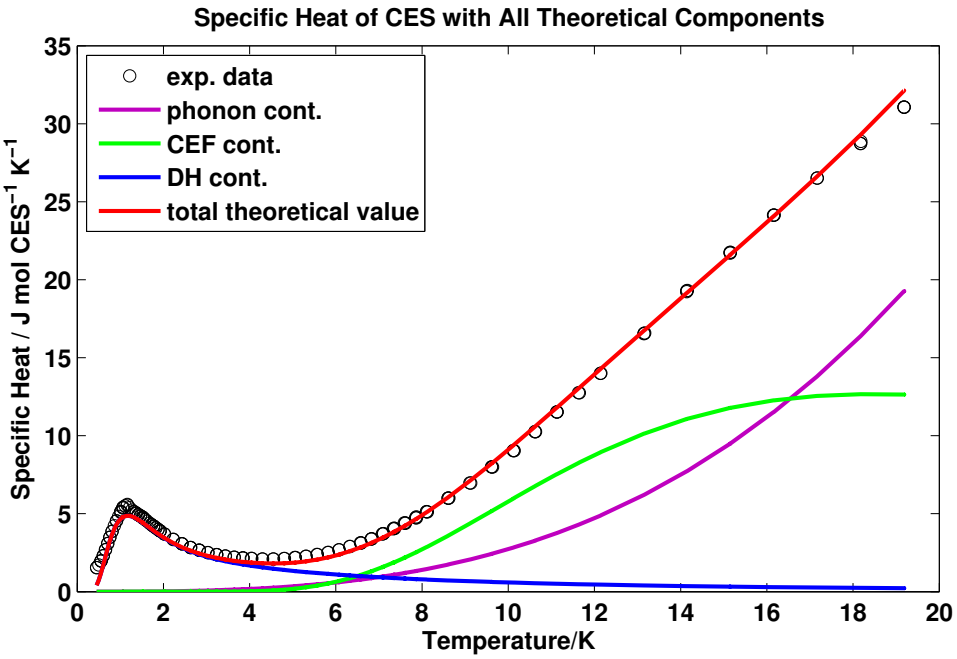

Figure 3.25: The heat capacity of $CdEr_2Se_4$ (black circles) plotted with its theoretical phonon (purple), crystal field (green), Debye-Hückel (red) and total theoretical (blue) components.

into high-temperature regions approaching 10 K, much higher than the 2 K previously thought to represent the limit of spin ice behaviour in figure 2.4, and in a high-density region not normally thought accessible to Debye-Hückel theory. There is furthermore reason to believe that the heat capacity of spin ices in the 10K region is larger than has previously been suggested.

The principal limitation of the theory is its failure to account for the complete heat capacity near the peak. The most obvious explanation of this is that the theory does not yet incorporate Bjerrum pairs of monopoles. This limitation has a counterpart in a persistent, but smaller overestimation of the specific heat at high temperatures.

Chapter 4

Magnetic Relaxation

Monopoles, being effective magnetic charges, can carry magnetic current and so mediate the process of magnetisation under field. In his original 2005 paper [3], Ryzhkin derived a theory of magnetic relaxation in spin ice on this basis. Recent work by Revell *et al.* [5] and Paulsen *et al.* [7] has examined relaxation at low temperatures and found Ryzhkin's description incomplete. In this section Paulsen *et al.*'s data will be examined in the light of Ryzhkin's original model, Revell *et al.*'s proposed model, and a new model proposed by Steven Bramwell [74] and the implications of their successes and failures for the monopole physics of spin ice will be explored.

4.1 Magnetic Relaxation Theory I

In section 2.4 Ryzhkin's 2005 theory [3] was outlined. It can be used to derive an expression for DC relaxation in one dimension. Recalling equation 2.24:

$$\mathbf{j_i} = \mu_i n_i \mu_0 (Q_i \mathbf{H} - \eta_i \Phi \mathbf{\Omega}),$$

converting vectors to scalars along one axis, substituting magnetic current density $J = \partial M/\partial t = jQ$, susceptibility $\chi_T = Q^2/\Phi$, and $M = Q\Omega$, the equation can be rewritten as

$$J = \kappa(H - \chi_T^{-1} M) \tag{4.1}$$

with monopole conductivity $\kappa = ucQ^2\mu_0$, where monopole mobility $u = u_+ = -u_-$, monopole concentration $c = c_+ + c_-$, and monopole charge $Q = Q_+ = -Q_-$. c is related to the dimensionless monopole density x as $x = cV_0$, where V_0 is the volume of a diamond lattice site.

So, substituting J for the partial differential, we obtain

$$\frac{\partial M}{\partial t} = \kappa(H - \chi_T^{-1}M). \tag{4.2}$$

Here H is the internal field H_i, but can be converted to a function of the applied field H_a with the substitution $H_i = H_a - DM$, where D is the demagnetising factor.

$$\frac{\partial M}{\partial t} = \kappa(H_a - aM), \tag{4.3}$$

where $a = D + \chi_T^{-1}$.

This becomes zero when $H_a = aM$, at which point the reaction field from the monopole movement (represented in the change in M) negates the applied magnetic field. This reaction field is not a phenomenon of magnetic fields but is an effective field created by the entropy cost of ordering the spin lattice underlying the monopole vacuum.

A monopole movement in a given direction consists in an Ising spin flip from a particular orientation to the opposite orientation [3]. Oppositely charged monopoles moving in the opposite direction utilise the same type of flip. Aggregate magnetic current polarises the spin network, introducing an entropy cost to further polarisation. This creates an effective reaction field, which is the cause of the impossibility of a sustained DC current in spin ice [42]. Under high fields, the network can be completely polarised, and monopole movement in the field direction becomes impossible as the available paths are all oriented against the direction of travel.

With the substitutions $M_0 = H_a/a$, $m = M/M_0$ and $\nu = a\kappa_0$, we obtain

$$\frac{\partial m}{\partial t} = \nu(1 - m). \tag{4.4}$$

This differential equation in m can be solved to yield

$$m(t) = 1 - e^{-\nu t}. \tag{4.5}$$

This is a straightforward expression for the magnetisation as a function of time in a DC field, which can be tested against experimental data.

4.2 Ryzhkin's Theory and Experiment

Ryzhkin's theory has previously been tested against AC relaxation data at temperatures of 4.5 K and above and found to be effective ([54] and see section 2.4.1). At those temperatures, the monopole population is approaching saturation. In this section, the test is performed at temperatures of 0.6 K and below where the monopoles instead approach the dilute limit, and different processes may come into play.

4.2.1 Experimental Methods

Paulsen *et al.* [7] performed a number of magnetic relaxation measurements on dysprosium titanate and have kindly made their data available for this investigation. Crystals of DTO were cooled to measurement temperature by a 'classic' or 'conventional' cooling method involving a thermal reservoir, or by a rapid 'magnetothermal avalanche quench'. The crystals were grown in oxygen flow but not annealed, and were of yellow colouration.

In conventional cooling, the sample is heated to 900 mK, then cooled to the measuring temperature over 3000 seconds, and regulated there for 600 seconds before the magnetic field is applied and measurement begins.

In an avalanche quench, the sample is magnetised by an applied field of -0.2 T, and cooled to 75 mK. Then, the magnetisation is reversed by an applied field of 0.2 T, which heats the sample to approximately 900 mK though the release of magnetic Zeeman energy from the spins. It then is allowed to rest for four seconds, during which it cools rapidly due to direct contact with the cold sample holder. Finally, the field is switched off, creating another quench and a return to 900 mK, then a rapid cooling into the sample holder.

The crystals were then exposed to a 5 mT magnetic field and the relaxation of the magnetisation measured at constant temperature.

4.2.2 Results

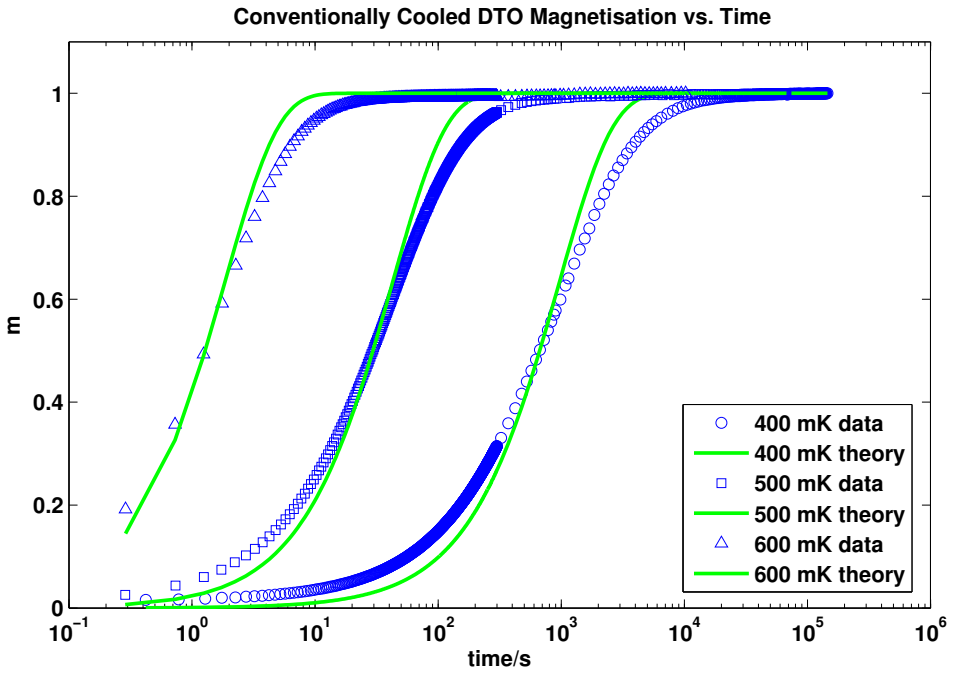

Figure 4.1: Magnetisation of conventionally cooled DTO (blue symbols) compared against theoretical results of Ryzhkin (green lines).

The value of the single parameter ν can be extracted from the 'half-life' of an experimental m vs. t curve, thus:

$$m(t_{1/2}) = 1/2 = 1 - e^{-\nu t_{1/2}}, \tag{4.6}$$

$$\nu = \frac{-\ln(1/2)}{t_{1/2}}, \tag{4.7}$$

where $t_{1/2}$ is the time taken for the magnetisation to reach half of its saturation value, which can be read off from the data directly.

This allows the theory to be compared directly against the data without free parameters, in Figure 4.1. Two problems are immediately apparent. Firstly, the

theoretical curve is the wrong shape, with too sluggish a start followed by too sharp an increase. Secondly, the theoretical curve assumes that magnetisation starts at zero at time zero. However, the experimental curve does not appear to be approaching that point. These results are similar in both avalanche quenched and classic cooled data sets.

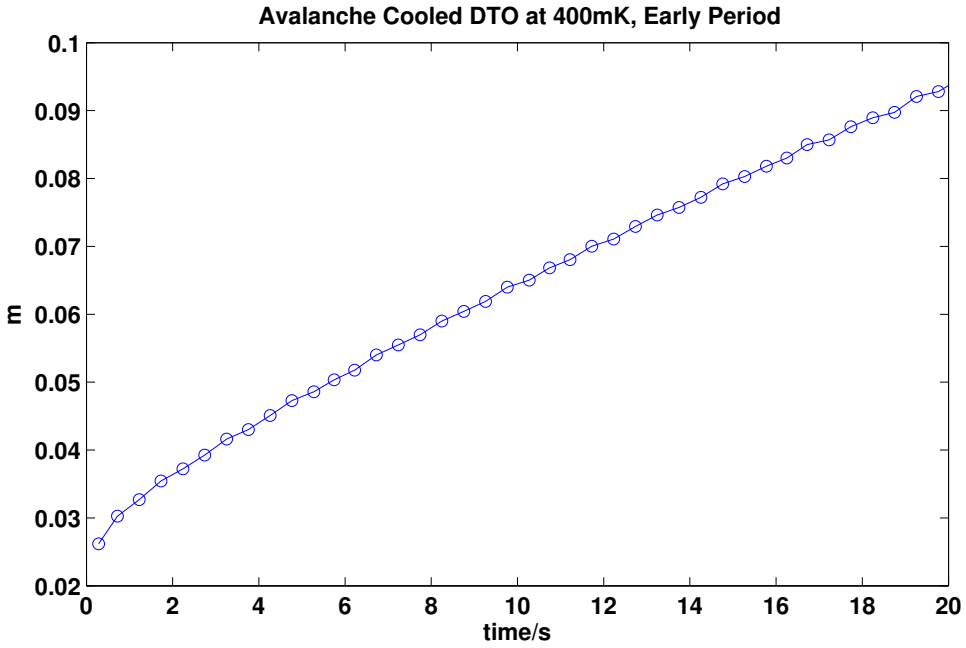

Figure 4.2: Avalanche quenched DTO from 0 to 20 s. Line is a guide for the eye and does not imply any continuity of measurement.

Examining the earliest time period of the 400mK curve on linear axes in Figure 4.2, d^2m/dm^2 appears to be negative, and so the curve convex, which is not consistent with the early stages of an exponential increase to a limit such as our expression describes, but is consistent with the late stages of one. This suggests that there is an initial, very fast process that increases the magnetisation to some low level, which is then overtaken by the more conventional process our expression attempts to describe. Recent work has suggested that this might be an adiabatic (involving no heat transfer) susceptibility [91].

This phenomenon will not be considered fully in this section, but to compensate for it the expression can be modified to have the boundary condition $m(0) = m_0$

$$m(t) = 1 - (1 - m_0)e^{-\nu t} \tag{4.8}$$

with m_0 being the maximum contribution of the initial process, to correct the results once the complete contribution is present. The earliest time points will remain erroneous until the initial process is properly accounted for.

4.3 Magnetic Relaxation Theory II

Ryzhkin's basic theory is clearly insufficient to describe spin ice relaxation behaviour. Three proposed modifications of the expression will be examined here: the linear Wien effect model, the stretched exponential model, and the recombination model.

4.3.1 Linear Non-Ohmic Model

In 2009, Bramwell *et al.* [59] reported that the second Wien effect occurs in dysprosium titanate.

As described in section 1.5.3, the second Wien effect or the 'field dissociation effect' is a phenomenon in electrolytes in which conductivity increases under electric fields due to the field dissociating bound ion pairs and so increasing the population of free charge carriers [48]. An analogous magnetic effect would be expected in spin ice under the magnetolyte model, due to magnetic fields both splitting bound Bjerrum pairs and inducing spin flips in otherwise ice-rule site pairs that lie along the field axis. This has significance for the theory of magnetic relaxation described above as it is mediated by movement of charge carriers.

Bramwell proposed adding a field-dependent term to the conductivity [74]. This approach has been shown to work extremely well in numerical simulations of the monopole conductivity in spin ice [61]. Beginning from the kinetic equation in equilibrium in a vacuum:

$$\frac{dx}{dt} = k_f(1 - x) - k_r x^2 \tag{4.9}$$

where k_f is the monopole formation rate, k_r is the monopole destruction rate and

x is the dimensionless monopole density. Initially we can simplify this by assuming $x \ll 1$ due to the low temperature to obtain

$$\frac{dx}{dt} = k_f - k_r x^2 \tag{4.10}$$

where the x^2 term remains due to the assumption $k_r \gg k_f$.

Bramwell introduces a linear wien effect on the formation rate k_f:

$$k_f = k_f^0(1+b) \tag{4.11}$$

an approximation of equation 1.114 valid for small b, where b is the Onsager factor [48]

$$b = \frac{Q^3|H|}{8\pi\mu_0 k_B^2 T^2}, \tag{4.12}$$

which is the magnetic equivalent of the electrical Onsager factor of equation 1.113 with substitutions $e \to Q$, $E \to H$ and $\epsilon_0\epsilon \to \mu_0\mu$ with $\mu = 1$.

Now if the equation is linearised with $x = x_0 + \Delta x$:

$$\frac{d\Delta x}{dt} = k_f^0 b - 2k_r x_0 \Delta x. \tag{4.13}$$

and write b as

$$b = \beta|H_a - aM|, \tag{4.14}$$

$$\beta = \frac{Q^3}{8\pi\mu_0 k_B^2 T^2}. \tag{4.15}$$

Using the substitution $m = M/M_0$ and the definition $b_0 = \beta H_a$ this can be simplified:

$$b = \frac{b_0}{H_a}|H_a - aM| = \frac{b_0}{H_a}\left|1 - \frac{a}{H_a}M\right| = \frac{b_0}{H_a}\left|1 - \frac{M}{M_0}\right|, \tag{4.16}$$

$$b = b_0|1 - m|, \tag{4.17}$$

recalling from Ryzhkin's magnetic current equation [3] that $H_a = aM_0$ with M_0 the equilibrium value of M.

At equilibrium under no field $dx/dt = 0$ and at equilibrium under field $d\Delta x/dt = 0$. Therefore

$$k_f = k_r x_0^2, \tag{4.18}$$

$$k_f^0 b = 2k_r x_0 \Delta x, \tag{4.19}$$

giving

$$\Delta x_0 = \frac{x_0 b}{2} \tag{4.20}$$

where Δx_0 is the maximum value of Δx reached at equilibrium. Now define

$$q = \Delta x / \Delta x_0.$$

This is a dimensionless measure of how close the magnetolyte is to saturation of additional Wien effect monopoles, and leads to

$$\Delta x = q\Delta x_0 = \frac{q x_0 b}{2}. \tag{4.21}$$

Now consider equation 4.3, Ryzhkin's magnetic current equation. If we consider that $\kappa = \kappa(x)$, a linear function, we can define

$$\kappa = \kappa_0(1 + \frac{\Delta x}{x_0}) = \kappa_0(1 + \frac{q b_0}{2}), \tag{4.22}$$

$$\frac{\partial M}{\partial t} = \kappa_0(1 + \frac{q b_0}{2})(H_a - aM). \tag{4.23}$$

If we make a final assumption that the Wien effect is instantaneous, so $q = 1$, we obtain

$$\frac{\partial M}{\partial t} = \kappa_0(1 + \frac{b}{2})(H_a - aM), \tag{4.24}$$

where $b = \beta|H_i| = \beta|H_a - aM|$, so using the substitutions $M_0 = H_a/a$, $m = M/M_0$, $\nu = a\kappa_0$ and $g = H_a\beta/2 = b_0/2$:

$$\frac{\partial m}{\partial t} = \frac{dM}{dt}\frac{1}{M_0} = \nu(1 + g(1 - m))(1 - m). \tag{4.25}$$

This can be solved under the boundary $m(0) = 0$ to yield

$$m(t) = 1 + \frac{1}{g - (1+g)e^{\nu t}}, \tag{4.26}$$

or with the offset boundary $m(0) = m_0$ to yield

$$m(t) = 1 + \frac{1}{g + \frac{1+g-m_0 g}{m_0 - 1} e^{\nu t}}. \tag{4.27}$$

A consequence of this addition is the appearance of an m^2 term in the expression 4.25.

4.3.2 Stretched Exponential

Revell *et al.* [5] reported that DTO magnetic relaxation proceeds as a stretched exponential with a slow long-time tail. On their own account this is surprising, as stretched exponentials are typically associated with disordered systems such as spin glasses. Spin glasses (see section 1.3) are characterised by disordered organisation and orientation of magnetic spins, induced by magnetic frustration and structural disorder. By contrast spin ices have ground state disorder in their spin configuration due to the large number of ice-rule compliant solutions, but ideally form a regular lattice with no structural disorder [13].

Their measurements took two forms: a direct-field quench at 5 mOe and a measurement of the imaginary susceptibility χ'' as a function of frequency, transformed into a time function via the fluctuation-dissipation theorem:

$$C(t) = \langle M(0)M(t)\rangle = 2kT \int_{-\infty}^{\infty} \frac{\chi''(\omega)}{\omega} cos(\omega t) d\omega. \tag{4.28}$$

Monte Carlo simulations reported in the same paper found that surface conditions could recreate the stretched exponential and the addition of spin-stuffing defects the long-time tail.

Their results are presented in figure 4.3, and an equivalent presentation of the Paulsen *et al.* [7] data in figure 4.4. It is important to note that the overlap between the two sets of data is limited. The Revell *et al.* [5] data ranges in temperature from 0.475 K to 1.1 K with most sets $>$ 0.65 K, while the three sample temperatures presented from the Paulsen *et al.* data range from 0.4 K to

0.6 K. Nevertheless the data sets demonstrate similar behaviour.

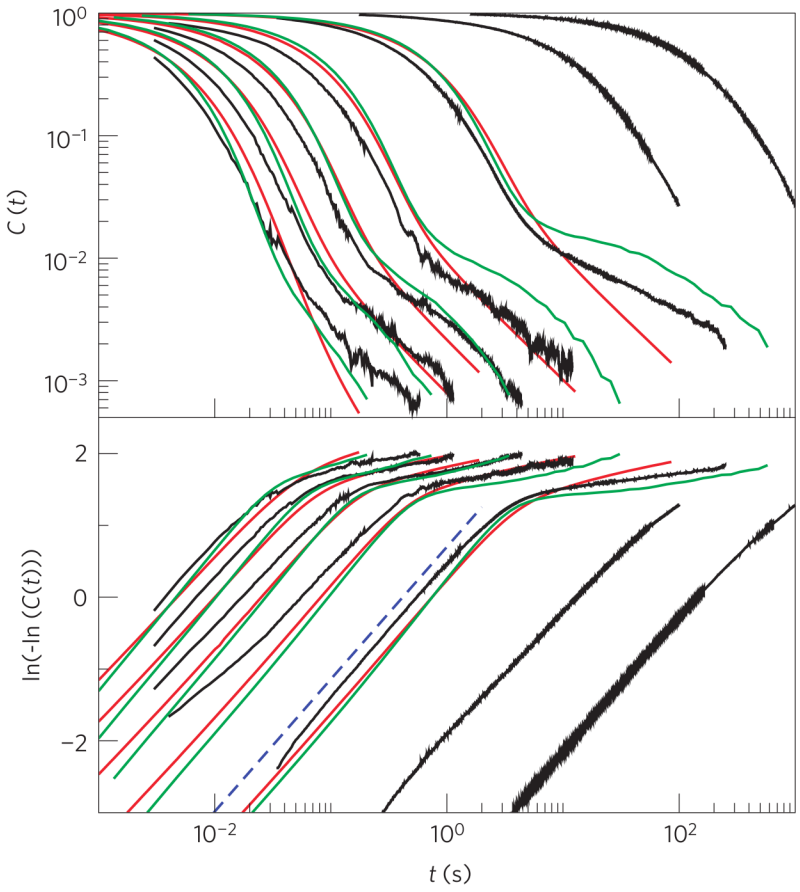

Figure 4.3: Black lines are direct-field quench measurements, red lines are determined from equation 4.28 and green lines are results of doped DSI simulations. From left to right, temperatures are 1.1 K, 1.0 K, 0.9 K, 0.8 K, 0.675 K, 0.55 K and 0.475 K. The blue dashed line represents a gradient of stretching factor $\beta = 0.8$. Reprinted by permission from Macmillan Publishers Ltd: Nature Physics (Revell *et al.* 2013 [5]), copyright 2013.

We see an initial exponential drop off in both, followed by long-time tails brought out by the logarithmic plot. The tails indicate a slowdown near saturation proposed by Revell *et al.* [5] to be caused by defect pinning, and this phenomenon will be considered in the second section. In this section the focus is on the development of the magnetisation before saturation is reached, the shape of which is unfortunately obscured by the logarithmic plot that highlights the long-time tail. It is this behaviour that is explained by Revell *et al.* using a stretched

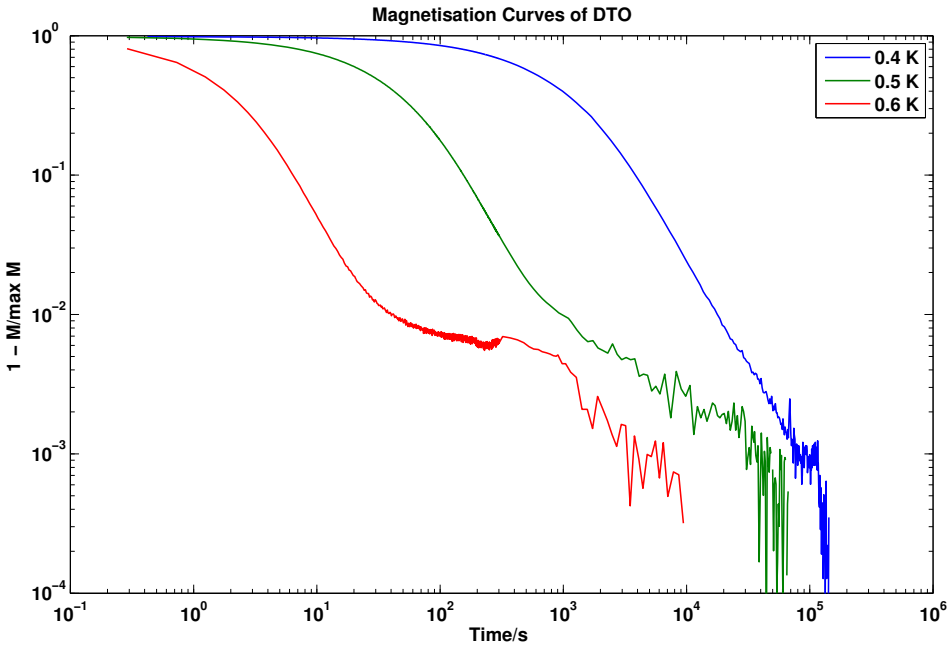

Figure 4.4: d.c. magnetisation curves of DTO at 400, 500 and 600 mK. Field strength 50 Oe. The long-time tail is clearly visible.

exponential.

An additional behaviour is visible in the Paulsen *et al.* data. After the long-time tail is established, a sharper drop-off reappears at even longer times, longer than those displayed on the Revell *et al.* data. However this is plausibly an illusion arising from the method used to invert the data to bring out the long-time tails. This method chooses the final point of the complete set of data as the reference value for the maximum magnetisation and as such the data will necessarily eventually collapse to a zero unplottable on logarithmic axes. As such the secondary drop-off is probably not significant.

As noted, data from two measurement methods are presented in the Revell *et al.* [5] figure, and in their figure it can be seen that the results in the pre-saturation region, though transformed onto equivalent axes and obscured by the logarithmic plot, differ significantly. The simulations in turn principally emulate the Fourier-transformed AC data rather than the directly measured data. The stretched exponential form displayed against the data is rendered plausible by the

work done depicted but has not been clearly tested against conventional magnetisation curves, and furthermore lacks a strong theoretical basis beyond the analogy between spin ices and spin glasses. As such it is here considered as one hypothesis among others.

Their expression is:

$$C(t) = \langle M(0)M(t)\rangle = e^{(-t/\tau)^{\beta}}. \tag{4.29}$$

A stretched exponential function in our notation with $m(0) = 0$ is:

$$m(t) = 1 - e^{-(\nu t)^{\beta}}, \tag{4.30}$$

or with $m(0) = m_0$:

$$m(t) = 1 - (1 - m_0)e^{-(\nu t)^{\beta}}. \tag{4.31}$$

As with the previous functions, the magnetisation was normalised with $m = M/M_{max}$ and ν was extracted from the data. This leaves one free parameter β, the stretching factor.

4.4 Comparison with Experiment

4.4.1 Fitting Multiparameter Theories to Experimental Data

Application of these theories to the data is not as straightforward as for the Ryzhkin [3] theory. The Ryzhkin theory had one parameter, ν, which could be taken from the data in a straightforward way. The new theories have two parameters internal to the theory, ν and either g or β, plus the offset parameter m_0 introduced to compensate for the low-temperature behaviour discussed above.

The best approach to take to the anomalous short-time offset m_0 depends on its origin. If it is a problem with the instrument that leads to the magnetisation value being incorrectly reported, then it should be dealt with by correcting this problem in the data itself. If it is a phenomenon in the sample of very fast or residual low-level magnetisation then the use of the m_0 limits above would be

appropriate, as it represents a real change in m, which produces a real change in the results according to the theories.

As the size of m_0 (in table 4.1) appears to vary with cooling method, which would affect the magnetic properties of the crystal via increased monopole population but not immediately obviously the instrument, my judgement is that a change in the theoretical limiting values is the most justified approach.

The remaining two values, ν and either g or β, can be collapsed into a single parameter by choosing the ν value to match the half-life of the data similarly to with the Ryzhkin model. This allows a single-variable fit to be performed assuming a known value of m_0, or a two-variable fit if m_0 is known.

The values for m_0 and ranges of values for β and g were determined by fitting over different ranges of the data. Originally, two-parameter fits were attempted over the entire curve, but several of these produced implausible negative values for m_0 to obtain marginal improvements in the curves nearer saturation.

The curves were divided into four sections, at 1/4, 1/2 and 3/4 of the maximum value of m. A two-variable fit of m_0 and g or β in the region $m < 1/4$ was performed for each temperature to determine a reference m_0, as the low-temperature region is most strongly dependent on the size of m_0. This value was used for single-variable fits over $0 < m < 1$ to produce the plots in figure 4.5. It was then used for fits in the region $m < 3/4$ and $1/4 < m$ to produce ranges for g and β.

Random error in the results is not large enough to be significant in this part of the investigation, though it creates manageable noise in section 4.5.

4.4.2 Results

In figure 4.5 the results of the complete range fits for the two improved models are compared against the conventionally cooled data from figure 4.1. Both are clear improvements over the plain expression, which is an expected result as they have an additional variable to fit.

In figure 4.6 residual plots highlight the differences more clearly. In each case the non-Ohmic conductivity model has a smaller maximum deviation from the experimental data than the stretched exponential. With the curves pinned to the data at the midpoint of the magnetisation process, the stretched exponential has

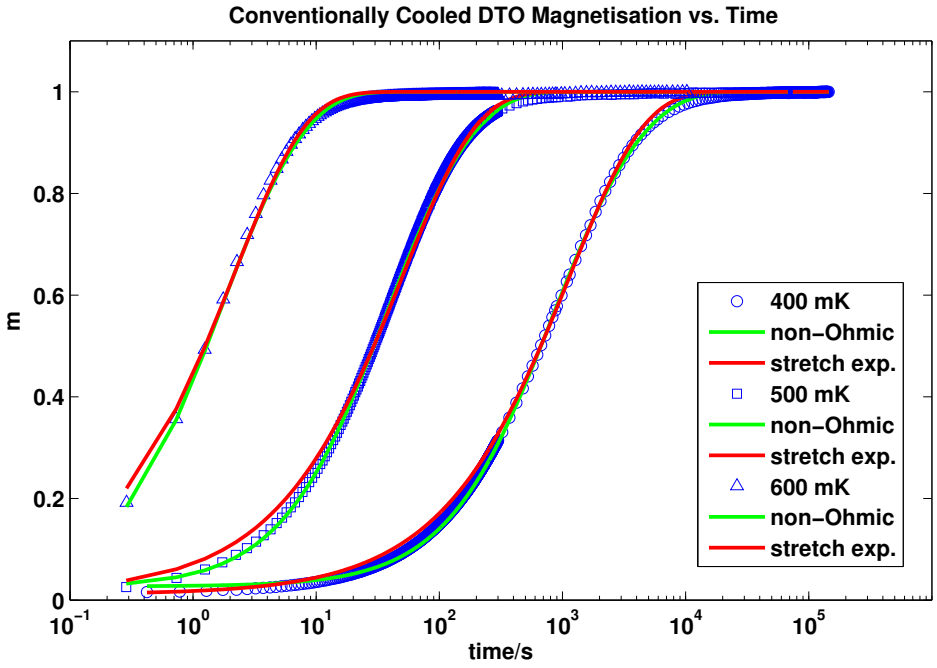

Figure 4.5: Conventionally cooled dysprosium titanate at 400 (blue circles), 500 (blue squares) and 600 mK (blue triangles), against respective linear non-Ohmic (green) and stretched exponential (red) curves for each temperature.

a tendency to overestimate the results and the non-Ohmic model to underestimate. In either case these tendencies could be removed by slight alterations to ν. Increases would have the effect of moving the curve left and the residual curve upwards, and decreases the opposite. However, this would be at the cost of accuracy in the central region.

Table 4.1 shows the parameter values for the fits. We see that β lies in the range $0.7 < \beta < 0.83$, consistent with the results of Revell *et al.* who found $0.7 < \beta < 0.8$. The g values range from $1.9 < g < 6.3$. However, the expression for the Onsager parameter (equation 4.12) predicts $g = 0.64$ at 0.4 K, $g = 0.41$ at 0.5 K, and $g = 0.28$ at 0.6 K. This is a difference of an order of magnitude and cannot be explained by appealing to uncertainty in the theory.

A solution is suggested by the work of Pomaranski *et al.* [66], who found that the thermal relaxation time of DTO is expected to be extremely long at low temperatures, more than 10^4 seconds below 1 K and with a runaway below 0.45 K. If this is caused by the monopole destruction rate becoming very slow

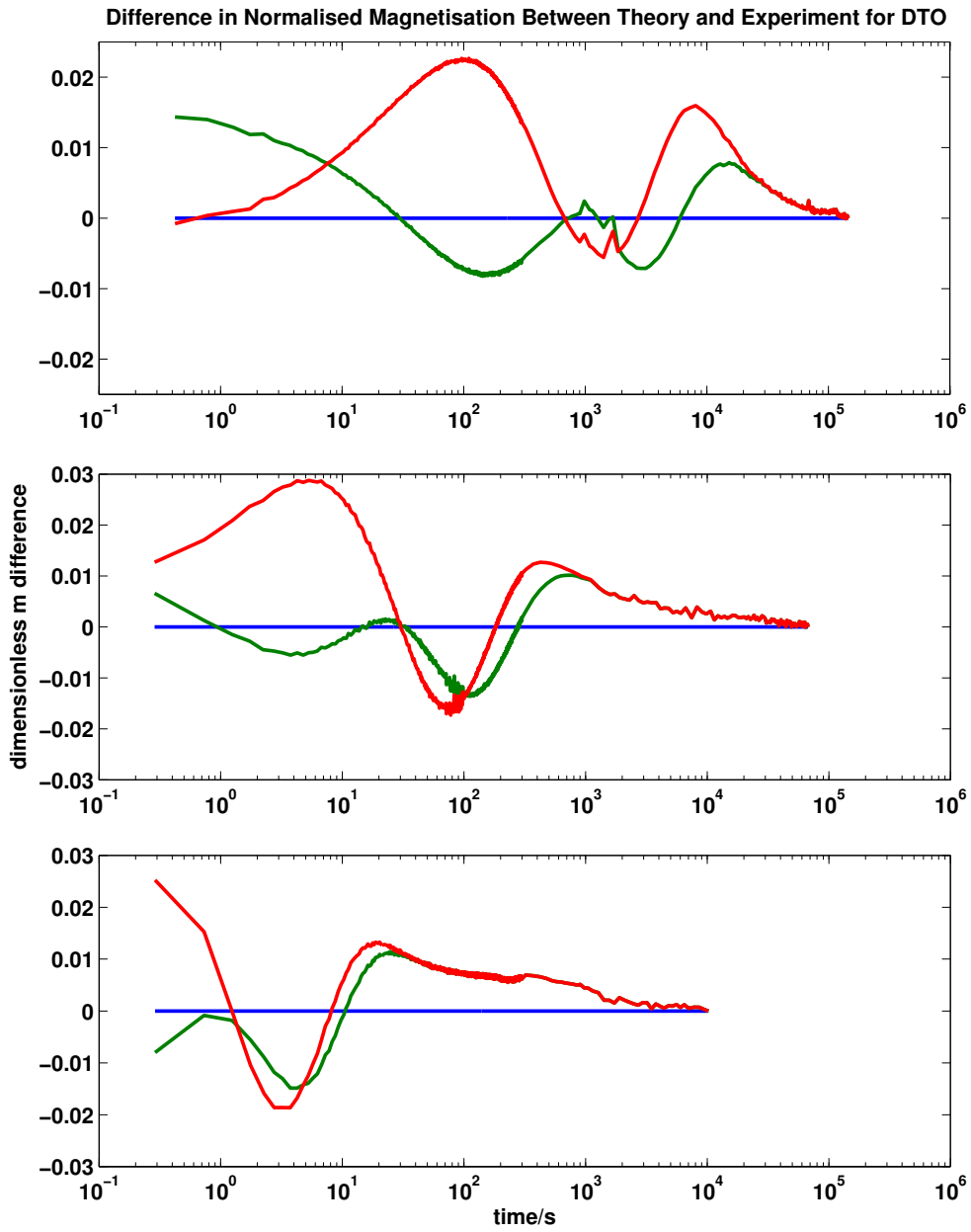

Figure 4.6: Difference between m values for the conventionally cooled experimental data (blue reference line) and linear non-Ohmic (green) and stretched exponential (red) best fits at 400 (upper), 500 (middle) and 600 mK (lower).

Table 4.1: DTO Relaxation Model Parameters (variable temperature)

Temperature	m_0	param.	low fit	high fit	full range
400 mK(cc)	0.0269	ν	1.86×10^{-4}	2.39×10^{-4}	2.37×10^{-4}
		g	6.3	4.6	4.6
500 mK(cc)	0.0241	ν	8.2×10^{-3}	6.4×10^{-3}	6.4×10^{-3}
		g	2.6	3.7	3.7
600 mK(cc)	0.0243	ν	2.2×10^{-1}	1.7×10^{-1}	1.7×10^{-1}
		g	1.9	2.9	2.9
400 mK(aq)	0.0376	ν	3.24×10^{-4}	2.9×10^{-4}	2.9×10^{-4}
		g	8.3	9.4	9.4
500 mK(aq)	0.0503	ν	1.03×10^{-2}	1.03×10^{-2}	1.03×10^{-2}
		g	2.4	2.4	2.4
600 mK(aq)	0.0601	ν	2.74×10^{-1}	2.72×10^{-1}	2.71×10^{-1}
		g	1.4	1.4	1.5

Temperature	m_0	param.	low fit	high fit	full range
400 mK(cc)	0.0114	ν	9.03×10^{-4}	8.71×10^{-4}	8.77×10^{-4}
		β	0.76	0.71	0.71
500 mK(cc)	0.0148	ν	2.08×10^{-2}	1.97×10^{-2}	1.99×10^{-2}
		β	0.79	0.71	0.72
600 mK(cc)	0.0218	ν	4.81×10^{-1}	4.57×10^{-1}	4.56×10^{-1}
		β	0.83	0.74	0.74
400 mK(aq)	0.0201	ν	1.9×10^{-3}	1.8×10^{-3}	1.8×10^{-3}
		β	0.72	0.65	0.66
500 mK(aq)	0.0318	ν	2.53×10^{-2}	2.45×10^{-2}	2.46×10^{-2}
		β	0.79	0.74	0.75
600 mK(aq)	0.0371	ν	5.14×10^{-1}	5.07×10^{-1}	5.07×10^{-1}
		β	0.82	0.79	0.79

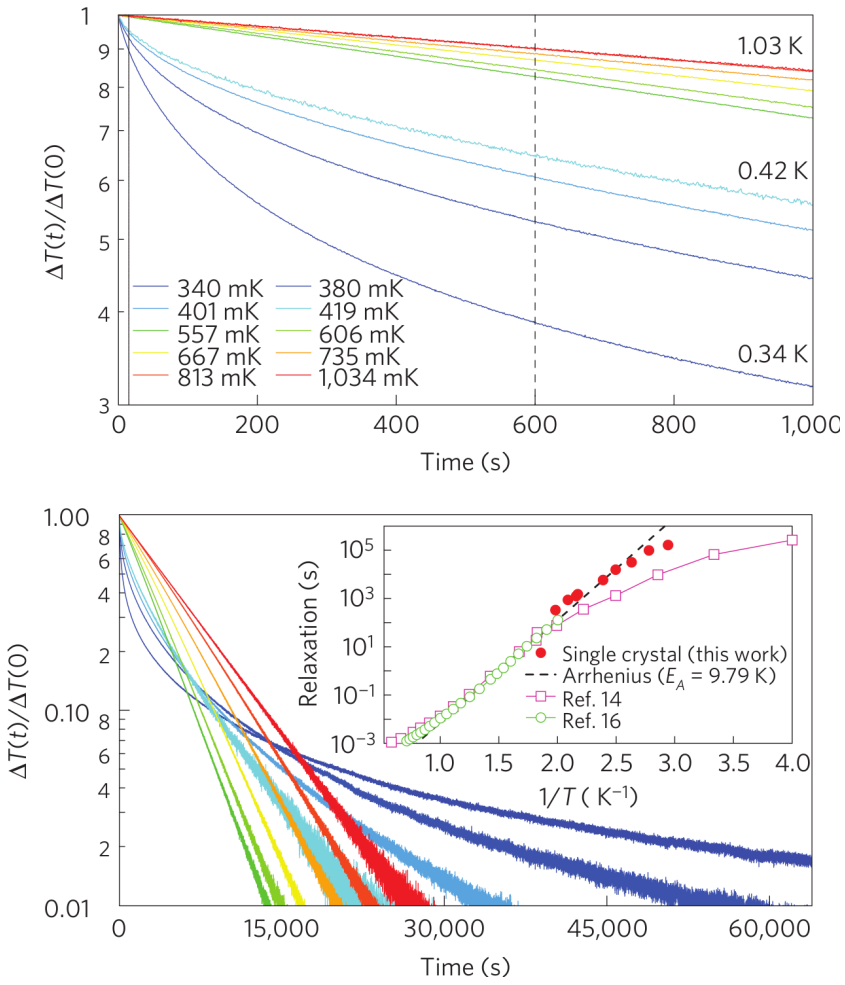

Figure 4.7: Normalised thermal relaxation versus time at stated nominal temperatures for a single $Dy_2Ti_2O_7$ crystal. Reprinted by permission from Macmillan Publishers Ltd: Nature Physics (Pomaranski *et al.* 2013 [66]), copyright 2013.

at low temperatures, due to low monopole population decreasing the likelihood of encountering a counterpart to annihilate with, spin freezing, monopole pinning or other factors, then an excess population of monopoles may persist to the start of experimental time at $t = 0$. Figure 4.7 is reproduced from Pomaranski *et al.* [66] and demonstrates the long thermal relaxation times.

The effect of these long relaxation times would be an excess population of monopoles at $t = 0$, which may be larger than the additional population introduced by the second Wien effect. When interpreted through the linear Wien effect model, this will lead to a very large apparent value for the Onsager parameter g.

It is possible to approach the description of the magnetisation directly from the assumption of an excess initial monopole concentration rather than through the Wien effect. This approach will be studied preliminarily in section 4.5.5 below.

4.4.3 Avalanche Quenching

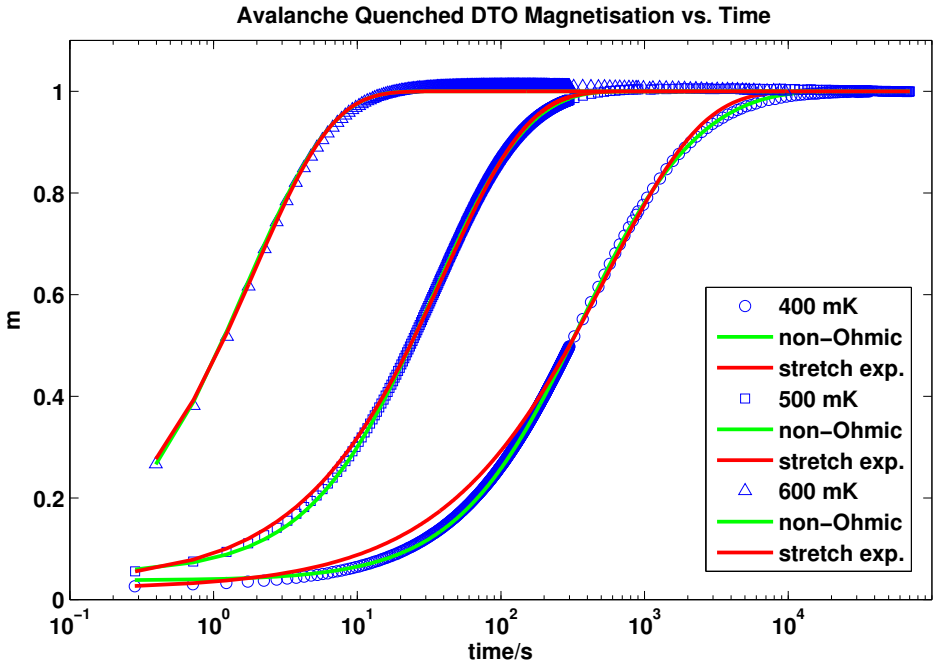

Figure 4.8: 'Avalanche quenched' dysprosium titanate at 400 (blue circles), 500 (blue squares) and 600 mK (blue triangles), against respective square magnetisation (green) and stretched exponential (red) curves for each temperature.

In figure 4.8 the results for the avalanche quenched data are displayed. The results are similarly superior to the Ryzhkin model as in the conventionally cooled data. At 400 mK the non-Ohmic model is superior except at the earliest times, but for 500 and 600 mK the difference is less pronounced. This is made clear in the residual plots in figure 4.9.

Of note in the avalanche quenched data is the magnetisation overshoot. Near saturation m reaches values greater than 1, then decays to the terminal value. Paulsen *et al.* [7] suggest that the avalanche quench places the crystal out of equilibrium such that it explores states with oscillatory behaviour. When interpreting

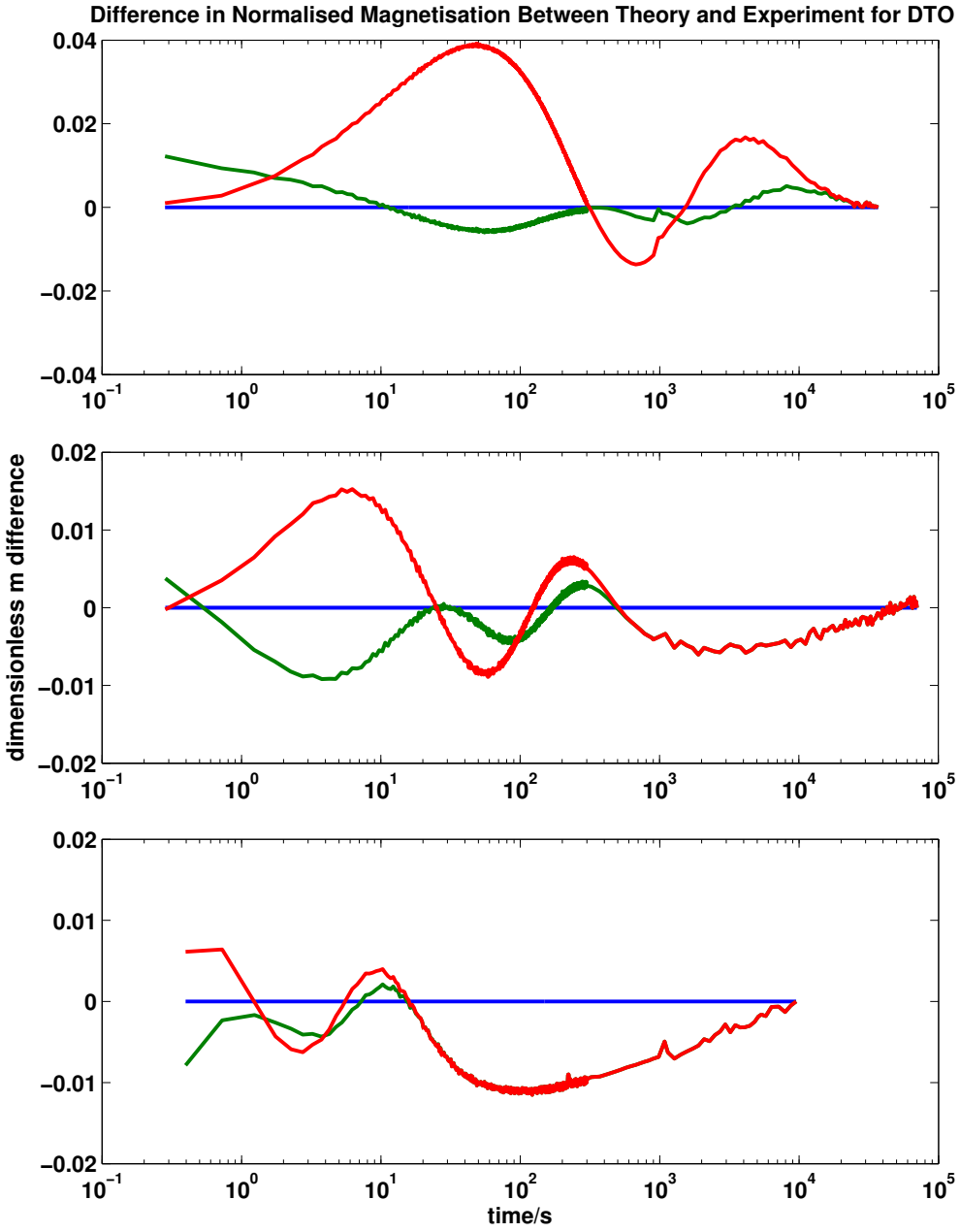

Figure 4.9: Difference between m values for the avalanche quenched experimental data (blue reference line) and linear non-Ohmic (green) and stretched exponential (red) best fits at 400 (upper), 500 (middle) and 600 mK (lower).

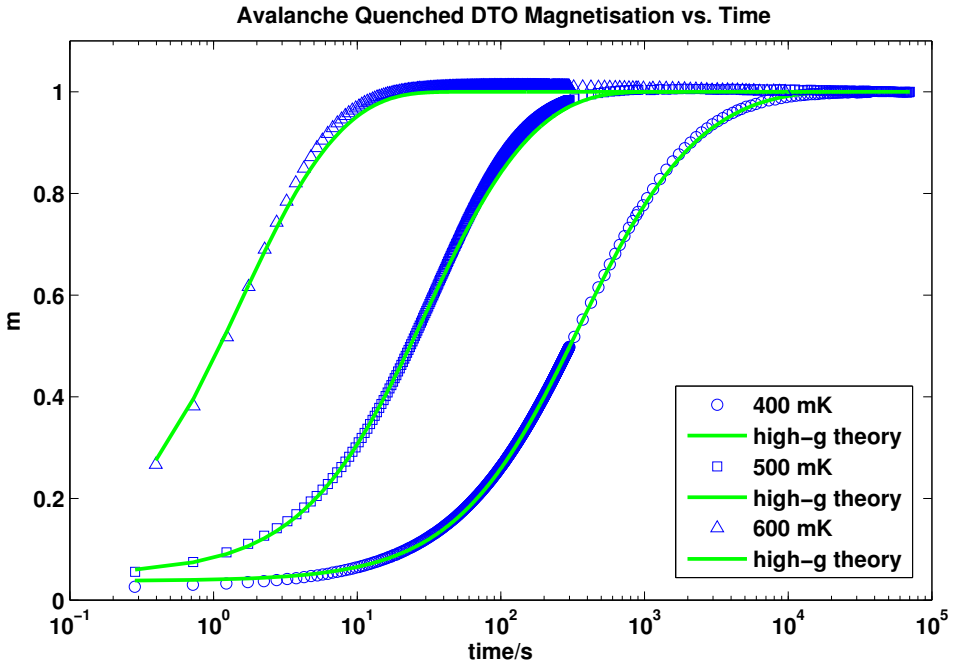

Figure 4.10: 'Avalanche quenched' dysprosium titanate at 400 (blue circles), 500 (blue squares) and 600 mK (blue triangles), against respective square magnetisation (green) curves, using conductivity (ν) values from the conventionally cooled data in table 4.1, with g = 12.3, 5, 3.6 respectively.

magnetisation and residual plots for avalanche data, one should bear the existence of the overshoot in mind.

If we look at the parameter results in table 4.1 we see the results for 500 and 600 mK are not what would be expected given our conclusions from studying the conventionally cooled data. The avalanche quenched 400 mK result for g is substantially increased from its conventionally cooled counterpart, but that of the other avalanche quenched values is reduced. As avalanche quenching increases monopole overpopulation, we should expect all g values to be increased.

Light is shed on this difficulty by considering the ν values. In theory ν is proportional to monopole density x absent the Wien effect or overpopulation, while g captures the time-dependent increase in these quantities (in effect, time-dependent increase in ν). If the only difference between the data at a given temperature is increased monopole concentration from rapid cooling, then their ν values should be identical and the g values should increase to account for the overpopulation.

However, in all three cases the ν values change from the original. To match the curve shape, the fits partially capture the monopole population increase with the ν value and then apply a smaller g value.

It is possible to use an alternative method: take ν values from the standard fits in each conventionally cooled case and increase g to obtain a good fit. In figure 4.10 the νs for 400, 500 and 600 mK are fitted with $g = 12.3$, 5 and 3.6 respectively. These values successfully approximate the curves, but with decreasing success as T increases. The fits yielded by the procedure are inferior to those generated by a free fit and the values themselves lie outside the estimated error range. Either the linear non-Ohmic model fails to describe the shape of the curve properly, or it fails to return parameter values that make sense in its own terms. Alternatively, the non-equilibrium behaviour that creates the magnetisation overshoot at these temperatures also alters the behaviour of the magnetisation before saturation.

Of the two improved models the linear non-Ohmic conductivity model has clearer microscopic foundations, but comparing the results across the conventional and classic cooled models demonstrates that either the model or our understanding of its meaning is insufficient.

More light will be shed on this by considering the data from another perspective.

4.5 Effective Conductivity and Monopole Population

Take equation 4.4, the normalised magnetic current equation:

$$\frac{dm}{dt} = \nu(1 - m),$$

where ν is the altered conductivity $a\kappa$. This can be rearranged to yield

$$\frac{dm/dt}{1 - m} = \nu,$$

which gives conductivity ν as an experimental variable, given $m(t)$ measurements [74]. In Ryzhkin's model ν has no dependence on time, but in the next section

it will immediately become clear that the quantity $(dm/dt)/(1-m)$ does change with time. The two improved theories that better capture the m vs. t behaviour produce different results for this quantity, so it is convenient to define:

$$\frac{dm/dt}{1-m} \equiv \tilde{\nu}$$

and call $\tilde{\nu}$ the 'effective conductivity'.

4.5.1 Avalanche Quenching and Conventional Cooling

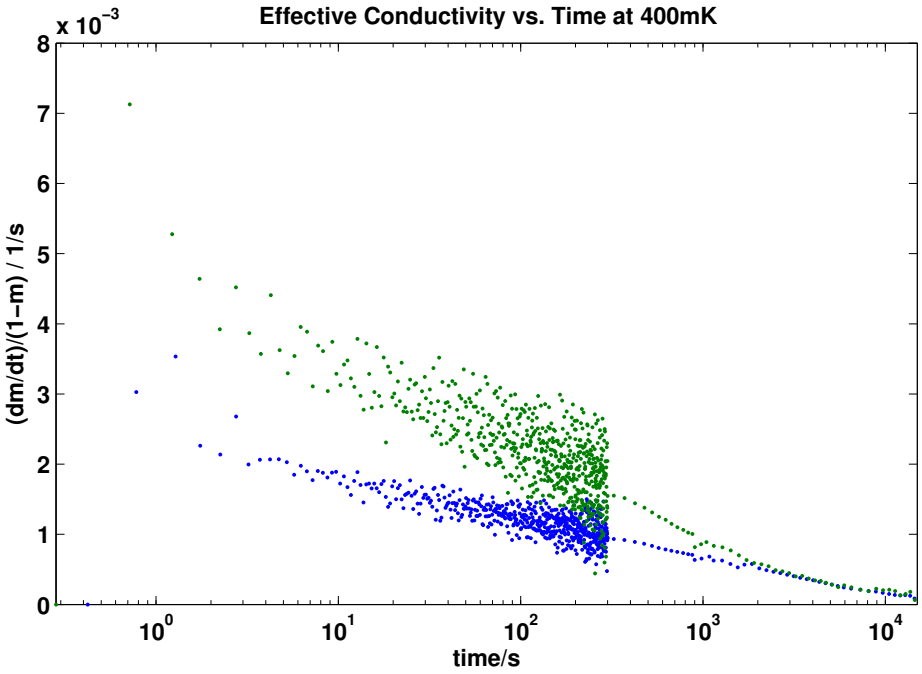

Figure 4.11: Effective conductivity $\tilde{\nu} = (dm/dt)/(1-m)$ for conventionally cooled (blue) and avalanche quenched (green) DTO versus t at 400 mK.

Assuming the conductivity is not otherwise affected by the choice of cooling process, examining the $\tilde{\nu}$ plots can reveal the effects of each process on the monopole population.

In figures 4.11, 4.11 and 4.13 the avalanche quenched and conventional cooled data for each temperature is displayed. The data is chaotic in regions where density of points relative to magnetisation rate is high enough that experimental

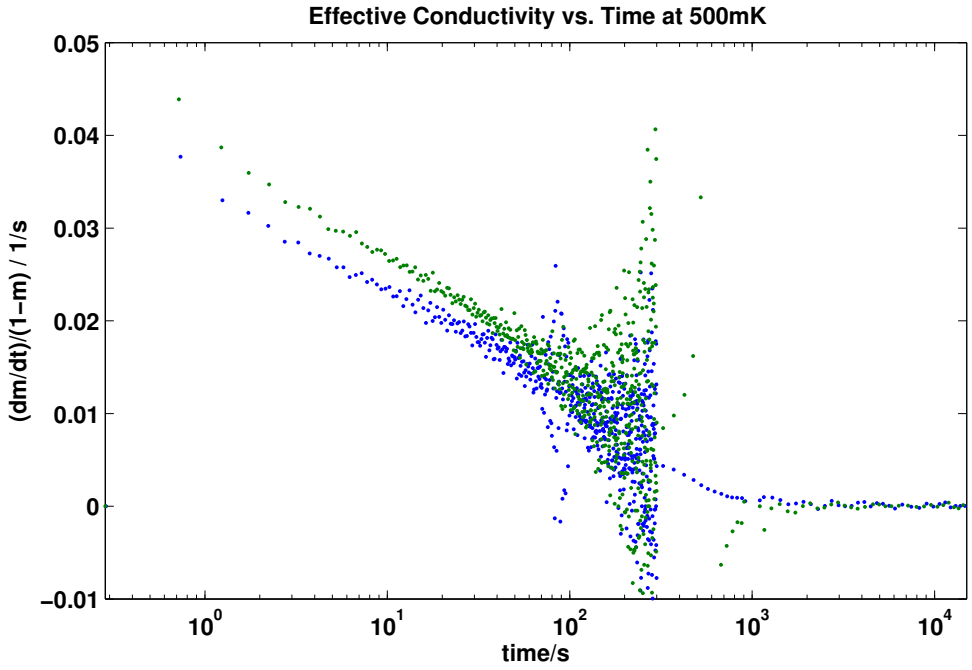

Figure 4.12: Effective conductivity $\tilde{\nu} = (dm/dt)/(1-m)$ for conventionally cooled (blue) and avalanche quenched (green) DTO versus t at 500 mK.

error, negligible above, causes significant changes in dm/dt. Additionally, at 500 and 600 mK the magnetisation overshoot causes $1-m$ to pass through zero, which creates a discontinuity in $\tilde{\nu}$. However, the behaviour of the effective conductivity is still easily perceptible outside these regions.

In each case the avalanche quenched data yields a higher $\tilde{\nu}$ than the conventional data. At 400 mK the difference is pronounced, but at 500 mK and 600 mK it is significantly attenuated. If we take ν and hence $\tilde{\nu}$ to be linear in x, this is consistent with the theory that spin ice takes a long time to equilibrate and so rapid cooling will leave it far from equilibrium with a high monopole population. Under this theory the greater difference between $\tilde{\nu}$ values at lower temperatures arises from the lower equilibrium value at the target temperature. The system converges towards the equilibrium value faster the further above equilibrium it is due to monopole recombination overcoming monopole creation processes, as pictured

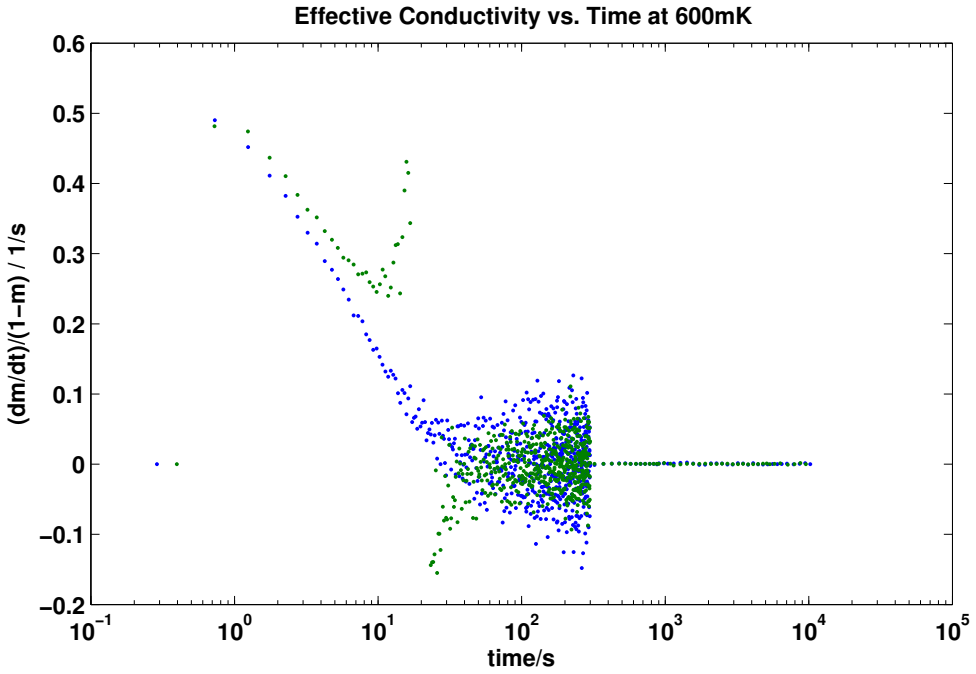

Figure 4.13: Effective conductivity $\tilde{\nu} = (dm/dt)/(1-m)$ for conventionally cooled (blue) and avalanche quenched (green) DTO versus t at 600 mK.

by the kinetic equation for the system:

$$\frac{dx}{dt} = k_f(1-x) - k_r x^2.$$

in which x is the monopole population proportion, k_f is the rate of monopole formation acting on $1-x$ free sites, and k_r is the monopole recombination rate proportional to the square of the population. As such the lower the target temperature for cooling, the more dramatic the difference will be between fast and slow cooling processes.

$\tilde{\nu}$ and so implicitly x both decrease over time, indicating that the monopole population is not in equilibrium. There are two factors in the above discussion which can produce this effect: the second Wien effect and the failure to equilibrate on experimental timescales. Either case will produce an overpopulation of monopoles at $t = 0$ which will then be reduced by recombination. A third factor is reported by Kaiser *et al.* [61]. They report that under fields, the equilibrium monopole population of a magnetolyte drops. Their expression is:

$$x(H) = x(0)\left(1 - \frac{2}{3}\left(\frac{\mu_0 \mu H}{k_B T}\right)\right). \tag{4.32}$$

This yields $x(H)/x(0)$ ratios of 0.27 at 400 mK, 0.53 at 500 mK, and 0.67 at 600 mK, suggesting a significant role for this effect here. In the real system we might expect there to be an overpopulation of monopoles arising from failed equilibration combined with an additional overpopulation arising from the Wien effect, which then declines to a lower equilibrium point established by the field.

An objection can be raised here that the increase in population arising from the second Wien effect should be permanent, as increasing the formation rate k_f will increase the equilibrium monopole population x_e. This neglects the importance of the reaction field. The reaction field as described by Ryzhkin [3] is a geometric polarisation of the spin network, and inhibits field-driven monopole formation in the same way it inhibits DC currents. Monopole pairs are formed by spin flips, and as the population of spins that can be flipped in the direction of the field diminishes, further polarisation becomes entropically disfavoured. The effect of the reaction field in eliminating the increase in k_f is realised in the additional $(1 - m)$ term that multiplies g in equation 4.25.

The assumption that the size of $\tilde{\nu}$ is linearly proportional to x at a given temperature also allows testing of the theory that there are mechanisms beyond insufficient sample equilibration involved in the magnetic relaxation behaviour of spin ice. At higher temperatures the monopole population will relax to equilibrium faster, and if sufficiently fast this would eliminate the non-equilibrium contribution to monopole population, leaving only the Wien effect and whatever other effects are involved. The possibility of this is presaged by the reduction of g with increasing temperature.

This is in fact what the data reveals, as can be seen in the 500 and 600 mK plots in figures 4.12 and 4.13. In these plots the avalanche quenched and classic cooled data are proportionally closer to one another than in the 400 mK, suggesting that the effect of rapid cooling is reduced and their behaviour is closer to equilibrium. Therefore at these temperatures the effect of experimental overpopulation is not very large and overpopulation is dominated by other factors.

However, even though overpopulation is of reduced importance at these tem-

peratures, g (see table 4.1) is still much larger than expected from the Wien effect, as discussed in section 4.4.2. This indicates that there are other factors affecting monopole population or movement, and supports a significant role for magnetic reduction of x_e and the surface effects discussed by Revell *et al.* [5].

An incidental implication of this result about overpopulation is that it demonstrates that the magnetisation overshoot discussed above cannot be the result of excessive population alone, but must be due to some other consequence of the avalanche quenching process, or another phenomenon.

4.5.2 Linear Non-Ohmic Model

Ryzhkin's simple model (of [3]) is an insufficient model for spin ice, but a similar transformation can be performed with the linear non-Ohmic model and the stretched exponential model.

From equation 4.25:

$$\frac{\partial m}{\partial t} = \nu(1 + g(1 - m))(1 - m),$$

$$\frac{dm/dt}{1 - m} = \tilde{\nu} = \nu(1 + g(1 - m)). \tag{4.33}$$

This describes the alteration of the conductivity from an initially increased level represented by the g factor as it reduces to a normal level with the saturation of m. Now take the expression for $m(t)$ in this model, using the non-offset form for simplicity as the offset does not enter into the expressions here in a significant way:

$$m(t) = 1 + \frac{1}{g - (1 + g)e^{\nu t}}. \tag{4.34}$$

From this one can derive:

$$\frac{dm/dt}{1 - m} = \tilde{\nu} = \nu \left(1 + \frac{1}{e^{\nu t}(1 + 1/g) - 1}\right). \tag{4.35}$$

An expression for $\tilde{\nu}$ in g, ν and t that can be tested directly using values derived from above fits.

It is also possible to determine the value of g from the limiting values of N. Take the following limits:

$$\tilde{\nu}(0) = \nu\left(1 + \frac{1}{(1+1/g)-1}\right) = \nu(1+g) = \tilde{\nu}_0,$$

$$\tilde{\nu}(\infty) = \nu\left(1 + \frac{1}{\infty(1+1/g)-1}\right) = \nu = \tilde{\nu}_e,$$

and obtain

$$g = \frac{\tilde{\nu}_0}{\tilde{\nu}_e} - 1, \tag{4.36}$$

i.e. if $\tilde{\nu}$ is a linear function of x, the value of g is determined by the ratio of x_0, the monopole population at $t = 0$, to x_e, the monopole population in equilibrium at that temperature in field.

4.5.3 Stretched Exponential Model

An expression for $\tilde{\nu}$ can also be obtained from the stretched exponential. By deriving from equation 4.30 the stretched exponential equation:

$$m(t) = 1 - e^{-(\nu t)^\beta},$$

$$\frac{dm}{dt} = \nu\beta(\nu t)^{\beta-1}e^{-(\nu t)^\beta} = \nu\beta(\nu t)^{\beta-1}(1-m), \tag{4.37}$$

$$\tilde{\nu} = \frac{dm/dt}{1-m} = \nu\beta(\nu t)^{\beta-1}. \tag{4.38}$$

We see that the stretched exponential introduces an effective $(\nu t)^{\beta-1}$ factor to the conductivity. If $\beta = 1$ then this is 1 and there is no change from the plain Ryzhkin model. If $\beta < 1$, then the conductivity changes according to a negative power law that passes through the plain model at $t = 1/\nu = \tau$, the relaxation time in Revell *et al.*'s paper [5].

While this has a similar effect to the non-Ohmic model in increasing and then diminishing the conductivity, it does not have an immediately obvious microscopic

interpretation.

4.5.4 Comparison with Experiment

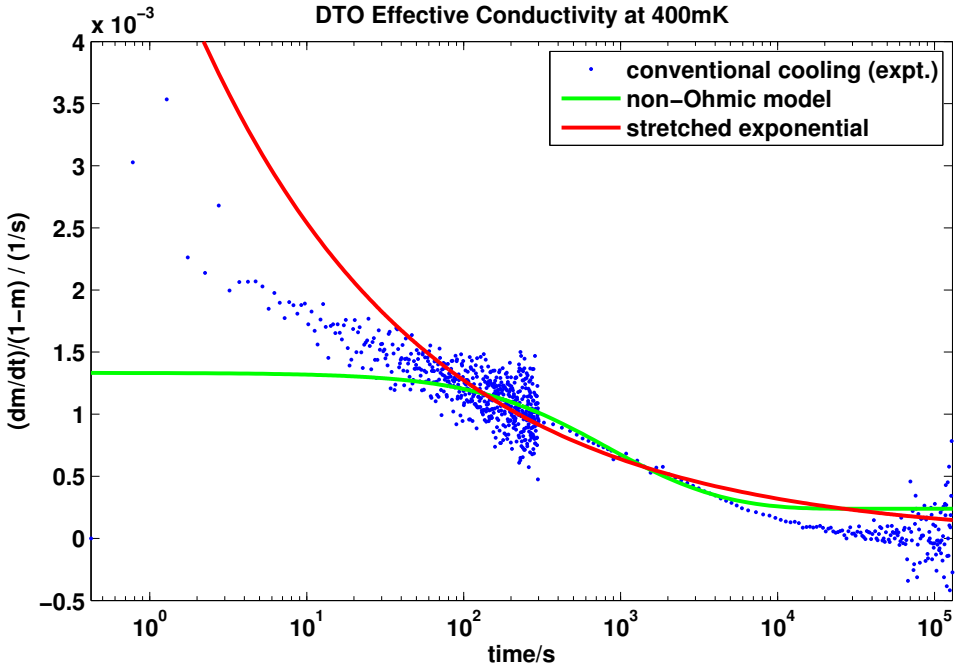

Figure 4.14: Effective conductivity $\tilde{\nu} = (dm/dt)/(1-m)$ versus t for DTO at 400 mK (blue dots), with theoretical predictions by linear non-Ohmic (green line) and stretched exponential (red line) models.

In figure 4.14 the results of these two methods are compared to results from the conventionally cooled magnetisation data at 400 mK. The conventionally cooled data are used for comparison to avoid the difficulties created by the $m > 1$ anomaly in the avalanche quenched data. The figures derived from full fits of the m vs. t data in table 1 were used to provide parameters.

We see that both models provide a good estimate of $\tilde{\nu}$ in the intermediate region of the decline in $\tilde{\nu}$ corresponding in time to the most rapid increase in m. However outside of this region they fail.

In the early time period the two models bifurcate. The stretched exponential experiences an upward runaway to infinity while the non-Ohmic model becomes flat as it approaches its limiting $\tilde{\nu}_0$ value.

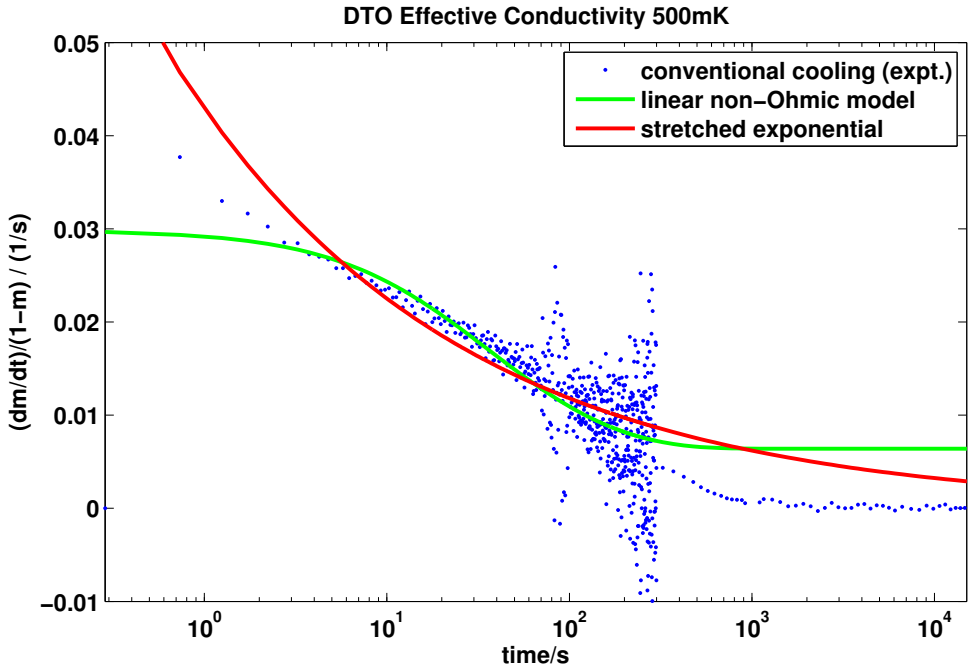

Figure 4.15: Effective conductivity $\tilde{\nu} = (dm/dt)/(1-m)$ versus t for DTO at 500 mK (blue dots), with theoretical predictions by linear non-Ohmic (green line) and stretched exponential (red line) models.

In the late time period both models fail to approach a low enough value of $\tilde{\nu}$. The stretched exponential continues its power-law decline while the non-Ohmic model approaches its limiting value of ν, representing the total extinguishing of the monopole superpopulation, but the experimental data falls off more rapidly than the stretched exponential to a level orders of magnitude smaller than the limiting value ν. This is the 'long-time tail' observed in the Revell *et al.* [5] measurements, caused by a reduction of dm/dt compared to the value it should have relative to $(1-m)$ in the above theories.

The explanation proposed by Revell *et al.* [5] is defect pinning. If an imperfection in the DTO crystal creates a lattice site which hosts monopoles at a lower energy than surrounding normal sites, a monopole that enters them will find itself surrounded by potential barriers and, as monopoles cannot be destroyed except by annihilation with opposite-charge poles, will remain there until thermally agitated out or so annihilated. In their paper Revell *et al.* [5] report that simulations of spin ice stuffed with additional Dy^{3+} spins reproduce the long-time tail.

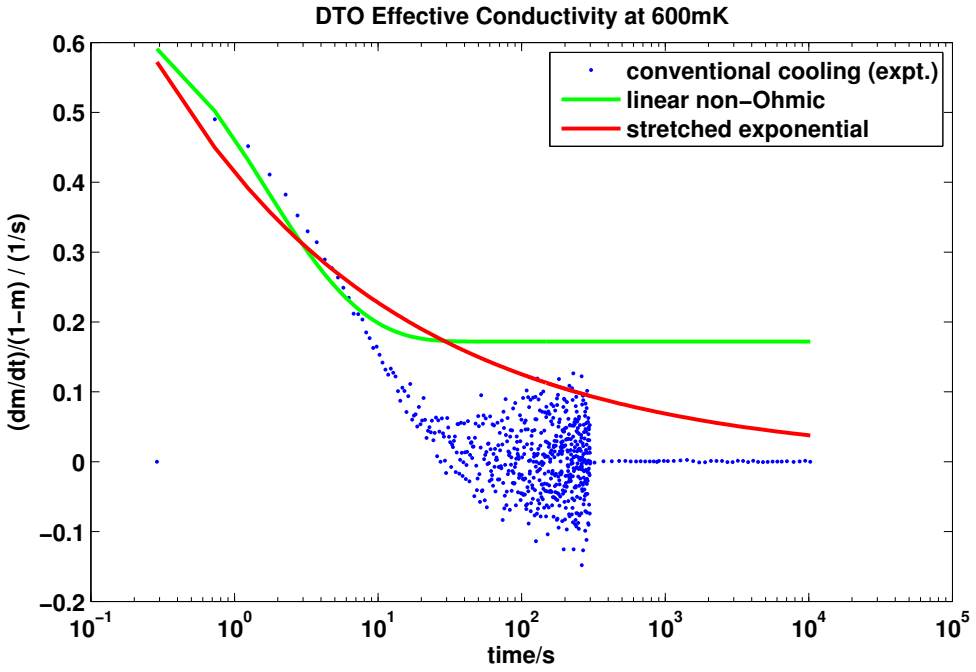

Figure 4.16: Effective conductivity $\tilde{\nu} = (dm/dt)/(1-m)$ versus t for DTO at 600 mK (blue dots), with theoretical predictions by linear non-Ohmic (green line) and stretched exponential (red line) models.

This effect manifests as a reduction of the mobility, and is much more pronounced near saturation than in the period of rapid magnetisation change. When the sample has not yet polarised, a large population of monopoles will be available to conduct magnetic current. As the magnetisation approaches saturation, the monopoles trapped in defects and unable to contribute to the polarisation of the network become proportionally more important in the already mostly polarised sample.

The pinning effect is also visible on close examination of the m vs. t plots. In figure 4.5, there is a slight overshoot of both models at all temperatures when m is near 1. It is this behaviour that is blown up and made visible in the logarithmic plot of figure 4.4 and the $\tilde{\nu}$ plots of figures 4.14, 4.15 and 4.16.

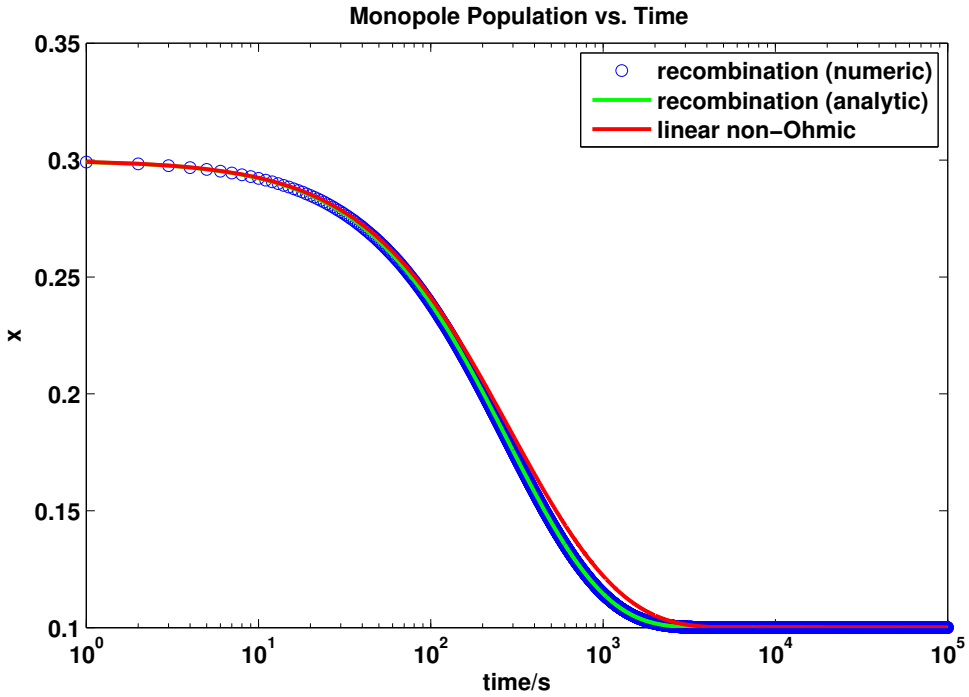

Figure 4.17: Numerical (blue circles) and real-analytic (green line) predictions for x in the recombination model, with $x_0 = 0.3$, $x_e = 0.1$, $k_r = 0.01$. The red line is the non-Ohmic model under appropriate parameters to replicate the boundary conditions.

4.5.5 The Recombination Model and Monopole Superpopulation

As noted in section 4.4.2, the system can be approached directly from the notion of recombination from overpopulation. Bramwell [74] developed this approach as follows: The kinetic equation for x is:

$$\frac{dx}{dt} = k_f(1 - x) - k_r x^2, \tag{4.39}$$

where k_f is the monopole formation rate, k_r is the monopole destruction rate and x is the dimensionless monopole density.

Under the conditions $x << 1$ and $k_f << k_r$, this can be approximated to:

$$\frac{dx}{dt} = k_f - k_r x^2. \tag{4.40}$$

At equilibrium $x = x_e$ and $dx/dr = 0$, so:

$$k_f = k_r x_e^2, \tag{4.41}$$

$$x_e^2 = \frac{k_f}{k_r} = k_e, \tag{4.42}$$

$$\frac{dx}{dt} = k_r[k_e - x^2], \tag{4.43}$$

where k_r is a rate with dimension $1/t$ and can be set to determine the unit of time. This can be solved with the boundaries $x(0) = x_0$ and $x(\infty) = x_e$ to yield:

$$x(t) = x_e \tanh\left[x_e k_r t + \tanh^{-1}\left(\frac{x_0}{x_e}\right)\right], \tag{4.44}$$

which, through equation 4.5, can be used to determine m as $\nu = \nu(x)$.

Equation 4.44 returns complex values for x if $x_0 > x_e$, which is the case in the systems being considered here. However under the assumption that the real part of the expression is the real quantity represented by x, it can be shown that this quantity gives the same result as a numerical solution of equation 4.43.

In figure 4.17 the results of plotting together the analytic solution, the numerical solution, and a non-Ohmic model with appropriate parameters to replicate the boundary conditions. The curves for the numerical and analytic solutions are identical, demonstrating that the real part of the analytic solution of equation 4.44 is a valid measure of x as predicted by recombination kinetics. The curve for the non-Ohmic model is similar but not identical, suggesting that a fully developed overpopulation model could refine the predictions of that model. However, as the Wien effect still exists in spin ice [61], a complete model would still have to account for the Onsager factor.

4.6 Magnetisation Behaviour Change with Field

More light can be shed by considering data taken at multiple fields. O. Petrenko [92] has supplied measurements of DTO in several fields at 500 mK. The DTO crystal was of yellow colour.

In figures 4.18 and 4.19 the data is plotted as M/H_a vs. t. Two features

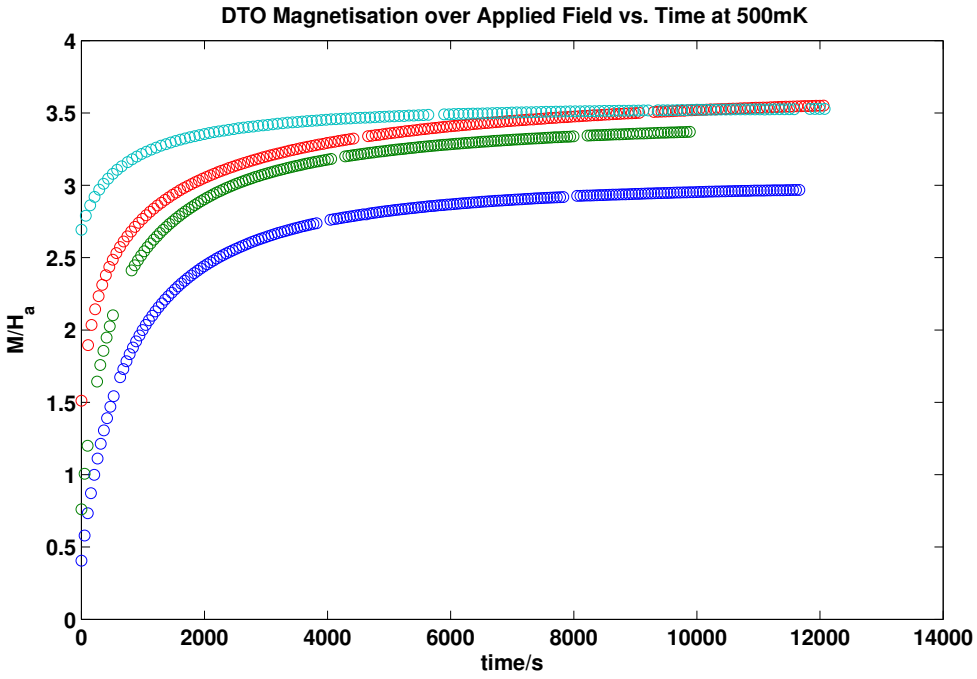

Figure 4.18: M/H_a vs. t curves for DTO at 0.01 (blue), 0.025 (green), 0.1 (red) and 0.25 T (teal).

are immediately clear: first, that the magnetisation does not saturate on the experimental timescale, and second, that the recorded magnetisations have large y intercepts, indicating a late start to the experimental clock. Visible in figure 4.19 is that the 0.1 T data is particularly far from saturation.

The former presents a problem for generation of $m = M/M_{max}$, which can be addressed by using a range of estimates of the discrepancy to produce a range of fitted values. The latter is a more extreme form of the m_0 offset considered above and can be addressed with the same techniques, with greater ease as there are explicit zero time values given for the magnetisation, removing the need to attempt to determine m_0 from curve fitting or other means of estimation.

In figure 4.20 the curves for 0.01, 0.025, 0.1 and 0.25 T are presented with non-Ohmic and stretched exponential fits. Notable is that the 0.1 T data has a worse fit in the upper half, was rejected as too far from saturation to be safely analysable. In table 4.2 parameter values are presented. As the curves are incomplete a segmented fitting procedure as was done for the Paulsen *et al.* [7] data is impractical. Instead

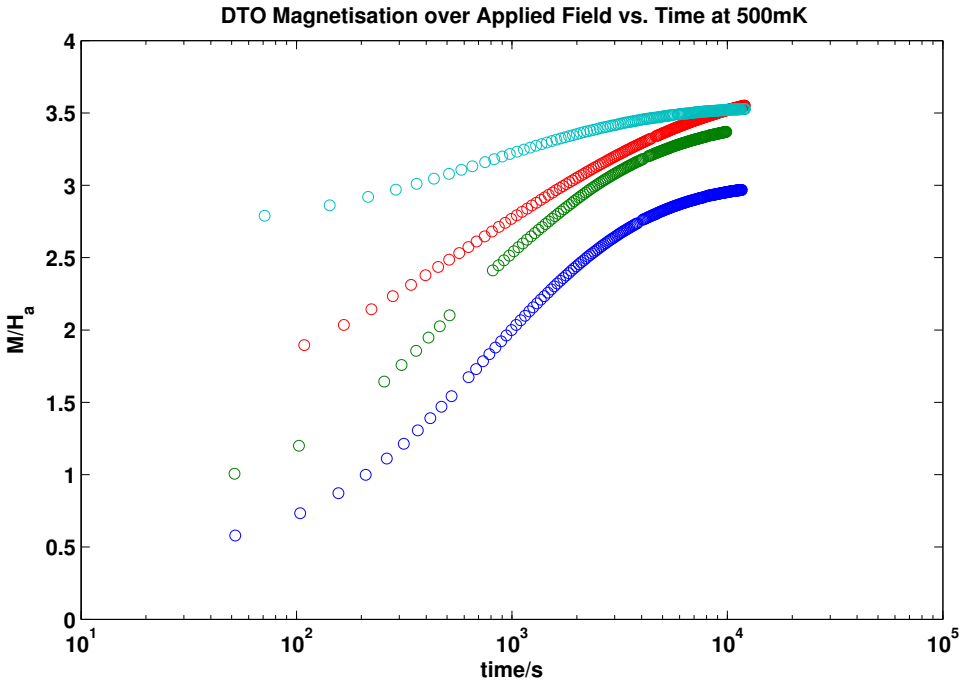

Figure 4.19: M/H_a vs. t curves for DTO at 0.01 (blue), 0.025 (green), 0.1 (red) and 0.25 T (teal) on logarithmic time axis.

there are two sets of values presented at each field strength, one fitted to the raw curves and one fitted to curves with a maximum M value increased by a factor of 1.01.

On table 4.2 we see that values of g increase with increasing field, with the exception of the unmodified 0.1 T data which was identified as anomalous above. This supports the theories that the non-Ryzhkin magnetic relaxation is due to field-dependent effects such as the Wien effect or field-dependent equilibrium population reduction. Notably, the progression of g with field in the 1.01× values is close to linear, with the exception again of the 0.1 T data. However, the significant difference between the two sets of values for g underlines their uncertainty. For the stretched exponential, ν does not change monotonically with field, though β consistently decreases with the exception of the anomalous 0.1 T set.

In figure 4.22 $\tilde{\nu}$ is plotted against t, under the assumption that the recorded maximum m is the actual maximum m. In this plot the four curves collapse onto one another, with the exception of the 0.1 T curve previously noted as being

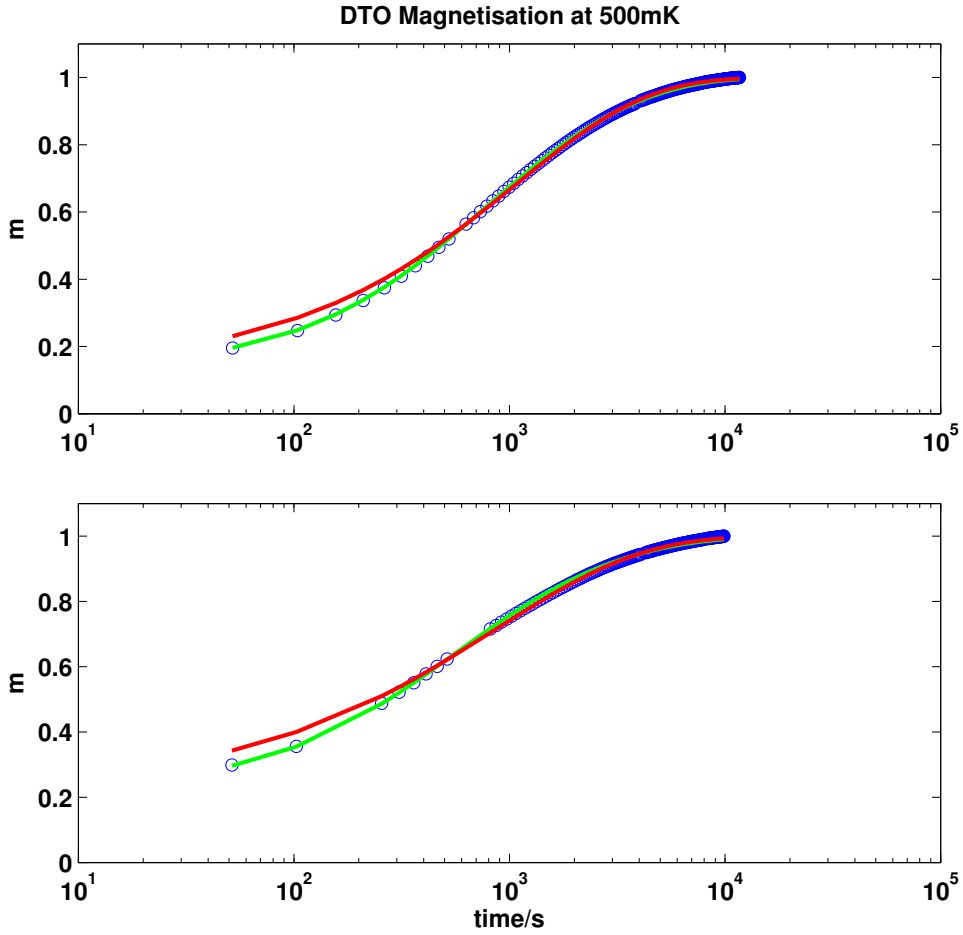

Figure 4.20: Approximate m vs. t curves for DTO (blue circles) against and linear non-Ohmic (green line) and stretched exponential (red line) best fits at $H_a = 0.01$ (upper) and 0.025 T (lower) applied fields.

far from saturation at its maximum point. This suggests that in this region of the curves $\tilde{\nu}$ has no strong field dependence. Given the substantial changes in g under the linear non-Ohmic model it might be expected for these curves to differ. However, examination of the fitted values for ν reveals minimal change with field, excepting for the 1.01× linear non-Ohmic model. In the linear non-Ohmic model ν defines the long-time limit of $\tilde{\nu}$, with g altering the early part of the curve (see equation 4.35). As the data begins midway through the magnetisation curves, substantial differences in the curve shapes could be 'hidden' before the $t = 0$ point. If $\nu(x)$ is minimally changed by field but g is altered strongly, this suggests the main factor altering the shape of magnetisation curves in applied fields is the

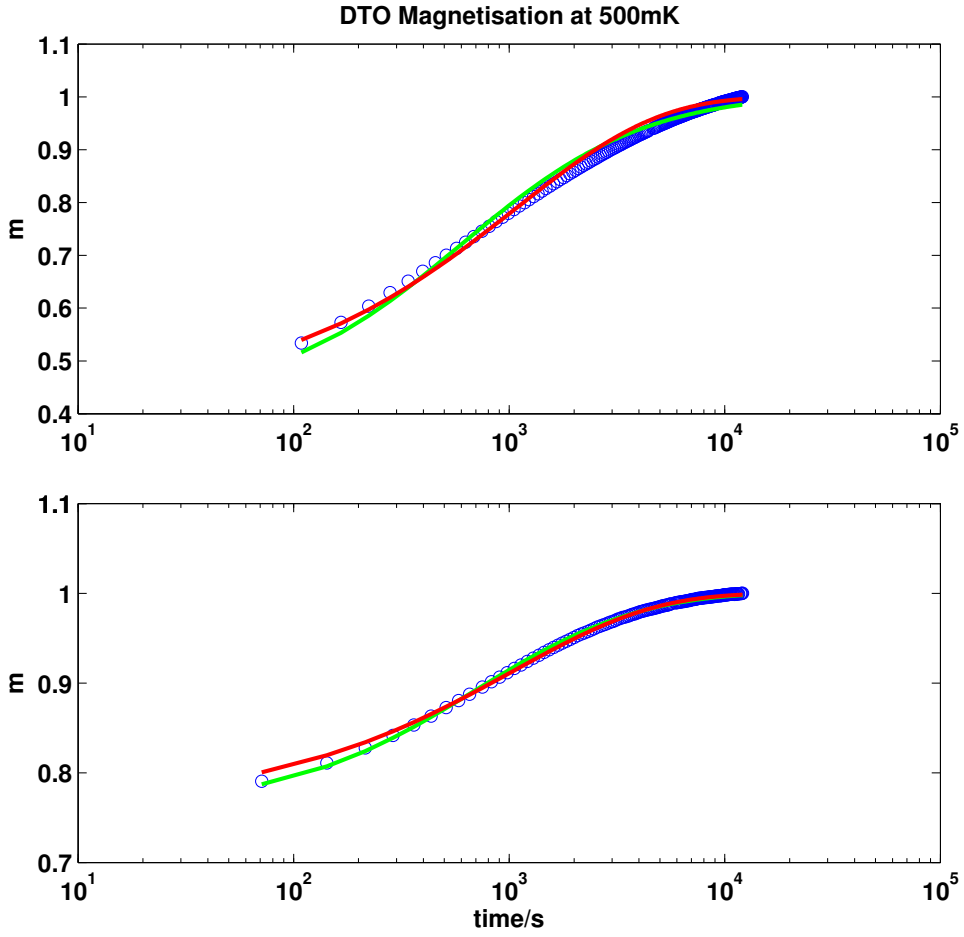

Figure 4.21: Approximate m vs. t curves for DTO (blue circles) against and linear non-Ohmic (green line) and stretched exponential (red line) best fits at $H_a = 0.1$ (upper) and 0.25 T (lower) applied fields.

Wien effect, not field-dependent reduction in x_e, which would come into play at long times. If, however, the curves are similar throughout their entire course, this would suggest that the Wien effect is not very important for spin ice magnetisation.

4.7 Summary

The magnetic relaxation behaviour of dysprosium titanate and, by analogy, other spin ices cannot be explained by taking a value for the magnetic conductivity at a given temperature and deriving a magnetisation curve from it. The (effec-

Table 4.2: DTO Relaxation Model Parameters (variable field)

Field	param.	$m/1.00$	$m/1.01$
0.01 T	ν	3.16×10^{-4}	2.47×10^{-4}
	g	4	5.4
0.025 T	ν	2.49×10^{-4}	1.72×10^{-4}
	g	8.7	13
0.1 T	ν	9.07×10^{-4}	3.23×10^{-5}
	g	31.2	87.4
0.25 T	ν	2.4×10^{-4}	5.33×10^{-5}
	g	23.4	112.8

Field	param.	$m/1.00$	$m/1.01$
0.01 T	ν	9.32×10^{-4}	8.96×10^{-4}
	β	0.71	0.69
0.025 T	ν	1.2×10^{-3}	1.1×10^{-3}
	β	0.64	0.62
0.1 T	ν	9.31×10^{-4}	8.68×10^{-4}
	β	0.58	0.55
0.25 T	ν	9.67×10^{-4}	8.26×10^{-4}
	β	0.66	0.58

tive) conductivity changes over the course of the relaxation process. There are several candidate mechanisms for this. Three of them affect the monopole population: the second Wien effect creating excess monopoles when a magnetising field is turned on [59], the long relaxation time of low-temperature spin ice leaving excess charge-carrying monopoles in the system [66], and the reduction of the equilibrium monopole population by applied fields [61]. Besides these population-based explanations, Revell *et al.* [5] suggest that surface effects and pinning of monopoles on lattice defects play a role, and have supported this contention with simulations that would not be affected by the failure to equilibrate with cooling.

The magnetisation curves can be approximated by using stretched exponentials, but more successful fits can be obtained by using a theory based on a linear approximation to the second Wien effect. However, this theory returns values for the Wien effect which are much larger than theoretically predicted, and shows signs of breaking down at high monopole concentrations. This suggests that factors

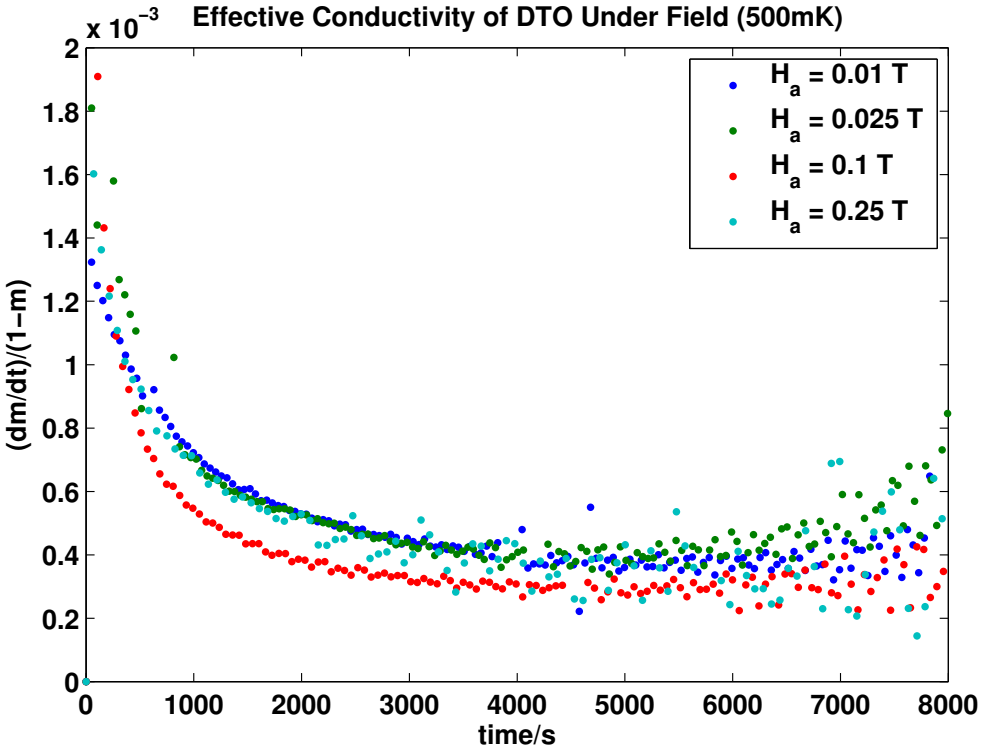

Figure 4.22: Effective conductivity $\tilde{\nu}$ versus time for DTO under applied fields of 0.01, 0.025, 0.1 and 0.25 T

beyond the Wien effect are important, and a more general recombination-based model such as that outlined above may achieve greater accuracy. However, such a model would still not account for surface effects or charge pinning.

Chapter 5

Praseodymium Zirconate

5.1 Quantum Spin Ice

Quantum spin ice is a variety of spin ice in which quantum fluctuations create a quantum spin liquid with additional excitations to classical spin ice [38]. In a theoretical quantum spin ice, there are transverse exchange couplings between spins on a much lower energy scale than the longitudinal couplings that generate the ice rule behaviour in classical spin ice. The manifold of ice rule states forms the background on which the transverse couplings act perturbatively, and reduce the barriers between different ice-rule states [93].

The first-order terms are exchange terms between rings defined on hexagonal loops tin the pyrochlore lattice. These rings of spins can be flipped without causing ice-rule violations. This regime of perturbatively small interactions on the background of the ice rules manifold defines a 'quantum spin liquid', with its own excitations. For appropriate parameter values the spin ice can manifest both 'visons' akin to electric charges (though not sources of the physical electric field as magnetic monopole excitations are of **H**), and gapless excitations with linear dispersion and two transverse polarisations, akin to photons [94].

Therefore, the quantum spin ice manifold has in theory an emergent quantum electrodynamics, akin to how the classical spin ice manifold has an emergent magnetic charge. However, experimental observation this behaviour is dependent on finding materials with the appropriate parameters. In recent years there has been

work on identifying and characterising real spin ices with quantum fluctuations.

In this section a report by Kimura *et al.* [8] of quantum fluctuations in a 'spin-ice-like' compound praseodymium zirconate ($Pr_2Zr_2O_7$, PZO) will be examined in light of the Debye-Hückel theory developed above, and their experimentally determined entropy compared to a new measurement using a different method. This will shed light on both the efficiacy of the method and the physics of PZO.

5.2 Praseodymium Zirconate

In 2013 Kimura *et al.* [8] reported that PZO has spin ice properties. PZO is a rare earth pyrochlore crystal like DTO and HTO, but outside of the dysprosium/holmium titanate/stannate/germanate group that has dominated spin ice research to date. Previous work by Matsuhira *et al.* [95] had established that PZO has spin freezing but no long-range correlations down to 76 mK, which are necessary but not sufficient conditions for spin ice.

Kimura *et al.* performed thermomagnetic, neutron scattering and heat capacity measurements. Particularly among the magnetic measurements, the inverse susceptibility of PZO at low temperatures (figure 5.1a reproduced from their paper) reveals an effective magnetic moment $\mu_{\text{eff}} = 2.5\mu_B$. This is significantly smaller than that of DTO. In DTO the very large magnetic moment of Dy^{3+} ions is necessary to overcome an antiferromagnetic exchange interaction and produce ferromagnetic spin ice behaviour, but in PZO a ferromagnetic superexchange interaction mediated by the oxygen atoms dominates to create the necessary interaction between the tetrahedral vertex spins [8].

The authors examined both elastic and inelastic scattering from PZO. The elastic scattering measurements (figure 5.2a reproduced from their paper) revealed the existence of pinch points similar to those in HTO [46]. In contrast, the inelastic scattering, while producing similar behaviour otherwise, has no evidence of pinch points. Kimura *et al.* argue that this demonstrates the existence not just of monopoles but monopoles with quantum dynamics [8]. The breadth of the pinch points they argue is representative of the density of ice-rule violating tetrahedra, i.e. magnetic monopoles.

The results of their heat capacity measurements are shown in figure 5.1f repro-

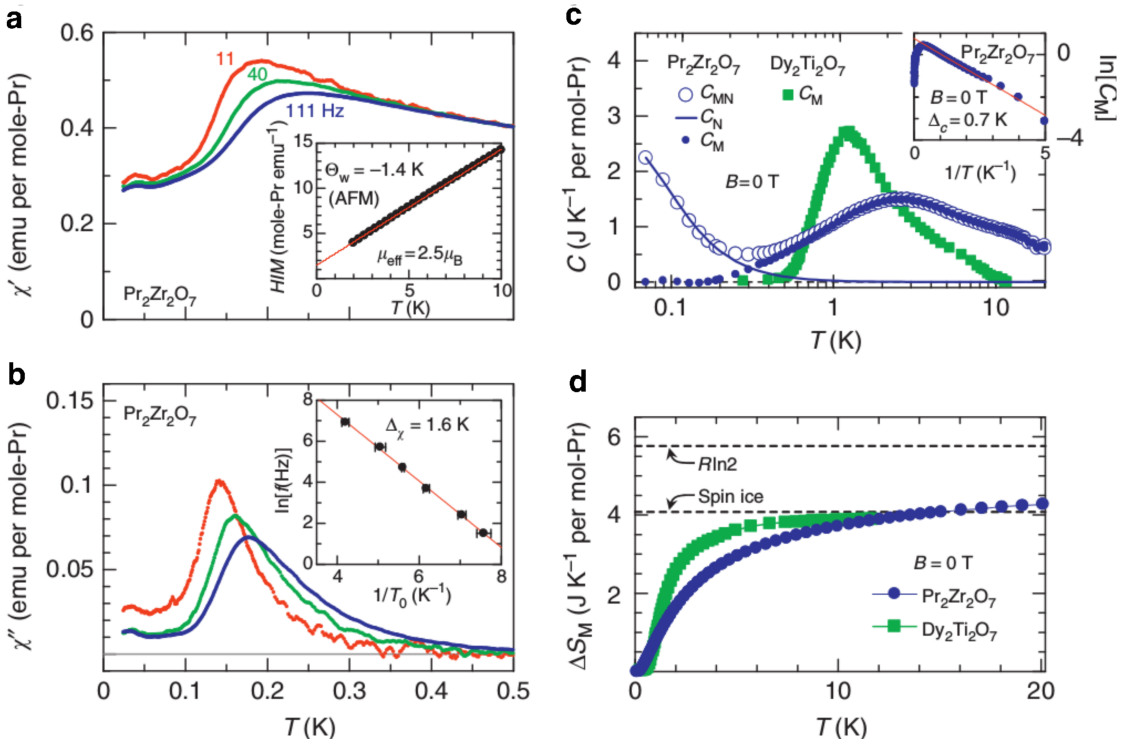

Figure 5.1: (a) is the real part of the AC susceptibility of PZO. The inset is the DC field H divided by the magnetisation M for 10 K > T > 2 K. (b) is the imaginary part of the AC susceptibility. (c) is the specific heat of DTO and PZO with magnetic (C_M) and nuclear (C_N) parts shown separately. The inset is C_M vs. $1/T$. (g) is the entropy of DTO and PZO from an $S_0 = 0$ baseline with reference lines at the spin ice maximum entropy and the maximum entropy minus the Pauling ground state entropy. Reprinted by permission from Macmillan Publishers Ltd: Nature Communications (Kimura *et al.* 2013 [8]), copyright 2013.

duced from their paper. The PZO heat capacity has the same single peak form as DTO, but a lower and broader peak. Kimura *et al.* noted this difference of shape and proposed that it was due to quantum dynamics. Figure 5.3 shows that even if PZO parameters are input to the Debye-Hückel theory developed in this thesis, it is impossible to achieve a heat capacity curve of the correct shape. The location of the peak suggests a chemical potential of approximately 6 K, but changes in chemical potential do not produce significant changes in peak height, and all Debye-Hückel curves lack the peak breadth of PZO, most noticeable at low temperatures where there is significant specific heat down to 0.2 K. This suggests that the monopole dynamics of PZO are sufficiently altered that classical Debye-Hückel theory is no longer an effective description.

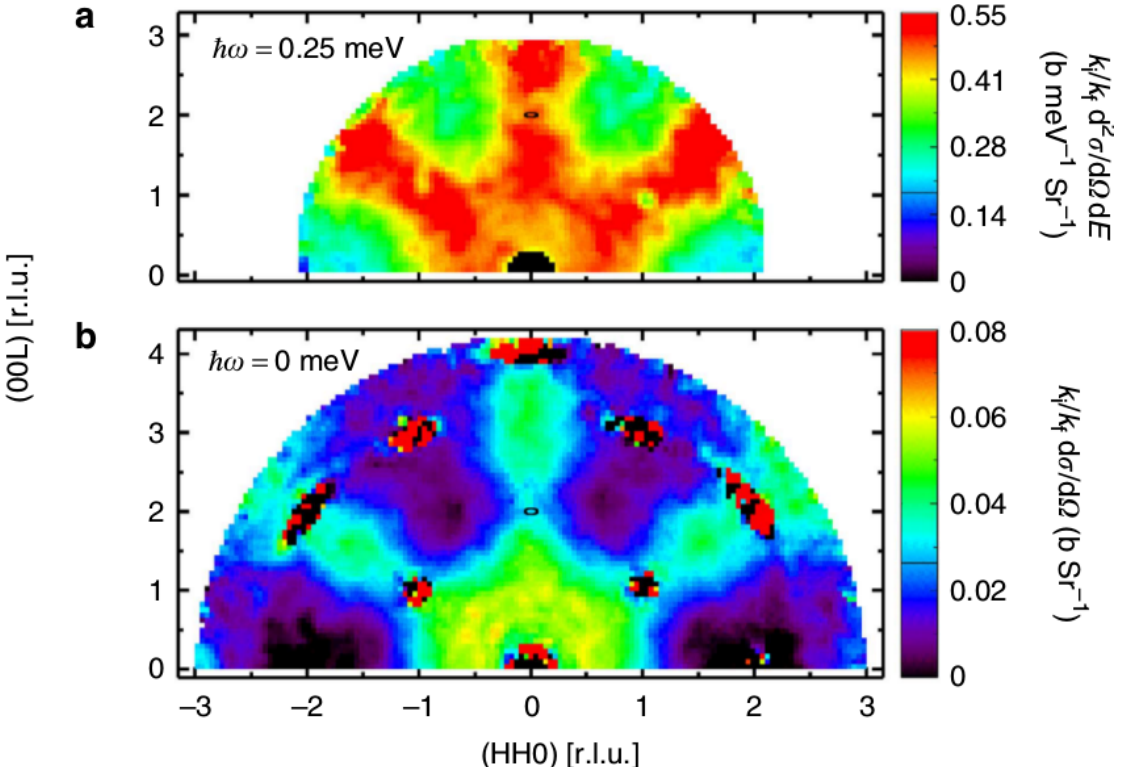

Figure 5.2: (a) is a Q-map of inelastic neutron scattering in PZO with energy transfer of 0.25 meV. (b) is the Q-map of elastic neutron scattering with pinch points clearly visible. Reprinted by permission from Macmillan Publishers Ltd: Nature Communications (Kimura *et al.* 2013 [8]), copyright 2013.

In figure 5.1d Kimura *et al.* plot the entropy of PZO against that of DTO, and compare it to the expected values for ideal spin ice. However, on their analysis while PZO does reach the spin ice saturation entropy, it has not yet saturated itself at this point and continues to increase past the expected maximum, suggesting a total entropy gain greater than for DTO. This implies either the saturation entropy is larger, or the ground state entropy is smaller, than for the classical spin ices.

5.3 Determination of Entropy from Magnetisation Measurements

In 2013 L. Bovo and S. T. Bramwell [75] outlined a new method of measuring the entropy of spin ices, based on Maxwell's relations.

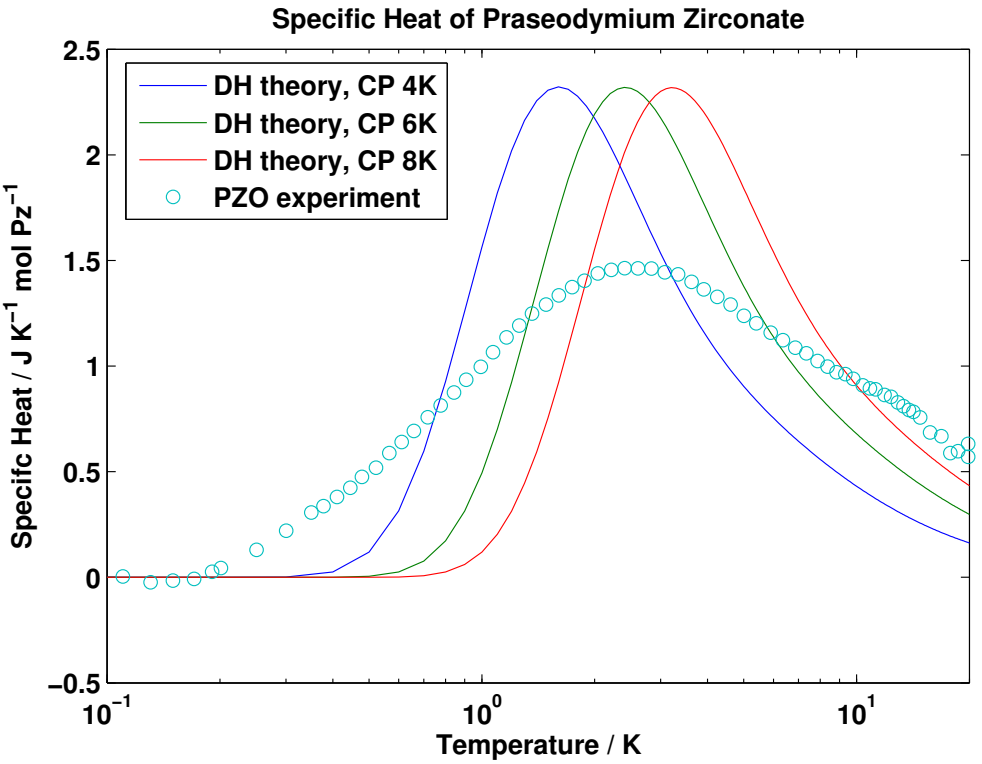

Figure 5.3: Specific heat of praseodymium zirconate estimated using Debye-Hückel Theory.

As outlined in section 1.2, thermodynamic systems in equilibrium are defined by sets of state variables, so related that all but one can be defined independently simultaneously. In magnetic systems the three variables are magnetic moment I, internal field H_i and temperature T [16]. The Maxwell relations can be defined among these three variables and S, yielding equations 3.45 and 3.46.

If one can obtain values for the change of magnetisation with temperature at a given field for a large number of closely-spaced fields, one can then numerically integrate the data at a given temperature across the fields up to H_i to obtain the entropy difference between the system in field H_i and zero field. If H_i is large enough to completely order the system magnetically, then it will have zero magnetic entropy under field, and the entropy change will be the total entropy contained in the magnetic interactions of the system at zero field.

Bovo *et al.* [75] applied this method to measuring the entropy of dysprosium titanate. Here it is applied to PZO as a further test of the method and to shed

light on the ground state entropy of the material.

It is worth noting at this point that the third law is only apparently violated in spin ice, as the work of Pomaranski. *et al.* [66] has shown that the entropy of DTO continues to drop toward a true ground state with sufficiently long relaxation times. In this method, this would manifest through changes to the quantities interpreted through equation 3.46. Particularly, as the entropy approaches zero $\partial I/\partial T$ would have to approach zero for all fields H_i. This implies that the magnetic properties of spin ice alter at least slightly if it is allowed to equilibrate fully.

Compared to determining the entropy via integration of the specific heat, this method has the advantage that it can make absolute measurements. Specific heat measurements can only determine the relative change in entropy between two temperatures, and require an absolute reference point to pin the derived curve to if they are to yield an absolute entropy value. In theory, the third law of thermodynamics guarantees $S = 0$ at $T = 0$ as an absolute reference point, provided one can get close enough to absolute zero, but as spin ice has demonstrated the true ground state may be impractical to attain in practice, leaving the question open what the effective ground state entropy of a system such as classical or quantum spin ice is, provided it can still be treated with equilibrium thermodynamics in practice.

5.4 Experimental Procedure

Magnetisation as a function of applied field was measured at different temperatures by L. Bovo, using a vibrating sample magnetometer for the Quantum Design PPMS. The field was applied along the [111] axis with strength ranging from 0 to 14 T at intervals of 0.01 T up to 0.4 T, 0.02 T up to 1 T, 0.1 T up to 7 T and 0.5 T up to 14 T. The measurement was taken every 0.1 K from 1.9 to 3.1 K, then at $T - 0.1$ K, T and $T + 0.1$ K for $T = 3.5$, 4, 4.5, 5, 6, 7, 8, 9 and 10 K. The PZO crystal weighed 0.0418 g with cuboid dimensions $0.168 \times 0.138 \times 0.324$ cm, yielding a demagnetising factor of approximately 0.19 [96].

5.5 Application of the Method

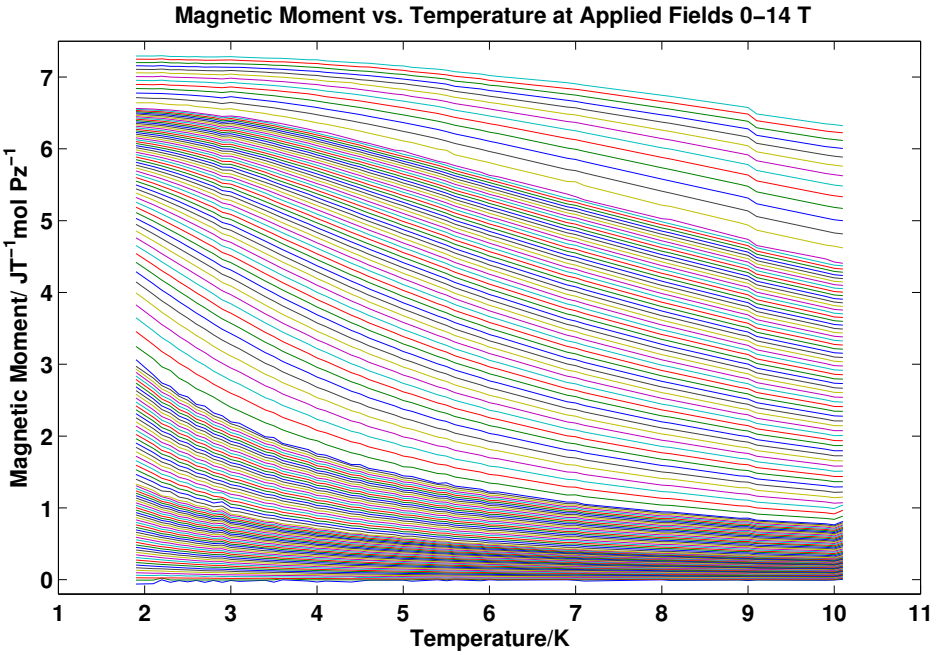

Figure 5.4: Experimental magnetic moment I vs T at internal field $0 < H_i < 14$ T in PZO. Lines are guides for the eye.

First, the data must be converted to measure I against the internal field H_i. By converting the I values to equivalent M values, the H_e value for each point can be transformed into an equivalent H_i value using the standard expression:

$$H_i = H_e - DM \tag{5.1}$$

where the demagnetising factor D is an approximate value for the shape of the crystal. After this transformation the values of H corresponding to the values of I or M will be inconsistent between the different temperatures, but interpolation of each data set to a set of standard H values can reestablish consistency.

In figure 5.4 I is plotted against T for all values of H. The general structure is visible in the decline in I as temperature increases, as occupancy of higher-energy states defined by the H field becomes more probable. Examination of the plot reveals two problems for the analysis: Firstly, the magnetisation does

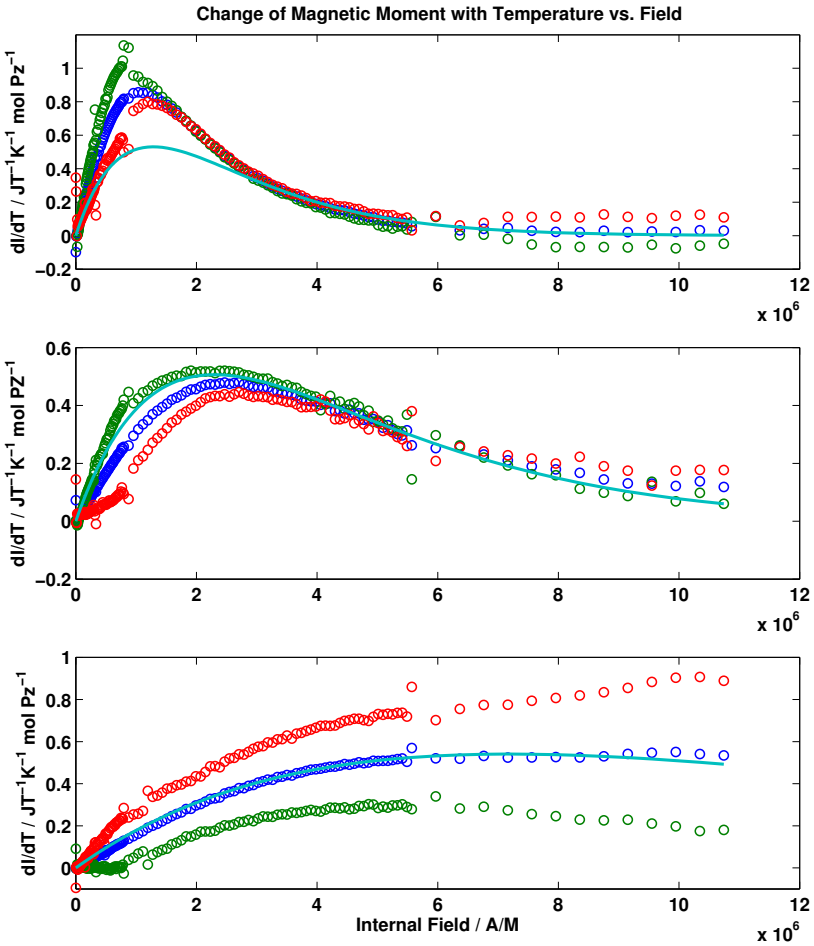

Figure 5.5: Temperature change in magnetic moment dI/dT vs. internal field H_i at 2.2 K (upper), 5 K (middle) and 9 K (lower). Blue lines are taken between $T - 0.1$ K and $T + 0.1$ K, green line are taken between $T - 0.1$ K and T, red lines are taken between T and $T + 0.1$ K. Teal lines are the expression aHe^{-bH} fitted between 3 and 10×10^6 A/M.

not saturate at temperatures higher than 3 K, which indicates that the entropy calculated at these temperatures will be systematically deficient. Secondly, there are numerous more minor irregularities which persist across a range of H values at various temperatures and will introduce errors into measures of $\partial I/\partial T$.

Each $\partial I/\partial T$ point was determined from a set of three I vs. T points at each given H_i value, with T values at the reference temperature and 0.1 T either side. The ΔI and ΔT were taken between each of the three possible pairs of points to produce three values for $\Delta I/\Delta T$ and hence $\partial I/\partial T$, consisting of a central 'reference' value (defined between the lowest and highest T) and upper and lower

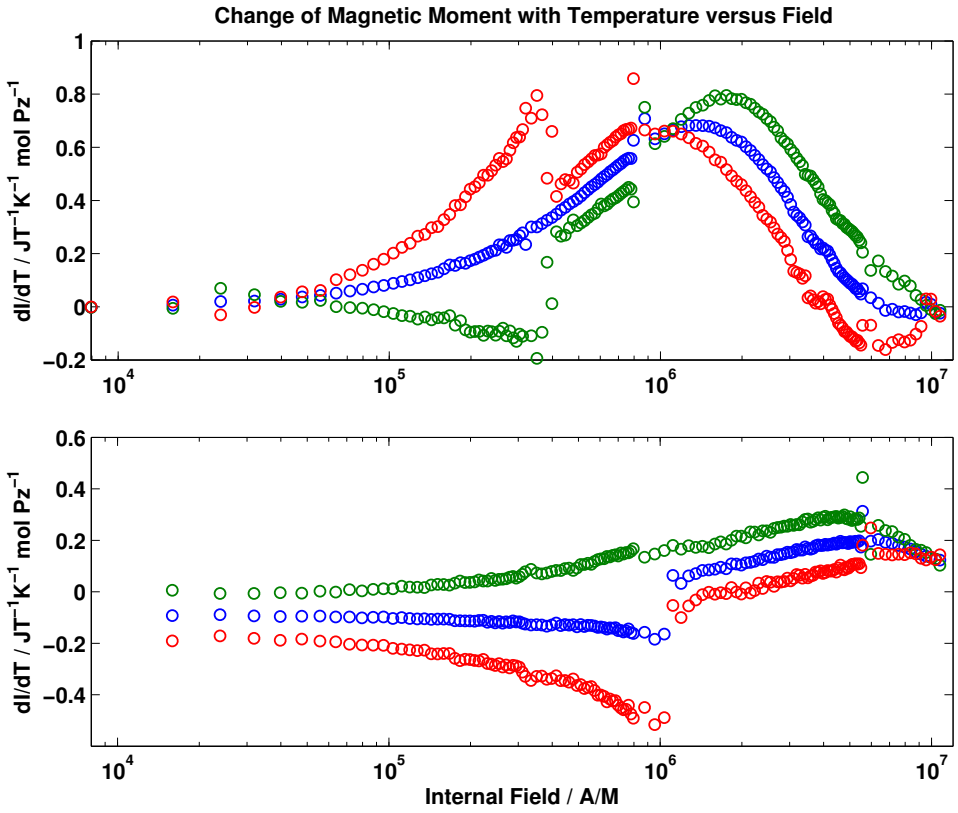

Figure 5.6: Temperature change in magnetic moment dI/dT vs. internal field H_i at 2.9 K (upper) and 10 K (lower). Blue lines are taken between $T - 0.1$ K and $T + 0.1$ K, green line are taken between $T - 0.1$ K and T, red lines are taken between T and $T + 0.1$ K, showing aberrant curve shapes.

bounds (defined between the lower or higher T and the central value).

To obtain the entropy from these points it is necessary to integrate them across all values of H_i. In figure 5.5 the three sets of $\partial I/\partial T$ values are plotted against H_i at three example temperatures. The value of the entropy at each temperature is determined by the area under the curves.

Notable in these plots is the large amount of noise in the curves. As at each temperature dI/dT is calculated for each of the three possible pairings of three close points, any one point being anomalous will produce two anomalous $\Delta I/\Delta T$ values and one unaffected by the anomaly. In each of the upper two graphs of figure 5.5, this can be clearly seen in the mirrored anomalous behaviour of the red and green curves around the well-behaved blue central curve. This approach means that the anomalies in the data do not dominate the calculation and instead

help define the error at each temperature. This source of error can be reduced by smoothing over larger temperature ranges, but this approach exacerbates the non-saturation problem described below as it requires obtaining points from higher temperatures where failure to saturate is more acute.

A second immediate problem with the application of this method is apparent in figure 5.5 (lower), where at maximum H the curve has not yet reached a point where the change in area is small. This is a manifestation of the failure of the sample to completely magnetise also visible in figure 5.4. It is reasonable to believe the curve has the same overall single peak shape as in 5.5 (upper), but at high temperatures the sample does not fully magnetise at experimentally accessible fields.

To attempt to compensate for this, a trial expression $\partial I/\partial T = aH_i e^{-bH_i}$ was used to approximate the shape of the curves and extend them past the limit of the data. If the expression is a good phenomenological fit to the data this will provide estimates of the entropy at higher temperatures at the cost of an increase in the error.

The results of this for 2.2 K can also be seen in figure 5.5. The teal curves, fitted by both a and b to the experimental data reference curves, are less divergent from it in the high-field region than the two error bounding curves and so does not introduce a major new source of error. However, a potentially significant systematic error can be seen at high H_i in the 5 K figure, where the trial expression goes to zero while the experimental data retains a long tail.

While at 2.2 K this does not produce a very large error, at 5 K the gap between the trial expression and the experimental data is clearly apparent. The failure of the magnetisation to saturate at these temperatures potentially introduces a major deficiency in calculated entropy. Examining figure 5.4, the change in M with T at maximum H becomes perceptible above 3 K, so systematically low values for the entropy may be expected above this temperature.

Some temperatures have more severe errors. In figure 5.6 (upper) the $\partial I/\partial T$ graph for 2.9 K displays a clearly aberrant form. At 2.9 K the PPMS changes its cooling mechanism, and this affects temperatures from 2.8 to 3 K. Similarly at 10K as seen in figure 5.6 (lower), the data has clearly been corrupted by instrumental error.

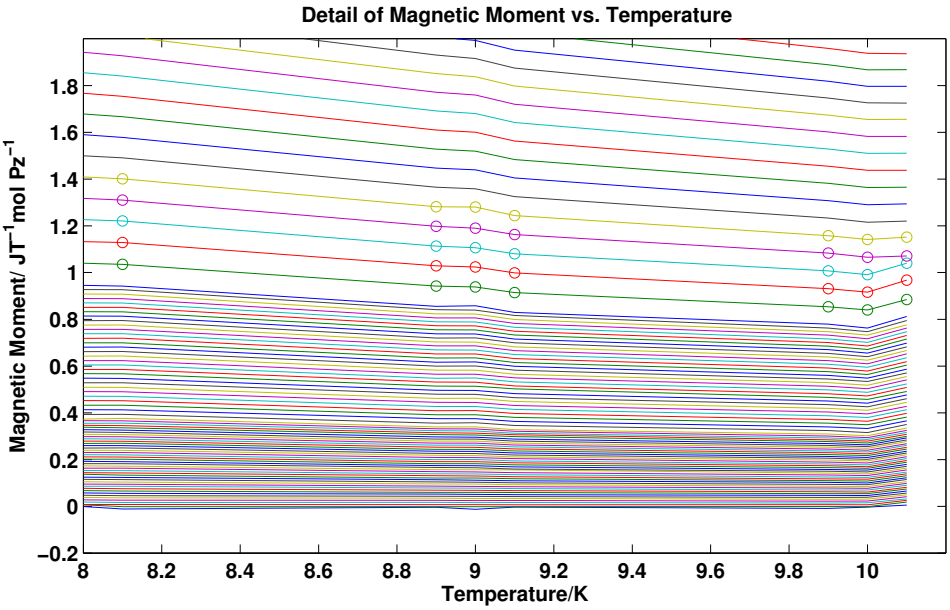

Figure 5.7: Experimental magnetic moment I vs T at internal field $0 < H_i < 14$ T in PZO. Detail of figure 5.4. Points marked with circles are at 1.1, 1.2, 1.3, 1.4 and 1.5 T applied field. Lines are guides for the eye.

The nature of this error can be seen in figure 5.7. At 10.1 K the magnetisation develops an upward 'kick' at low field that persists until applied field 1.4 T, at which point it abruptly vanishes. This creates the discontinuity visible in the 10 K data in figure 5.6. Similar, though smaller anomalies appear at other temperatures and fields, such as the one visible in figure 5.7 at 9K. The cause of these anomalies is unknown, but that they appear for particular temperatures and persist over a range of fields suggests that they are random errors associated with the instrument, as the order of operations of the experiment is to measure in increasing field at a fixed temperature. It is also possible that they represent some inconsistent behaviour in the sample itself.

Additionally to these corrupt sets, the I vs. H data for 2 K and 8.1 K is missing due to experimental error. These absences make it impossible to produce a full trio of $\partial I/\partial T$ curves at 2, 2.1 and 8 K as in each case only one of the three point pairs can be defined.

Due to the ample supply of points at other temperatures, these temperatures have been excluded from the entropy plots in the next section. The absences do

not significantly affect the results, but they do underline the difficulty of and care required for measuring the entropy using magnetic saturation.

5.6 Comparison with Previous Measurements

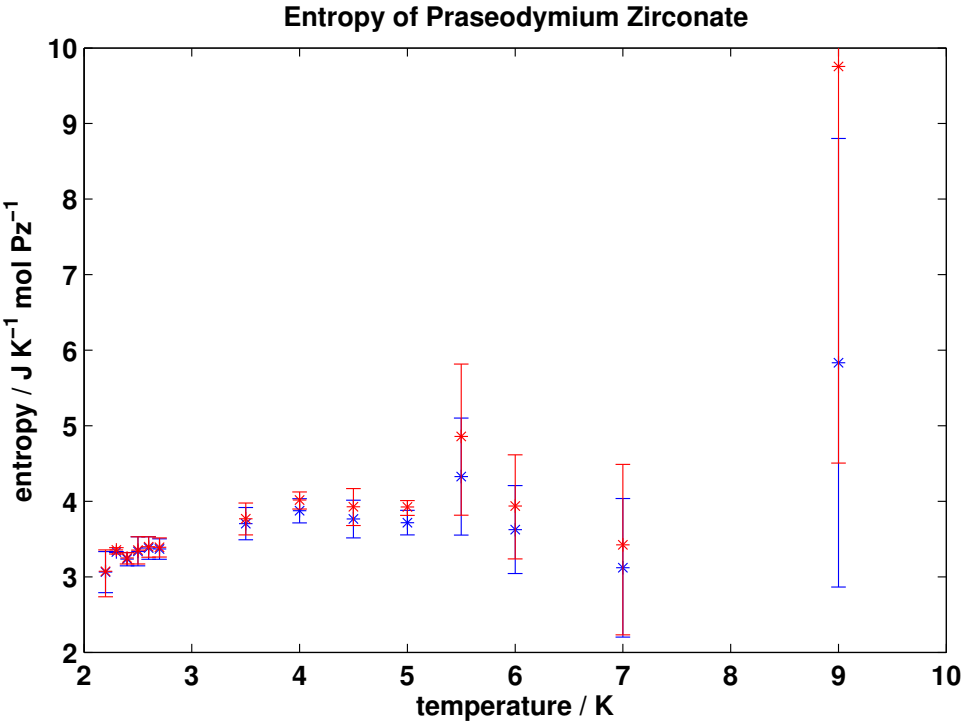

Figure 5.8: Entropy of PZO vs. temperature. Blue uncorrected, red with data extended using phenomenological expression.

The results of the calculation of entropy from the magnetic quench data can be seen in figure 5.8, with and without the phenomenological extension. As one would expect, the extension increases the estimated entropy at each point. Above 5 K the random errors become large, and by 9 K the data has become effectively unusable. Above 4 K the decline in the entropy values expected from incomplete saturation becomes apparent, as there is no consistent increase in the calculated entropy despite figure 5.1g showing a continued increase in the entropy derived from specific heat until it approaches saturation near 10 K. Therefore, for comparison with the Kimura *et al.* data, the magnetic saturation data will be discarded above 4 K as

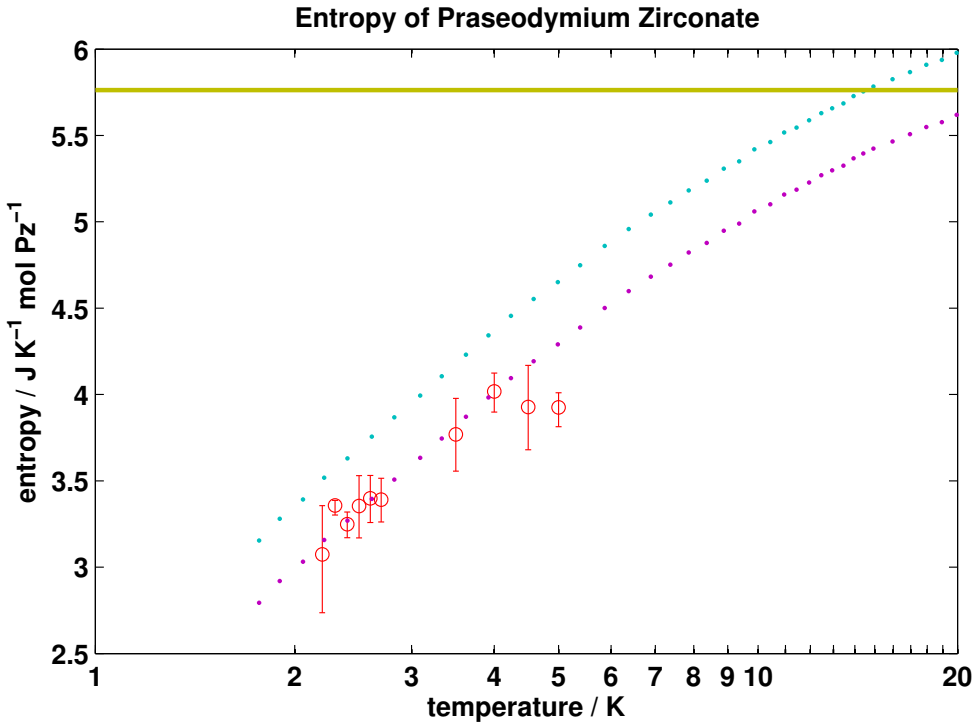

Figure 5.9: Entropy of PZO vs. temperature. Red circles are absolute values derived from magnetisation measurements with phenomenological extension. Teal and purple points are data from [8] with an assumed ground state entropy of $R/2\ln(3/2)$ (teal) or $R/2\ln(3/2)-0.36$ (purple). Yellow line is drawn at the spin ice maximum entropy $R\ln(2)$.

systematically unreliable as well as prone to large error. Sufficient points remain between 2 and 4 K to judge the effectiveness of the method in this region, and extract useful results.

In figure 5.9 the extended data is plotted alongside the results of Kimura *et al.* using different estimates of the ground state entropy S_0. Multiple values are used because specific heat over a temperature range only defines the change in entropy over that range, and must be added to a value for the entropy at the lower limit to return an absolute entropy value. As the temperature range for this data comes close to zero, the third law of thermodynamics might be expected to imply that the lower limit should be zero, but as discussed above, the ground state entropy of spin ice is not zero on short experimental timescales as it does not equilibrate on such timescales. However, it is also not a given that the apparent ground state entropy of PZO will be the same as that of classical spin ice. As such, two different

values of S_0 are combined with the Kimura data and compared against the data from this report.

The first estimate assumes S_0 is equal to the Pauling entropy [21]:

$$S_0 = (R/2)\ln(3/2)\ \mathrm{JK^{-1}mol\ Pz^{-1}}, \tag{5.2}$$

based on the spin ice properties of PZO. This produces absolute values larger than those calculated using the magnetic saturation method. As the calculations are expected to contain a deficiency due to incomplete saturation and high-H deficiency of the extension expression, this is not unexpected. However, the discrepancy at low temperatures is more than expected given that figures 5.4 and 5.5 suggest the sample has almost saturated at these temperatures. Furthermore, at high temperatures the expected entropy crosses over the spin ice maximum entropy $R\ln 2$, and is visibly continuing to increase. While it is theoretically possible that this high maximum entropy is correct and due to unknown properties of PZO, the disagreement with the absolute measurements at low temperatures suggests that instead, the ground state entropy of PZO is reduced.

The second estimate takes $S_0 = (R/2)\ln(3/2) - 0.36\ \mathrm{JK^{-1}mol^{-1}}$, a value which does not have theoretical justification, but which brings the Kimura *et al.* data in line with our absolute value derived from magnetic saturation. As known systematic errors in the magnetic saturation value such as the failure to saturate imply higher values than those calculated, this provides a lower bound on the ground state entropy of PZO, with allowances for the remaining random errors. Using this absolute scaling, the Kimura *et al.* data and ours are in agreement until 4 K save for an outlying point at 2.3 K. Above 4 K, the experimental absolute entropy values fall away from the specific heat derived values. This is the same point at which the lack of saturation in figure 5.4 becomes visible.

At high temperatures, the specific heat derived data approaches but does not cross the $S = R\ln 2\ \mathrm{JK^{-1}mol^{-1}}$ entropy value of a saturated spin ice state. This result suggests that the ground state entropy of PZO on short timescales is $S_0 = (R/2)\ln(3/2) - 0.36\ \mathrm{JK^{-1}mol^{-1}}$, with phenomena not found in the classical spin ices reducing the entropy from the Pauling entropy $S_P = (R/2)\ln(3/2)\ \mathrm{JK^{-1}mol^{-1}}$. One possibility is that the quantum fluctuations enable the system to search for

the true ground state of the ice rules manifold more quickly than classical spin ice. In this case the low temperature specific heat would increase with extended relaxation times, more rapidly than found by Pomaranski *et al.* [66], and the third law would be reestablished in PZO more quickly than for classical spin ices.

Regarding the magnetic saturation method in general, this investigation demonstrates that it can produce meaningful results that shed light on current debates. It also demonstrates that there are significant obstacles to its application. Extremely powerful magnetic fields are required to completely eliminate magnetic entropy in materials such as PZO, and the measurements are prone to error even at low temperatures. However, it should be noted that if good specific heat data exists for the material, only one reliable absolute entropy point is required to place relative entropy data derived from specific heat on an absolute scale, and this point can be taken with great care at a low temperature where saturation is possible.

Chapter 6

Conclusion

The above work demonstrates that a complete version of Debye-Hückel theory can approximate the magnetic heat capacity of the spin ices dysprosium titanate, holmium titanate and cadmium erbium selenide. In particular, it demonstrates that the theory is still effective above 2 K, where previous work [4] considered the spin ice phase to have broken down and the theory to not be effective.

Making the theory effective in this high-temperature region requires incorporating terms for 'double charges', higher-energy defects where all constitutive spins are oriented in or out of the tetrahedron. The addition of these terms predicts significant magnetic heat capacity up to 10 K or higher. By contrast, the theory is notably unsuccessful in the region near $T = 1$ K, where the heat capacity reaches a Schottky peak. The heat capacity predicted by Debye-Hückel theory in this region is consistently much lower than that observed in experiment.

This points to the most important deficiency of the given theory: a failure of the theory to account for bound monopole pairs (Bjerrum pairs), and possibly higher correlations as described by Zhou *et al.* [36]. However, a naïve addition of terms for Bjerrum pairs fails, leading to a grossly overestimated heat capacity, and incorrect values for the total entropy, in my view because no clear distinction can be drawn between bound and free monopoles at high monopole densities.

A second theoretical deficiency is that the main theory presented above was formulated for a continuum. Debye-Hückel theory for a lattice has been derived [80], but the solution is only formally valid for the class of Bravais lattices which

does not include the diamond lattice, and its performance in this context was slightly inferior to the continuum model. Further work on lattice Debye-Hückel theory could determine that if combined with a proper theory of Bjerrum pairing it yields a more effective theory of spin ice, or that the worse performance is simply a true reflection of the fundamental limitations of the theory.

One proposed spin ice for which the theory was not effective was praseodymium zirconate (PZO), which has a heat capacity peak lower and broader than can be achieved with Debye-Hückel theory. PZO is identified by Kimura et al. [8] as exhibiting quantum monopole dynamics, which would place it among the ranks of the quantum spin ices, a type of spin ice where quantum fluctuations act on the set of spin ice states. This type of material has attracted significant scrutiny in recent years (see Gingras et al. 2014 [38]). This failure of Debye-Hückel theory for a quantum ice suggests that in such materials monopole interactions are significantly altered, and determining how, and whether the theory can be extended to cover them, is a promising line of research.

For classical spin ices, this work demonstrates the importance of careful study of the heat capacity, particularly in the 2 to 10 K region. What initially appear as reliable conclusions regarding non-monopolar factors may cause significant errors in the estimation of the magnetic specific heat if even slightly erroneous. While theory and argument for persistence of the monopolar specific heat into this region has been presented, its exact level by 10 K cannot be stated with complete confidence for any of the materials presented here. The success of Debye-Hückel theory in particular and the persistence of monopolar behaviour in general is similarly somewhat uncertain at such high temperatures, though the errors only become large above approximately 7 K, below which the theory is clearly established as effective. This work also reveals a direction for exploration of additional spin ice materials. While previous work [36] has indicated that novel behaviour may be accessible at lower monopole chemical potentials, synthesising spin ices with higher chemical potentials would enable study of monopole behaviour at higher temperatures, where it interacts with thermally activated phenomena such as crystal field excitations. It would also enable testing the theory that higher chemical potentials will be more successfully described by Debye-Hückel theory.

For locating such new spin ices, the possibilities of pyrochlores such as dys-

prosium or holmium titanate, stannate or germanate are known, but the spin ice behaviour in the spinel $CdEr_2Se_4$ raises the prospect of discovering additional spin ices in alternative crystal structures. The spinel $CdEr_2S_4$, with sulphur replacing selenium, has been suggested to be another spin ice candidate in recent work by Legros et al. [97]. Beyond mere spin ice, recent simulations by Guruciaga *et al.* [98] have mapped the possibilities of varying values of J and D that produce either monopole liquids or an ordered phase of interpenetrating double monopole sublattices, which might be called spin anti-ice, and suggest transitions between the two are possible at different temperatures in the same material. Expanding the catalogue of real spin ices would enable these claims to be tested experimentally.

More generally, this work has demonstrated that Debye-Hückel theory is effective at high concentrations of charged particles, provided the temperature is high enough that the average electrostatic or magnetostatic interaction energy is smaller than the average thermal energy. This result could be translated back into the original Debye-Hückel context and suggests that the theory may be successful at describing hot electrolytic solutions.

The above work also studies the DC magnetic relaxation of spin ice. It confirms the result of Revell *et al.* [5] that the original 2005 model of Ryzhkin [3] is not able to describe the relaxation behaviour of spin ice, but is inconclusive on prospective replacements.

Two main improved models were tested: A stretched exponential proposed by Revell *et al.* [5] and a model based on the Wien effect proposed by Bramwell [74]. Their performance when fitted to relaxation data is similar. However, the strength of the Wien effect required to obtain a good fit is much higher than that predicted by Wien's theory. This is evidence for the influence of a failure of the monopole population to reach equilibrium, as seen in the work of Pomaranski *et al.* [66], which will have an effect similar to a strong Wien effect. In addition to these effects, we should expect to see a contribution from the surface effects identified in simulations by Revell *et al.* [5], but not given a complete description or theoretical treatment in that publication.

The quantity $(dm/dt)/(1-m) = \tilde{\nu}$, called here 'effective conductivity', confirmed the existence of defect pinning as identified by Revell *et al.* [5], and also revealed ways in which the models tested were failing to correctly describe the

relaxation of spin ice that were not easily perceivable in magnetisation graphs. When applied to data across differing field strengths, the curves of change in $\tilde{\nu}$ over time collapse onto one another in the experimental time range, which may suggest a diminished role for the field-dependent Wien effect in magnetisation, but the limitations of the variable field data prevent a firm conclusion. The quantity has a clear physical interpretation as the rate of magnetisation change controlled for changes in both the applied field and the Ryzhkin reaction field, and may be of interest to future investigators.

Future work can attempt to isolate and characterise these effects individually. Extended equilibration times before measurement will allow samples to equilibrate properly down to lower temperatures, which will isolate the non-equilibrium effects from the Wien and surface effects.

A characterisation and theoretical study of the surface effects noted as important by Revell *et al.* [5] may validate the use of a stretched exponential to describe them or suggest a new form - in either case, the mere success of a stretched exponential in one case does not imply that it is the best or most theoretically justified expression to do so. Depending on the nature of the surface effects, it may also be the case that they can be distinguished from the Wien effect by the latter's field dependence. Theoretical, empirical or simulation studies may also yield values for the parameters used in the many expressions in this paper that will reduce the requirement to introduce uncertainty with multivariable fits. As with Debye-Hückel theory, a magnetisation curve with no fitted parameters may be compared with the experimental curves to reveal deficiencies in the theory. By paying attention to all three effects, a complete theory of spin ice magnetisation behaviour may be achievable.

While the m_0 zero time offset may merely be a parochial experimental error it should be checked for in future, as if it is replicated it will be either a universal experimental error or a genuine phenomenon, and either is of interest. Observing it clearly requires obtaining data as early as possible after the magnetic field is switched on.

In the final section of this work, a method of absolute magnetic entropy measurement proposed and used by L. Bovo [75] was tested on PZO. PZO was found to have a ground state entropy reduced from that of classical spin ice, and additionally

its specific heat profile does not match that of a Coulomb gas described by Debye-Hückel theory. This suggests that the ground state of PZO on short timescales is not the ice rules manifold of classical spin ice, and its higher-temperature physics are also distinct such that Debye-Hückel theory is no longer even an approximate description as for classical spin ice.

The method itself was discovered to be unable to produce accurate measurements at high temperatures, but provided better data at lower temperatures. Stronger magnetic fields would make available use of the magnetic saturation method at higher temperatures to clearly determine the magnetic specific heat, and materials with magnetic behaviour which saturates at lower applied fields will be more accessible than spin ices.

Easier is to use the method at lower temperatures for samples which are not amenable to conventional specific heat measurement. Powder samples are difficult to measure with traditional calorimetry as the physical structure and so thermal relaxation profile of the powder is uncertain. The magnetic saturation method, by virtue of not relying on thermal relaxation for its data, is not affected by this problem so long as the magnetisation process does not cause uncompensated heating in the sample itself. Additionally, the method can directly measure the entropy of materials whose zero point magnetic entropy is uncertain.

Taken together these results suggest that despite the profusion of work on spin ice over the last two decades, and the branching out of study into artificial and quantum spin ices, classical spin ice remains a source of interesting physics, and one that can shed light on these other ices by comparison.

Bibliography

[1] J. Preskill. Magnetic monopoles. *Annual Review of Nuclear and Particle Science*, 34:461–530, 1984.

[2] S. T. Bramwell and M. J. P. Gingras. Spin Ice State in Frustrated Magnetic Pyrochlore Materials. *Science*, 294:1495–1501, 2001.

[3] I. A. Ryzhkin. Magnetic relaxation in rare-earth oxide pyrochlores. *Journal of Experimental and Theoretical Physics*, 101:481–486, 2005.

[4] C. Castelnovo, R. Moessner, and S. L. Sondhi. Debye-Hückel theory for spin ice at low temperature. *Physical Review B*, 84:144435, 2011.

[5] H. M. Revell, L. R. Yaraskavitch, J. D. Mason, K. A. Ross, H. M. L. Noad, H. A. Dabkowska, B. D. Gaulin, P. Henelius, and J. B. Kycia. Evidence of impurity and boundary effects on magnetic monopole dynamics in spin ice. *Nature Physics*, 9:34–37, 2013.

[6] G. Sala, M. J. Guttman, D. Prabhakaran, D. Pomaranski, C. Mitchelitis, J. B. Kycia, D. G. Porter, C. Castelnovo, and J. P. Goff. Vacancy defects and monopole dynamics in oxygen-deficient pyrochlores. *Nature Materials*, 13:488–493, 2014.

[7] C. Paulsen, M. J. Jackson, E. Lhotel, B. Canals, D. Prabhakaran, K. Matsuhira, S. R. Giblin, and S. T. Bramwell. Far-from-equilibrium monopole dynamics in spin ice. *Nature Physics*, 10:135–139, 2014.

[8] K. Kimura, S. Nakatsuji, J. J. Wen, C. Broholm, M.B. Stone, E. Nishibori, and H. Sawa. Quantum fluctuations in spin-ice-like $Pr_2Zr_2O_7$. *Nature Communications*, 2013.

[9] I. S. Grant and W. R. Philips. *Electromagnetism*. Wiley, 2^{nd} edition, 1990.

[10] P. A. M. Dirac. Quantised singularities in the electromagnetic field. *Proceedings of the Royal Society A*, 133, 1931.

[11] B. Cabera. First Results from a Superconductive Detector for Moving Magnetic Monopoles. *Physical Review Letters*, 48:1378–1381, 1982.

[12] J. D. Jackson. *Classical Electrodynamics*. Wiley, 3^{rd} edition, 1998.

[13] S. Blundell. *Magnetism in Condensed Matter*. Oxford, 1^{st} edition, 2001.

[14] M. J. Harris, S. T. Bramwell, D. F. McMorrow, T. Zeiske, and K. W. Godfrey. Geometrical Frustration in the Ferromagnetic Pyrochlore $Ho_2Ti_2O_7$. *Physical Review Letters*, 79(13):2554–2557, 1997.

[15] M. J. Harris, S. T. Bramwell, P. C. W. Holdsworth, and J. D. M. Champion. Liquid-Gas Critical Behaviour in a Frustrated Pyrochlore Ferromagnet. *Physical Review Letters*, 81(20):4496–4499, 1998.

[16] C. B. P. Finn. *Thermal Physics*. CRC Press, 2^{nd} edition, 1993.

[17] F. Mandl. *Statistical Physics*. Wiley, 2^{nd} edition, 1988.

[18] G. Toulouse. Theory of frustration effect in spin-glasses. 1. *Communications on Physics*, 2(4):115–119, 1977.

[19] J. D. Bernal and R. H. Fowler. A Theory of Water and Ionic Solution, with Particular Reference to Hydrogen and Hydroxyl Ions. *Journal of Chemical Physics*, 1(8):515–548, 1933.

[20] L. Pauling. *The Nature of the Chemical Bond*. Cornell University Press, 2^{nd} edition, 1948.

[21] L. Pauling. The Structure and Entropy of Ice and of Other Crystals with Some Randomness of Atomic Arrangement. *Journal of the American Chemical Society*, 57:2860–2864, 1935.

[22] W. F. Giauque and J. W. Stout. Entropy of Water and the Third Law of Thermodynamics. The Heat Capacity of Ice from 15 to 273K. *Journal of the American Chemical Society*, 58(7):1144–1150, 1936.

[23] E. A. DiMarzio and F. H. Stillinger Jr. Residual entropy of ice. *Journal of the Chemical Physics*, 40:1577, 1964.

[24] J. H. Bilgram and H. Gränicher. Defect Equilibria and Conduction Mechanisms in Ice. *European Physical Journal B*, 18(4):275–291, 1974.

[25] J. E. Greedan. Geometrically frustrated magnetic materials. *Journal of Materials Chemistry*, 11:37–53, 2001.

[26] J. S. Gardner, M. J. P. Gingras, and J. E. Greedan. Magnetic pyrochlore oxides. *Reviews of Modern Physics*, 82:54–101, 2010.

[27] J. Villain. Insulating spin glasses. *Zeitschrift für Physik B*, 33:31–42, 1979.

[28] J. S. Gardner, S.R. Dunsiger, B. D. Gaulin, M. J. P. Gingras, J. E. Greedan, R. F. Kiefl, M. D. Lumsden, W. A. MacFarlane, N. P. Raju, J. E. Sonier, I. Swainson, and Z. Tun. Cooperative paramagnetism in the geometrically frustrated pyrochlore antiferromagnet $Tb_2Ti_2O_7$. *Physical Review Letters*, 82(5):1012–1015, 1999.

[29] H. R. Molavian, M. J. P. Gingras, and B. Canals. Dynamically induced frustration as a route to a quantum spin ice state in $TB_2Ti_2O_7$ via virtual crystal field excitations and quantum many-body effects. *Physical Review Letters*, 98:237202, 2007.

[30] J. D. M. Champion, M. J. Harris, P. C. W. Holdsworth, A. S. Wills, G. Balakrishnan, S. T. Bramwell, E. Cizmar, T. Fennell, J. S. Gardner, J. Lago, D. F. McMorrow, M. Orendac, A. Orendacova, D. McK. Paul, R. I. Smith, M. T. F. Telling, and A. Wildes. $Er_2Ti_2O_7$: Evidence of quantum order by disorder in a frustrated antiferromagnet. *Physical Review B*, 68, 2003.

[31] C. Castelnovo, R. Moessner, and S. L. Sondhi. Magnetic monopoles in spin ice. *Nature*, 451:42–45, 2008.

[32] S. T. Bramwell, M. J. Harris, B. C. den Hertog, M. J. P. Gingras, J. S. Gardner, D. F. McMorrow, A. R. Wildes, A. L. Cornelius, J. D. M. Champion, R. G. Melko, and T. Fennell. Spin correlations in $Ho_2Ti_2O_7$: A dipolar spin ice system. *Physical Review Letters*, 87(4):047205, 2001.

[33] A. P. Ramirez, A. Hayashi, R. J. Cava, R. Siddharthan, and B. S. Shastry. Zero-point entropy in 'spin ice'. *Nature*, 399:333–335, 1999.

[34] P. W. Anderson. Ordering and Antiferromagnetism in Ferrites. *Physical Review*, 102(54):1008–1014, 1956.

[35] H. Kadowaki, N. Doi, Y. Aoki, Y. Tabata, T. J. Sato, J. W. Lynn, K. Matsuhira, and Z. Hiroi. Observation of Magnetic Monopoles in Spin Ice. *Journal of the Physical Society of Japan*, 78(10):103706, 2009.

[36] Zhou H. D. *et al.* High pressure route to generate magnetic monopoles in spin ice. *Nature Communications*, 1:1–2, 2011.

[37] X. Ke, B. G. Ueland, D. V. West, M. L. Dahlberg, R. J. Cava, and P. Schiffer. Spin-ice behaviour in $Dy_2Sn_{2-x}Sb_xO_{7+x/2}$ and Dy_2NbScO_7. *Physical Review B*, 76(21), 2007.

[38] M. J. P. Gingras and P. A. McClarty. Quantum spin ice: a search for gapless quantum spin liquids in pyrochlore magnets. *Reports on Progress in Physics*, 77:056501, 2014.

[39] J. Lago, I. Zivkovic, B. Z. Malkin, J. Rodriguez Fernandez, P. Ghigna, P. Dalmas de Reotier, A. Yaounac, and T. Rojo. $CdEr_2Se_4$: A new erbium spin ice system in a spinel structure. *Physical Review Letters*, 104(1):247203, 2010.

[40] R. F. Wang, C. Nisoli, R. S. Freitas, J. Li, W. McConville, B. J. Cooley, M. S. Lund, N. Samarth, C. Leighton, V. H. Crespi, and P. Schiffer. Artificial 'spin ice' in a geometrically frustrated lattice of nanoscale ferromagnetic islands. *Nature*, 439:303–306, 2006.

[41] C. Nisoli, R. Moessner, and P. Schiffer. *Colloquium* : Artificial spin ice: Designing and imaging magnetic frustration. *Rev. Mod. Phys.*, 85:1473–1490, 2013.

[42] L. D. C. Jaubert and P. C. W. Holdsworth. Magnetic Monopole Dynamics in Spin Ice. *Journal of Physics: Condensed Matter*, 5(4):258–261, 2011.

[43] B. C. den Hertog and M. J. P. Gingras. Dipolar interactions and origin of spin ice in ising pyrochlore magnets. *Physical Review Letters*, 84(15):3430–3433, 2000.

[44] M. E. J. Newman and G. T. Barkema. *Monte Carlo Methods in Statistical Physics*. Clarendon Press, 1999.

[45] S. V. Isakov, R. Moessner, and S. L. Sondhi. Why spin ice obeys the ice rules. *Physical Review Letters*, 93(16):167204, 2004.

[46] T. Fennell, P. P. Deen, A. R. Wildes, K. Schmalzl, D. Prabhakaran, A. T. Boothroyd, R. J. Aldus, D.F. McMorrow, and S. T. Bramwell. Magnetic Coulomb Phase in the Spin Ice $Ho_2Ti_2O_7$. *Science*, 326(5951):415–417, 2009.

[47] P. Debye and E. Huckel. The theory of electrolytes 1: lowering of freezing point and related phenomena. *Physikalische Zeitschrift*, 1923.

[48] W. Moore. *Physical Chemistry*. Longman, 4^{th} edition, 1978.

[49] L. Onsager. Deviations from ohm's law in weak electrolytes. *Journal of Chemical Physics*, 2:599–615, 1934.

[50] L. Bovo, X. Moya, D. Prabhakaran, Yeong-Ah Soh, A. T. Boothroyd, N. D. Mathur, G. Aeppli, and S. T. Bramwell. Restoration of the third law in spin ice thin films. *Nature Communications*, 2014.

[51] C. Jaccard. Thermodynamics of irreversible processes applied to ice. *Journal of Physics: Condensed Matter*, 3:99–118, 1964.

[52] D. J. P. Morris, D. A. Tennant, S. A. Grigera, B. Klemke, C. Castelnovo, R. Moessner, C. Czternasty, M. Meissner, K. C. Rule, J.-U. Hoffman, K. Kiefer, S. Gerischer, D. Slobinsky, and R. S. Perry. Dirac Strings and Magnetic Monopoles in the Spin Ice $Dy_2Ti_2O_7$. *Science*, 326:411–414, 2009.

[53] I. A. Ryzhkin and M. I. Ryzhkin. Screening of the magnetic field by magnetic monopoles in spin ice. *Journal of Experimental and Theoretical Physics Letters*, 93:426–430, 2011.

[54] L. Bovo, J. A. Bloxsom, D. Prabhakaran, G. Allepi, and S. T. Bramwell. Brownian motion and quantum dynamics of magnetic monopoles in spin ice. *Nature Communications*, 2013.

[55] K. S. Cole and R. H. Cole. Dispersion and absorption in dielectrics i. alternating current characteristics. *Journal of Chemical Physics*, 9:341–351, 1941.

[56] L. D. C. Jaubert, M. J. Harris, T. Fennel, R. G. Melko, S. T. Bramwell, and P. C. W. Holdsworth. Topological-Sector Fluctuations and Curie-Law Crossover in Spin Ice. *Physical Review X*, 3:011014, 2013.

[57] J. Snyder, B. G. Ueland, J. S. Slusky, H. Karunadasa, R. J. Cava, and P. Schiffer. Low-temperature spin freezing in the $Dy_2Ti_2O_2$ spin ice. *Physical Review B*, 69:064414, 2004.

[58] K. Matsuhira and Y. Hinatsu and K. Tenya and T. Sakakibara. Low temperature magnetic properties of frustrated pyrochlore ferromagnets $ho_2sn_2o_7$ and $ho_2ti_2o_7$. *Journal of Physics: Condensed Matter*, 12, 2002.

[59] S. T. Bramwell, S. R. Giblin, S. Calder, R. Aldus, D. Prabhakaran, and T. Fennell. Measurement of the charge and current of magnetic monopoles in spin ice. *Nature*, 461(7266):956–U211, 2009.

[60] S. T. Bramwell and S. R. Giblin. Comment on 'spin ice: Magnetic excitations without monopole signature using muon spin rotation'. *ArXiV*, 1111.4168v1, 2011.

[61] V. Kaiser, S. T. Bramwell, P. C. W. Holdsworth, and R. Moessner. ac wien effect in spin ice, manifest in nonlinear, nonequilibrium susceptibility. *Physical Review Letters*, 115:037201, 2015.

[62] S. R. Dunsiger, A. A. Aczel, C. Arguello, H. Dabkowska, M. H. Du, T. Goko, B. Javanparast, T. Lin, F. L. Ning, H. M. L. Noad, D. J. Singh, T. J. Williams,

Y. J. Uemura, M. J. P. Gingras, and G. M. Luke. Spin ice: Magnetic excitations without monopole signatures using muon spin rotation. *Physical Review Letters*, 107, 2011.

[63] M. Lees, L. J. Chang, and G. Balakrishnan. Magnetic correlations in yttrium diluted $Ho_{2-x}Ti_2O_7$ spin ice, 2011.

[64] G. C. Lau, R. S. Freitas, B. G. Ueland, B. D. Muegge, E. L. Duncan, P. Schiffer, and R. J. Cava. Zero-point entropy in stuffed spin-ice. *Nature Physics*, pages 249–253, 2006.

[65] G. Ehlers, J. S. Gardner, Y. Qiu, P. Fouquet, C. R. Wiebe, L. Balicas, and H. D. Zhou. Dynamic spin correlations in stuffed spin ice $Ho_{2+x}Ti_{2-x}O_{7-\delta}$. *Physical Review B*, 77, 1905.

[66] D. Pomaranski, L. R. Yaraskavitch, S. Meng, K. A. Ross, H. M. L. Noad, H. A. Dabkowska, B. D. Gaulin, and J. B. Kycia. Absence of pauling's residual entropy in thermally equilibrated $Dy_2Ti_2O_7$. *Nature Physics*, 2013.

[67] B. Klemke. *Thermal Properties of Dysprosium Titanate in the Spin-Ice State*. PhD thesis, Technischen Universität Berlin, 2011.

[68] R. G. Melko, B. C. den Hertog, and M. J. P. Gingras. Long-range order at low temperatures in dipolar spin ice. *Physical Review Letters*, 87(6):067203, 2001.

[69] R. G. Melko and M. J. P. Gingras. Monte Carlo studies of the dipolar spin ice model. *Journal of Physics: Condensed Matter*, 16:R1277–R1319, 2004.

[70] H. W. J. Blöte, R. F. Wielinga, and W. J. Huiskamp. Heat capacity measurements on rare earth double oxides $r_2m_2o_7$. *Physica*, 43:549–568, 1969.

[71] Z. Hiroi, K. Matsuhira, S. Takagi, T. Kayama, and T. Sakakibara. Specific heat of kagomé ice in the pyrochlore oxide Dy2Ti2O7. *Journal of the Physical Society of Japan*, 72:411–418, 2003.

[72] R. Siddharthan, B. S. Shastry, A. P. Ramirez, A. Hayashi, R. J. Cava, and S. Rosenkranz. Ising Pyrochlore Magnets: Low-Temperature Properties, "Ice Rules," and Beyond. *Physical Review Letters*, 83(9):1854–1857, 1999.

[73] R. Siddharthan, B. S. Shastry, and A. P. Ramirez. Spin ordering and partial ordering in holmium titanate and related systems. *Physical Review B*, 63:184412, 2001.

[74] S. T. Bramwell. Private communication.

[75] L. Bovo and S. T. Bramwell. Determination of the entropy via measurement of the magnetization: application to the spin ice $Dy_2Ti_2O_7$. *Journal of Physics - Condensed Matter*, 25, 2013.

[76] V. Kaiser. Private communication.

[77] I. A. Ryzhkin and R. W. Whitworth. The configurational entropy in the jaccard theory of the electrical properties of ice. *Journal of Physics: Condensed Matter*, 9:395–402, 1997.

[78] I. A. Ryzhkin, M. I. Ryzhkin, and S. T. Bramwell. Dynamic susceptibility and dynamic correlations in spin ice. *Europhysics Letters*, 104:1–5, 2013.

[79] N. Bjerrum. *Matematisk-Fysiske Meddelelser udg af Det Kongelige Danske Videnskabernes Selskab*, 7:43–57, 1926.

[80] V. Kobelev, A. B. Kolomeisky, and M. E. Fisher. Lattice models of ionic systems. *Journal of Chemical Physics*, 116(17), 2002.

[81] D. Prabhakaran and A. T. Boothroyd. Crystal growth of spin-ice pyrochlores by the floating-zone method. *Journal of Crystal Growth*, 318:1053–1056, 2011.

[82] R. D. Shannon and C. T. Prewitt. Effective ionic radii in oxides and fluorides. *Acta Crystallographica Section B - Structural Crystallography and Crystal Chemistry*, 25:925–946, 1969.

[83] J. Emsley. *The Elements*. Oxford, 1989.

[84] M. B. Johnson, D. D. James, A. Bourque, H. A. Dabkowska, B. D. Gaulin, and M. A. White. Thermal properties of the pyrochlore $Y_2Ti_2O_7$. *Journal of Solid State Chemistry*, 182:725–729, 2009.

[85] J. R. Hook and H. E. Hall. *Solid State Physics*. Wiley, 2^{nd} edition, 2008.

[86] V. Kaiser. *The Wien Effect In Electric and Magnetic Coulomb Systems: From Electrolytes to Spin Ice*. PhD thesis, Ecole Normale Superieure de Lyon, 2014.

[87] J. Kang, M. Ruan, X. Chen, C. Liu, W. Liu, F. Guo, and J. Chen. Growth and magneto-optical characteristic of $Dy_2Ti_2O_7$ crystal. *Optical Materials*, 36:1266–1269, 2014.

[88] Q. J. Li, L. M. Xu, C. Fan, F. B. Zhang, Y. Y. Lv, B. Ni, Z. Y. Zhao, and X. F. Sun. Single crystal growth of the pyrochlores $R_2Ti_2O_7$ (r=rare earth) by the optical floating-zone method. *Journal of Crystal Growth*, 377:96–100, 2013.

[89] T. Yavors'kii, T. Fennell, M. J. P. Gingras, and S. T. Bramwell. $Dy_2Ti_2O_7$ spin ice: A test case for emergent clusters in a frustrated magnet. *Physical Review Letters*, 101, 2008.

[90] G. C. Lau, R. S. Freitas, B. G. Ueland, P. Schiffer, and R. J. Cava. Geometrical magnetic frustration in rare-earth chalcogenide spinels. *Physical Review B*, 72, 2005.

[91] C. Paulsen and S. T. Bramwell. Private communication.

[92] O. Petrenko and S. T. Bramwell. Private communication.

[93] L. Balents. Quantum spin liquids. *Nature*, 1464:199–208, 2010.

[94] M. Hermele, M. P. A. Fisher, and L. Balents. Pyrochlore photons: The u(1) spin liquid in a s=1/2 three-dimensional frustrated magnet. *Physical Review B*, 69(6), 2004.

[95] K. Matsuhira, C. Sekine, C. Paulsen, M. Wakeshima, Y. Hinatsu, T. Kitazawa, Y. Kiuchi, Z. Hiroi, and S. Takagi. Spin freezing in the pyrochlore antiferromagnet $Pr_2Zr_2O_7$. *Journal of Physics: Conference Series*, 145:012031, 2009.

[96] A. Aharoni. Demagnetising factors for rectangular ferromagnetic prisms. *The Journal of Applied Physics*, 83:3432–3434, 1998.

[97] A. Legros, D. H. Ryan, P. Dalmas de Réotier, A. Yaouanc, and C. Marin. Er mössbauer spectroscopy study of magnetic ordering in a potential spin-ice system: $CdEr_2S_4$. *Journal of Applied Physics*, 117:17C701, 2015.

[98] P. C. Guruciaga, S. A. Grigera, and R. A. Borzi. Monopole ordered phases in dipolar and nearest-neighbors ising pyrochlore: From spin ice to the all-in-all-out antiferromagnet. *Physical Review B*, 90:184423, 2014.